POWER HARVESTING FROM SHOCK WAVES:
THE AXIAL BLADELESS TURBINE
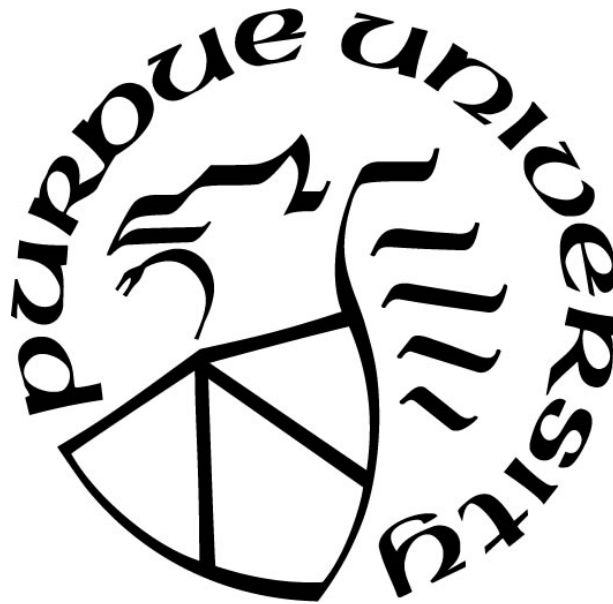
by

James Braun

A Dissertation

Submitted to the Faculty of Purdue University

In Partial Fulfillment of the Requirements for the degree of

Doctor of Philosophy

School of Mechanical Engineering

West Lafayette, Indiana

August 2019

THE PURDUE UNIVERSITY GRADUATE SCHOOL
STATEMENT OF COMMITTEE APPROVAL

Dr. Guillermo Paniagua
> School of Mechanical Engineering

Dr. Johnathan Poggie
> School of Aeronautics and Astronautics

Dr. Sergey O. Macheret
> School of Aeronautics and Astronautics

Dr. Terry R. Meyer
> School of Mechanical Engineering

Approved by:
> Dr. Jay Gore
>> Head of the Graduate Program

To my Mother, Sister and the Others

Balance ton quoi, un jour peut-être ça changera

(Angèle, 2019)

ACKNOWLEDGMENTS

I would like to thank my advisor Guillermo Paniagua for the countless past, present and future discussions, over the phone, on the plane or around a good glass of Petal wine. The light he sheds on complex technological matter struck me from the moment I met him in 2013 in the VKI, when he asked me if I was 'up for a challenge'. I'm proud to say that the journey so far was in fact a Challenge. This quest for problem solving was already nurtured to me by Kris Delcroix, who taught us about the Ancient Greek philosophers and learned to take nothing for granted. I would also like to acknowledge many other good professors from the Sint Jan Berchmanscollege, such as Mme Duville, Mijnheer Liessens and Mme Cappaert. Education boils down to a mix of family, friends and environment. Thomas, Alexis, Laurent and Antoine showed me the value of cross-cultural thinking, open-mindedness and self-criticism, and I will be eternally grateful to them. At the university, an entirely new world opened, this thanks to Klaas, Maarten, Smedts, Ellen, Dorien, Daphne, Marielien, … with wonderful memories. The countless hours studying in Halle with Thomas and Lexy created a special bond between us that will hopefully last for several decades to come and nourished the idea that science in fact is a fascinating marvel. A special mention goes to the grandparents of Thomas, their heartwarming hospitality made the impossible possible, and we all graduated. From the other spectrum, Alice, Astrid, Tessa, Nico and Antoine reminded me on a weekly basis with the Scouts as well as with VPT how empty and shallow life would be if one would only think about himself. The eagerness to perform cutting-edge research continued in the von Karman institute for Fluid Dynamics, and I would like to thank all my international friends, with a special mention to Bayindir and the *Container* group – Jacky, Lizzy and Nicol. I'd like to take the time to remember Eric Van den Bulcke, my official supervisor from the KUL. His wise words to go out, conquer the world and return with 'useful engineering skills' still daily resonate. While I embarked my PhD at Purdue, Jorge Sousa welcomed me with open arms after proving myself first worthy of his time. I greatly admire his passion and knowledge about supersonic and infrasonic flow and proudly call myself his student (even if it's hard to admit). *Mama* Valeria… I guess without her, I was still stuck somewhere in Belgium trying to fill out all the documents to go to Purdue (or still stuck in Brazil). Our daily or hourly discussions were filled with most intense moments of stress, anger but also happiness, success and heartwarming moments. No pain, no gain. And I'm now proud to say we are business partners, hence I'd like to raise a glass to Petal Solutions.

Πάντα ῥεῖ,

James Braun

TABLE OF CONTENTS

LIST OF TABLES

LIST OF FIGURES

NOMENCLATURE

Roman Symbols

$\dot{m}$	Mass flow [kg/s]
$\tilde{m}$	Reduced mass flow [-]
$\tilde{n}$	Reduced speed [-]
c_p	Heat capacity [kJ/kg K]
A	Amplitude of the wavy wall [m]
d	Axial hub entrance distance [m]
f	Frequency [Hz]
h	Hub-to-shroud height [m]
h_{ad}	Adiabatic heat transfer coefficient [W/(Km^2)]
H_f	Power spectral density [1/Hz]
L	Axial length of the turbine [m]
L_C	Characteristic length for the Strouhal number [m]
M	Mach number [-]
m	Mode number [-]
p	Pressure [Pa]
p_{loss}	Mass-flow averaged total pressure loss [-]
Q	Heat flux [W/m^2]
P	Power [kW]
R	Radius [m]
Re	Reynolds [-]
RPM	Rotational speed [rpm]
s	Entropy [J/(kgK)]
s	Oblique shock angle [deg]
St	Strouhal [-] $= \dfrac{f L_{charactersitic}}{u}$
t	Time [s]

T	Temperature [K]
T	Torque [Nm]
V	Voltage [V]
W	Number of waves [-]
y	Tangential coordinate [m]
y^+	Non-dimensional wall distance [-]
z	Axial coordinate [m]

Greek symbols

α_{flow}	Flow angle in the absolute frame of reference [deg]
α_{helix}	Helix angle [deg]
β	Relative flow angle [deg]
γ	Flow angle with respect to the helix angle [deg]
δ	Shock angle [deg]
$\delta 2$	Momentum thickness [mm]
Δt	Time step between frames [ms]
λ	Eigenvalue of an eigenmode [-]
λ	Wavelength of the incoming light [mm]
θ	Tangential angle [rad]
θ_i	Angle between local normal and incident light [rad]
ω	Rotational speed [rad/s]
τ	Shear stress [Pa]
$\tilde{\tau}$	Reduced torque [-]
φ	Mode number [-]
φ	Phase of the shock [-]
Φ	Phase of the fringe [rad]
μ	Dynamic viscosity [Pa.s]
ν	Kinematic viscosity [m^2.s]

Abbreviations

2D	Two-Dimensional
3D	Three-Dimensional
ALTP	Atomic Layer Thermopile
BOS	Background Oriented Schlieren
CFD	Computational Fluid Dynamics
CFL	Courant Friedrichs Lewy number
CFD++	CFD solver developed by Metacomp Technologies
CPU	Central Processing Unit
DNS	Direct Navier Stokes
DMD	Dynamic Mode Decomposition
FFT	Fast Fourier Transform
FLEET	Femtosecond Laser Electronic Excitation Tagging
HP	High Performance
LEAF	Linear Experimental Aero-thermal Facility
PETAL	Purdue Experimental Turbine Aerothermal Lab
PIV	Particle Image Velocimetry
POD	Proper Orthogonal Decomposition
SPOD	Spectral Proper Orthogonal Decomposition
PSP	Pressure Sensitive Paint
(U)RANS	(Unsteady) Reynolds Averaged Navier Stokes
RMS	Root Mean Square
SA	Spalart Allmaras
SBLI	Shock boundary layer interaction
SST	Menter's Shear Stress Transport
STD	Standard deviation
TRL	Technical Readiness Level
TVD	Total Variation Diminishing

Subscripts

AC	The unsteady fluctuations around the mean of a signal
ad	Adiabatic
DC	The mean value of an unsteady signal
irr	Irreversibility
is	Isentropic
nom	Nominal
0	Total/stagnation conditions
1	Inlet of the turbine
2	Outlet of the turbine
3	Outlet of the turbine if used as bottoming cycle
ϑ	Tangential component
SS	Steady-state value or value from steady simulation
p	Contribution from pressure
ref	Reference
rel	In the relative frame of reference

ABSTRACT

Author: Braun, James. PhD
Institution: Purdue University
Degree Received: August 2019
Title: Power Harvesting from Shock Waves: The Axial Bladeless Turbine
Committee Chair: Guillermo Paniagua

A new class of bladeless turbines was developed which allows for power extraction from harsh environments with minimal maintenance cost. This is achieved through a wavy hub surface that promotes shocks and expansion fans and hence generates torque besides trust if used as bottoming or topping cycle.

A numerical procedure to design, mesh, and model this new expansion device through steady and unsteady Reynolds Averaged Navier Stokes simulations is outlined. Then, the full three-dimensional flow field is replicated using a two-dimensional geometry to enable a simpler test section with full optical access at the Purdue Experimental Turbine Aerothermal Lab. Pressure, heat flux, and skin friction are computed via several measurement techniques to provide an accurate estimation of the uncertainties on the power, efficiency, and heat flux of the bladeless turbine. High-frequency pressure sensors (160 kHz) along with a high-frequency heat flux sensor (atomic layer thermopile) are used to characterize the unsteady phenomena on the hub and the shroud. Unsteadiness in the flow field is assessed through 10 kHz shadowgraph, density gradients are quantitatively assessed via 3 kHz Background Oriented Schlieren, and unsteady velocity components and flow angles are characterized with 1 kHz Femtosecond Laser Electronic Excitation Tagging. A reduced order model is constructed with Spectral Proper Orthogonal Decomposition to retrieve the dominant frequencies in the flow field, which could be associated with a multitude of shock-boundary layer, shock-shock, and shock-shear layer interactions.

A parametric study and multi-objective optimization to maximize power extraction while minimizing pressure loss and heat flux are performed. The operational envelope and scaling of the bladeless turbine are described for several reduced mass flows, reduced speeds, and swirl angles. Based on all the gathered simulations, a guideline for the design of bladeless turbines is provided.

Finally, the operation of the bladeless turbine is analyzed considering the unsteady propagation of a rotating oblique shock throughout the passage. Non-dimensional parameters to generically describe rotating shocks are discussed, and their influence on the operation of the turbine is assessed. Correction terms for the power and pressure loss during the unsteady operation of the bladeless turbine are developed with results of this section.

CHAPTER 1.   INTRODUCTION

1.1   Scientific background

Conventional turbomachinery is constraint by maximum inlet turbine temperature, high maintenance cost as well as flow distortion across the different rows. Furthermore, novel turbine-based combined cycles include combustors delivering high subsonic to supersonic axial outlet flows [1], alas conventional turbines are designed to operate efficiently at inlet Mach numbers of around 0.1 and require advanced cooling and special materials to withstand such conditions. Paniagua et al. [2] showed that a conventional turbine subjected to an inlet Mach number of 3.5 has pressure losses over 80% and is unstarted. Unstarting is a phenomenon in which the isentropic limit (for subsonic flows) or the Kantrowitz limit [3] (for supersonic flows) is not satisfied and the turbine cannot ingest the entire inlet mass flow. Consequently, a pressure or shock wave builds up in front of the turbine and travels upstream towards the combustor. Hence, new classes of expansion devices are currently being developed and investigated that can efficiently handle such high-subsonic and supersonic flows.

The first new class of turbines in which the Mach number is below one integrates ad-hoc diffusers with the turbine [4], as depicted in Figure 1.1a. Efficiencies beyond 80% can be achieved. However, such devices are prone to boundary-layer separation at off-design operation which may result in a significant pressure loss [5].

For supersonic inlet conditions, special axial turbines were developed in which the axial Mach number remains supersonic throughout the passage [6]. The supersonic turbine is characterized by slender blade shapes to limit shock losses with a low amount of turning (Figure 1.1b). This turning (and consequent power extraction) is constrained by the Kantrowitz limit. Through an engine analysis, it was proven that for supersonic flights, a low-pressure ratio turbojet equipped with a supersonic turbine could be up to five percent more fuel efficient than conventional turbojet engines [7].

The third class of expansion machines consists of radial outflow turbines, such as the design discussed by Inhestern et al. [8] and as described in a provisional patent [9]. In this type of turbine, high Mach numbers can be efficiently converted into higher amounts of power at the expense of a radial supersonic jet leaving the turbine.

The fourth class of such fluid machine is the bladeless turbine (Figure 1.1c). Vinha et al. [10] proposed an axial bladeless turbine (MBDA patent EP 2868864 [11]) operating in the steady supersonic flow regime (flows with Mach number around 3.5 and an inlet relative swirl angle of 16 degrees). In this smooth/flat axial bladeless turbine, the power is extracted by only using the viscous forces. Additionally, a pre-swirler or nozzle guide vanes are needed to generate power (absolute inlet flow angle of 30 degrees [10]). The power extraction was explained through velocity triangles, and the effect of the viscous forces was studied via steady Reynolds Averaged Navier Stokes (RANS) simulations. Bladeless power extraction provides significant benefits for flows exposed to high speeds. Nikola Tesla introduced this concept for radial bladeless turbines in 1913, driven only by the viscous forces of the flow impinging on the rotating disks [12]. Li et al. [13] recently carried out experimental and numerical work for a Tesla turbine exposed to an incompressible fluid. Neckel and Godinho [14] designed convergent-divergent nozzles for Tesla turbines using air as working fluid. Schmidt reported the use of radial bladeless turbines for power production from biomass combustion and achieved efficiencies from 11 to 16% [15]. For an axial turbine, a power extraction up to 0.4 MW was achieved for a bladeless turbine with a length of 0.7 m and with a hub radius of 0.345 m and an inlet flow angle of 30 deg. [10]. Unlike the bladed turbines, the current concept can handle a wide range of supersonic operating points, without experiencing unstarting, with simpler end wall cooling, and easier maintenance costs. Bladeless turbines may be additionally used as a topping or bottoming cycle, to drive the auxiliary power system, at the expense of limited pressure losses documented in this manuscript. Currently, the only identified contributor to the power generation within bladeless turbines is the shear force. The unexplored mechanism to extract power through shock waves in bladeless turbines could significantly increase the power extraction. The first documentation of shock waves and their interaction with the boundary layer dates back to the 1940s (Ferri [16], Donaldson [17], and Fage and Sargent [18]).
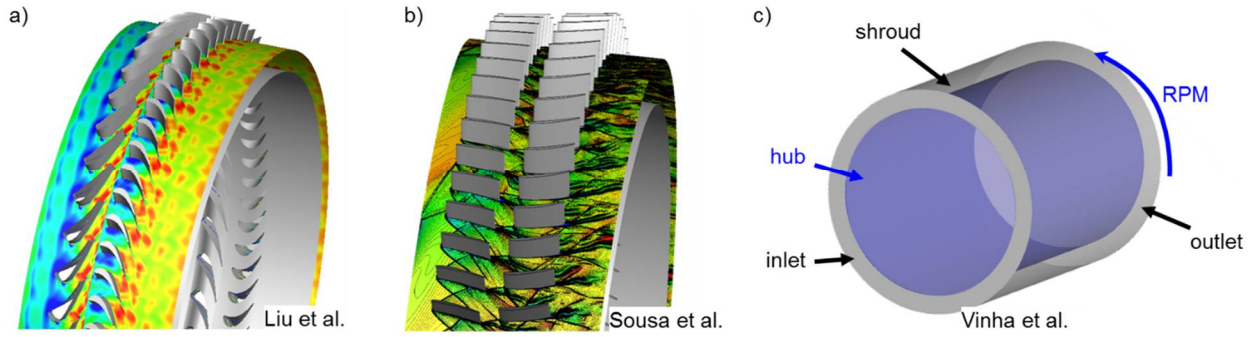
Figure 1.1 New classes of fluid machines for high inlet Mach number flows: a) subsonic turbine with a modified end wall, b) supersonic axial turbine and c) bladeless turbine

For these new types of turbines, most studies were based on steady state results. Conventional subsonic turbines operate at *steady state* inlet conditions with an inlet Mach number around 0.1 and turbulence intensity of the order of magnitude of 10-20% for state-of-the-art combustors [19]. This level of unsteadiness can drastically increase when dealing with new engine architectures. For supersonic flows, a canonical test case is a rotating oblique shock. Figure 1.2 shows this test case in which the unsteadiness is a rotating oblique shock moving through the turbine channel, as described in [20]. For unsteady supersonic turbines, moving shocks can cause a 100% increase of pressure loss throughout the stator and rotor [21]. Fernelius et al. [22] experimentally retrieved efficiencies of 61% for conventional subsonic turbines for an inlet flow oscillating at 40 Hz and with an amplitude of unsteadiness of 40%. Currently, no device can survive in a wide range of extreme conditions while efficiently extracting power.
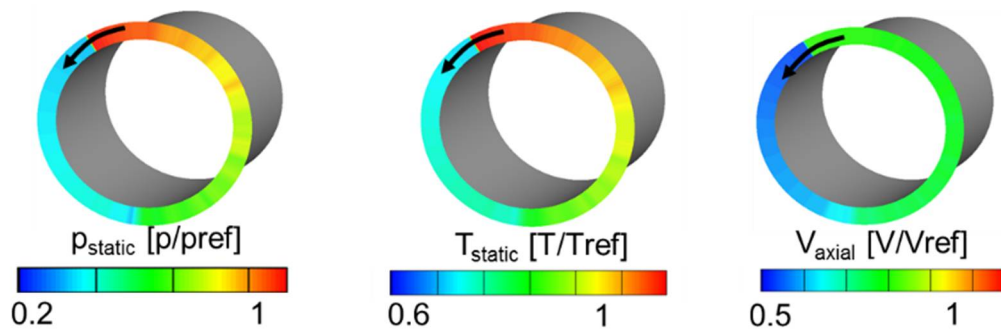
Figure 1.2 Canonical test case of a rotating oblique shock that propagates through a channel at supersonic speeds

1.2   Objectives

The main objective of this thesis is to ***engineer and characterize a power extraction device without airfoils suitable for high inlet Mach numbers and understand the fundamental flow principles that control the work exchange.*** Current bladeless turbines designs are constrained to a limited range of applications for two main reasons.

First, <u>limited power extraction:</u> power extraction is over 50 times less compared to supersonic turbine designs and is only possible in flows with a tangential velocity component. Additionally, these tangential velocity components need to be higher than the rotational speed of the hub. The only force contributing to the power is the viscous force, no public literature is available in which the pressure forces are exploited.

Second, <u>heat management:</u> heat flux levels in this type of turbines have not been investigated. For supersonic and hypersonic applications, heat flux is critical and needs to be characterized in detail so that appropriate cooling mechanisms can be implemented within the hub and shroud.

To address the main objective, three other objectives are to be fulfilled:

Determine the uncertainty on the numerical results: The most recent publications [10] mention numerical results up to 0.4 MW/m. However, uncertainty on the numerical results and accuracy of the solvers for this type of operation is not reported.W Uncertainty on power, efficiency, and heat flux levels are required to correct and develop high accuracy tools.

Geometrical optimization of this new class of axial bladeless expansion system and define its operational envelope: Since the last decade, multi-objective optimization strategies for turbomachinery applications have gained great interest [23][24]. Differential evolution algorithms in which every individual (a geometry with a specific feature) is consequently meshed, solved, and post-processed, allow for a cost-effective way to optimize complicated jobs [25]. This new expansion device is required to operate in harsh conditions with minimum pressure loss and heat flux while maximizing power extraction and correctly conditioning the flow for successive downstream components. Additionally, all features of the new turbine need to be investigated to enable design schemes for future engine manufacturers. Finally, the operational envelope of new

turbines is constrained by both on- and off design performance and hence needs to be evaluated as well.

Determine the operation when the passage is exposed to rotating oblique shocks: The effect of unsteady flows has not been considered in bladeless turbines. Moving/rotating shock waves might enhance power extraction due to the sudden pressure rise behind the shock or reduce the power due to sudden flow angle variations behind the shock wave and induce additional pressure losses. Additionally, the passing of a shock wave at supersonic speeds, induce high local heat flux values that need to be quantified.

1.3   Methodology

To address **the abovementioned objectives**, a research methodology that consists of five points is followed:

(A)   Development of the numerical and experimental tools to be able to numerically quantify the properties of the turbine and its associated uncertainties:

To analyze this new type of turbine, a numerical strategy like conventional subsonic turbines is followed, i.e. appropriate meshing software and solving tools need to be selected. For the supersonic experiments in the Linear Experimental Aerothermal Facility (LEAF) at the Purdue Experimental Turbine Aerothermal Lab (PETAL), a series of high frequency and low-frequency measurement techniques are developed to enable the quantification of the different surface properties and supersonic flow field features.

(B)   Characterize the main flow mechanisms through three-dimensional simulations and conceive a procedure to go from a complex three-dimensional geometry to a two-dimensional model:

The baseline turbine is planned to be exposed to a Mach 1.25 inflow. The generated power is assessed along the axial direction and mass-flow averaged total pressure loss is also evaluated. To dissect the power extraction and loss mechanisms in a complex three-dimensional unsteady flow,

the problem is simplified to a steady two-dimensional problem. This allows for a more fundamental analysis both experimentally, through testing in the LEAF facility, and numerically.

(C)   Detailed experimental analysis of the simplified turbine passage with both low- and high-frequency measurement systems:

An experimental validation of the simplified bladeless turbine passage is started by building a suitable and modular test article. The critical steady-state turbine performance parameters (surface pressure, skin friction and heat flux on the hub) are assessed through an array of measurement techniques. The flow structures are analyzed via Schlieren and shadowgraph visualization. Molecular tagging (FLEET) and Background Oriented Schlieren (BOS) deliver velocity and density gradient fluctuations. Piezo-resistive sensors (Kulites) and an Atomic Layer Thermopile (ALTP) quantify pressure and heat flux fluctuations which allow for a frequency analysis on the wall. Model reduction tools such as Proper Orthogonal Decomposition and Spectral Proper Orthogonal Decomposition tools are used to analyze the spatio-temporal behavior. Finally, an uncertainty analysis on efficiency, power and heat flux is performed by considering all the reported measurements.

(D)   Optimization of the bladeless turbine via numerical tools after obtaining the uncertainty:

First, the most important features of the bladeless turbine are characterized, and the operational envelope is analyzed for several reduced mass flows and mechanical speeds as well as swirl angles. Irreversibility is assessed to retrieve the loss mechanisms. A two-dimensional RANS solver is coupled to a differential evolution multi-objective optimizer where the wavy surface is parameterized based on a cubic spline interpolation. The procedure is scripted to automatically generate the profile, mesh the geometry, and solve the RANS equations. The shape is optimized to maximize power and minimize pressure loss and heat flux.

(E)   Assessment of unsteadiness of the bladeless turbine exposed to a plurality of rotating shock waves to identify power, pressure loss, and heat flux:

Unsteady boundary conditions enable quantifying the operation of the bladeless turbine exposed to the rotating shocks via unsteady Reynolds Averaged Navier Stokes (URANS) simulations and comparing against the mass-flow averaged steady operational point. The rotating oblique shock parameters are characterized by non-dimensional numbers to generalize the results. Based on the shock speed and the shock amplitudes, corrections are proposed to account for the unsteady power, total pressure loss and heat flux.

1.4   Outline of the manuscript

Each chapter addresses a step in the methodology to fulfil the different objectives according to the order described in the Section 1.3. Chapter two outlines all numerical as well as experimental tools needed to quantify the uncertainty on the obtained numerical results (**A**). The third chapter details the proposed design of the fluid machine that operates at steady supersonic axial speeds. First, the parametrization, meshing, and solving of the baseline case is addressed along with the breaking down of the work extraction principle from a three-dimensional unsteady problem onto a two-dimensional steady phenomenon (**B**). The fourth chapter outlines the experimental campaign to test this two-dimensional model of the bladeless turbine in PETAL's linear wind tunnel (**C**). Chapter six discusses the operational envelope and introduces an implemented numerical routine coupled to a multi-objective optimizer. A two-dimensional approach is proposed to increase power while reducing heat load and total pressure loss throughout the channel. The chapter is concluded with design guidelines for bladeless turbines based on all the assessed geometries (**D**). In the last chapter, the canonical test case of a rotating shock traveling throughout the bladeless turbine is dissected via URANS simulations (**E**). Time-averaged of mass-flow averaged total pressure loss and power are calculated for multiple non-dimensional parameters of the traveling shock. Finally, steady and unsteady heat flux are compared.

CHAPTER 2.   EXPERIMENTAL AND NUMERICAL TOOLS

Numerical and experimental tools developed for this study are discussed in this chapter.

2.1   Numerical Tools

To investigate this particular supersonic passage with a systemic method, the geometry requires to be discretized and solved with high fidelity.

2.1.1   Mesh generation

For fast calculations and simplified two-dimensional geometries, a **structural** grid is generated. The surface is parametrized in Matlab and subsequently imported into Ansys Icem CFD. Icem CFD employs quadrilateral grid cells for two-dimensional meshes. The first layer thickness, y+ is below one for the two-dimensional simulations to ensure that the viscous sublayer is correctly solved.

More complicated geometries are meshed via an **unstructured** mesher Hexpress from Numeca. Hexpress can fit non-conformal body-fitted hexahedral unstructured meshes on the two- and three-dimensional bladeless turbine shape. Furthermore, ad-hoc boundary layer insertion is possible in the final step of the five-step mesh procedure:

- The first step consists of an initial mesh generation that covers the simplified boundaries of the entire computational domain.

- The second step adapts the initial mesh to the geometry, such that the cells generated in step 1 satisfy the geometry. In this step, custom curve and surface refinements can be added to the mesh.

- In the third step, the mesh is snapped onto the geometry while covering the edges and corners. Additional cells are inserted to retrieve smooth hexahedral cells.

- Distorted cells are removed through the optimization step.

- The final step is the viscous layer insertion in which a user-defined number of viscous layers is added with a certain expansion ratio.

2.1.2   Numerical Solver

The commercial software CFD++ developed by Metacomp Technologies [26] was used for the numerical simulations. This is a finite-volume density-based solver where the convective fluxes are calculated with the Harten-Lax-Van Leer-contact approximate Riemann scheme [27]. Interpolation of the spatial variables is performed through a second-order total variation diminishing (TVD) polynomial interpolation with a continuous limiter for stability reasons. We use an implicit time-integration method based on dual-time stepping with a fixed global time step and local Courant–Friedrichs–Lewy (CFL) number variation. Local iteration is accelerated through a multigrid acceleration scheme based on 4 multigrid cycles. For the unsteady simulations, the time step is kept at 1×10^{-6} s and the inner iterations per time step were set to a convergence of 0.01.

Type of boundary conditions

Subsonic inlet: Total pressure and temperature are imposed at the inlet. The user can select a uniform inlet or impose a pressure and temperature profile.

Supersonic inlet: All velocity components, pressure, and temperature are imposed. This can be either a uniform value or a user-defined non-uniform inlet. Additionally, unsteady inlet boundary conditions can be imposed, and unsteady pressure, temperature and velocity components are then imported from a *.txt* file generated from a Matlab script. This is then consecutively converted into a CFD++ file in which temperature, pressure and velocity components are prescribed.

Walls: Adiabatic simulations are selected by default and a zero heat flux is imposed at the walls. For heat flux calculations, however, isothermal walls are used. In all simulations, the boundary layer is solved up to the wall without the need for wall functions. Hence for all meshes, the first layer wall thickness (y^+) below 1 was required.

Outlet: By default, a back pressure is imposed. The boundary condition is characteristics-based, hence if all characteristics are traveling downstream (e.g., for supersonic flows), the outlet pressure is interpolated from the internal field and hence ignoring the imposed back pressure.

Periodicity: For the three-dimensional simulations of the turbine passage, periodic boundary conditions are employed to reduce computational cost.

Conjugate heat transfer**:**

To solve the **heat conduction** in the solid via the Fourier equation, the conjugate heat transfer solver of Metacomp is used. As boundary condition, the *solid-to-fluid* is used to connect the fluid and the solid blocks. With the zonal boundary conditions at the interface, CFD++ allows for a coupled solution to be computed simultaneously across all zones, with a two-way transfer of heat across the zonal boundaries formed between the zones. Thermal conductivity, density and specific heat of the solid heat need to be provided and are considered constant throughout the material

Grid sensitivity

A grid independence study was performed for each case to determine the grid density based on a grid convergence study [28], and more detailed information can be found in [29]. Dependence of the numerical accuracy with the first cell size (in terms of y+), time discretization, and the total number of cells were retrieved based on the Richardson extrapolation method [30]. For unsteady simulations, the method of Clover and Clark can be employed through the intersection of several fuzzy sets to assess periodic convergence [31].

2.1.3 Computational resources

Most of the simulations were run on Rice cluster, which is a High performance (HP) computing cluster. The cluster consists of Intel Xeon –E5-2660 v3 processor @ 2.6 Ghz (64 GB RAM) on the RICE Purdue cluster. Typically, three-dimensional steady simulations required 1 node with 16 cores with a CPU time of eight to twelve hours. Two-dimensional simulations were run on two to four cores. The three-dimensional full unsteady simulation required up to three nodes

and around two to three weeks of simulation time to achieve periodic convergence. Post processing was performed in Matlab and Tecplot.

2.1.4   Model reduction tools

Reduced order models are numerical tools designed to extract the critical features of a high-dimensional dataset. Such features -also referred to as modes- can later be used to describe the main physical processes happening in the dynamical system of interest. Three methods that target coherent structures in space, time or a combination of those are introduced here.

2.1.4.1   Spatial modes

Proper orthogonal decomposition (POD) is selected to define the spatial modes ($\varphi(x)$) of the system. Via this technique, basis functions are retrieved in which most of the energy of the system is concentrated. If one assumes snapshots of a certain quantity $q(x,t)$ (e.g., pressure, temperature, density gradient, etc.) as a function of time (t) and space (**x**), one can build a correlation tensor as

$$K = q_{nxm} \ q_{nxm}^{T} \ \in \ \mathbb{R}^{nxn} \qquad \text{Eq. 2.1}$$

Farhat and Amsallem [32] reported that the eigenvalues from either multiplying $q_{nxm} \ q_{nxm}^{T}$ or $q_{nxm}^{T} q_{nxm}$ will be equal and hence the multiplication with the smallest dimension should be selected to reduce the computational burden. The eigenvalue problem for this is stated as:

$$K\varphi_i(x) = \lambda_i \varphi_i(x) \ \text{with i=1,...,N} \qquad \text{Eq. 2.2}$$

Each mode can then be reconstructed as:

$$a(t)_j = q(x,t)\varphi(x) \qquad \text{Eq. 2.3}$$

The entire flow field can be reconstructed with:

$$q(x,t) = \sum_{j=1}^{\infty} a(t)_j \varphi(x) \qquad \text{Eq. 2.4}$$

The eigenvectors are orthogonal and provide a complete basis, and the spatial features of the flow can be optimally characterized by these modes [33]. If, however, the dominant coherent structures happen both in time and space, POD might not be the most suitable method to analyze the flow. In POD, time is a stochastic parameter, and the order of the timesteps does not matter.

2.1.4.2 Temporal modes

To find the optimal models that are temporally coherent, Dynamic Mode Decomposition (DMD) [34][35] is preferred which is similar to POD for space. For zero-mean flow, DMD is equivalent to a discrete Fourier transform (DFT). DMD, however, is not suitable if the structures are strongly coherent in both space and time [36].

2.1.4.3 Spatio-temporal modes

To be able to analyze modes that are dependent on both time and space, recently Spectral Proper Orthogonal Decomposition (POD) was proposed by Sieber et al. [36]. Additionally, Towne et. al compared SPOD with traditional POD and DMD[37] [33] with an open source code available at [38] for Matlab. Towne et al. conclude that SPOD highlights structures that evolve coherently in time and space.

The algorithm consists of a two-step procedure. In the first step a data set ('block') is assembled based on a certain windowing and overlap that the user can define. A Fast Fourier Transform (FFT) is applied to this windowed data matrix and stored. The second step aims at finding coherent structures for each frequency using POD. The modal energy is also solved for each mode and each frequency.

There exists another class of model reduction technique based on the linearized Navier-Stokes equations. Such methods are typically faster and simpler to comprehend, as they neglect the non-linear processes. Successful applications of Linear Stability Analysis for high-speed flows include [39] [40]. However, these methods are very sensitive to the base flow results and are typically applied to fundamental problems where an analytical expression exists for the base flow

or can be calculated with very fine DNS calculations. Therefore, this approach is not selected for the present research.

2.1.5   Optimization tool

A two-dimensional optimization is performed in which the Reynolds Averaged Navier Stokes solver is coupled with a differential evolution multi-objective optimization routine developed at the von Karman Institute, called Computer Aided Design And Optimization Tool for Turbomachinery Applications (CADO) [23]. CADO is based on the NSGA-II algorithm [41]. Andreoli et al. [42] presented a strategy to optimize the cooled tip of a turbine airfoil. De Maesschalck et al. presented a similar technique to optimize carved turbine tips [43]. Braun et al. [44] describe a two-dimensional optimization strategy to reduce drag and increase lift for a three-dimensional aerodynamic vehicle.

2.2   Experimental tools

The Linear Experimental Aerothermal Facility (LEAF) facility [45] is operated for the experiments. Therefore, high accuracy and high-frequency optical measurement techniques were utilized and developed to quantify the flow field and surface properties.

2.2.1   Linear Experimental Aerothermal Facility

To experimentally test the shock structure that drives the power extraction, a suitable test section was built able to fit into a linear wind tunnel at Purdue [46]. Figure 2.1 shows the lab with the linear experimental aero-thermal facility (LEAF). The vacuum pump needs to run approx. six hours to reach 30-40 mbar, which guarantees up to 30-50 sec of testing time according to the model of Dutton [47]. As depicted in Figure 2.1a), the PETAL lab has two wind tunnels: a linear wind tunnel (LEAF) and an annular wind tunnel. The high-pressure side of the wind tunnel is connected to the pressurized air tanks in Zucrow and contain 56 m^3 of dry air at 14 bar. The exhaust of the wind tunnel is attached to a 280 m^3 vacuum tank. For this low TRL viability study, the linear wind tunnel is employed (Figure 2.1b). The linear test section is completely transparent for optical access through two lateral Quartz windows and is aimed at technical readiness level (TRL) 1 and 2 tests. Through the vacuum pump and high-pressure line, a wide variety of pressure ratios can be set, allowing for testing from low subsonic to Mach 6 through a wide range of Reynolds numbers.

The linear wind tunnel is rated of providing air mass flows up to 30kg/s, air temperatures up to 700K and pressures up to 8 bar in the settling chamber.
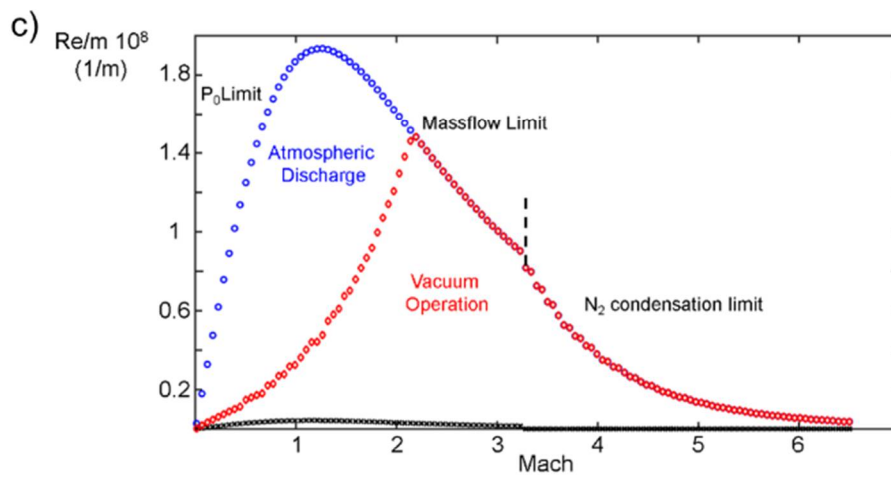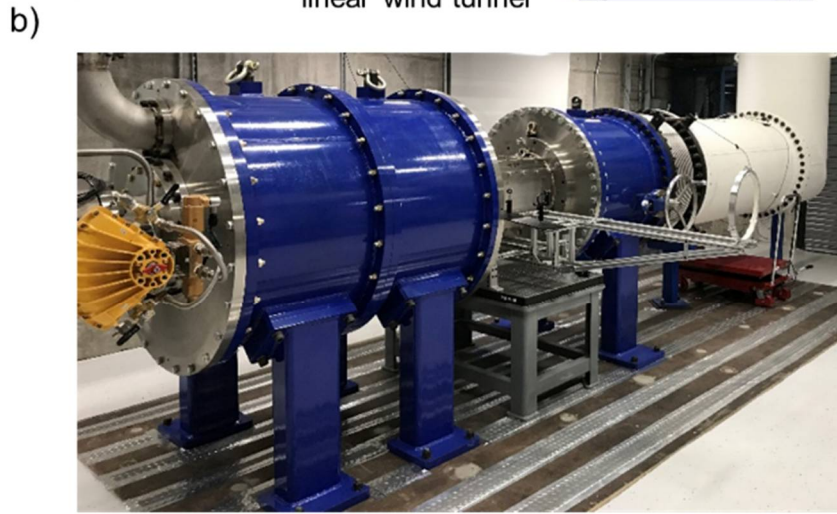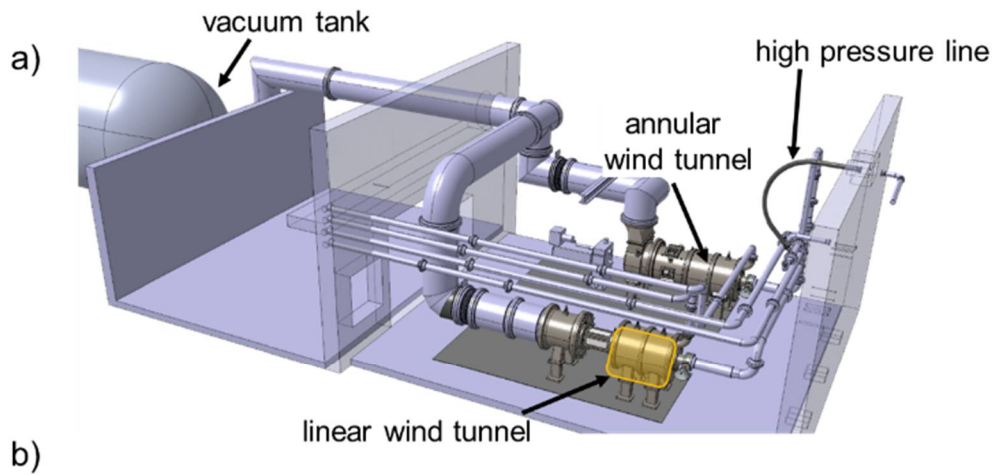
Figure 2.1 a) PETAL Facility, b) LEAF wind tunnel and c) operational envelope [48]

Table 2.1 shows the measurement techniques used or developed (*) and comprises techniques to resolve the steady state and transient phenomena in the supersonic regime.

Table 2.1 Measurement technique tested in the framework of the bladeless turbine

Measurement technique	Type of measurement	flow quantity	frequency
Static pressure taps	Point measurement	p_{static}	~ Hz
Kiel probe	Point measurement	p_{total}	~ Hz
Schlieren/Shadowgraph (*)	Surface/volume measurement	density gradients	2 kHz/ 10 kHz
Surface Interferometric Skin Friction (*)	Point measurement	τ	~ Hz
K-type (surface) thermocouples	Point measurement	T_{total}, $T_{surface}$ and Q	~ Hz
Femtosecond Laser Eletronic Excitation (FLEET)	Point measurement	Velocity components	1 kHz
Background Oriented Schlieren (BOS)	Surface measurement	Density gradients	3 kHz
Atomic Layer Thermopile	Point measurement	Q	kHz/MHz
High-frequency pressure transducers (Kulite) (*)	Point measurement	P_{static}	100 kHz

2.2.2   Low-frequency measurement systems

2.2.2.1   Pressure sensors

Calibration of the Scanivalve modules was performed with a precise Druck DPI612 absolute pressure calibrator with a precision of 0.005% full scale (FS) range. Figure 2.2 illustrates the comparison between the Scanivalves and the absolute pressure sensor. The R^2 value contains 5 nines, and the error is below 0.1%, which is below the stated uncertainty of the manufacturer (+- 230 Pa).
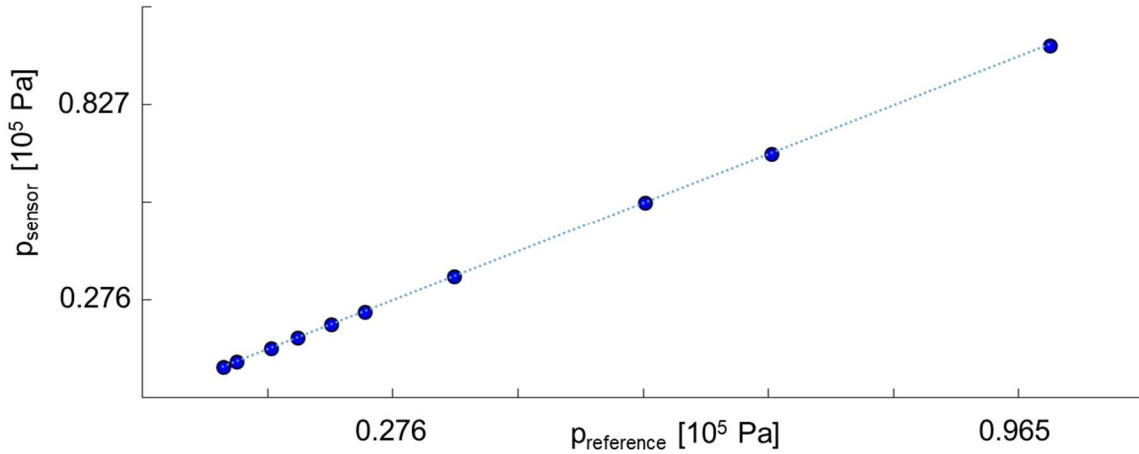
Figure 2.2 Calibration of the Scanivalve pressure transducers for steady state pressure measurements

To correct for the drift, the relative error between the different pressure readings at vacuum are recorded and compared to the mean vacuum level. As observed in Figure 2.3, in which the relative difference between the pressures at each sensor as a function of the sensor number is described, the relative error is below 1% for most sensors. If the discrepancy is above 1%, the sensor is discarded for post-processing. This discrepancy is most likely due to leakage between the test article and the transducer. For the highlighted test in Figure 2.3, the relative difference between the taps is <0.6% and was below 100 Pa for all sensors except for one which had a discrepancy of 160 Pa.
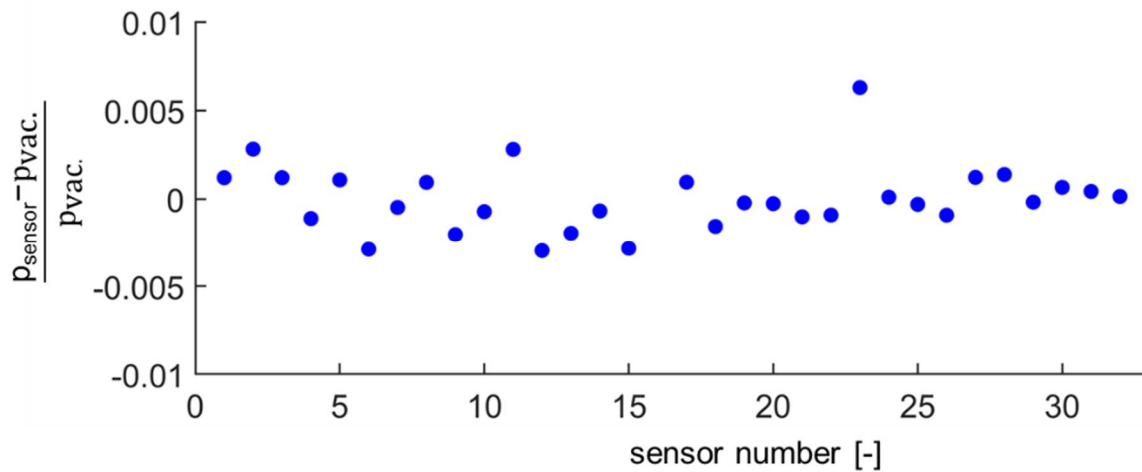
Figure 2.3 Relative variation between the 32 pressure readings at vacuum condition

In Figure 2.4, the width of the pressure tap diameter is investigated to analyze the ability to resolve sharp gradients induced by shocks. The abscissa represents the axial distance of the test article, and three diameters ranging from 0.8 mm to 2.4mm are investigated. The relative difference between the maximum value retrieved within that region and the minimum value is plotted on the ordinate. For the smallest hole diameter, the discrepancy is around 5% (near the axial location z=0.35m), however, is more than doubled if the diameter is tripled. Similarly, around z=0.4m, this effect is intensified due to the increase of local curvature of the geometry and discrepancies now range from 10% to 40%. Hence if one wants to capture the gradients of the pressure to correctly measure the steady power extraction, the smallest diameter should be selected. In this case, the smallest diameter of 0.8 mm was chosen, which was a trade-off between spatial resolution and manufacturability of the hole. It should be noted that for high-frequency effects, a decrease of hole diameter is accompanied by a decrease of frequency resolution if the cavity diameter is held constant (see Section 2.2.3.3).
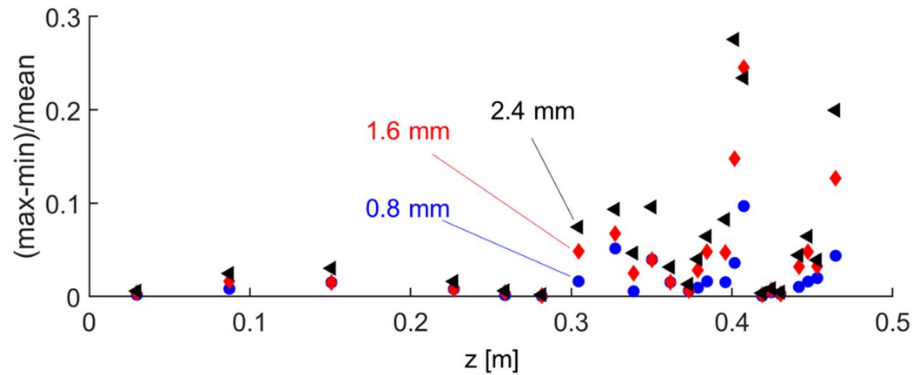
Figure 2.4 Influence of the pressure sensor tube diameter on the gradients in the pressure field

50 static pressure taps were drilled into the test article and were connected via tubes of 1.6 mm diameter to Scanivalve DSA modules. Total pressure Kiel probes were used to measure the total pressure. Due to the length of the pneumatic tubes that connect the test section to the acquisition system (approx. two meter), the frequency response of the system is in the order of Hertz.

Figure 2.5 shows the repeatability of the static pressure measurements on the hub surface as a function of a reference pressure, which was the static pressure at z_{ref} =0.0696m. During several

months, multiple tests were performed, and the max-to-min discrepancy between several tests was below 2%.
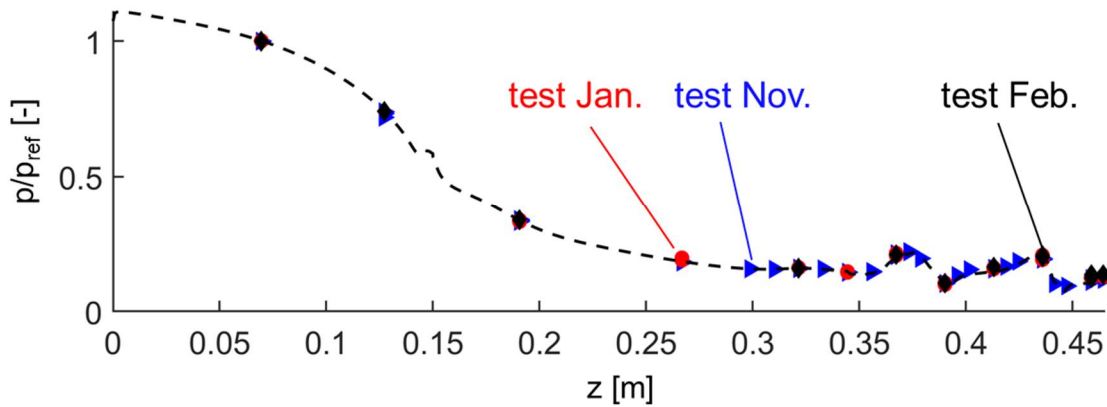
Figure 2.5 Repeatability of the tests: static pressure as a function of the axial length

2.2.2.2 Schlieren

The Schlieren system is of a Z-type configuration, and the camera is a Basler AG camera with a frame rate up to 50 frames/s at maximum resolution. A Schlieren/shadowgraph system (Figure 2.6) was installed in the wind tunnel and was mounted on the same optical rail set up as for the FLEET to be able to change between several measurement techniques in a fast way. Alternatively, the low-speed camera can be switched by a high-frequency camera (e.g., SAZ Fastcam) with frequency recordings up to 1 MHz. The main limitation of the Schlieren/shadowgraph is the light source, which was an off-the-shelf LED. For shadowgraph visualization, 10 kHz could be achieved, and for Schlieren this was reduced to 2 kHz, due to the knife edge that constrained the light on the receiving side.
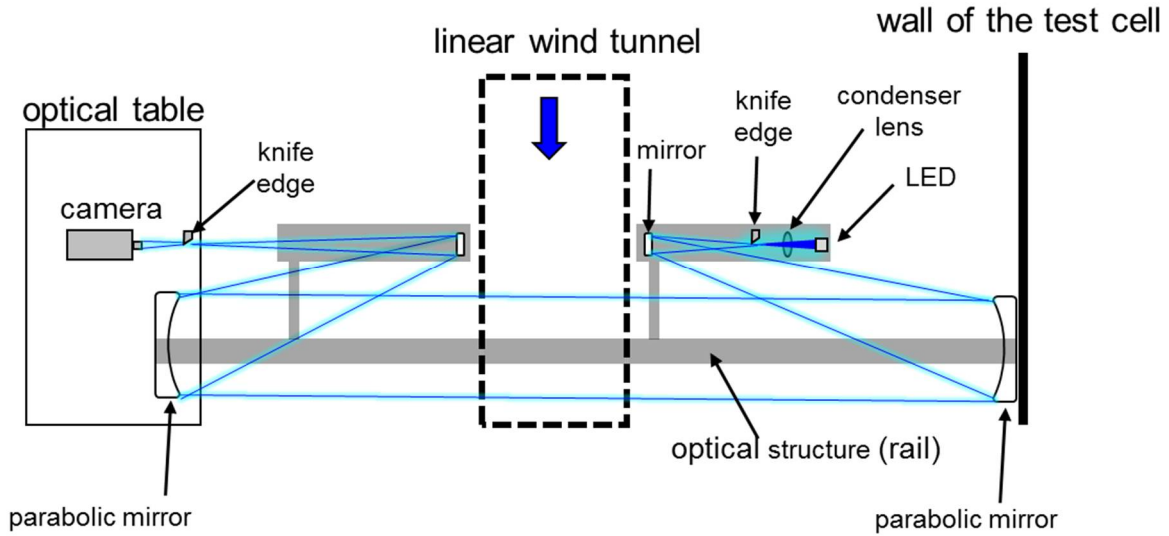
Figure 2.6 Schematic of the top view of the Schlieren system for the LEAF wind tunnel

Figure 2.7 shows the setup in the LEAF facility, and Figure 2.7a zooms in on the receiving side with the camera, knife edge, and both mirrors as well as the wind tunnel. In Figure 2.7b the emitting side with the LED (6500K LUXEON Z White LED attached to a 3V coin cell battery) is visible.
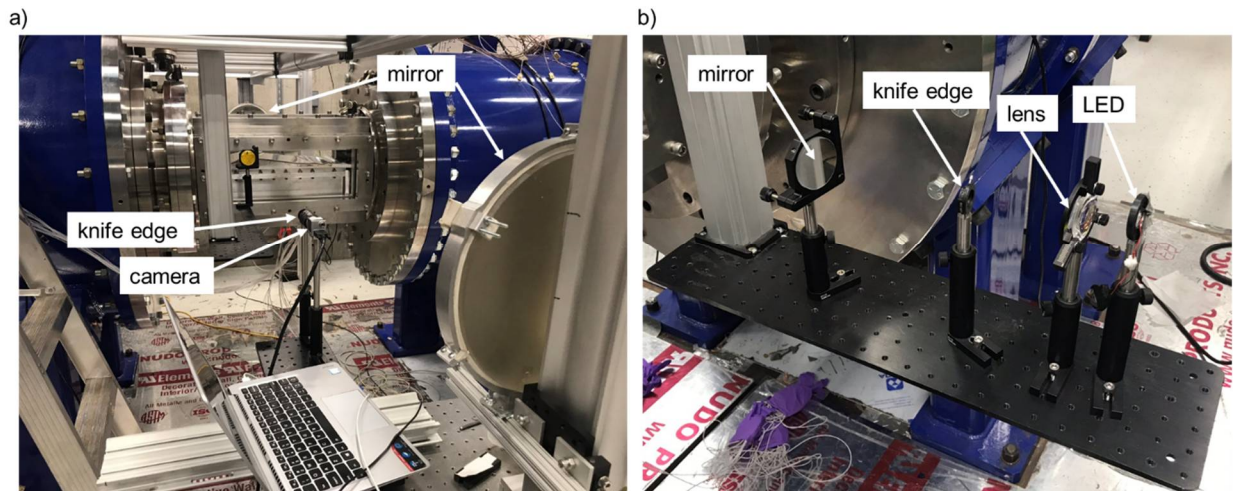
Figure 2.7 Schlieren setup in the LEAF facility: a) receiving side and b) emitting side

2.2.2.3   Oil skin friction technique

The Oil-film Interferometry (OFI) or Surface Interferometric Skin-Friction (SIFS) described by Naughton and Brown [49] was implemented for a high-speed wind tunnel to measure the skin friction. This method calculates the skin friction based on the deformation of an oil droplet due to shear. Eq. 2.5 shows the one-dimensional thin oil film equation ([50]):

$$-\mu \frac{\partial h}{\partial t} = \frac{\tau_x}{2} \frac{\partial h^2}{\partial x} \qquad \text{Eq. 2.5}$$

Because oil is a high viscosity fluid, the movement of the oil can be represented as a low Reynolds number flow [51] and the wall shear stress can be approximated by Eq. 2.6 that relates the wall shear stress with the height (y/x) of the oil and the time (t) that the shear was applied.

$$\tau_{wall} = \frac{\mu_0}{t * \frac{y}{x}} \qquad \text{Eq. 2.6}$$

The SIFS method describes how an interference pattern is generated when quasi-monochromatic light is reflected off from the surface of the oil layer. The distance between those fringes can be calculated and related to the height of the oil and be used to determine the skin friction. Eq. 2.7 relates the height of the oil and the interference pattern. λ is the illumination wavelength, n_f and n_a are the refractive index of both the oil and the fluid medium, and θ_i is the incidence of the light and Φ the phase of the fringe. The fringe pattern as a function of its axial length is a sinusoidally varying function [52].

$$h(x) = \frac{\lambda \Phi(x)}{4\pi} \left(\frac{1}{\sqrt{n_f^2 + n_a^2 \sin^2(\theta_i)}} \right) \qquad \text{Eq. 2.7}$$

SIFS is a widely accepted measurement technique and was used in both low speed as high speed (Mach 0.3 till Mach 1.05 flow[53]). Figure 2.8a shows the layout in the LEAF wind tunnel with a schematic overview of the oil shear. In Figure 2.8b, a sequence of an oil droplet (1000 centistokes oil) in time subjected to shear is photographed. On the last picture, small fringes

become apparent due to constructive and destructive interference. In a second step, the images are mapped onto the physical 3D domain via the toolbox developed by Liu et al. [54] and online available [55] (Figure 2.8c). The fringes are visible at the onset of the oil droplet from point A through point B. The intensity of the fringes is extracted (Figure 2.8c), and the oil height is calculated based on Eq. 2.6 and Eq. 2.7. Figure 2.8d plots the skin friction as a function of the time samples. Uncertainty quantification of this measurement technique is described by Zilliac [56] and Pailhas et al. [57]. Additionally, Naughton and Hind described an unsteady version of this method in 2013 [58], which can be exploited with a high-speed camera. Husen et al. [51] described a continuous method (LOFT) in which of marks were applied within the oil via lasers to retrieve the unsteady skin friction on an entire surface.
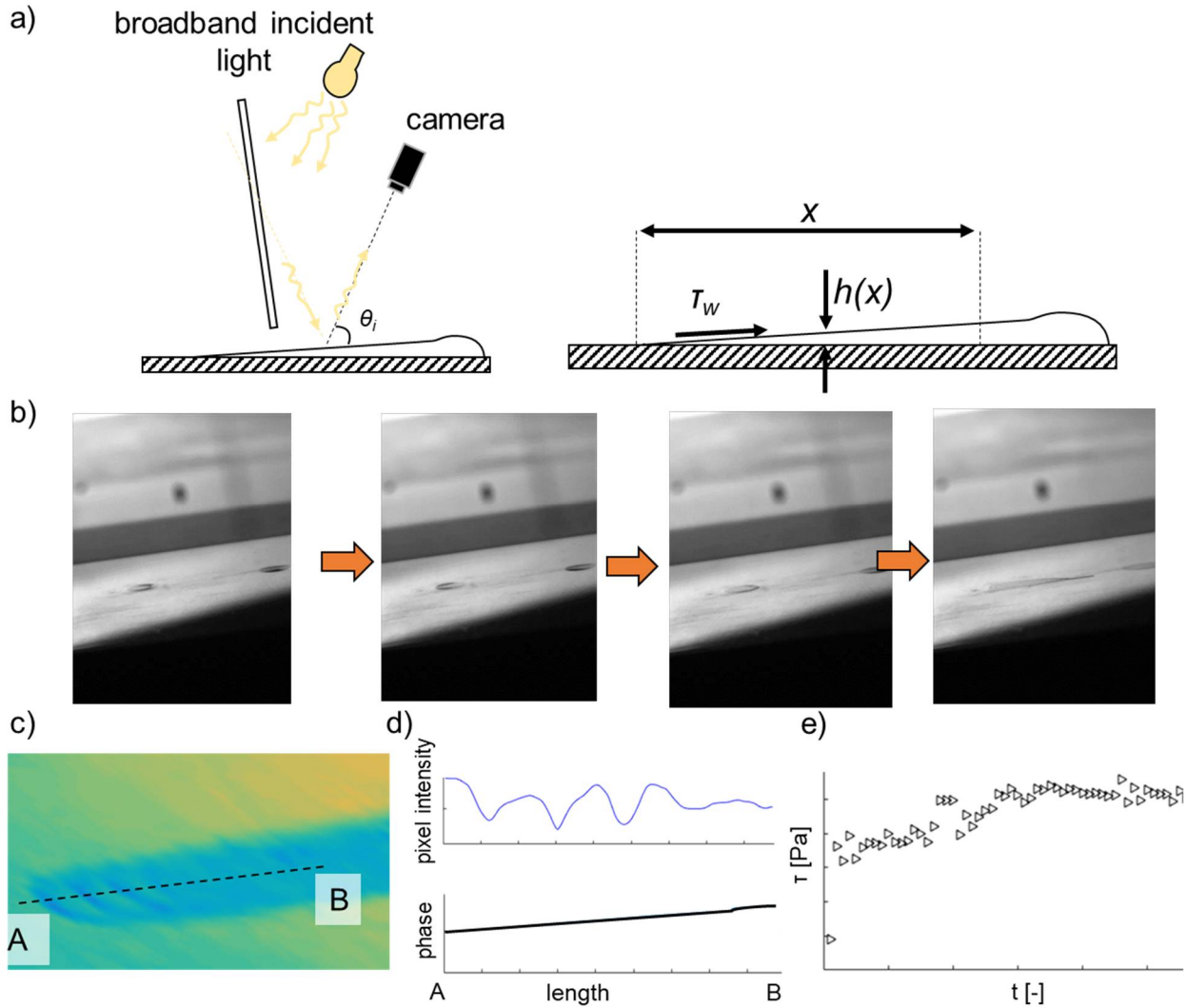
Figure 2.8 a) SIFS method [51] b) sequence of oil submitted to shear in the LEAF, c) single droplet plotted on the surface, d) extraction of the fringes and transformation to phase and e) shear stress as a function of time

Typically, for long duration tests, a single picture of the fringes results in accurate skin friction measurements. For these supersonic tests however, due to the effect of starting shock wave, unstarting shock wave and the short testing time (< one minute), the camera was recording for the entire sequence from the start of the shear until the end of the test so that only the region in which stable flow was achieved, was taken into account.

The viscosity of the oil was determined via a Brookfield viscometer (DV-II+). Table 2.2 shows the values of viscosity with a 10% deviation from the original data at room temperature. Four points at four different temperatures were measured with a high dependency on the

temperature, as also observed by Villafane et al. [59]. The uncertainty of the Brookfield viscometer is +-1% of the range in use.

Table 2.2 Calibration of the oil viscosity

Calibration point	Temperature [deg C.]	Viscosity [cst]
1	20	~1100
2	3	~1500
3	-4	~2000
4	-16	~2600

The methodology of Moffat [60] was applied to retrieve the uncertainty on the skin friction measurement. The uncertainty on the oil viscosity, calibration as well as optics were assumed to be random errors. From Table 2.3, the total uncertainty is around 14% for a mean skin friction value of around 94 Pa (taken from a typical experiment).

Table 2.3 Uncertainty on the skin friction

Quantity	Mean value	Uncertainty	Uncertainty on τ	sensitivity
Oil viscosity	1000	10.00%	10.00	100.00%
Calibration		2%		37%
Wavelength	592	7%		93%
Light incidence		10%		8.45%
Mean skin friction	93	**Total uncertainty**	**14.12%**	

2.2.2.4   Thermocouples for heat flux measurements

The thermocouples (both surface thermocouples as well as total temperature thermocouples) were calibrated in a Fluke 9171 metrology well with uncertainty of 0.005 deg. K. Figure 2.9 shows a calibration curve of the thermocouples in which eight different temperatures

were maintained until steady state was reached. The uncertainty of the temperature was around 0.3K, similar to Saavedra's findings [48].
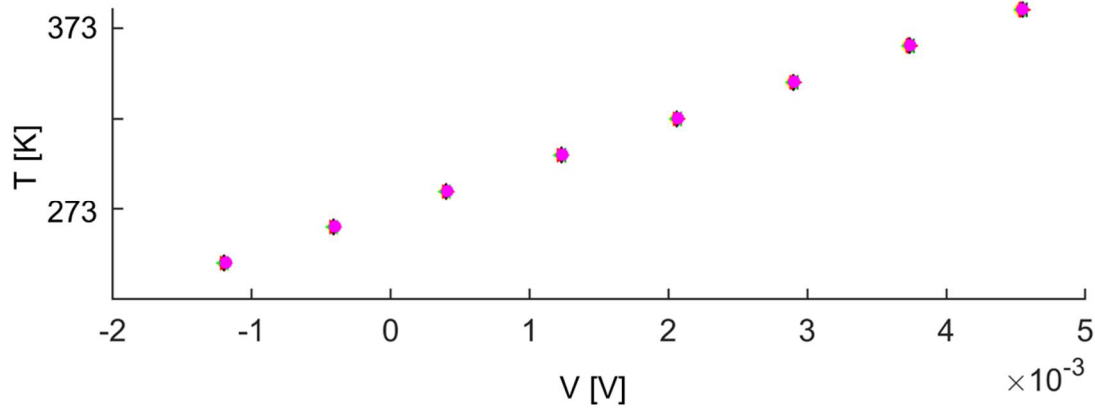
Figure 2.9 Thermocouple calibration

To retrieve the heat flux, the surface thermocouple data is used as input into a numerical solver (Saavedra et al. [61]). The code is based on a one-dimensional unsteady heat conduction equation and uses a Crank Nicholson discretization with resulting temperature field that depends on time and distance. This temperature field is then used to compute the heat flux. The heat flux uncertainty is calculated in, and further details can be found in Bhatnagar and Paniagua [62].

Table 2.4 Uncertainty on the heat flux

Quantity	Mean value	Uncertainty	Uncertainty on Q	sensitivity
Aluminum Thickness	0.05	1.00	0.58	58.49
Aluminum conductivity	180	4.00	1.44	35.96
Aluminum density	2700	3.70	0.96	26.04
Aluminum heat capacity	897	1.11	0.06	5.13
Kapton film thickness	$7.00 \ 10^{-5}$	14.29	11.12	77.83
Kapton Thermal Conductivity	0.12	3.00	2.99	99.81
Kapton density	1420	0.05	0.02	30.26
Kapton heat capacity	1090	1.00	0.30	29.92
Front temperature	305	0.30	1.78	593.23
Back temperature	299	0.30	2.95	983.19
Mean heat flux	$5.83 \ 10^3$	**Total uncertainty**	**12.16%**	

2.2.3   High-frequency measurement systems

2.2.3.1   Femtosecond Laser Electronic Excitation Tagging

To retrieve the flow components, the femtosecond laser electronic excitation tagging (FLEET), which is a type of molecular tagging is used, as described by Fisher et al. [63]. With FLEET a focused femtosecond laser beam dissociates nitrogen that emits light in the range of 560-660 nm visible range. This is then imaged with an intensifier and high-speed camera (Figure 2.10a) and by tracking the movement in time, velocity components are retrieved. The setup in the LEAF facility is visualized in Figure 2.10b. The excitation of the molecules happened through a femtosecond laser with a maximum repetition of 1 kHz. The laser light is triggered in the laser lab [45] and via an array of lenses arrives in front of the quartz windows, and focusses in the test section. The benefit of molecular tagging compared to particle image velocimetry [64][65] is the

fact that FLEET does not require seeding, hence no correction is needed to track the particles through the shock in contrast to large diameter particle seeding. Burns et al. used FLEET measurements on transonic airfoils with an incoming Mach number of 0.85 [66]. Uncertainty based on their measurements was around 5%. In another publication, Burns et al. [67] use FLEET in the range of Mach 0.2-0.7 for high pressure and low-temperature conditions at 1 kHz repetition rate.
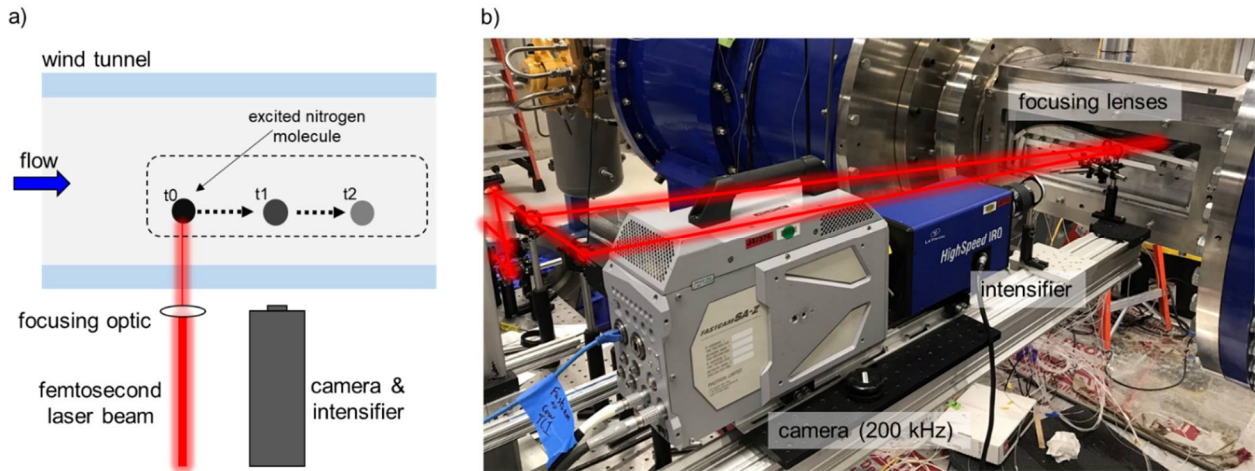
Figure 2.10 a) FLEET principle and b) FLEET setup

2.2.3.2 Background Oriented Schlieren

Background Oriented Schlieren (BOS) [68] is an optical measurement technique in which the quantitative density gradients within the flow field are solved. BOS employs the relationship between the fluid refractive index and a fixed dot pattern. Dalziel et al. [69] as well as Raffel et al. [70] first mentioned using this type of measurement technique in 2002. Rajendran et al. [71] proposed a method to increase the spatial resolution of BOS by proposing an improved tracking mechanism. A schematic of the principle of BOS is depicted below in Figure 2.11. The light source travels through the wind tunnel and due to the difference in refractive index between the 'flow' and 'no-flow' condition, a difference in deflection (ΔY) is recorded, and the density gradients are calculated.
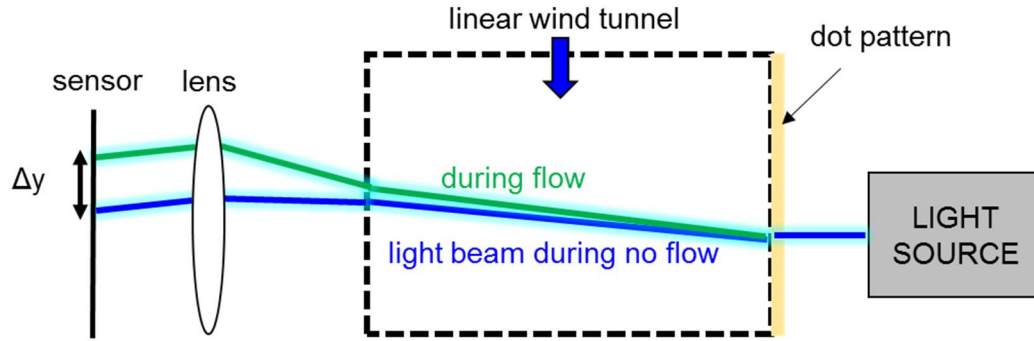
Figure 2.11 Schematic overview of the background oriented Schlieren (BOS)

The receiving side of the BOS setup is displayed in Figure 2.12a: the light travels throughout the wind tunnel and is captured by a high-speed camera. Figure 2.12b shows the dot pattern that was placed behind the quartz window to track the gradients.
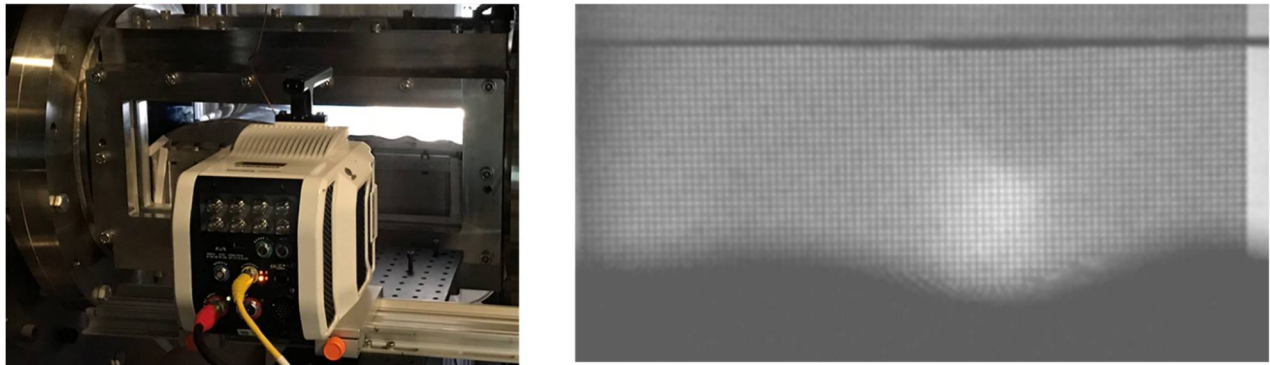
Figure 2.12 a) Setup of the BOS for the LEAF facility and b) dot pattern at no flow conditions

Density gradients were post-processed through the PRANA (PIV, Research and ANAlysis) software, developed by Prof Vlachos at Purdue University. As correlation technique, the Robust Phase Correlation described by Eckstein and Vlachos [72], was employed. A more detailed description of the software can be found in [73].

2.2.3.3   Fast response pressure sensors

Fast response Kulites (type XCE-062-50A Ultra-Miniature High-Temperature Pressure Probe) were used with a frequency response up to 120 kHz. The Kulites are connected to a

Precision filter instruments conditioning box (Model 101777 Triple Output Kulite Conditioner). The low pass filter has a cut off frequency of 322 Hz at -3 dB and the high pass filter has a bandpass frequency from 200 Hz up to 160 kHz. The sampling frequency for the Kulites was set to 512 kHz to ensure no aliasing is present. The Kulites were calibrated from atmospheric to ~ 10 kPa. Figure 2.13a shows the raw voltage for 7 Kulites as a function of the vacuum level. A linear fit was used for the calibration (Figure 2.13b).
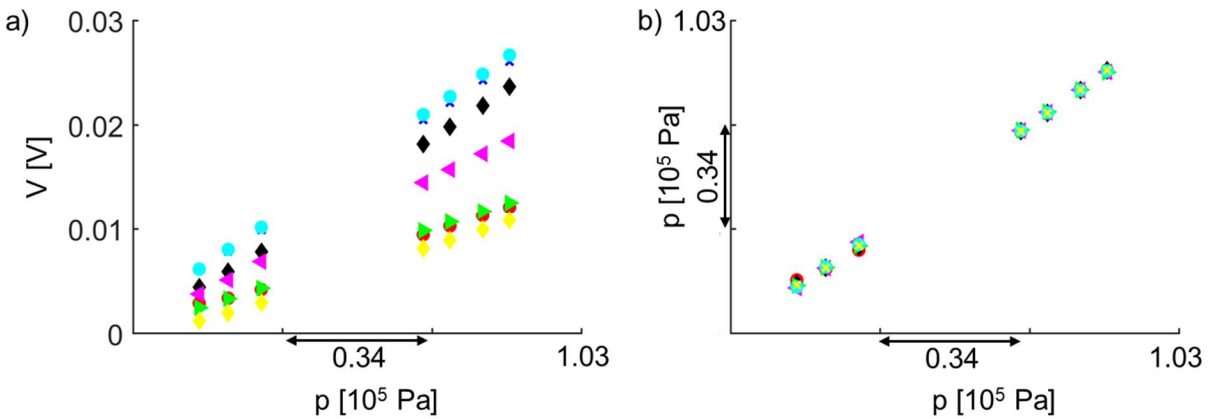
Figure 2.13 Calibration of the Kulites: a) raw pressure reading of seven Kulite sensors as a function of pressure and b) calibrated signal as a function of pressure

Based on the following equation, the uncertainty on the high-frequency pressure transducers was analyzed [48]:

$$\frac{\partial p}{p} = \sqrt{\left(\frac{\text{slope } x \text{ voltage}}{p}\right)^2 \left(\left(\frac{\partial \text{slope}}{\text{slope}}\right)^2 + \left(\frac{\partial V}{V}\right)^2\right) + \left(\frac{\text{intercept}}{p}\right)^2 \left(\frac{\partial \text{intercept}}{\text{intercept}}\right)^2} \qquad \text{(Eq. 4)}$$

Figure 2.14 depicts the uncertainty as a function of the absolute pressure level. Uncertainty for most Kulites was below 3% for the higher pressures, however, increases for decreasing pressures for some Kulites which might be due to leakage from the sensor insert and the test article.
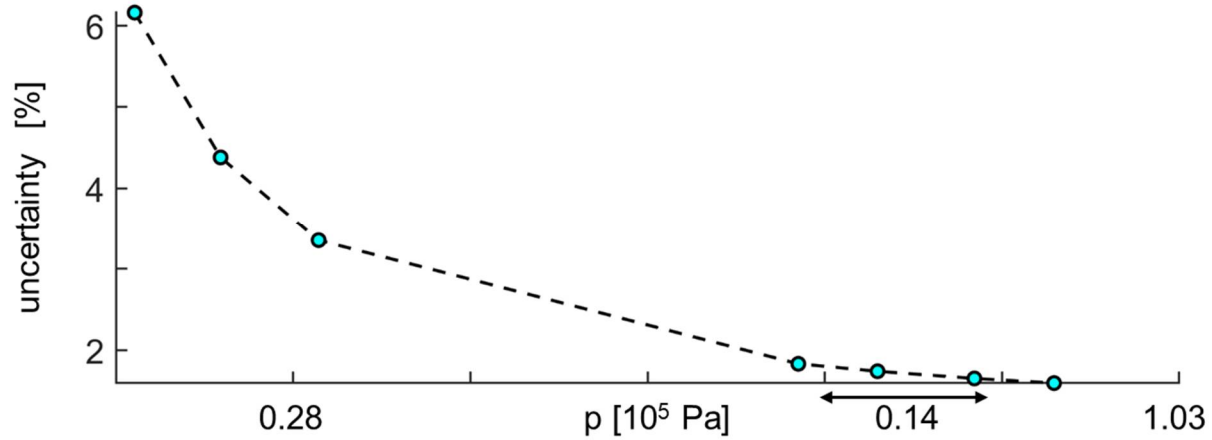
Figure 2.14 Uncertainty of a high-frequency pressure transducer as a function of pressure

Figure 2.15 plots the frequency content for a typical experiment. The amplitude of the FFT was calculated as the pressure fluctuation over its mean pressure level (a window of two seconds of data was chosen, with a resulting frequency resolution of 0.5 Hz). The data of no flow ('noise') is compared to the flow data. The low pass filter (blue signal, up to 300 Hz) is plotted next to the high-frequency data (up to 160 kHz). As observed, the low pass and high pass filter have similar values at 300 Hz, and noise levels (black) for each filter are well below the signal levels, the RMS signal-to-noise ratio is above 9 up to 10 kHz below which it starts to decay due to the fact that the signal reaches the noise level for high frequencies.
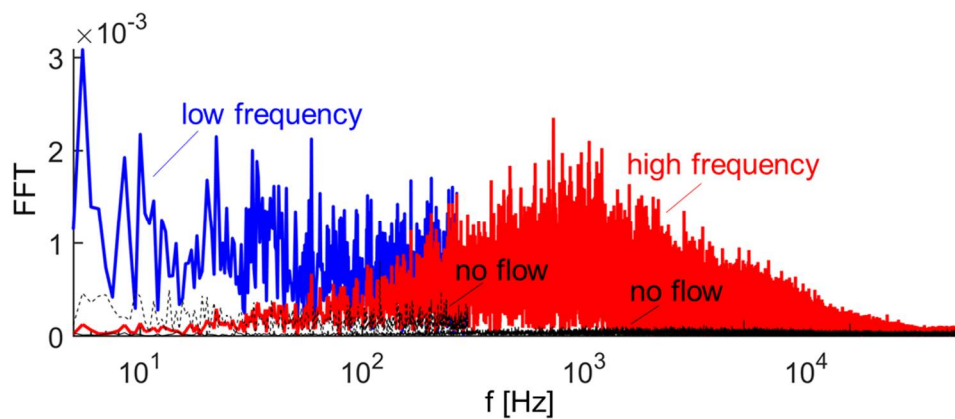
Figure 2.15 Noise versus flow data for the low-frequency and high-frequency channel from the Precision Filter Instruments conditioning box for a typical test

In Table 2.5, the influence of the recess length of the sensor with a recess diameter of 0.8 mm is calculated based on Liu et al. and Paniagua [74]. A recess of 4 mm introduces a reduction of frequency content down to only 20 kHz. For this test, the sensor recess depth was estimated to be between 1 and 3 mm as. Furthermore, Paniagua and Denos [75] developed correlations to correct for the dynamic response of sensors.

Table 2.5 Frequency response versus the recess depth for a tube diameter of 0.8 mm

hole depth [mm]	frequency response [kHz]
0.5	156.3
1	80.8
2	41
3	27.6
4	20.8

2.2.3.4   Atomic Layer Thermopile

An atomic layer thermopile (ALTP) is a sensor that generates an output proportional to the heat flux without any conversion required apart from the calibration, and a temporal response of the order of µs. Lengfellner et al. [76], as well as Budai et al. [77], demonstrated that when an Yttrium Barium Cupric Oxide ($YBa_2Cu_3O_{7-d}$) crystal is exposed to a temperature gradient, large voltage differences appear. The crystal consists of a repeating lattice of Yttrium and Barium layers separated between layers of copper oxide which can be considered as several atomic thermocouples connected in series and is called an atomic layer thermopile. This ALTP is deposited on a $SrTiO_3$ substrate, as seen in Figure 2.16a. Roediger et al. [77] and Jenkins et al. [78] demonstrated this type of sensor for MHz heat flux measurements. Figure 2.16b shows the frequency of two types of ALTPs, with measurement rates of at least 1 MHz. Figure 2.16c displays the calibration of the ALTP, as reported by Bhatnagar and Paniagua [62]. The reported uncertainty for this MHz heat flux sensor lies between 25% and 10% depending on the levels of heat flux.
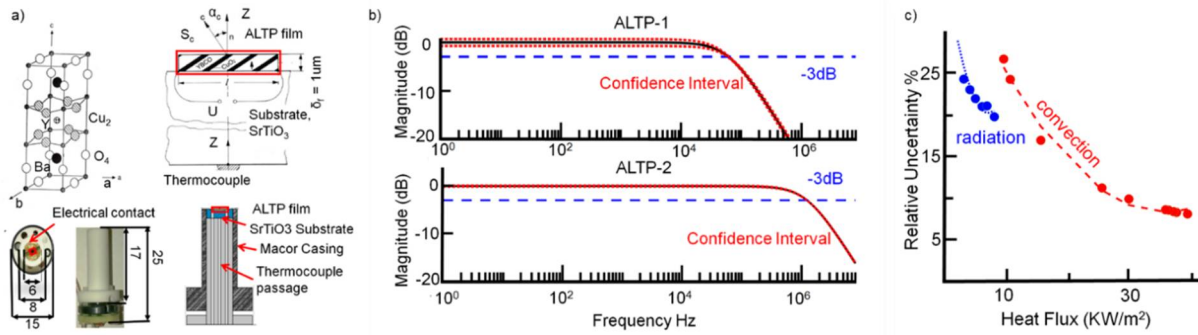
Figure 2.16 a) Layout of the atomic layer thermopile (ALTP) heat flux sensor, b) frequency response of two types of ALTP designs and c) uncertainty of the ALTP as a function of the heat flux level [62]

CHAPTER 3.   DESIGN AND OPERATION OF THE BLADELESS TURBINE WITH STEADY INLET CONDITIONS

Bladeless power extraction provides significant benefits for flows exposed to high speeds. Nikola Tesla first introduced this concept in 1913 where a radial bladeless turbine was driven only by the viscous forces of the flow impinging on the end walls.

3.1   The wavy design

Figure 3.1 illustrates the principle of operation of the bladeless turbine investigated in this work. The radius of the hub is 0.094m and height of the channel is 0.02m. The shroud is assumed to be fixed and not rotating. Figure 3.1a displays a bladeless turbine with a wavy surface. This wavy surface consists of multiple periodic wavy contours and each has a rise that results in a 'hill' and subsequent descent that ends in a 'valley'. The wavy hub geometry generates additional compression waves, shocks, and expansion fans that can lead to increased power extraction. The baseline geometry that was investigated has an amplitude-to-channel height of 10% and contains 20 waves in the tangential direction. The helix angle of the wavy contour is 45 degrees with respect to the axial direction. Figure 3.1b presents a cross-sectional view of the bladeless turbine with a periodic waviness across the channel length.
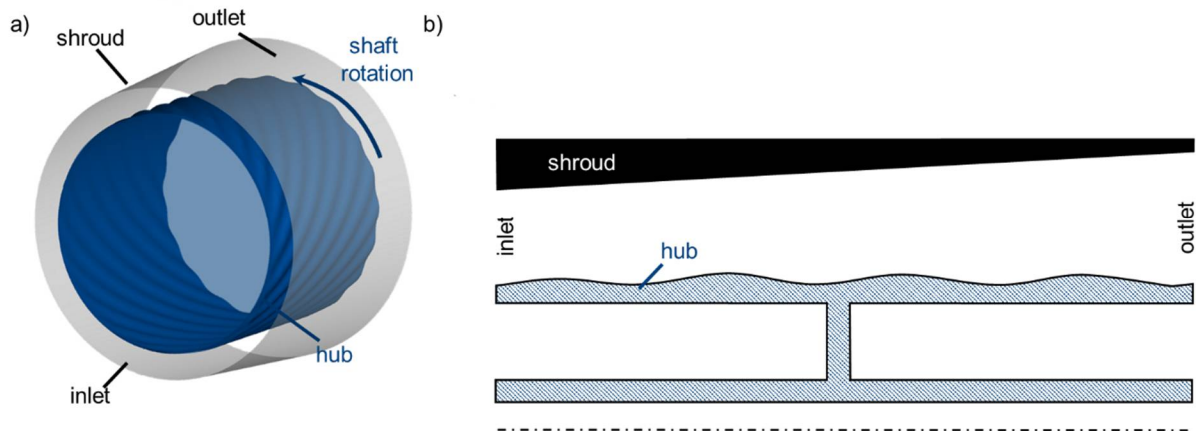
Figure 3.1 Bladeless turbine concept: a) three-dimensional view of the turbine with wavy hub surface and b) cross-sectional area of the bladeless turbine

3.2   Numerical methodology to analyze the bladeless turbine

This geometry was subsequently generated and meshed. In a first step, an IGG file was built from a Matlab script and loaded into IGG (Numeca), an interactive geometry modeler. The Matlab routine consisted of a routine in which helix angle, amplitude-to-channel height, and length of the turbine are inputted. Once imported in IGG, a Parasolid (a 3D solid model software) was created and imported into Hexpress, an unstructured mesher from Numeca. Both at the hub and casing endwalls, the non-dimensional first layer thickness (y+) was below 1 to ensure adequate solving of the viscous sublayer. Figure 3.2a shows the entire mesh, which was around 8 million cells for this geometry. Figure 3.2b features a close-up image of the mesh on the wavy hub surface where a refinement was added to ensure detailed capturing of the subsequent compression and acceleration regimes.
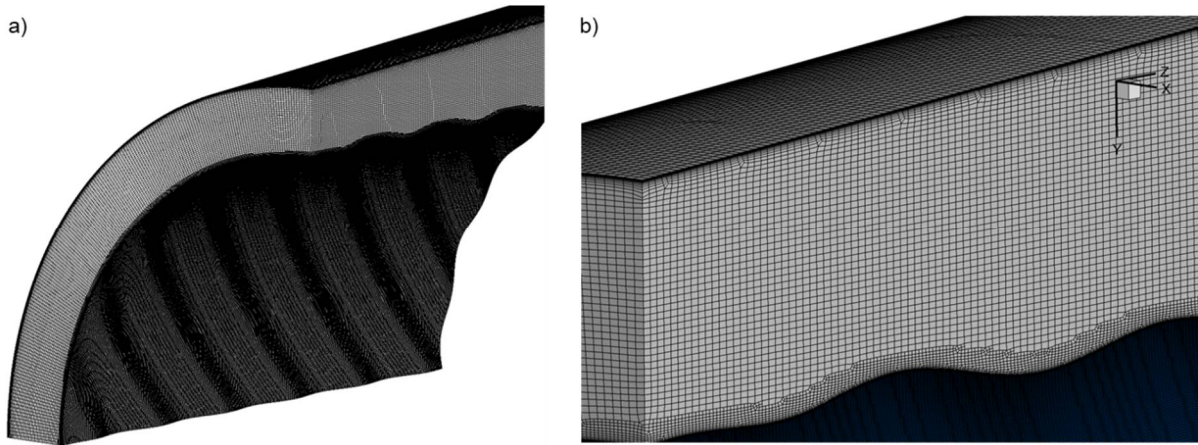
Figure 3.2 a) Mesh of the bladeless turbine and b) close-up on the wavy hub

The numerical domain is illustrated in Figure 3.3. The shroud of the bladeless turbine was modeled as a no-slip wall, the hub as no-slip wall in the relative frame of reference (set by the rotational speed of the shaft). The outlet was a mixed supersonic-subsonic boundary condition with a certain back pressure. At the inlet a static pressure, temperature and velocity components were imposed to reach supersonic conditions (the inlet Mach number was 1.25 for the baseline case). Steady Reynolds Averaged Navier-Stokes equations were solved with CFD++ and the turbulence closure was provided with the k-omega SST turbulence model. This turbulence model was selected based on its ability to capture the turbulence effects in the near-wall region as well as in the free stream. The fluid was solved in the relative frame of reference of the hub. The

momentum that was exercised on the hub was automatically saved, both the viscous and the inviscid contribution. The boundary conditions and main assumptions for the CFD setup are summarized in Table 3.1.

Table 3.1 Boundary conditions and simulation settings

boundary	boundary conditions
hub	moving wall
shroud	no-slip wall and adiabatic wall
outlet	mixed supersonic-subsonic
inlet	velocity, static pressure & temperature
period 1 &2	periodicity (90 deg.)
CPU time	~ 9.2 hours
# CPU's	16 (Purdue RICE cluster)
turbulence model	k-omega SST
gas constant	287
specific heat ratio	1.4

To simplify the analysis and interpret the trends, a calorically perfect gas with a specific heat ratio of 1.4 and a gas constant of 287 was used. The influence of the temperature on the specific heat ratio was verified with a thermally perfect gas (air) and a deviation of 7% in torque and 4% difference in total pressure loss was retrieved. Periodicity of 90 degrees was assumed for the simulations. However, a half wheel bladeless turbine was run to justify this choice, and the difference in torque was below 0.3%.
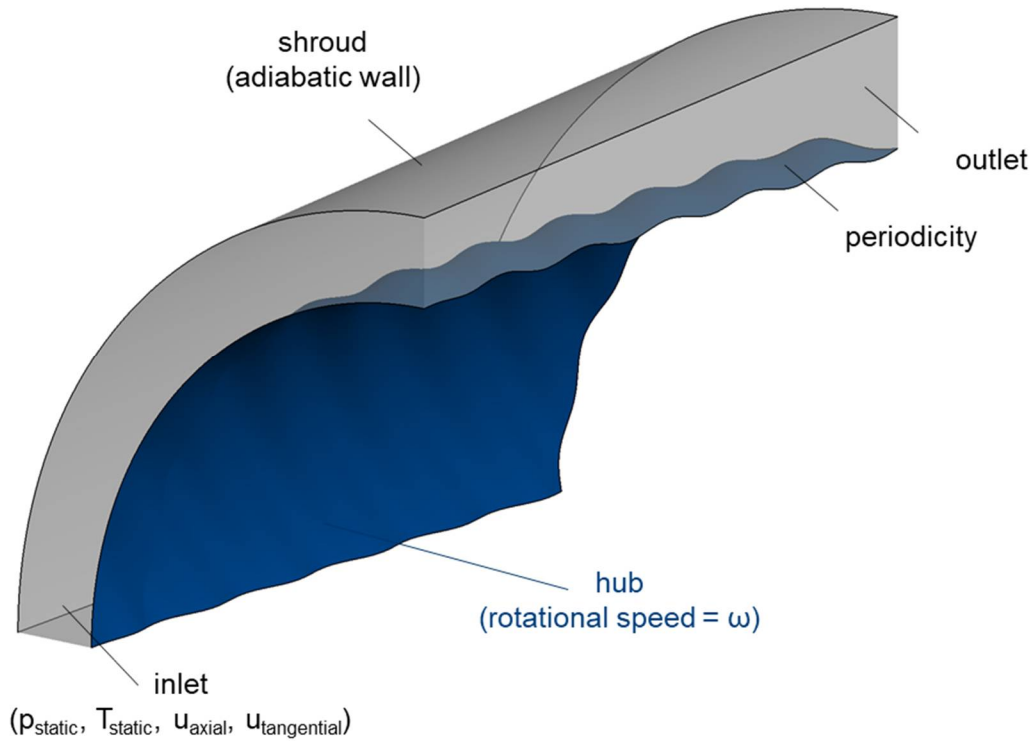
Figure 3.3 Numerical domain and boundary conditions

The passage would be choked with the designed inlet flow of M= 1.25 and induce a traveling pressure wave upstream if the channel were straight (constant inlet-to-outlet area), a phenomenon described by Sousa et al. [5] and Liu et al. [21] for supersonic axial turbines. Hence, the turbine passage was opened by 50% (seen in Figure 3.1b and Figure 3.3) to prevent unstarting and hence the formation of detrimental pressure waves that would move upstream towards the combustor.

In Figure 3.4a, the convergence of torque for a typical simulation is illustrated. After 1000 iterations the change in viscous and inviscid torque on the hub is less than 0.01%. Hence 2000 iterations were selected as a convergence criterion.

a)

τ [Nm]

inviscid

viscous

10^1

10^0

0   500   1000   1500

iterations [-]

b)

16.8

16.2

15.6

15

14.4

τ [Nm]

6   11

grid size [M cells]
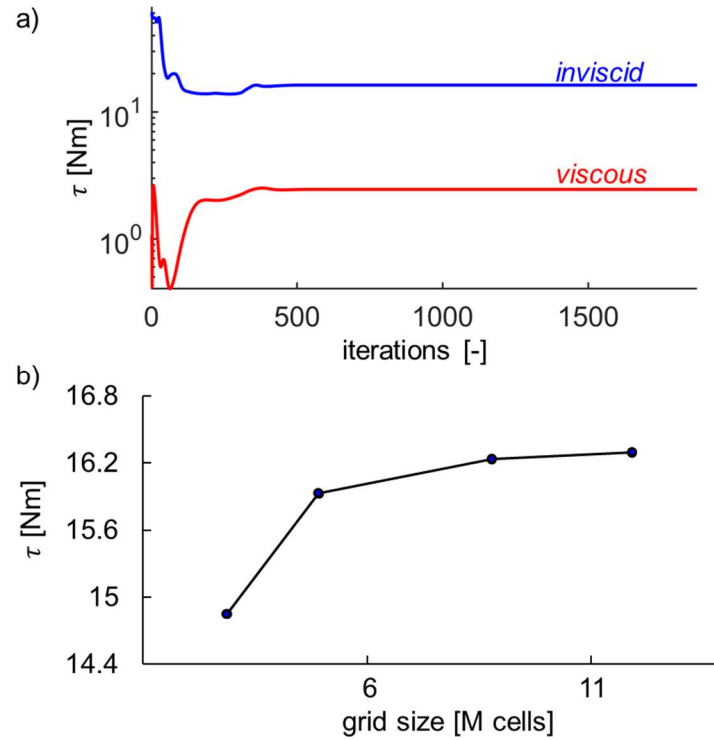
Figure 3.4 a) Convergence and b) grid sensitivity analysis

Figure 3.4b indicates the mesh convergence: four meshes were investigated (ranging from 2.9 until 11.9 million cells), and the torque is visualized. The y+ for each mesh was kept constant while the mesh was refined by a factor 1.2 in radial, tangential and axial direction. Figure 3.4b depicts an asymptotic behavior for the mesh convergence, and hence, a mesh of 8 million was selected for this study. The relative difference between the finest (11.9M) and the finer (8M) mesh was 1% for the torque on the hub and 1% discrepancy in total pressure loss (inlet-to-outlet), as concluded from Table 3.2.

Table 3.2 Total pressure loss for multiple grid levels

mesh size	$(p_{loss} - p_{loss,finest}) / p_{loss,finest}$
2.88M	0.05
4.92M	0.005
8.79M	0.01
11.9M	0

3.3 Performance results of the baseline

3.3.1 Aerodynamic performance

A baseline bladeless turbine that consists of a wavy hub with an amplitude-to-channel-height of 10% (A=2 mm) and a total number of 20 tangential waves was selected. A positive helix angle of 45 degrees was selected for the baseline design. The geometrical features that describe the baseline case are tabulated in Table 3.3.

Table 3.3 Baseline design of the bladeless turbine

boundary	boundary conditions
R [m]	0.094
L [m]	0.15
d [m]	0.02
A [m]	0.002
h [m]	0.02
α_{helix} [deg]	45
$\alpha_{flow\ angle}$ [deg]	0
W [-] (full wheel)	20
ω [rad/s]	1800

In Figure 3.5, the different flow structures that contribute to the power extraction in bladeless turbines with a wavy surface become apparent. Due to the helix angle inclination and the rise and descent of the wavy contour, shock waves arise, which are accompanied by an increase in static pressure during the rise (deceleration of the flow) and a decrease of pressure during the descent of the wavy contour (acceleration of the flow). Due to the pressure difference and inclination of the wavy contour, an axial and tangential force on the hub is created which results in torque on the shaft (hub). In contrast to flat/smooth bladeless turbines, torque can be generated from pressure forces from axial inflow (flow with no tangential component, $\alpha_{flow\ angle}$ =0 deg.). The hub (Figure 3.5) is colored by pressure, and the inlet and section at a constant tangential location

are shaded by the Mach number. Zone 'A' lies within a rise of the wavy contour, and a drastic pressure increase is observed, zones 'B' and 'C' show locations at the descent of the wavy contour in which the flow should accelerate. Close to the hub, the flow is, however, not axial (marked by low Mach number regions) and is detached from the axial core flow. This effect lowers the power extraction.
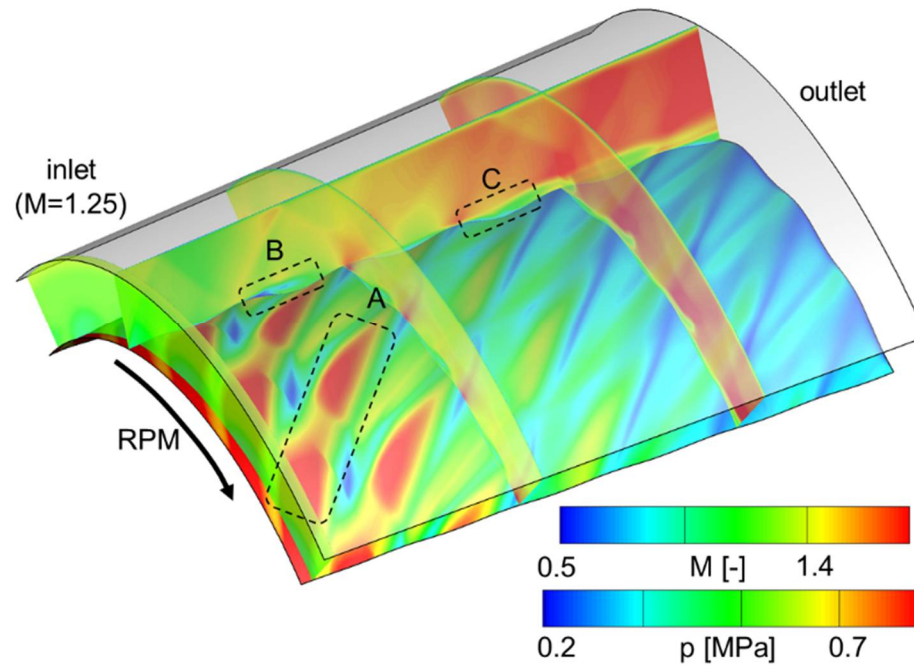
Figure 3.5 Flow field of the bladeless turbine for a Mach number of 1.25 at the inlet

Figure 3.6a depicts the pressure contour on the hub as a function of the axial distance and $R\vartheta$ coordinate. The transition from flat inlet to the first hill of the wavy contour is accompanied by a large pressure increase (0 till 0.02 m downstream of the inlet), due to the generation of compression and shock waves. Downstream of the first 'hill', the pressure decreases due to the expansion fans beyond which a periodic interaction of increase and decrease of pressure is observed. Figure 3.6b displays the tangential shear stress on the hub with locally negative values downstream of the valleys which marks flow that does not follow the axial core flow and hence does not participate in pressure decrease and limits power extraction (observed at 0.04 m from the inlet). The contribution of the pressure and viscous forces at each axial location is integrated along the tangential plane and is depicted in Figure 3.6c.

The inviscid contribution to the power extraction at one axial location (blue curve) is calculated as:

$$P_{inviscid} = \omega \times \int_{z=0}^{z=L} \int_{\theta=0}^{\theta=360} p.R\,d\theta\,dz \; , \frac{P_{inviscid}}{L} = \omega \times \int_{\theta=0,\; z=C}^{\theta=360, z=C} p.R\,d\theta \qquad \text{Eq. 3.1}$$

With the viscous contribution (red curve) at one axial location:

$$P_{viscous} = \omega \times \int_{z=0}^{z=L} \int_{\theta=0}^{\theta=360} \tau.R\,d\theta\,dz \; , \frac{P_{inviscid}}{L} = \omega \times \int_{\theta=0,\; z=C}^{\theta=360, z=C} p.R\,d\theta \qquad \text{Eq. 3.2}$$

The total contribution (black curve) is:

$$P_{total} = P_{invsicid} + P_{viscous} \qquad \text{Eq. 3.3}$$

The contribution of the pressure to the power (inviscid contribution, colored in blue) at each axial location is always positive and highest during the initial rise (0 till 0.02 m downstream of the inlet). The viscous contribution (due to the shear stress) is always negative as a result of the axial inflow. Local regions of lower power/length are due to detachment in the flow.

The ratio of the viscous-to-the-total power is 28% for the baseline case. The reduction and enhancement of power extraction along the axial chord is function of the shock interactions as well as local separation downstream of the wavy contours and is highly dependent on the Mach number at the inlet. In Figure 3.6d, the cumulative power as a function of the axial coordinate is calculated for each contribution. Power extraction is highest at the inlet, followed by a linear decay along the axial distance, at an approximate rate equal to 0.4 MW/m, which could be used to perform a quick length assessment of bladeless turbines. In contrast to bladeless designs with similar dimensions and without wavy surface [10], where no power can be extracted in this situation, 63 kW of power was extracted. The total pressure loss from inlet to outlet was 7.6% and constituted an increase of 3.3% points compared to a nozzle with the same area ratio and axial length. Total temperature ratio (T_{01}/T_{02}) was 1.0012 ($\Delta T_0 \sim 3K$).
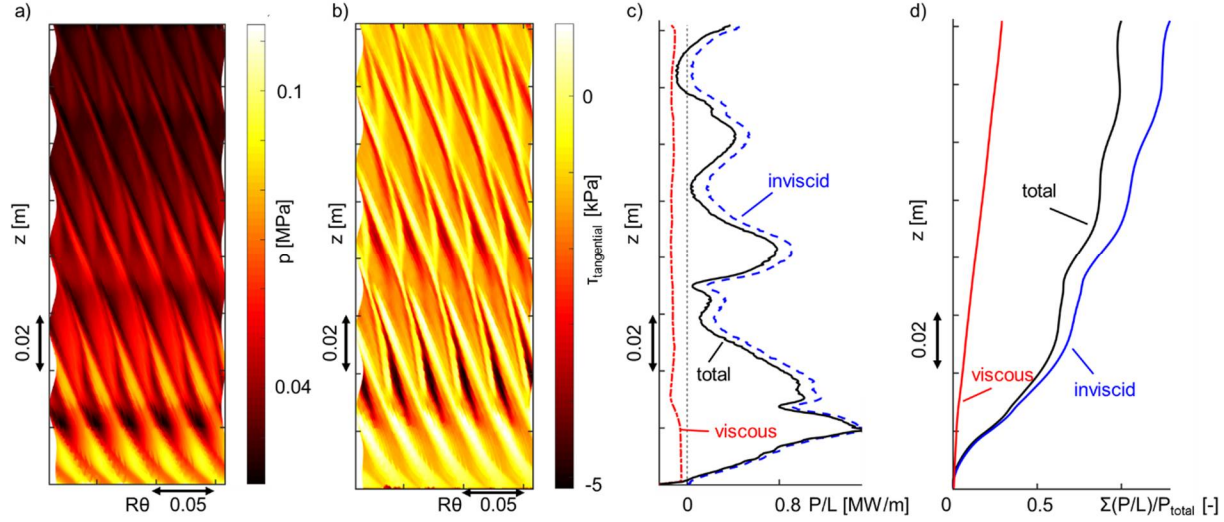
Figure 3.6 a) Pressure, b) tangential shear stress c) power/length along the axial length and d) cumulative power

To estimate the ratio of actual power extraction (P=$\mathbf{T}$·ω) to the power extraction in an ideal system, the efficiency from the conventional turbomachinery literature was employed, with the mechanical efficiency defined as:

$$\eta_{mechanical} = \frac{P}{\left(T_{0\ inlet} - T_{0\ outlet,\ isentropic}\right) * \dot{m} * c_p}$$
Eq. 3.4

And with the total-to-total thermodynamic efficiency:

$$\eta_{thermodynamic} = \frac{T_{0\ inlet} - T_{0\ outlet}}{\left(T_{0\ inlet} - T_{0\ outlet,\ isentropic}\right)}$$
Eq. 3.5

For the baseline turbine with a small wavy surface amplitude, efficiencies lie around 6% because the losses are generated through shocks and the channel is fairly long compared to the amount of power that is extracted in the aft part of the turbine. In contrast to subsonic turbines, supersonic turbines are not constrained by a downstream pressure ratio if the back pressure is low enough to guarantee supersonic flow. The obtained pressure ratio across the supersonic passage is, however, a function of the geometry of the turbine.

3.3.2 Heat flux assessment

To calculate the convective heat transfer coefficient, Moffat et al. [79] and Popp et al. [80] introduced the concept of the adiabatic wall temperature and adiabatic heat flux coefficient by the following equation:

$$q = h_{ad}(T_{ad} - T)$$

Eq. 3.6

With several isothermal simulations, the h_{ad} and T_{ad} can be retrieved [61]. Figure 3.7a visualizes the heat flux of the unwrapped bladeless turbine. Peaks of heat flux are present in the zones of compression and higher pressures and local minima are present in the acceleration and separation regions. Figure 3.7b shows the adiabatic heat transfer coefficient based on two isothermal simulations (1000K and 1400K). The tangential fluctuations at one axial location in terms of $\frac{Q_{max}-Q_{min}}{Q_{mean}}$ are growing from around 40% to 120% near the aft-section of the turbine. The adiabatic heat transfer coefficient follows a similar trend as the heat flux and local minima are in the acceleration and separation region, which are characterized by lower static pressure. In Figure 3.7c, the adiabatic wall temperature is computed and is around 2000K for this inlet total temperature of 2660K. At the onset of the separation regions, the adiabatic wall temperature is artificially high because the adiabatic heat transfer coefficient is near zero in that region due to the small difference in heat flux between the two isothermal cases. Figure 3.7d plots the average heat flux as a function of the axial direction. From inlet to outlet a decrease of 44% is observed with respect to the maximum heat flux upstream of the section. Hence, the highest heat flux lies in the region with the highest pressures and consequent highest local power extraction.
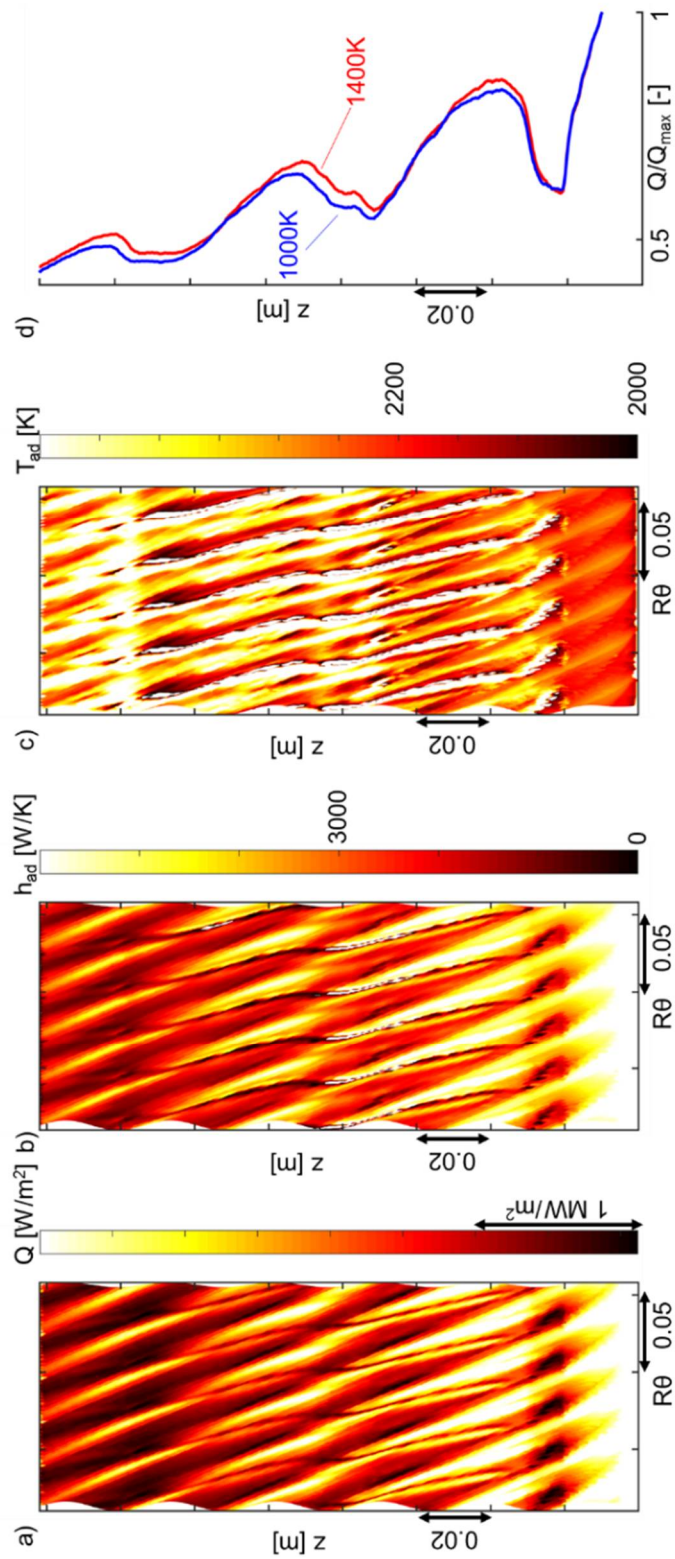
Figure 3.7 a) Heat flux, b) adiabatic heat flux coefficient, c) adiabatic temperature and d) mean axial heat flux over the maximum heat flux

3.4   From a three-dimensional representation towards a two-dimensional model

To study the flow features within the bladeless turbine, two tangential cuts of the Mach number of a bladeless turbine exposed to a steady inlet of Mach 2.1 are plotted in Figure 3.8. The contours highlight the compression zones and formation of shock waves (decrease of Mach number) due to the rise of the wavy contour as well as flow acceleration at the descent of the wavy contour and local detachment from the main core flow (identified by low Mach numbers). Figure 3.8b depicts the static pressure contour of a tangential cut in the bladeless turbine. On the other hand, Figure 3.8c illustrates the pressure contour of the same hub and shroud geometry solved in a two-dimensional frame with a steady inlet Mach number of 2.1.
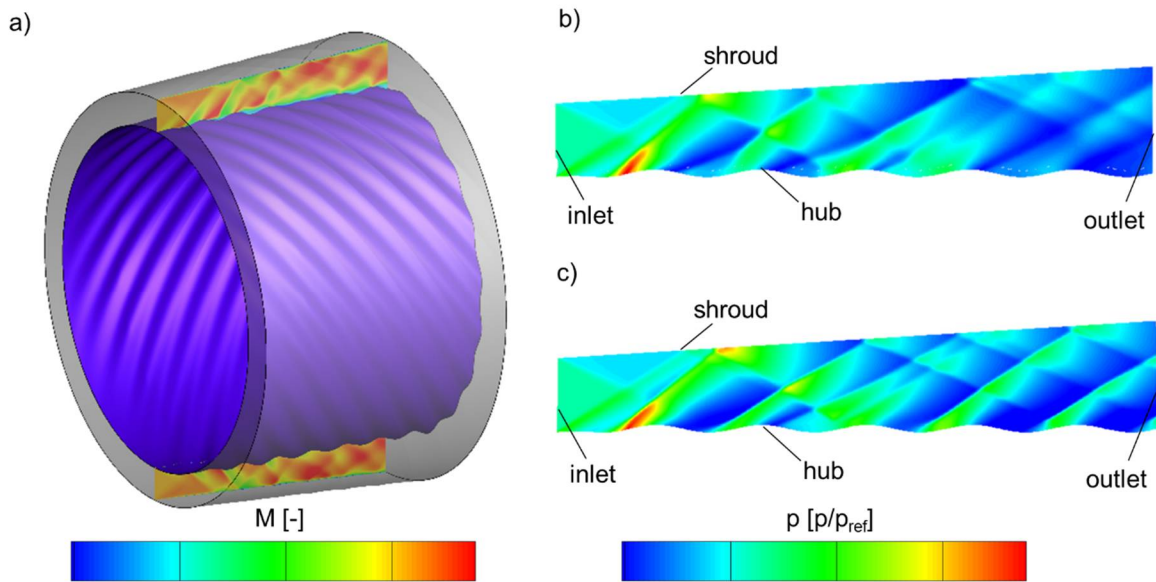
Figure 3.8 a) Mach contour of a bladeless turbine, b) 3D RANS pressure contour and c) pressure contour of the 2D RANS model

Several similarities exist between the two-dimensional and three-dimensional model: a strong compression shock compresses the flow, followed by an expansion and a recompression at the onset of the second wavy contour. Similar flow features are seen for the third wavy contour. From this analysis, it is concluded that the main flow features that determine the power to the turbine (the static pressure on the hub) are preserved for the first two consecutive waves in the two-dimensional representation.

The two-dimensional simulation provides additional insights into the physical mechanism and reveals the roots of the power generation. A zoom of the two-dimensional RANS simulation (Figure 3.9) reveals several zones of interest. A first set of compression waves (1) compresses the flow (2), followed by an acceleration zone in which the pressure decreases (3), followed by a detachment shock (4) and ultimately into a separation zone (5). This mechanism is repeated for the second and third wavy contour and results in a positive pressure force (in the z direction). The same shock pattern is observed for a bladeless turbine exposed to a steady inlet (Figure 3.9b). The inclination of the helix angle for the bladeless turbine provides a net force in the tangential direction of the wave and generates torque to rotate the hub. Similar flow structures were detected by Sun et al. [81] who performed Direct Navier Stokes (DNS) simulations of a wavy wall structure to study the curvature and Mach number effects in a turbulent flow. Tyson and Sandham [82] investigated the wavy wall structures for several amplitude-to-wavelength ratios. Gorle et al. [83] performed a RANS/DNS comparison and discussed the uncertainty quantification for the RANS simulations.
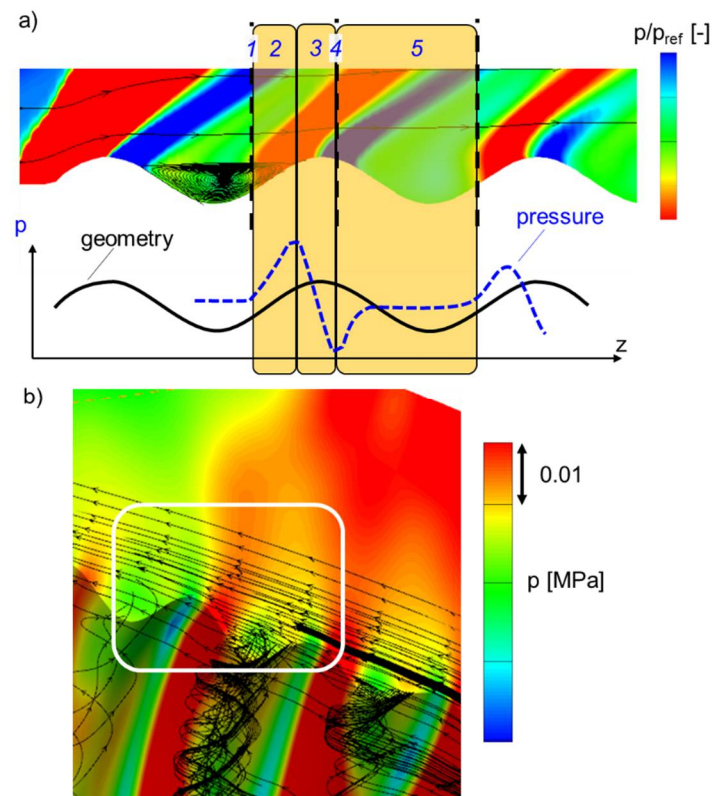
Figure 3.9 a) Mechanism behind the power extraction and b) features of the power extraction in a bladeless turbine with steady supersonic inlet

Figure 3.10 summarizes the quantitative comparison between the three-dimensional bladeless turbine and the two-dimensional simplified geometry. Figure 3.10a shows the pressure contour and Figure 3.10b plots the pressure of the 3D and 2D simulation as a function of the axial distance. The acceleration throughout the first and second wavy contour for both the three-dimensional simulation and the two-dimensional representation is comparable as well as the shear stress evolution. The reason behind the local mismatch for the third wave is due to the three-dimensional features in the bladeless turbine: the flow is more prone to follow the direction set by the helix angle in contrast to the two-dimensional case in which the flow is forced to travel in the axial direction. The skin friction (Figure 3.10c) follows a similar trend. Figure 3.10d depicts the integrated quantity pressure force ($F_{pressure} = \int p.dx$) which is the prime driver for the power extraction and the cumulative sum is calculated in Figure 3.10e. The discrepancy between the two dimensional and three dimensional representation (Figure 3.10f) is below 15% until around 50% of the axial length. This confirms that by testing these two-dimensional features, the physics that dominate the bladeless turbine can be demonstrated and numerical tools can be validated.
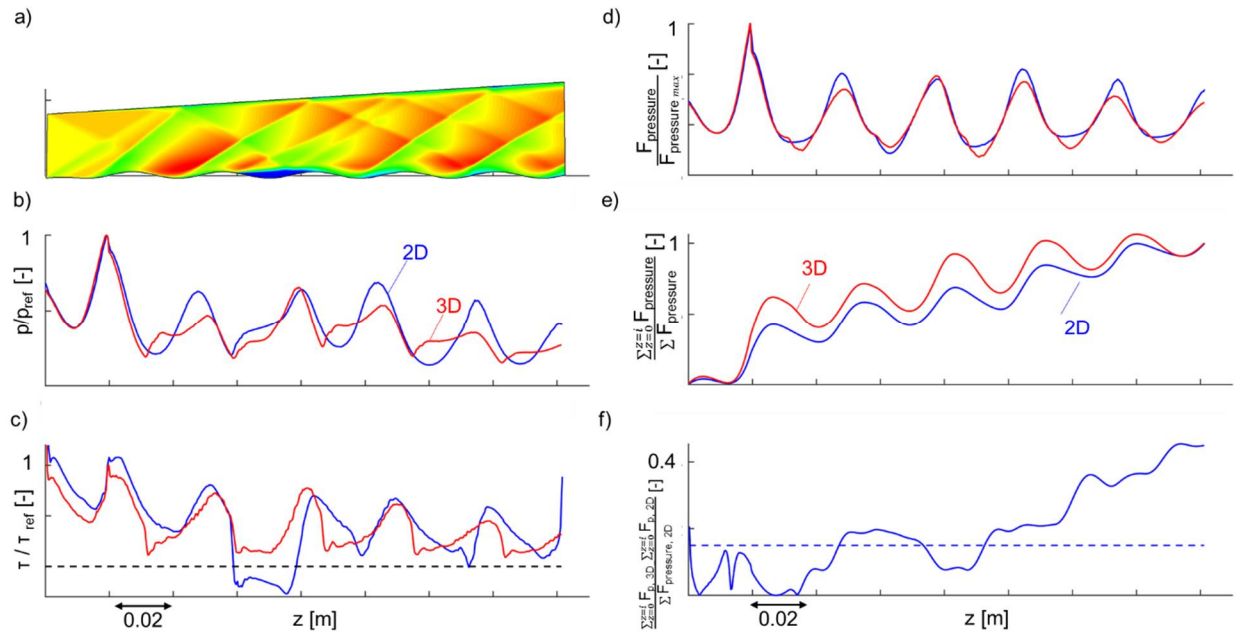
Figure 3.10 Quantitative comparison of the two-dimensional and the three-dimensional flow field: a) pressure contour, b) hub pressure, c) skin friction, d) pressure force, e) cumulative pressure force and f) discrepancy between the 3D simulations and the 2D model

The mass-flow averaged total pressure loss from inlet to outlet is compared in Table 3.4. Up to 25% of the channel length, the total pressure loss is comparable. At 50% of the axial length (in which approx. 80% of the power generation takes place) the discrepancy increases to 33%.

Table 3.4 Total pressure loss of the three-dimensional bladeless turbine versus the two-dimensional model

	z/L=0.125	z/L =0.25	z/L=0.5
pressure loss (2D)	0.0178	0.056	0.144
pressure loss (3D)	0.0183	0.057	0.109
discrepancy [%]	2.6	2.1	33

CHAPTER 4. EXPERIMENTAL ASSESSMENT AND UNCERTAINTY QUANTIFICATION

4.1 Experimental setup

To experimentally test the wavy surface, only the first three consecutive waves are considered (Figure 3.10) as the previous analysis demonstrated that such a two dimensional geometry mimics the behavior of the three dimensional bladeless turbine and additionally, around 80% of the power production occurs within the first 50% of the section for the baseline case. The design of the test section is based on several Reynolds Averaged Navier Stokes (RANS) simulations. Figure 4.1a represents a Mach contour from a two-dimensional RANS simulation of the convergent-divergent section in which the flow is accelerated from Mach 0.1 (inlet conditions coming from the settling chamber) to Mach 2. Downstream, the three successive wavy contours (waves) are visible. Several shock features are present and will be discussed in more detail through this chapter, ranging from the compression waves originating at the onset of the first wavy contour and resulting into a shock wave, shock-boundary layer interactions at the shroud, separation shocks in the hub and shock-shock interactions in the flow field.

To achieve Mach 2 flow at the onset of the first wave, the convergent-divergent nozzle was designed through Bezier curves which guarantee curvature continuity. Figure 4.1b depicts the shape of the convergent-divergent part as well as the wavy hub geometry. The first derivative of the divergent nozzle was ensured to be continuous to guarantee a smooth flow. To increase the spatial resolution, the inlet height and bladeless turbine were scaled up. The entire length of the test section is 0.54m and is referred to as L in the chapter.
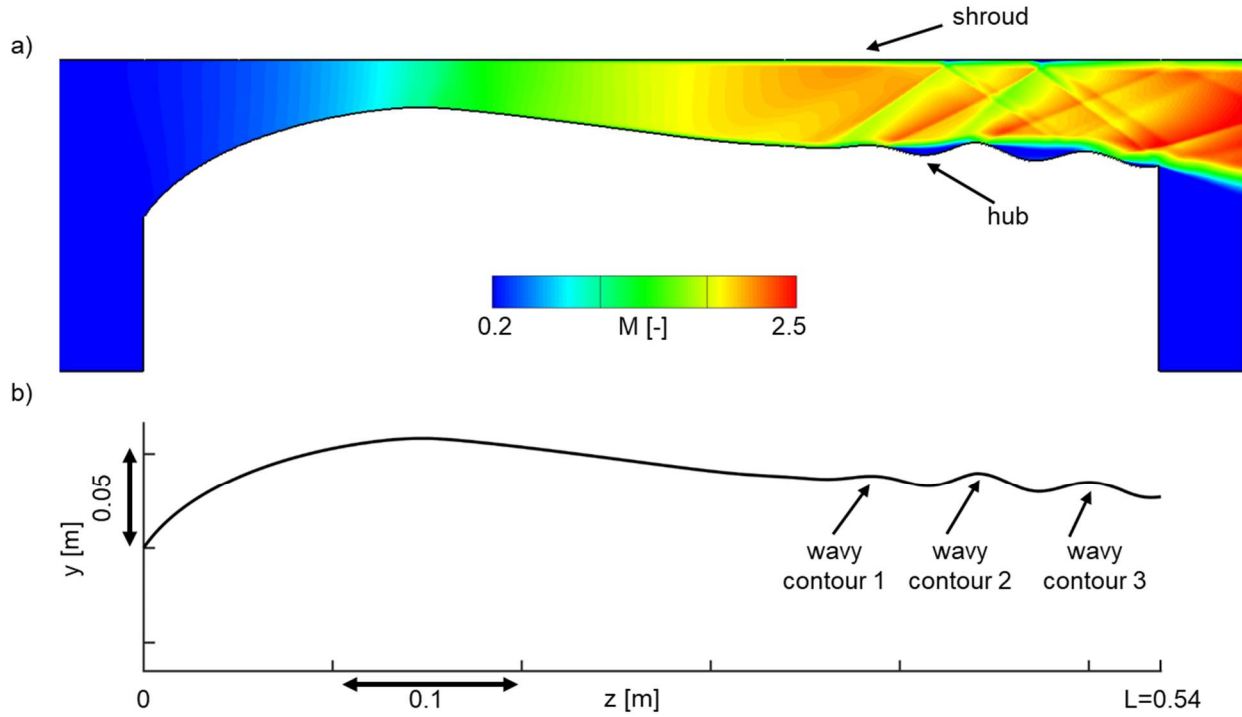
Figure 4.1 Design of the test section: a) contour of the Mach number and b) geometry of the convergent-divergent nozzle with the three wavy contours (waves)

To be able to convert the flow leaving the settling chamber from the linear wind tunnel from a circular cross-section to a squared cross section, a contraction was designed by Saavedra [48] and is visualized in Figure 4.3a. Behind the contraction, the convergent divergent nozzle can be mounted. To be able to test multiple geometries, high modularity was one of the main assets for the design of the test article. Figure 4.2 reveals that the test article consists of four pieces that can be assembled through bolts. The first piece (1) is the convergent part and the second piece is the convergent-divergent nozzle (2). the third piece is the wavy article (3) and the fourth piece is the baseplate (4) and creates the correct area ratio between the upper wall and the test article. Figure 4.2b depicts the actual manufactured piece out of aluminum.
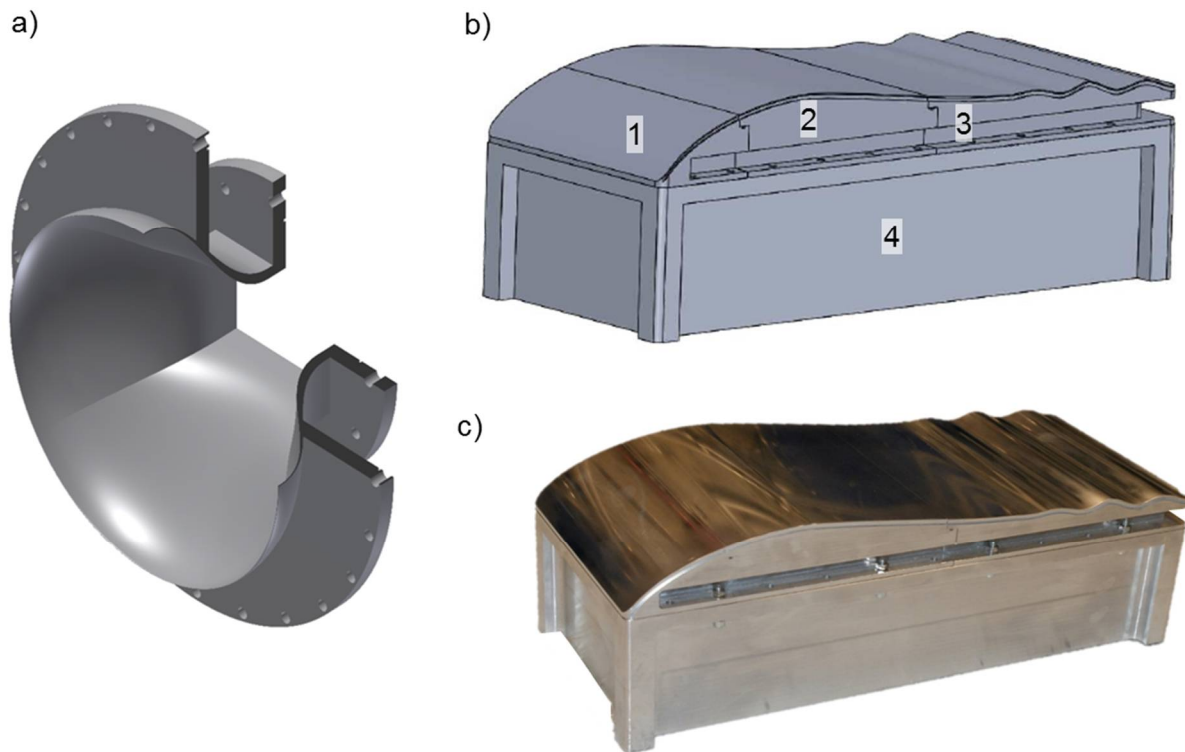
Figure 4.2 a) Contraction from the settling chamber into the test section [48], b) CAD rendering of the entire test article and c) CNC machined test article in aluminum

The final CAD rendering of the supersonic convergent-divergent-wavy wall test article within the wind tunnel is portrayed in Figure 4.3a. The four individual pieces are first assembled outside of the test section and then mounted into the linear wind tunnel. The mounted test article is seen in Figure 4.3b. The two quartz windows are mounted and allow for complete optical access for the optical measurements.

a)
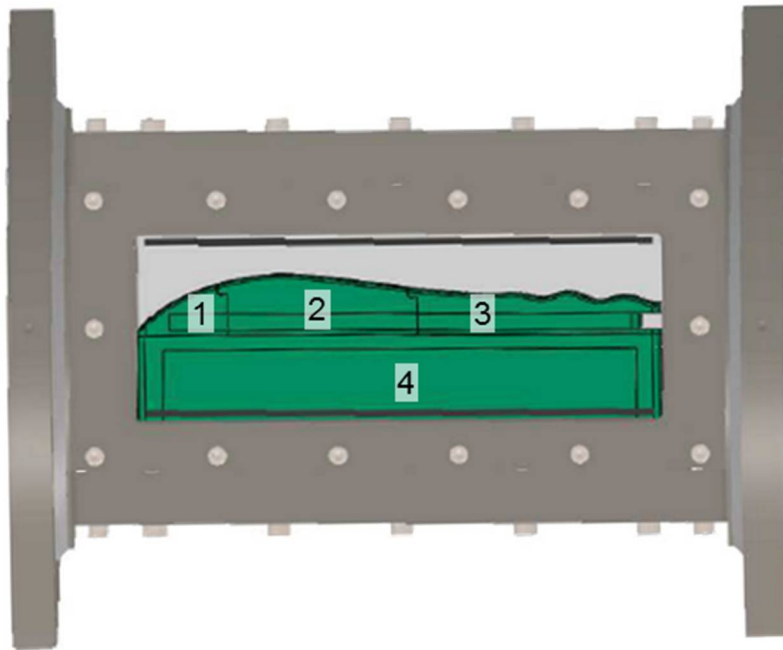
b)
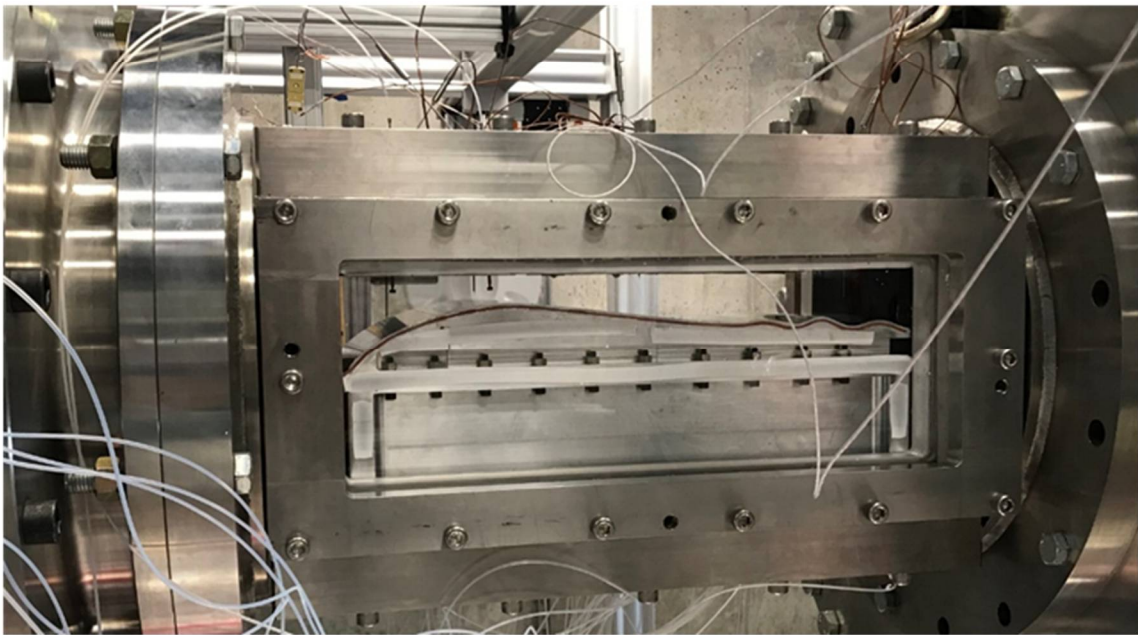
Figure 4.3 CAD design of the test article inside the wind tunnel and b) the convergent-divergent nozzle with a wavy surface

4.2 Steady-state measurements

This subsection consists of capturing the steady-state performance values of the bladeless turbine. The methodology consists of the combination of four measurement techniques (Figure 4.4):

- With Schlieren, the flow field phenomena that occur due to the presence of the hub waves are studied together with a first estimate of the flow angle fluctuations because of the multiple shock boundary layer interactions and the uncertainty on the shock angle predictions from the RANS simulations.

- The surface pressure measurements deliver a quantitative measure of the separation points. Additionally, the inviscid contribution to the power is approx. four times larger than the viscous contribution (Section 3.4), hence precise pressure measurements are critical to estimate the uncertainty on the power extraction from the RANS predictions.

- Precise skin friction measurements through the SIFS technique in the divergent section and compression ramp allow determining the actual contribution of the viscous contribution.

- The heat flux contribution at discrete locations is estimated with surface thermocouples along the compression and acceleration zones.

Ultimately, this is combined in an overall uncertainty of the bladeless turbine on power extraction, efficiency, and heat flux in Section 4.4.
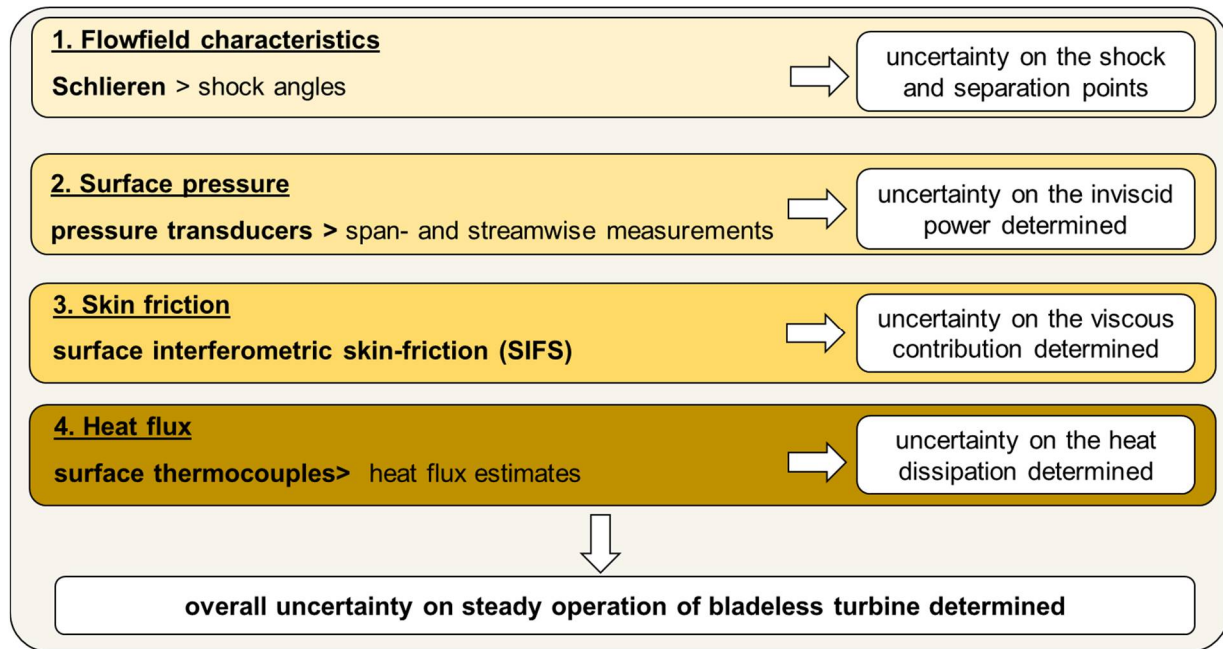
Figure 4.4 Methodology to predict the overall uncertainty for the steady-state operation of the turbine

4.2.1 Shock structures

In Figure 4.5, the Schlieren flow visualization of the start-up and shut down during one test is highlighted. For this experiment, the camera was focused on the first wavy contour downstream of the divergent section (Figure 4.1b). When the valve opens, a steady shock wave forms at t=0.26s, which arises from the compression waves due to the presence of the first wavy contour. The shock wave confirms supersonic flow regime within the test section. A separation shock is established in the rear part of the first wavy contour and arises because of the presence of the second wavy contour downstream. The position of the first compression ramp is relatively steady (from t=0.26 till t=12.2). The formation of the boundary layer is also captured (e.g., t=0.26 to t=12.2s). During shutdown (t=12.58s) a fast (detached) pressure wave travels upstream behind which the flow is subsonic and eventually slows down to no-flow (t=12.58s).
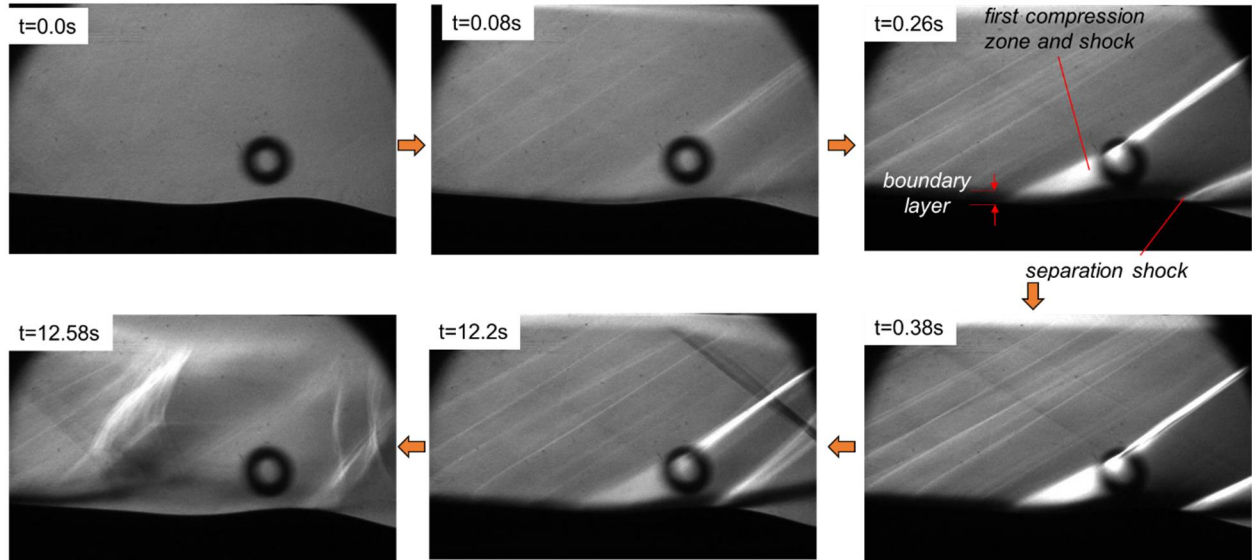
Figure 4.5 Start-up and shut down via Schlieren visualization

Figure 4.6a shows a snapshot in time of a typical Schlieren image during a test. At the onset of the hill of the first wavy contour, a first compression zone and consequent shock are formed, followed by a separation shock and a shear layer in the valley, with a similar pattern for the second wavy contour. From the Schlieren imaging, unsteadiness is observed in the shear layer as well as the separation and downstream recompression zone. This can be explained by the interaction of the shear layer with the consequent compression shock, as described by Leger et al. [84] and Deshpande and Poggie [85] and will be further dissected in the section about the high-frequency phenomena (Section 4.3). The numerical Schlieren from the RANS simulations (visualized in Figure 4.6b) captures the relevant shock structures such as the compression shock, reflected shock and shear zone adequately.
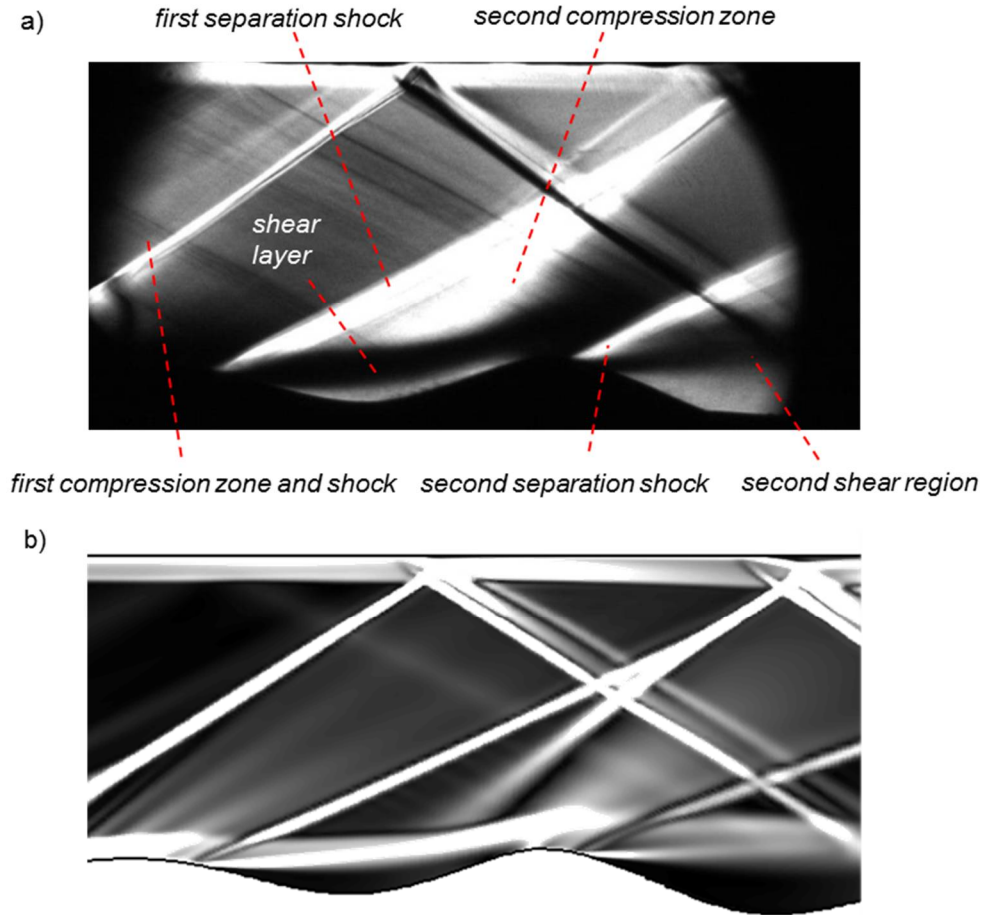
Figure 4.6 a) Schlieren focusing on the first and second wavy surface and b) numerical Schlieren

With an automatic flow pattern detection program based on binarization of the Schlieren data, similar to [86], the shock angles at multiple locations are extracted and compared to CFD. The colored zones in Figure 4.7a depict the locations of two shocks that are investigated. The first one is the compression shock (red) and the separation shock (blue). The colored region bounds the limits in which the shock was found to be moving. The compression shock (red) is relatively steady, and the colored region displays the 5% and 95% confidence interval of the shock position. The first separation shock (blue) is oscillating and as a result, the shear layer as well. Figure 4.7b shares a view on the downstream section with the reflection shock (magenta) and the second separation point (green and yellow), which becomes increasingly unsteady. Figure 4.7c portrays the flow fluctuations of the several shock structures as a function of time and higher oscillations are found for the second shock reflection (yellow).
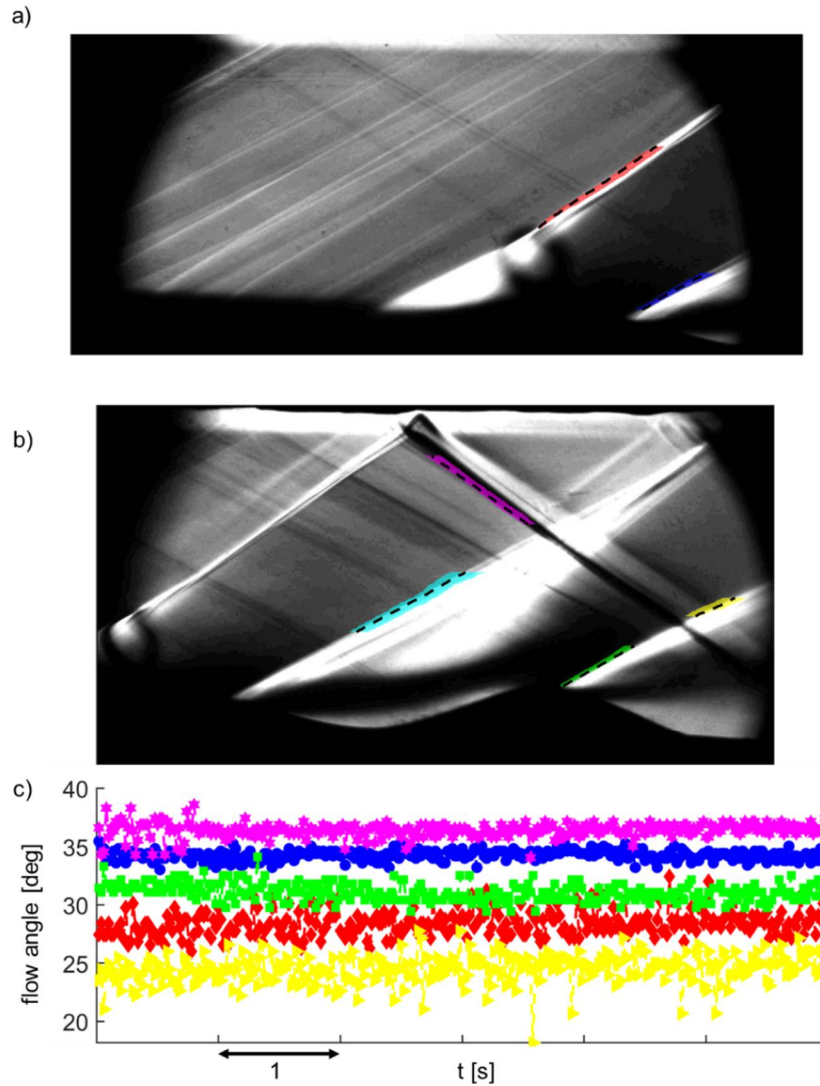
Figure 4.7 Observed unsteadiness for the low-frequency Schlieren experiments: a) the compression shock and first separation shock, b) separation shock, the shock reflection and second separation shock and c) shock angle variation as a function of time

Table 4.1 depicts the flow angles, their standard deviation (STD) and the comparison with two-dimensional RANS. The flow angles are computed at two fixed heights of the channel and the angle is computed relative to the hub for all angles except for the reflected shock in which the reference plane was the shroud. The compression shock angle computed from the RANS simulation lies within the uncertainty of the experimental Schlieren. The discrepancy of the first separation shock is two degrees and will also affect local deviations in hub pressure (discussed in Section 4.2.2). The flow angle is slightly higher in the experiment, which means that the shock is

stronger and hence, lower Mach numbers behind the shock wave are found with consequently higher pressures. Thus, the onset of separation is slightly mispredicted, but due to the relatively large gradients in curvature, this can result in locally high deviations in pressures and heat flux on the hub. The reflection shock is matched within 1.5 degrees and the second separation shock within two degrees, like the first separation shock. Due to an accumulation of uncertainty downstream of the first wavy contour, the uncertainty on the shock angles increases. It is also observed that further away from the onset of the two separation shocks, the angle decreases but the standard deviations increase from 2.5% to 5%, owing to a growing unsteadiness within the flow field.

Additionally, the relative axial displacement is calculated and compared to the compression shock. The axial displacement of the first separation shock measured further away from the hub (cyan) is approx. four times higher than the movement of the compression shock.

Table 4.1 Flow angles retrieved from the Schlieren: unsteadiness and comparison with RANS

	$\delta_{shock,\ mean}$[deg.]	$\delta_{shock,\ mean}/ \delta_{shock,\ STD}$ [-]	2D RANS	$\Delta z/ \Delta z_{ref}$[-]
compression shock (red)	34.25 (+/-0.9)	0.012	34.28	1
separation shock (blue)	28.4 (+/-0.6)	0.037	26.0	2.4
reflection (magenta)	36.4 (+/-0.36)	0.017	34.6	2.6
second separation shock (green)	31 (+/- 0.56)	0.024	29.05	1.6
second separation shock downstream (yellow)	24.5 (+/- 1.1)	0.05	-	3.2
first separation shock downstream (cyan)	29 (+/-0.4)	0.044	-	4.7

4.2.2   Pressure force

Figure 4.8 displays the total pressure during a typical run. When the valve opens, a peak is seen in the total pressure, and this is due to the operation of the facility. To reach the right mass flow at the correct temperature, a second line- the purge line- is used and when the desired test conditions are met, the valve towards the test section is opened and afterward, the purge line is closed. The red line depicts the total pressure upstream in the test section and shows a constant pressure during the supersonic regime, the blue line (downstream) however fluctuates due to unsteady shock interactions. This test duration was around 100 seconds. At the end of the experiment, the test section valve is again opened, and the pressure equalizes to the atmospheric pressure.
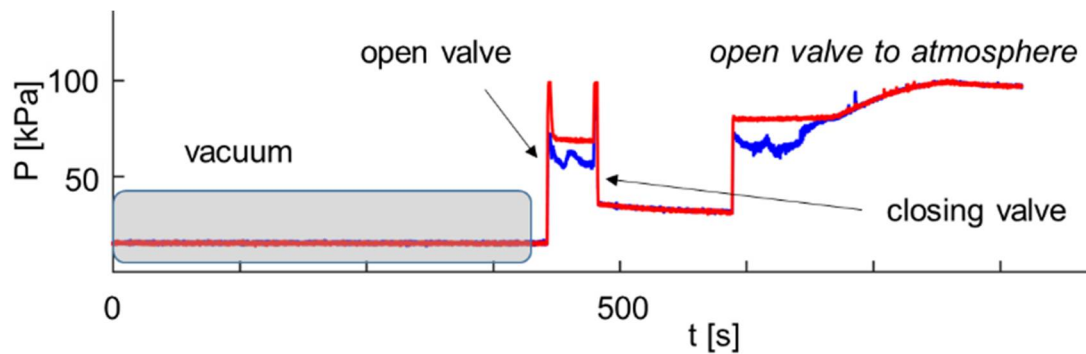
Figure 4.8 Total pressure signature of one entire test run

Figure 4.9a displays the non-dimensional static pressure distribution on the hub. Figure 4.9b visualizes the height of the test article as a function of the axial distance and indicates the locations of the static pressure taps. In Figure 4.9c, the discrepancy between the RANS and the experiments is calculated and several zones of interested are highlighted. Region A depicts the subsonic-supersonic section with the first compression ramp in which the discrepancy between the RANS and the experiment remain below a maximum of 4.9% (at a location of x=0.355m). Area B is the region where separation occurs and discrepancy raises to 13%. Afterward, in zone C the flow attaches again with discrepancy below 4%. Region D is characterized by a second separation zone in which the discrepancy is between 10-15%. Finally, the flow attaches again in region E and discrepancy drops below 14%. In the separated region, the pressure predicted by the RANS results is lower, which can be explained due to a slight mismatch between the point of separation and

reattachment in the CFD. The RANS and URANS tools are usually adequate to predict the onset of the separation bubble, however, they over-predict the extent of the separation bubble.
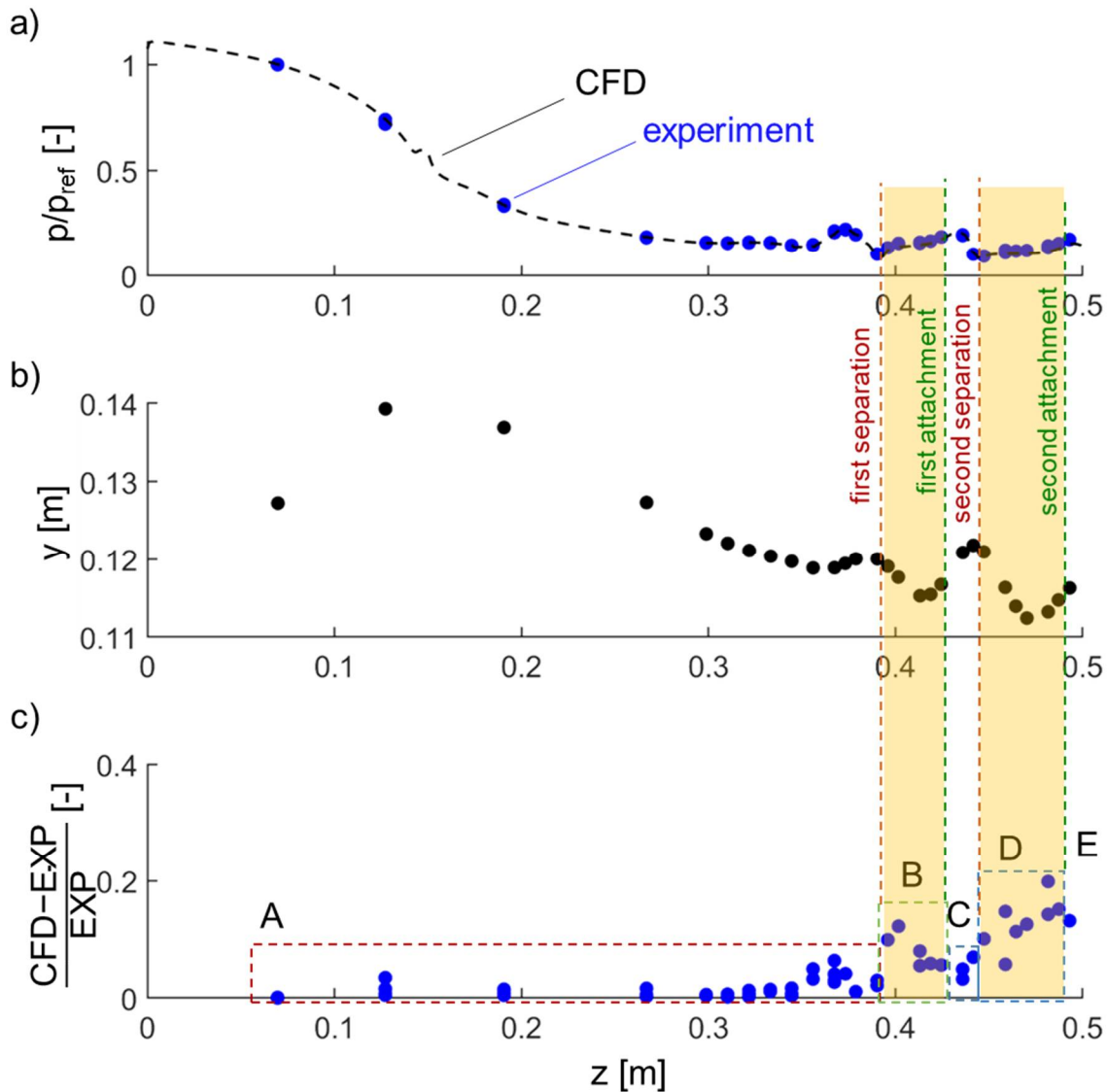
Figure 4.9 Comparison between the experiments and the RANS results: a) pressure as a function of the axial distance, b) height of the test article as a function of axial distance and c) the discrepancy as a function of the axial distance

Span-wise variation of static pressure at the inlet of the convergent section was below 1%. At the throat, spanwise variation was maximum and had a measured value of 3 % and decreased to 1.5% at the start of the wavy surface. Figure 4.10 plots the relative difference between eight

different experiments and the RANS results. In all regions the discrepancy between experiments is below 4%, however at the second separation, the variation is larger (at an axial location of z=0.45m to 0.5m), which might be explained due to a difference in back pressure for the different experiments, three-dimensional effects as well as the test-to-test variations in Reynolds number.
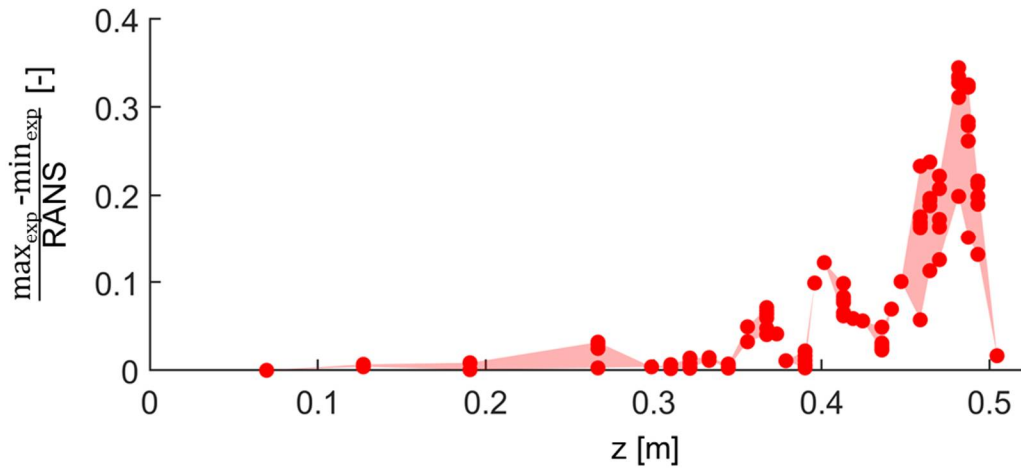
Figure 4.10 Test-to-test discrepancy along the axial distance

4.2.3   Surface roughness

Two models have been tested, an aluminum test section (Figure 4.11a), with a mean roughness of 6 micrometers (max and min values of 80 micrometers), and was CNC machined. A second one was 3D printed from Fullcure material, also used for biomedical applications (Figure 4.11b). The roughness of the latter is 100 micrometers (maximum value of 900 micrometers) and is mostly due to the surface finish of the 3D printer, which was an Eden350 3D printer with an uncertainty printing of 0.1 to 0.3 mm. The roughness was tested with a Mitutoyo SJ210 Surface roughness Tester.
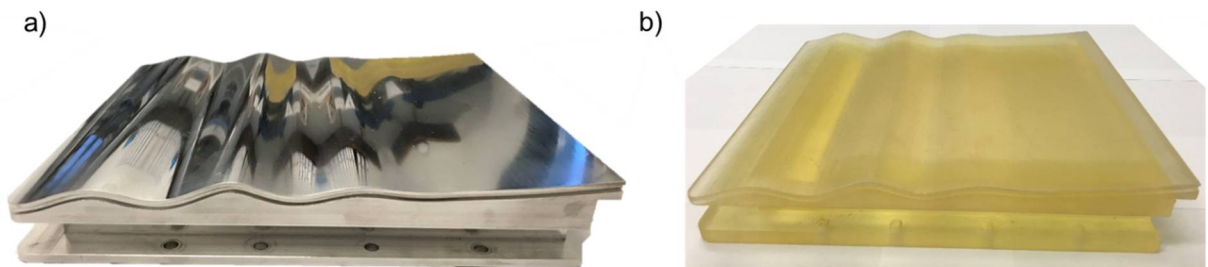
Figure 4.11 Aluminum wavy test article and b) additive manufactured wavy test article

The pressure is plotted in Figure 4.12 for both types of material as a function of the axial distance. The blue dots represent the aluminum test article while the red dots indicate the 3D printed article. The additive manufactured wavy article follows the same trend as the wavy aluminum article in the divergent part (undisturbed by the successive compression and acceleration ramps) however at the compression ramp (1) and separation onset (2) the pressures are underestimated by up to 20% in the compression ramp. Additionally, in the separation zone (3) pressures are overpredicted by 15%. These could all come from a slight difference in shock separation location and could be due to the slight differences in geometry due to the manufacturing process. The black encircled points show points at the 30% and 70% span, which mean that additionally, three dimensional effects in the wind tunnel could be higher for the 3D printed wavy article than for the aluminum piece in which the spanwise variations were seen to be varying up to 25%, in contrast to the aluminum piece in the flow was predominantly two-dimensional.
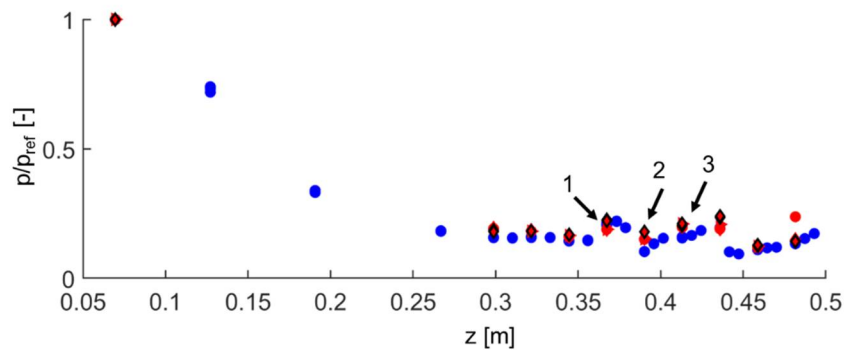
Figure 4.12 Static pressure distribution of the 3D printed wavy surface (red) and the aluminum (blue) test article

4.2.4 Skin friction

Figure 4.13a-b and c show the calibration target at multiple tangential positions (the distance in between each calibration target was 6.35 mm) and the circular calibration marks a diameter of 6.35 mm. Through the calibration procedure, the two-dimensional picture can be mapped onto the model space [87] and the physical distance can be retrieved. In Figure 4.13d the exactness of the points of the calibration is plotted and demonstrates that most points of the calibration fall within the predicted value.
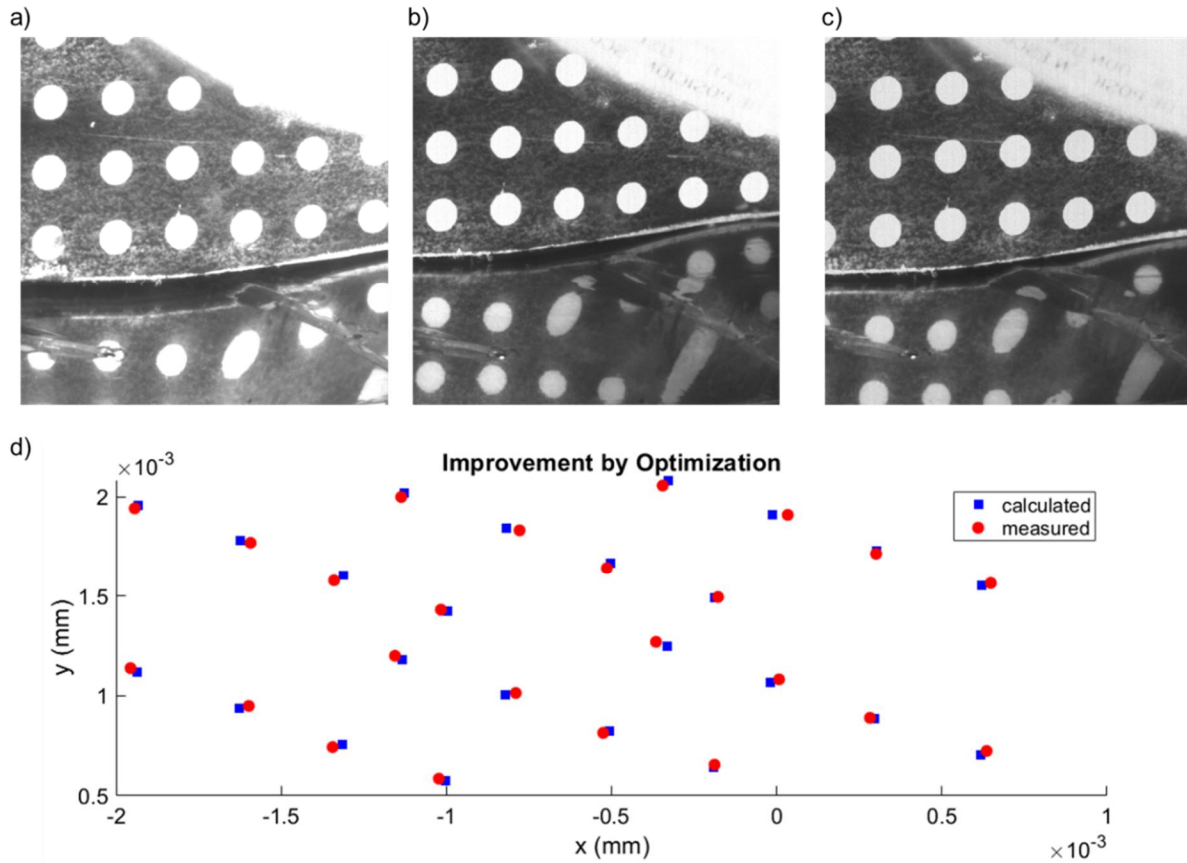
Figure 4.13 Camera calibration: a) at x=6.35mm, b) at position x=12.7mm, c) at position x=19.05mm and d) projection of the reference points of the camera onto the model space

     The oil droplets that were placed on the hub surface are visualized in Figure 4.14. Three oil droplets were placed on the surface before switching on the vacuum pump (Figure 4.14a, t=0s). At t=0.5s, during actual blowdown, the oil dots move. At t=42.5 fringes appear, and this is the time step for which the shear stress is calculated in the compression region. Figure 4.14b depicts a sequence of oil drops that were placed in the divergent part and fringes are apparent at t=50s.
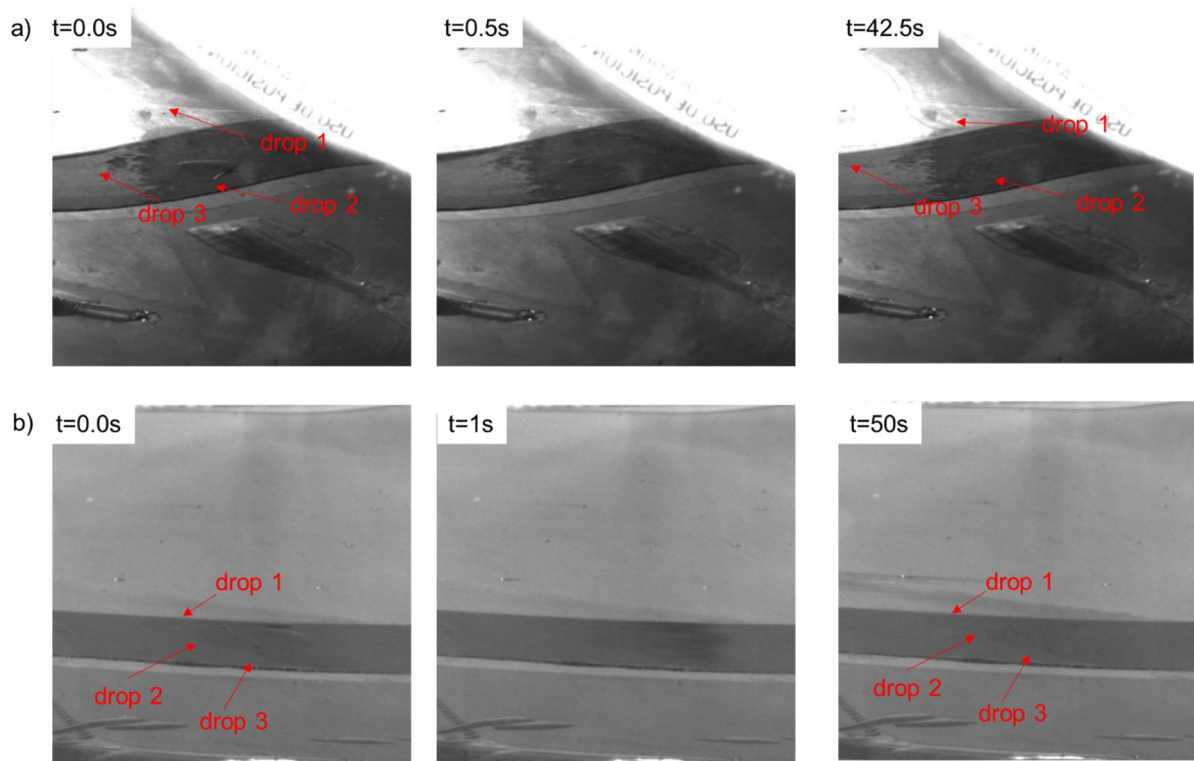
Figure 4.14 Time sequence of the oil droplet movement during a supersonic test: a) in the compression region of the first wavy surface and b) in the divergent section

Figure 4.15 shows the oil droplets of Figure 4.14 after calibration, mapped onto the physical surface to measure the actual distance between the fringes that have been formed. Figure 4.15a highlights the fringes on the compression ramp, while Figure 4.15b focuses on the fringes in the divergent section.
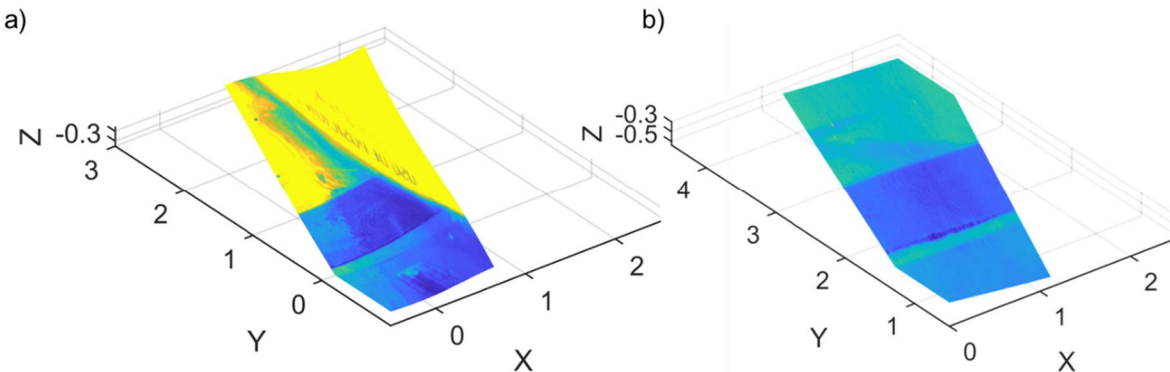
Figure 4.15 Pictures mapped onto the physical surface: a) fringes in the compression region of the first wavy surface and b) fringes in the divergent section of the nozzle

Figure 4.16a visualizes where the skin friction was measured by plotting the geometry. Figure 4.16b displays the measured skin friction as a function of the axial distance (according to Eq. 2.6 and Eq. 2.7). The different colors depict different test conditions. Two turbulence models are investigated, Spalart Allmaras (SA) and K-omega SST. Spalart Allmaras predicts a shear stress that is around 10% higher than SST. However, the onset of separation and attachment are similar for both turbulence models. The RANS predictions and experiments fall within an averaged discrepancy of 20%. Interestingly, similar trends are found in the compression region (test 3).
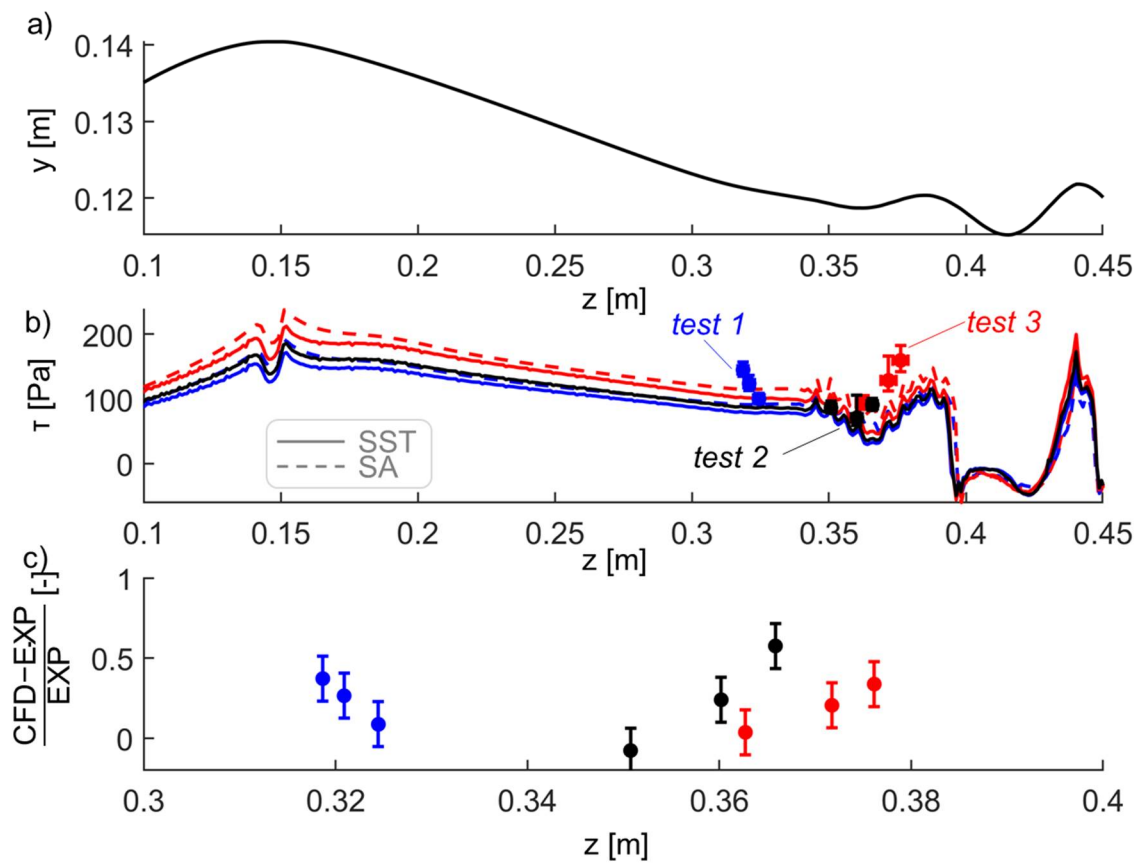
Figure 4.16 Skin friction: CFD vs experiments: a) geometry, b) shear stress as a function of the axial distance and c) discrepancy of the numerical with the experimental data

4.2.5   Heat flux

To retrieve the heat flux at several locations, surface thermocouples are used as discussed in Section 2.2. The total thickness of the thermocouple sheet is below 0.2 mm to ensure that the flow field is disrupted as least as possible by the presence of the surface thermocouple and does not generate additional compression and expansion fans which would alter the temperature reading. The surface thermocouples are glued on the surface of the wavy surfaces with Kapton tape (Figure 4.17a). A typical run is shown in Figure 4.17b where the total temperature rises to 450K and temperature stability in five seconds is below five Kelvin. The surface temperature is colored in red for two thermocouples and the back temperature in black, which remains quasi-constant. The heat flux is calculated based on the method described by Saavedra et al. [61] in which the back-wall temperature (blue) and surface temperature (red) are an input boundary condition.
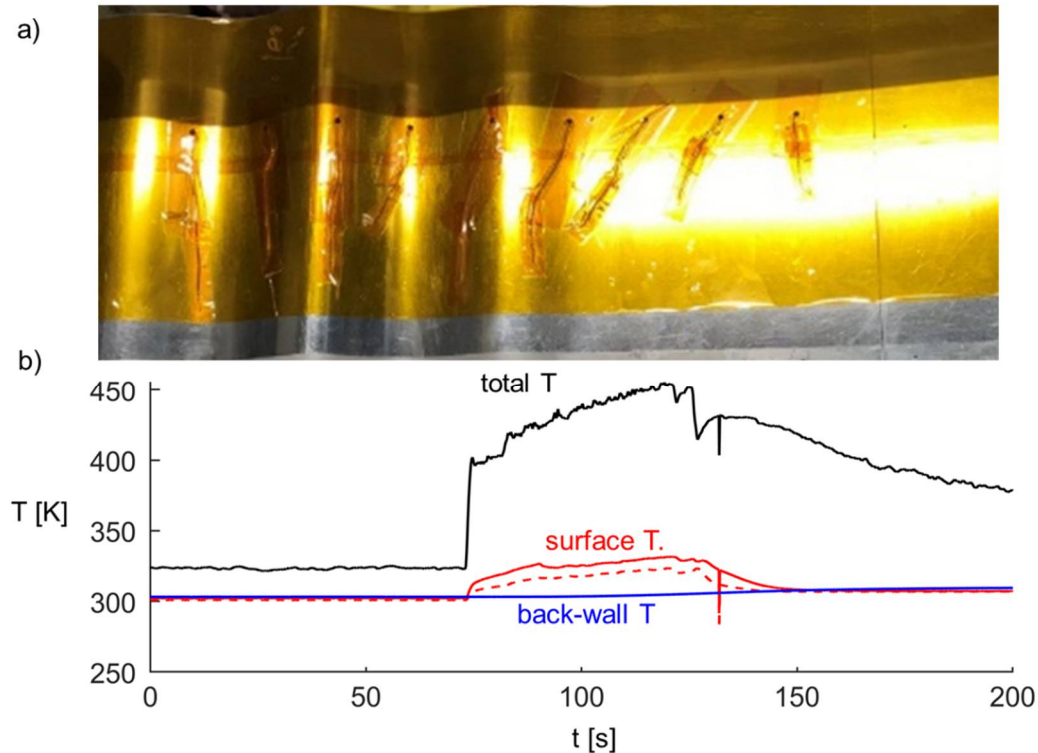
Figure 4.17 a) View of the surface thermocouples on the hub surface and b) thermocouple response as a function of time for one test

To compare these results to computational fluid dynamics, a conjugate heat transfer analysis is performed and compared to an isothermal approximation. The computational domain is visualized below (Figure 4.18a) and a constant temperature was applied at the back of the solid

as well as the inlet total temperature and inlet total pressure retrieved from the experiments. The temperature contour reveals slight temperature gradients in the solid at the summit of the convergent-divergent section and the wavy contours. Figure 4.18b compares a RANS isothermal simulation to a RANS conjugate heat transfer (CHT) simulation in the region after the divergent section. At the onset of the wavy contour, both simulations are similar, however at the first reattachment location the CHT predicts a slightly higher heat flux of 25% compared to the constant wall temperature case, and in the separation region, the heat flux signature is slightly different. Downstream of the second wavy contour, the predicted heat flux by the CHT simulations is 26% higher. Due to the differences, the CHT results are used to further compare the experiments with the numerical models and to quantify the uncertainty on the heat flux. The discrepancy between the two simulations can be explained due to the interaction of the solid and the fluid in regions of high gradients of curvature between the successive wavy contours which is not modeled with isothermal simulations.
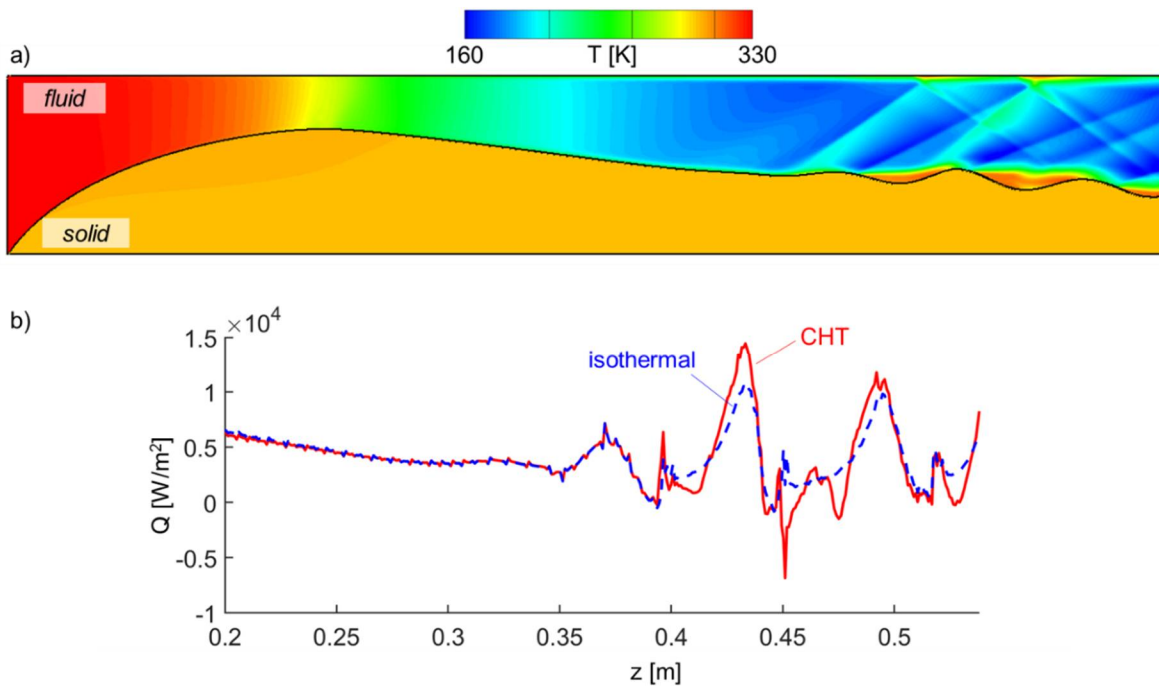
Figure 4.18 a) Computational domain for the conjugate heat transfer analysis and b) a conjugate heat transfer (CHT) simulation versus an isothermal RANS simulation

Figure 4.19b and Figure 4.19c depict the heat flux as a function of axial distance for two tests with surface thermocouple arrays placed at different axial locations. The errorbars show the

range of minima and maxima during the supersonic operation. The magenta regions in Figure 4.19a indicate separation regions in which 10% discrepancy was found for the static pressure, and hence an increased discrepancy in heat flux can be expected within those regions. The first test (Figure 4.19b) shows that within the divergent section the heat flux is accurately captured (a maximum discrepancy of 10%), however in the first separation region the heat flux is off by 60% and matches downstream relatively well in the attachment regions. In the second separation region, the heat flux is off by 100%, and near the second recompression region (z~0.47m), the heat flux discrepancy again reduces to 30% discrepancy. For the second test case, similar trends are found, which concludes that near the attached regions the heat flux is reasonably well predicted by the computational models, and this discrepancy in heat flux is higher in the detached regions with values up to 100% discrepancy.
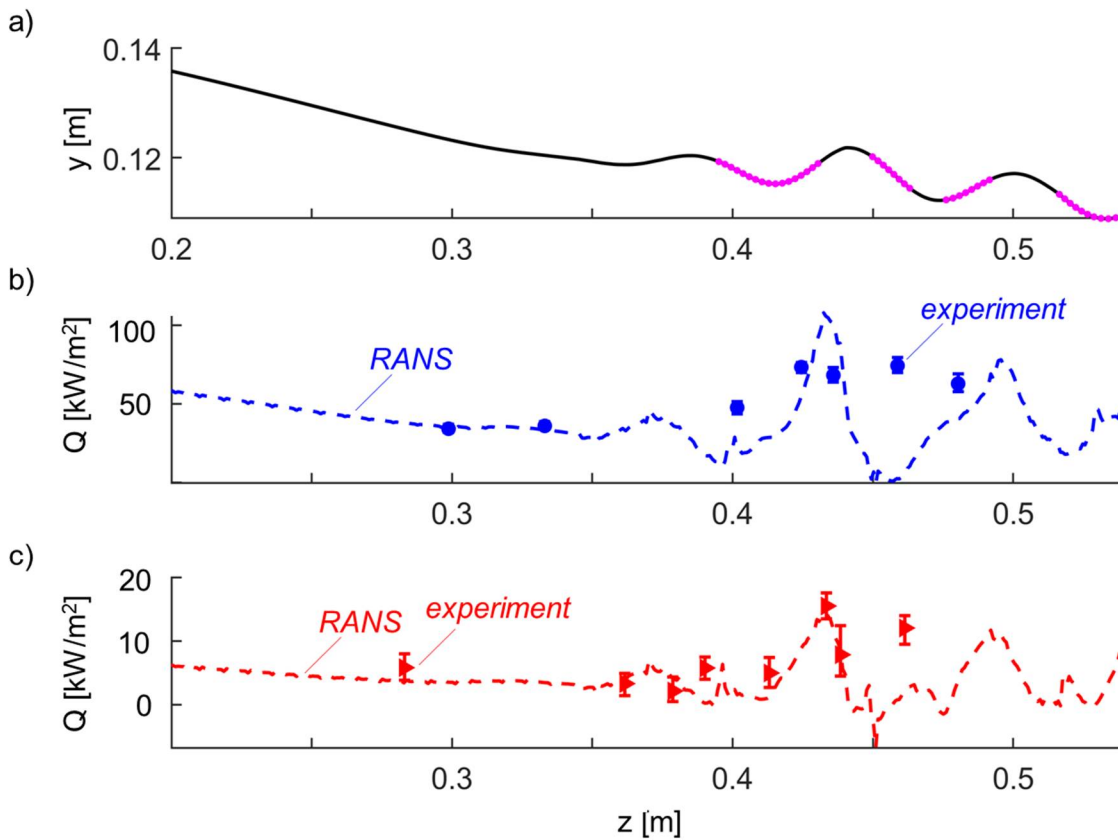
Figure 4.19 Heat flux of the RANS versus experiments: a) axial distance versus height with the separation zone colored in magenta, b) test 1: heat flux as a function of the axial distance and c) test 2: heat flux as a function of the axial distance

4.3   High-frequency effects in the bladeless turbine

In the RANS simulation, the flow structures are represented as a steady phenomenon. In reality, however, these structures are inherently unsteady and might affect the operation of the bladeless turbine, both from an aerothermal as well as a structural aspect.

Second, when the bladeless turbine is used as a bottoming cycle in a nozzle or for components downstream of the bladeless turbine, the assessment of the flow field fluctuations is critical.

Third, during startup and shutdown of the turbine, a transient shock wave will pass through the turbine and might endanger the structural integrity because of pressure fluctuations as well as transient heating.

Figure 4.20a displays the shadowgraph visualization of an unsteady RANS simulation, and the simulation time step was one microsecond. In contrast to the experimental data (Figure 4.7), the RANS predicts no unsteadiness. Figure 4.20b and Figure 4.20c plot the pressure and skin friction along the hub surface. Both RANS and URANS display an identical behavior.
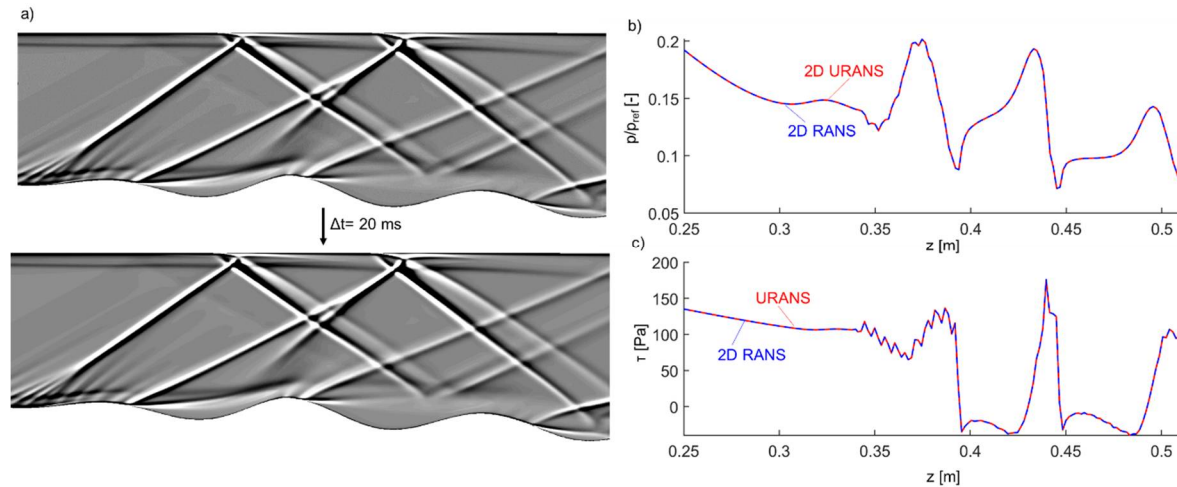
Figure 4.20 URANS simulation on the wavy geometry: a) instantaneous numerical shadowgraph images, b) RANS versus URANS for the pressure distribution along the axial direction and c) RANS versus URANS for the skin friction distribution along the axial direction

The strategy to dissect the high-frequency phenomena is highlighted in Figure 4.21. Several tools are used in this section: to quantify the shock angle fluctuations, during 'steady-state' operation as well as during start and shut down, high-frequency shadowgraph is used with a maximum frequency of 10 kHz. With Background oriented schlieren (BOS), the density

fluctuations up to 3 kHz are quantified, and molecular tagging at 1 kHz reveals the fluctuations in the velocity and flow angle fluctuations. The variation in power due to hub pressure variations is measured with high-frequency Kulite sensors with frequency response of 100 kHz. Finally, with the ALTP heat flux sensor, the surface heat flux variation at a distinct location in the divergent section is investigated (25.6 kHz).

The subsection is divided into eight subsequent parts:

- Identification of the different shock structures and their dominant frequencies: Section 4.3.1.
- Quantification of the unsteady fluctuations at the hub and shroud in Section 4.3.2.
- The spatial coherence of the shock structures from the shadowgraph data is analyzed via Proper Orthogonal Decomposition (POD) to identify structures with most energy content in Section 4.3.3.
- The dominant frequencies of hub and shroud are investigated in Section 4.3.4 via power spectral density.
- Via Spectral POD (SPOD), the spatial and temporal structures with the highest energy content are dissected in Section 4.3.5.
- Flow field variations in velocity and density gradients are measured along the axial direction in Section 4.3.6.
- Finally, the startup is addressed in Section 4.3.7 while sudden shut down as well as gradual shut down is discussed in Section 4.3.8.
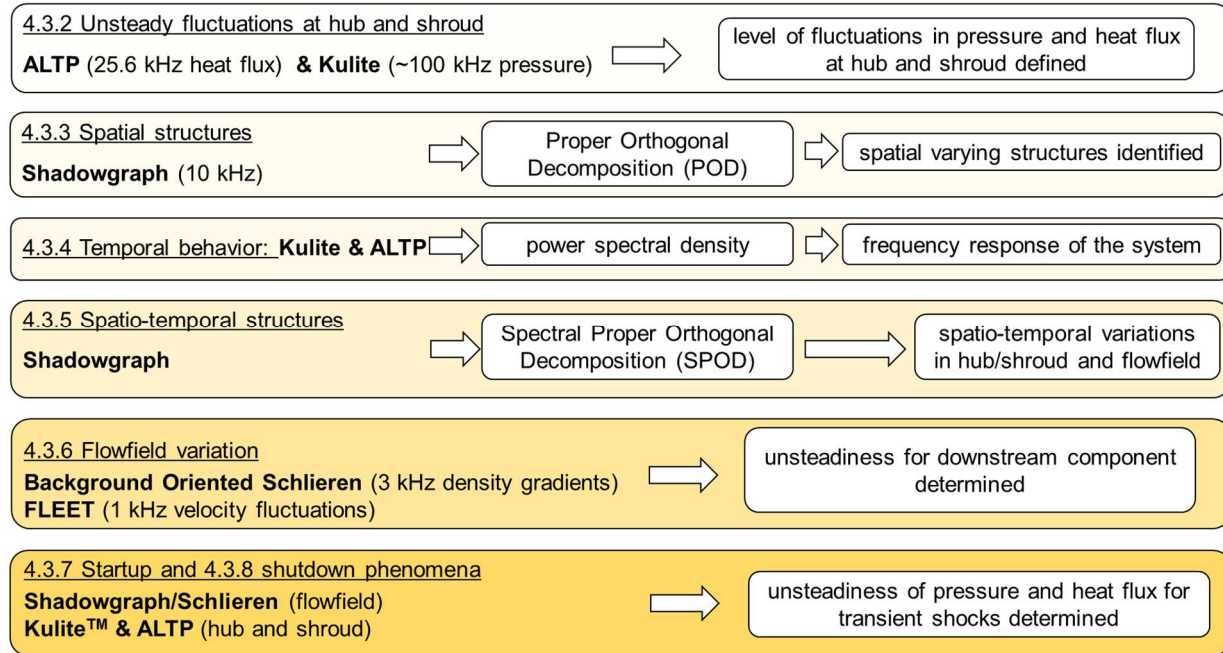
Figure 4.21 Strategy to analyze the high-frequency phenomena

4.3.1 Shock structures and their frequency response

The topic of shock-boundary layer interaction (SBLI) is a research topic that was first studied in the 1940s. Dolling performed an extensive review on the SBLI [88]. A comprehensive review of how low-frequency phenomena are introduced in SBLIs is given by Clemens and Narayanswamy [89]. Generally, two mechanisms are believed to be responsible for the unsteadiness, either emanating from the upstream turbulent boundary layer or from the downstream separated flow.

Poggie and Smits [90] found that the upstream boundary layer could have a substantial influence on the intensity of the pressure fluctuations and the shock movement. This was also confirmed by Touber and Sandham [91] who analyzed several forcing functions on the incoming boundary layer. They however also mentioned that the low-frequency unsteadiness does not necessarily come from upstream or downstream but is intrinsic to the system.

The separation region could also trigger the shock unsteadiness. Via DNS simulations, Wu and Martin [92] found that the low-frequency shock motion was mainly determined by the separated flow region and that the upstream incoming flow gave rise to smaller-scale unsteadiness.

In terms of (upstream) flow control, Narayanaswamy et al. [93] showed the influence of pulsed plasma jet actuation on the control of the shock boundary layer interaction. Zhao et al. [94] studied nanosecond dielectric barrier discharge (DBD), and induced vortex structures were observed.

Clemens and Narayanswamy concluded that at least four topics remain unraveled: 1) three-dimensional effects, 2) system dynamics, 3) scaling and 4), internal flows which are dominated by multiple shock reflections that create additional upstream and downstream unsteadiness.

The bladeless turbine is suitable to investigate these internal flow phenomena because it is characterized by a subsequent event of compression and separation shocks emanating from the hub and causing shock boundary layer interactions on the shroud. An overview of the four investigated regions of the two-dimensional model is depicted in Figure 4.22:

- The compression ramp generates a first shock boundary layer interaction (SBLI1). For shock-boundary layer interactions that are a consequence of reflected shocks, Strouhal numbers lie between 0.02 and 0.04 [89].

- Due to the acceleration in the rear part of the first wavy contour, and subsequent change in curvature to compress the flow again in the second wavy contour, a first separation shock in separation region 1 appears. This separation shock will turn the flow again towards the center. A shear layer separates the region between the supersonic core flow and separation region until the flow is recompressed by a recompression shock. In terms of the frequency response of shock-shear layer interactions, blunt flat plate experiments by Kiya and Sasaki [95] demonstrated fluctuations in the range of Strouhal numbers of 0.12. Deshpande and Poggie found Strouhal numbers of around 0.16 [85] from a flat backward-facing step. The length scale was taken as the cavity length. Furthermore, in [96], Deshpande and Poggie describe how shedding structures affect the reattachment motion.

- The interaction of the separation shock with the reflected shock of SBLI1 generates a shock-shock interaction and will cause a second shock boundary layer interaction (SBLI2).

- Finally, on the hub, a second separation region appears in the rear part of the second wavy contour.
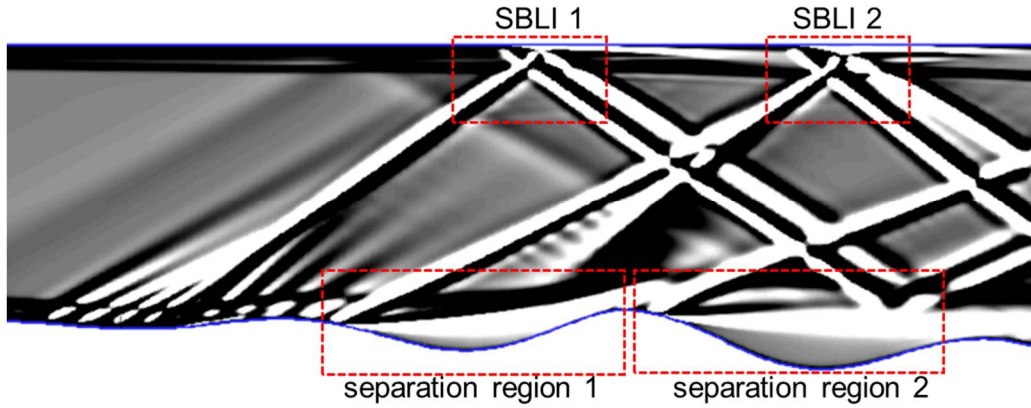
Figure 4.22 Section of the bladeless turbine with the highlighted regions in which the unsteadiness is investigated

Inlet characteristics corresponding to the domain of Figure 4.22 are calculated in Table 4.2. At 0.3 m from the inlet, the mass-flow averaged Mach number is 2, the momentum thickness is ~ 2 mm, and the Reynolds number is ~ 91.10^3.

Table 4.2 Inlet characteristics of the wavy geometry

Inlet BL	z [m]	M	$\delta 2$ [mm]	$Re_{\delta 2}$
	0.3	2.01	2	91.10^3

From RANS simulations each of these regions can be quantified in terms of separation length based on the averaged skin friction ($L_{separation, RANS}$). The Strouhal number and dominant frequency were calculated based on the latter and is summarized in

Table 4.3. From this, the dominant frequency of the first SBLI should lie between 1-3 kHz and the separation zone should fluctuate between 1.3 and 2.3 kHz. The characteristic length (L_C) for which the length is defined as the distance between the extrapolated incident and the reflect shocks with the wall (based on Dussauge et al. [97]) was given as well.

Table 4.3 Estimation of the dominant frequencies based on the characteristic length

	L$_{separation, RANS}$ [mm]	L$_C$	M [-]	St	f [kHz]
First SBLI	7	9	2.08	0.02-0.04 [89]	1.15-2.9
Separation zone	36		2.16	0.1-0.16 [85]	1.4-2.3
Second SBLI	11	14.4	2.04	0.02-0.04 [89]	0.7-1.8
Second Separation zone	43		2.1	0.1-0.16	1.2-1.9

Characterization of the spectrum at the inlet of the test section is crucial and Figure 4.23 displays the spectrum of velocity measured with a hot wire during the commissioning of the wind tunnel. At these Mach numbers, inlet turbulence was around 3 - 4% [98][99].
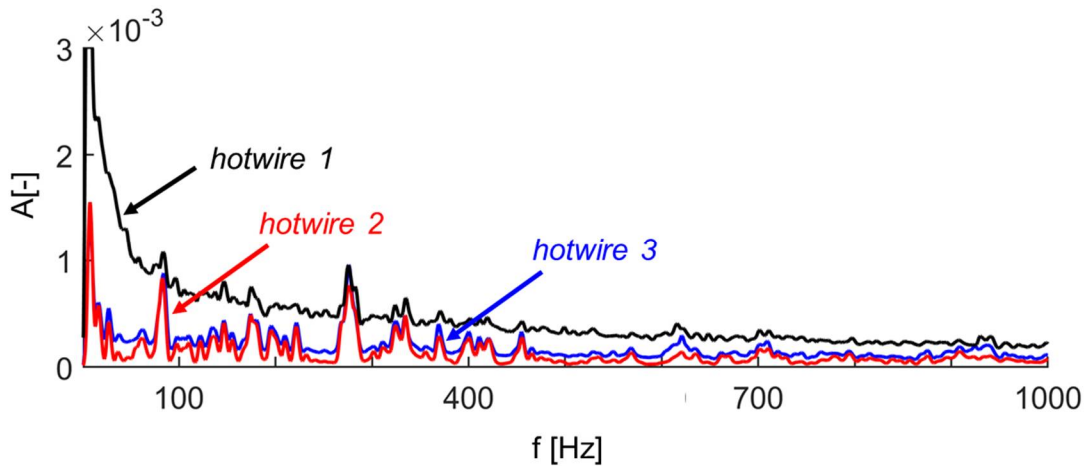
Figure 4.23 Inlet turbulence based on hotwire measurements from wind tunnel commissioning testing [48]

4.3.2   Surface pressure and heat flux fluctuations

Firstly, the hub and shroud fluctuations are analyzed in terms of maximum and minimum fluctuations as well as the standard deviation (STD). Figure 4.24 shows the time response of four Kulites as a function of time filtered at 100 kHz. The blue curve represents the pressure in the convergent section at Mach 0.4. Similar to the total pressure contour (Figure 4.8), first a stable region is seen in which the purge valve is still opened and followed by an increase in pressure

(mass flow) until stable conditions are reached, for this test around 1.5 bar. Figure 4.24b plots the comparison of the low-frequency pressure data with the high-frequency pressure sensors (Kulites) and have a good agreement. Additionally, the minima and maxima pressure values (drawn as error bars) are picked up by the Kulites, owing to the unsteadiness that was not captured by the low-frequency pressure acquisition system.
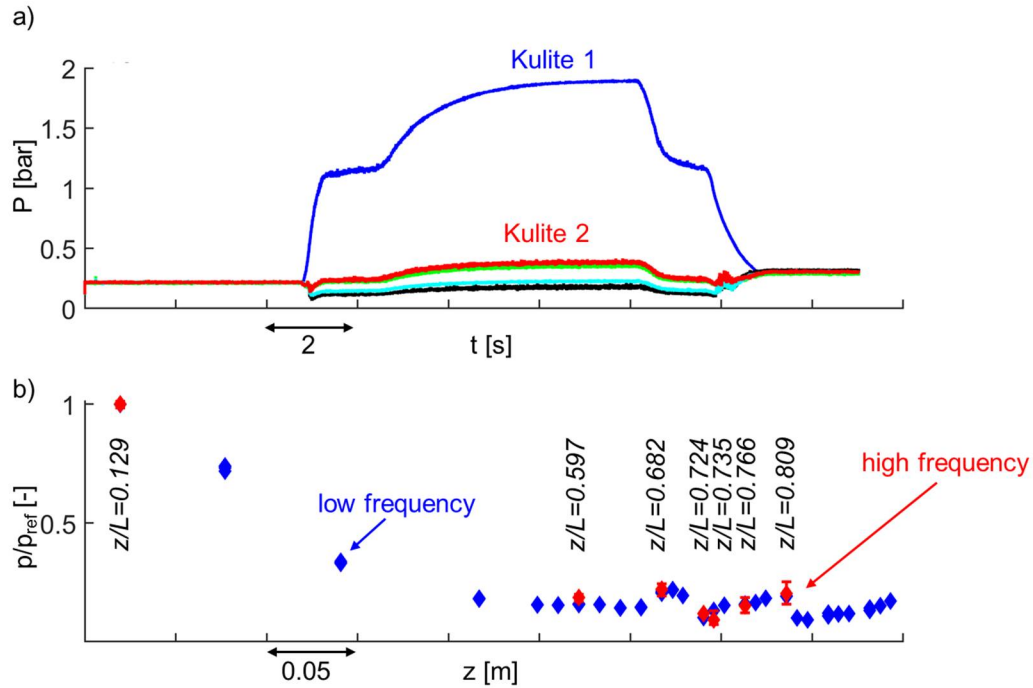
Figure 4.24 a) Time response of the high-frequency sensors and b) pressure as a function of the axial distance for the low and high-frequency pressure sensors

In Figure 4.25a the ratio of the local maximum and minimum flow variation compared to the local mean is calculated as a function of the axial distance. At the inlet, flow distortion is below 1%. This increases in the divergent section up to 10% and is further elevated in the compression ramp to 11%. A local peak of 35% is measured in the separation region and then remains steady around 20% in the subsequent compression and reattachment region. In terms of STD, at the inlet, the STD is 0.2 %, 0.7% at the divergent part, 3% at the separation point and around 2.3% at the outlet of the test section.

When the data is compared against the upstream total pressure fluctuation (Figure 4.25a), a quasi-linear trend is observed. The maximum inlet fluctuations are around 1.6% and rise to about

5%. In terms of STD, ratios are around ten times lower with the highest STD around 0.5 % at the outlet of the turbine. The inlet STD value is around 0.2%.
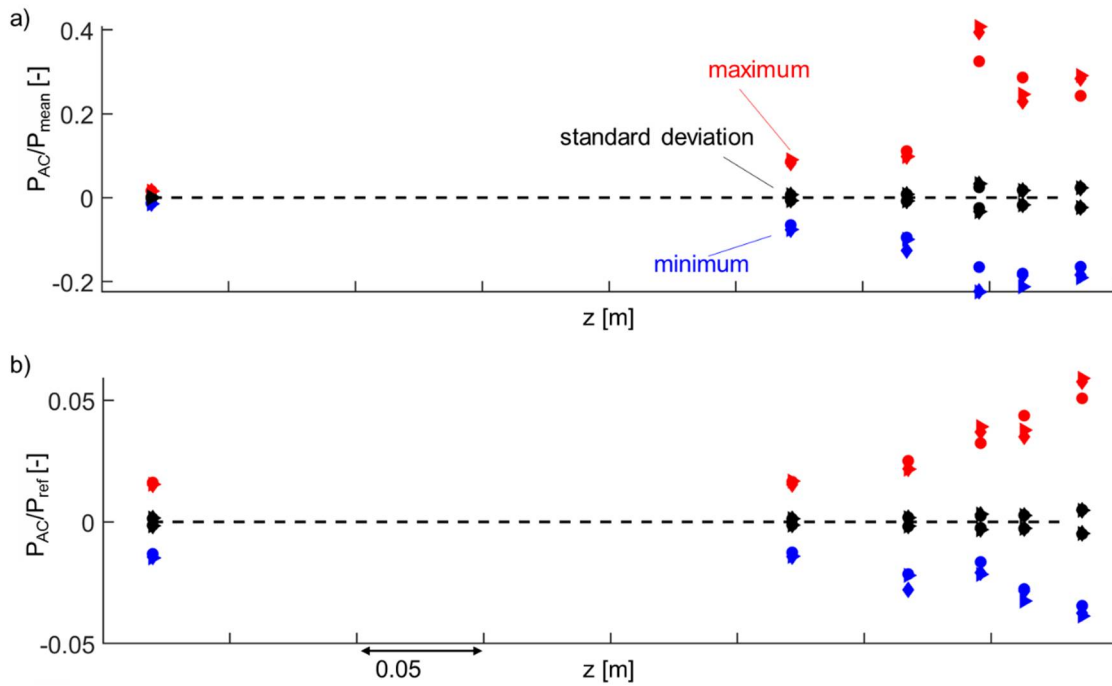
Figure 4.25 Unsteadiness during steady-state operation of the bladeless turbine: a) maxima, minima and standard deviation of the pressure non-dimensionalized by the local static pressure and b) maxima, minima and standard deviation of the pressure fluctuations non-dimensionalized by the reference static pressure in the convergent section

The histogram below (Figure 4.26) reveals the distribution of the ratio of the unsteady fluctuations over the local mean. The decrease of color corresponds to an increase in z/L (with z corresponding to the axial length and L to the axial length of the test article). An increase in z/L corresponds to an increase in pressure fluctuations. Downstream of the first wavy contour (~z/L=0.81), the 1% and 99% percentile correspond to a -14% and +8% in pressure fluctuations. Interestingly, near the inlet, the distribution behaves like a normal distribution and further downstream, a skewed distribution is observed similar to hot wire data of Orlu and Alfredsson near the boundary layer (y+<100) [100]. Thomas et al.[101] also observed skewness in the probability density function of the frequency of shock crossing events.
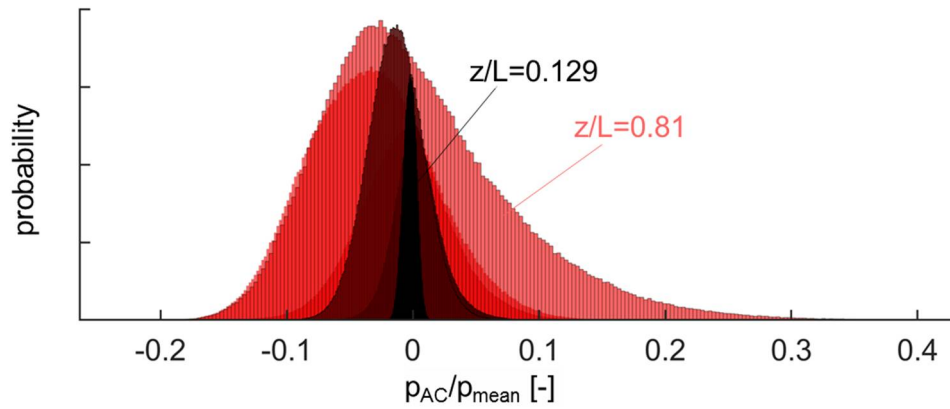
Figure 4.26 Histogram of the unsteady pressure content

The Atomic Layer Thermopile (ALTP) was used to measure the heat flux in the divergent section (at ~z/L=0.57). Figure 4.27a plots the heat flux data as a function of time with a sampling of 25.6 kHz. A high heat flux peak was observed during startup, followed by a region of heat flux that is steadily increasing. The temperature trend for the total temperature, the surface temperature, and a back wall temperature substrate thermocouple are depicted in Figure 4.27b. The back wall- and surface thermocouple are fed into the heat flux code to retrieve heat flux and can be compared with the ALTP. More in-depth analysis of the heat flux comparison can be found in Bhatnagar and Paniagua [62].
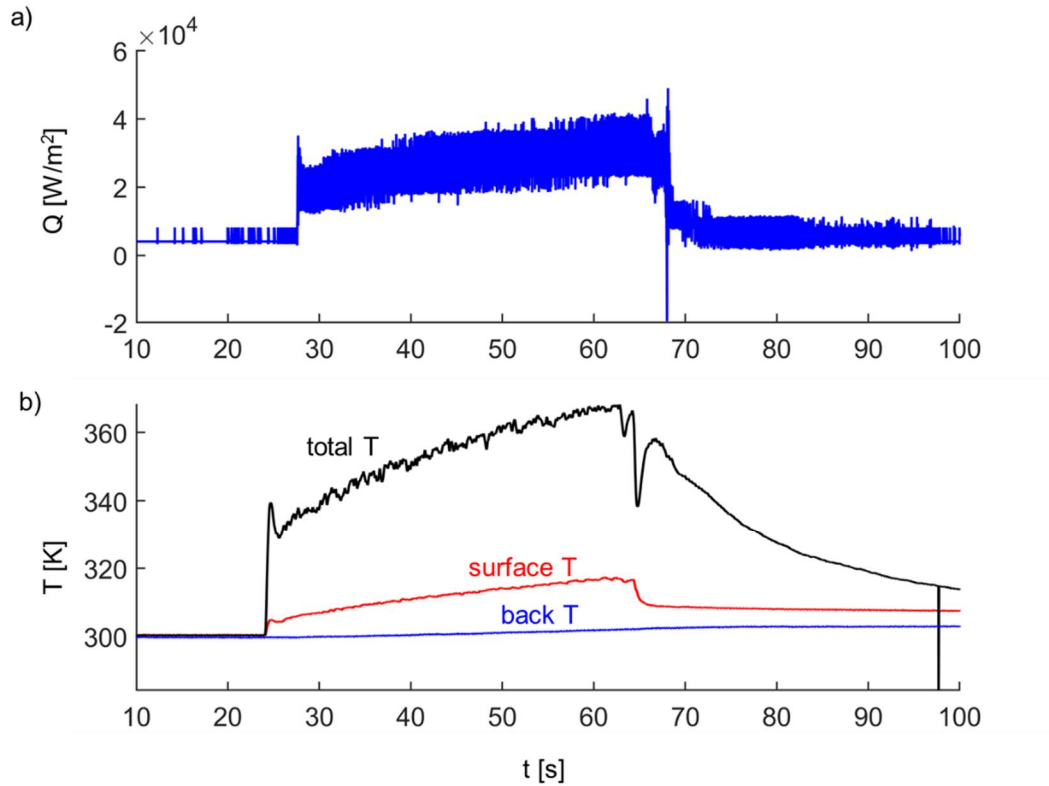
Figure 4.27 a) Heat flux and b) temperature at the shroud (z/L=0.57)

Figure 4.28a features the histogram of the heat flux fluctuations for several tests. The standard deviation (STD) value of the heat flux is around 10% of the mean flow and is a magnitude higher than what is found in the hub for pressure fluctuations at a similar z/L distance. The 1% and 99% quantile have a negative fluctuation of -18% up to positive contributions of 25%. In contrast to the Kulites which had a normal and skewed distribution, the ALTP histogram data features a bimodal distribution rather than a distribution around a mean level. When the signal is high pass filtered, a normal distribution was obtained (Figure 4.28b).
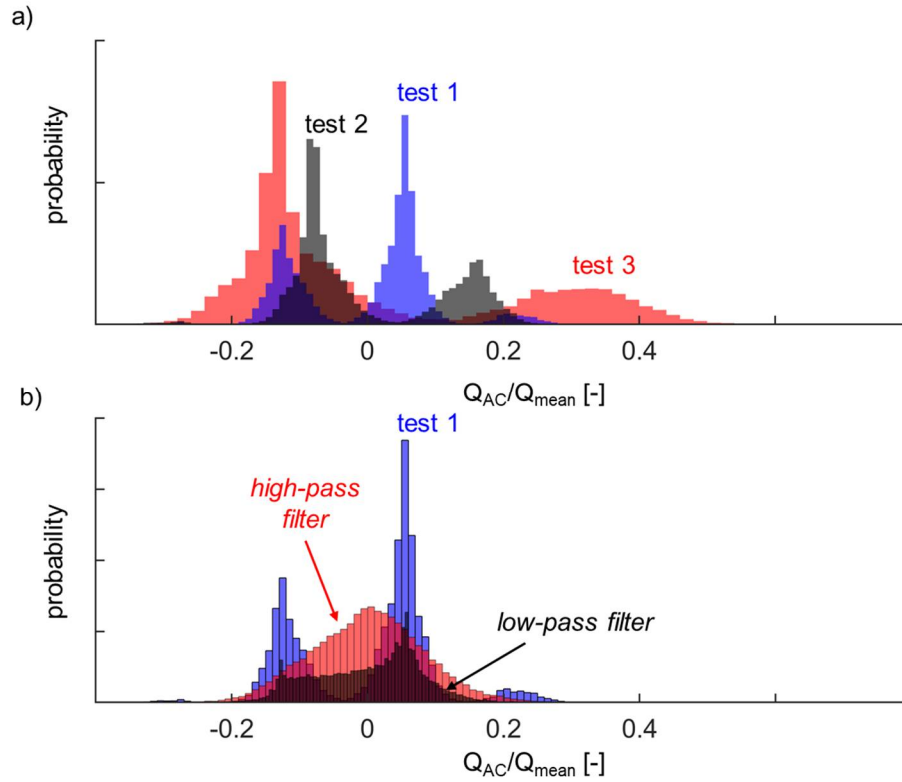
Figure 4.28 a) Histogram from three tests and b) histogram of the low pass filtered, high pass filtered and original data (z/L=0.57)

4.3.3   Spatial structures

Figure 4.29 depicts a shadowgraph image sequence for a duration of twelve milliseconds with a one-millisecond interval. From this set of 10 kHz shadowgraph images, the compression shock remains steady. However, the separation shock, the subsequent shock boundary layer interactions, the second shock-boundary layer interaction, and the second separation region have a higher signature of unsteadiness.
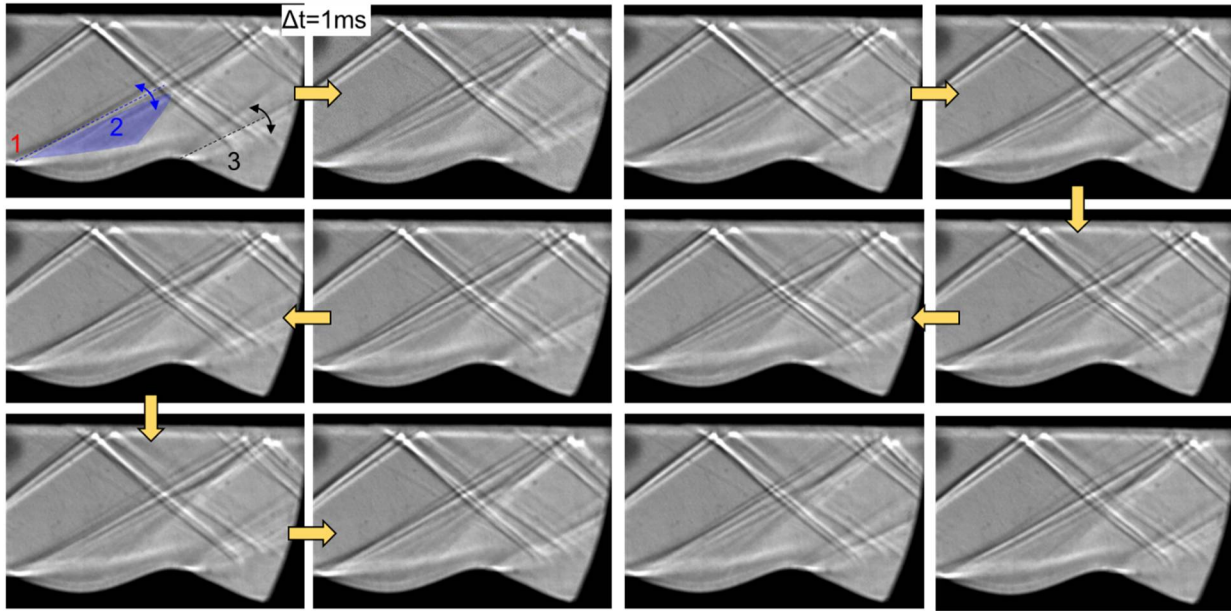
Figure 4.29 Unsteadiness of the separation shocks during steady operation focused on the separation shock (1), the recompression zone (2) and the second separation shock (3)

Figure 4.30 depicts the shock angle fluctuations that were tracked with the high-frequency shadowgraph data. The average angle of the first compression shock is around 34.6 degrees, similar to the predicted value as the low-frequency Schlieren (Figure 4.7). The separation shock that emanates from the separation point, has an oscillating behavior and is varying around 26.7 degrees with fluctuations up to 1.6 degrees. The unsteadiness increases around the second separation point (3) with STD up to 4.5 degrees in contrast to the low-frequency Schlieren in which a lower unsteadiness was measured. Additionally, around the second SBLI, near the shroud, high unsteadiness is observed, owing to the strength of this SBLI and the interaction between all the different shock structures.
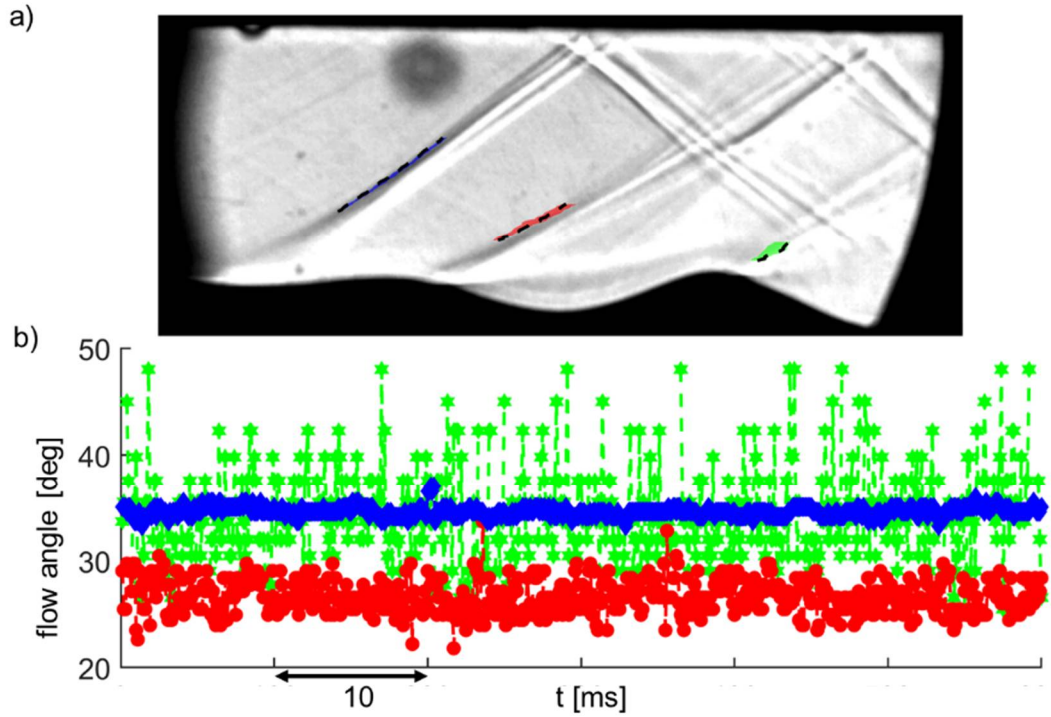
Figure 4.30 Quantification of the shock angle variations: a) instantaneous shadowgraph with the flow angles variations and b) mean flow angles as a function of time

Table 4.4 summarizes the measured angles and additionally shows the displacement of the different shock structures compared to the compression shock. The second separation shock features the largest displacement in terms of axial displacement.

Table 4.4 Shock angles and axial displacement from the 10 kHz Shadowgraph measurements

	$\delta_{shock, mean}$[deg.]	$\delta_{shock, mean}/ \delta_{shock, STD}$ [-]	$\Delta z/ \Delta z_{ref}$[-]
compression shock	34.60 (+/-1.2)	0.0133	1
first separation shock	26.7 (+-0.7)	0.059	1.4
second separation shock	34.4(+/- 2)	0.13	2.45

From 1200 shadowgraph images, Proper Orthogonal Decomposition (POD) is performed. Figure 4.31a plots the eigenvalues as well as the cumulative energy. Figure 4.31b to Figure 4.31i

show the first eight modes ordered according to the highest eigenvalue. Figure 4.31b indicates that a high amount of the energy emanates from the two shock boundary layer interactions at the shroud. In Figure 4.31bc, the reflection from the second SBLI as well as the compression/separation and reflective shocks emphasized. In Figure 4.31bdgehi, modes appear in which both the first and second separation region near the hub region are flapping. These eight modes represent 46% of all the flow energy and approximately 78 modes reach the 80% threshold.
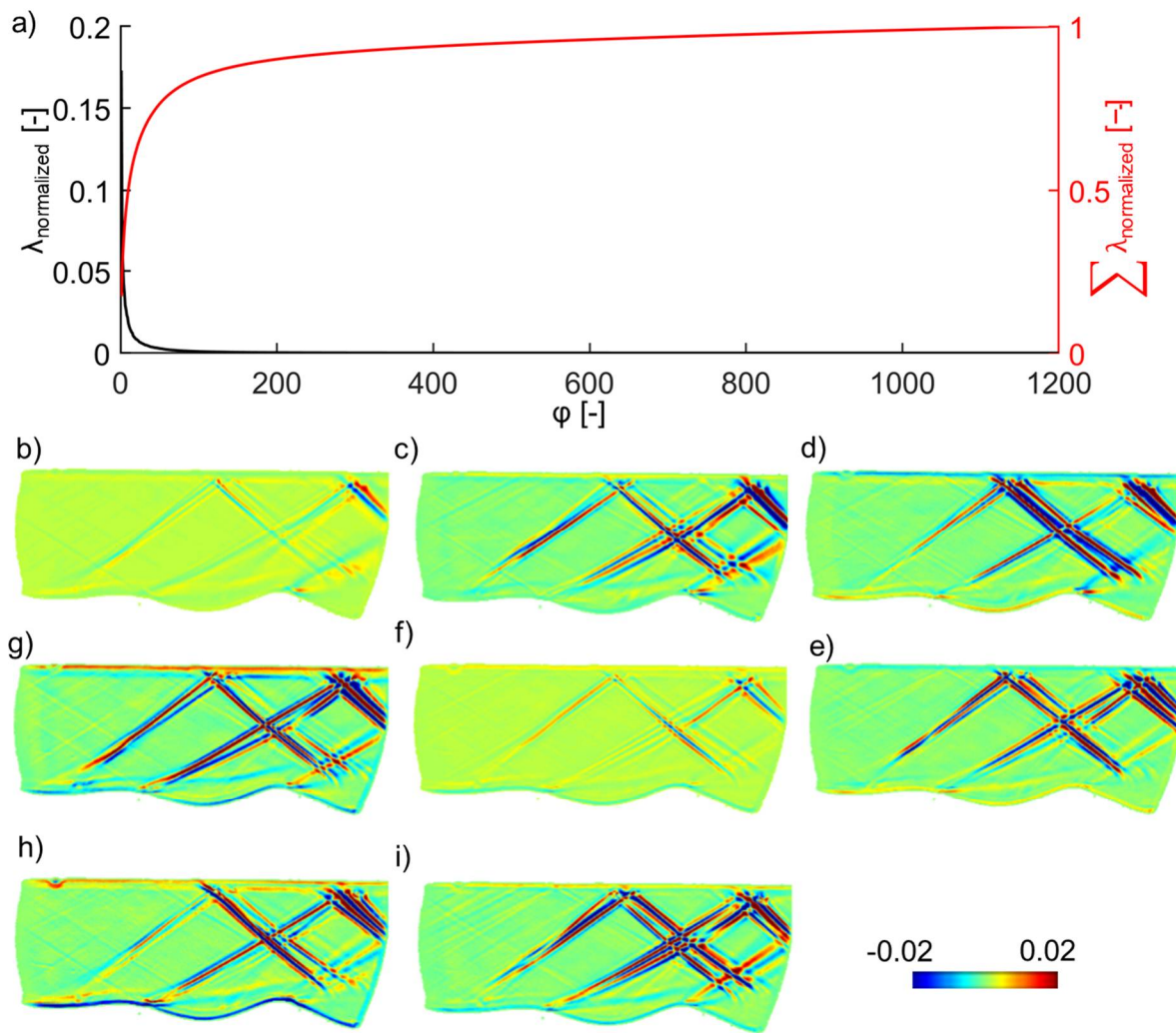
Figure 4.31 Proper orthogonal decomposition on the entire flow field: a) eigenvalue as a function of the mode and b) until i): first eight modes

To investigate the modes and spatial structures close to the hub, POD in the vicinity of the hub was performed with the same 1200 snapshots. The eigenvalues (Figure 4.32a) indicate that eight modes contain 51% of all the energy. Approximately 87 modes contain 80% of all the energy of the modes which is similar to the POD of the entire flow field. The first mode (Figure 4.32b) features the flapping of the second shear layer, influenced or induced by the second shock boundary layer interaction (SBLI2) emanating from the shroud. Mode two (Figure 4.32c) highlights the three shocks as well as the shear layer flapping. The third mode (Figure 4.32d) shows the structure of the first separation shock and the reflected shock from the SBLI1. The fourth mode illustrates a structure connecting the compression shock and the shear layer. Additionally, other spatially coherent structures are observed within the separation region.

The growth of the POD modes in this flow is slow and is dominated by multiple shock boundary layer interactions. This may lie in the fact that POD considers snapshots mutually independent and, therefore, each mode contains contributions from a variety of frequencies. This is consistent with the observation of Towne et al. [33] who investigated a turbulent jet with POD and concluded that POD modes did not necessarily capture meaningful coherent structures. Furthermore, shock-boundary layer interactions are characterized by broad frequencies spectrum excitations. Hence, the characterization of the temporal and spatio-temporal features can be further dissected via the Fast Fourier Transform (FFT), Dynamic Mode Decomposition (DMD) or Spectral POD (SPOD). Datta [102] used DMD and POD to describe the flow features of a single SBLI and the DMD contained several frequencies with high energy content. Schmidt et al. performed DMD [103] on Schlieren data. Berry et al.[104] use POD and DMD on an expansion ramp nozzle up to 100 kHz. They showed that some spatial correlations were able to be isolated with DMD whereas POD could not.
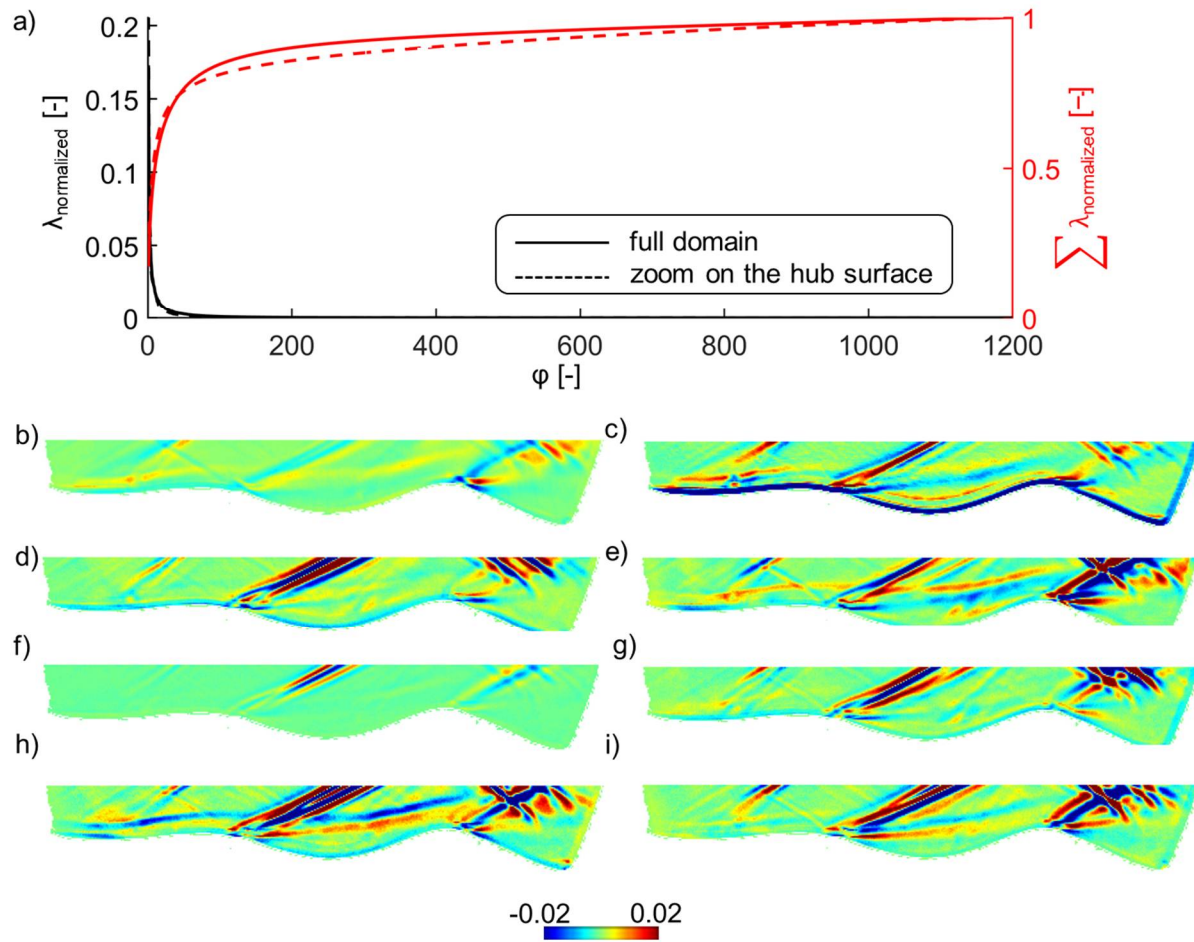
Figure 4.32 Proper orthogonal decomposition on a close-up region near the hub surface: a) eigenvalues and b) until i): first eight modes

4.3.4   Temporal analysis via wall spectra at hub and shroud

Firstly, the wall spectrum at the hub is discussed. Figure 4.33 plots the Fast Fourier Transform of the calibrated Kulite signal that was non-dimensionalized by the local steady-state value. This spectrum indicates zones of low frequencies which are excited across the first separation shock (at z/L=0.735).
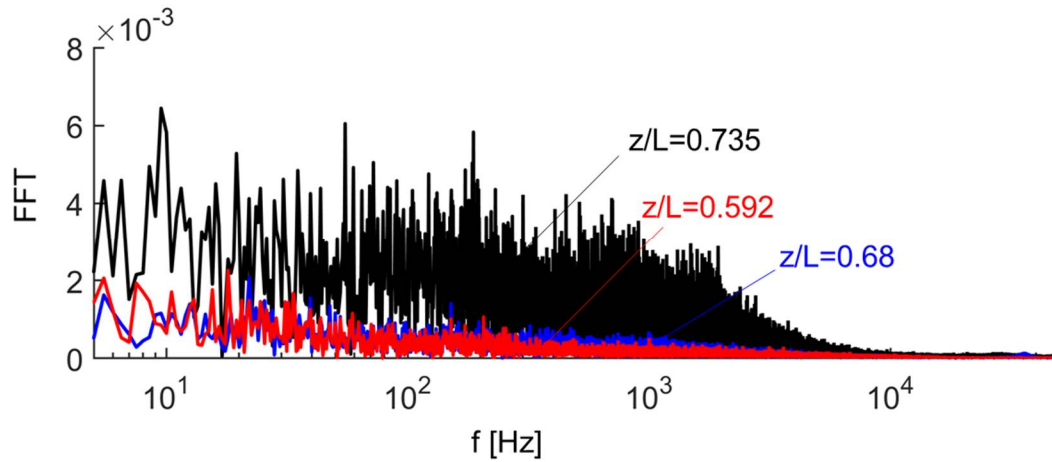
Figure 4.33 Original hub pressure spectrum

Figure 4.34a shows the power spectral density (PSD) times the frequency, as a function of frequency and Strouhal number. For the characteristic length of the Strouhal number, the separation length of the first separation region is used. The frequency content in the inlet region is significantly lower than in the divergent section, note the amplification of the low-frequency content throughout the nozzle (St ~ 0.01) as well as enhancement around a St equal 0.1. Figure 4.34b plots the Kulites upstream of the first separation shock (z/L=0.592 and z/L=0.68) and the Kulite downstream of the first separation shock (z/L=0.735), and again, the signal is amplified by a factor 10. Two distinct regions are observed, a region near low Strouhal numbers between 0.094 and 0.013 (~130 till 180 Hz) and a region near a Strouhal number of 0.05 and 0.15 (~700-2000 Hz). This second peak lies within the range of Strouhal numbers retrieved from the literature (

Table 4.3). The Kulite at a location of z/L=0.68 lies in the first compression ramp; however, no new frequency regimes are excited, which could be attributed to the absence of shocks. Figure 4.34c highlights the hub spectra of the Kulites right downstream of the first separation shock (z/L=0.735), the Kulite in the separation region (z/L=0.766) as well as the Kulite in the re-attached region (z/L=0.809). The peak around a Strouhal number of 0.01 is damped for the two latter Kulites. In the region of higher Strouhal numbers, however, higher amplitudes are observed. At a Strouhal of around 0.85, the power spectral density content for both signals downstream of the separation shock decays and occurs at a higher frequency than the Kulite just downstream of the separation shock, which decreased after a Strouhal number of around 0.2. Hence, by moving downstream, larger structures are broken into smaller scales at a consequently higher frequency due to turbulence dispersion. Additionally, we observe that the separation region (red curve) does not feature a distinct peak around a St of 0.12, and this was also observed by Deshpande and Poggie [85] who measured wall spectra in the separated region. For the blue signal, which lies upstream of the second separation shock (z/L=0.809), a region of energy around a Strouhal number of 0.1 reappears, which could be attributed to the second separation shock region that should have a dominant frequency around 1 - 2 kHz (see

Table 4.3).

These hub spectra indicate that major unsteadiness is found near the separation shocks, and dominant frequencies were observed both upstream and downstream of the separation shock with expected frequency excitation in a region of St 0.1-0.2 but also with a significant contribution at a lower Strouhal number of around 0.013 which appears at z/L=0.735 and at z/L=0.68.
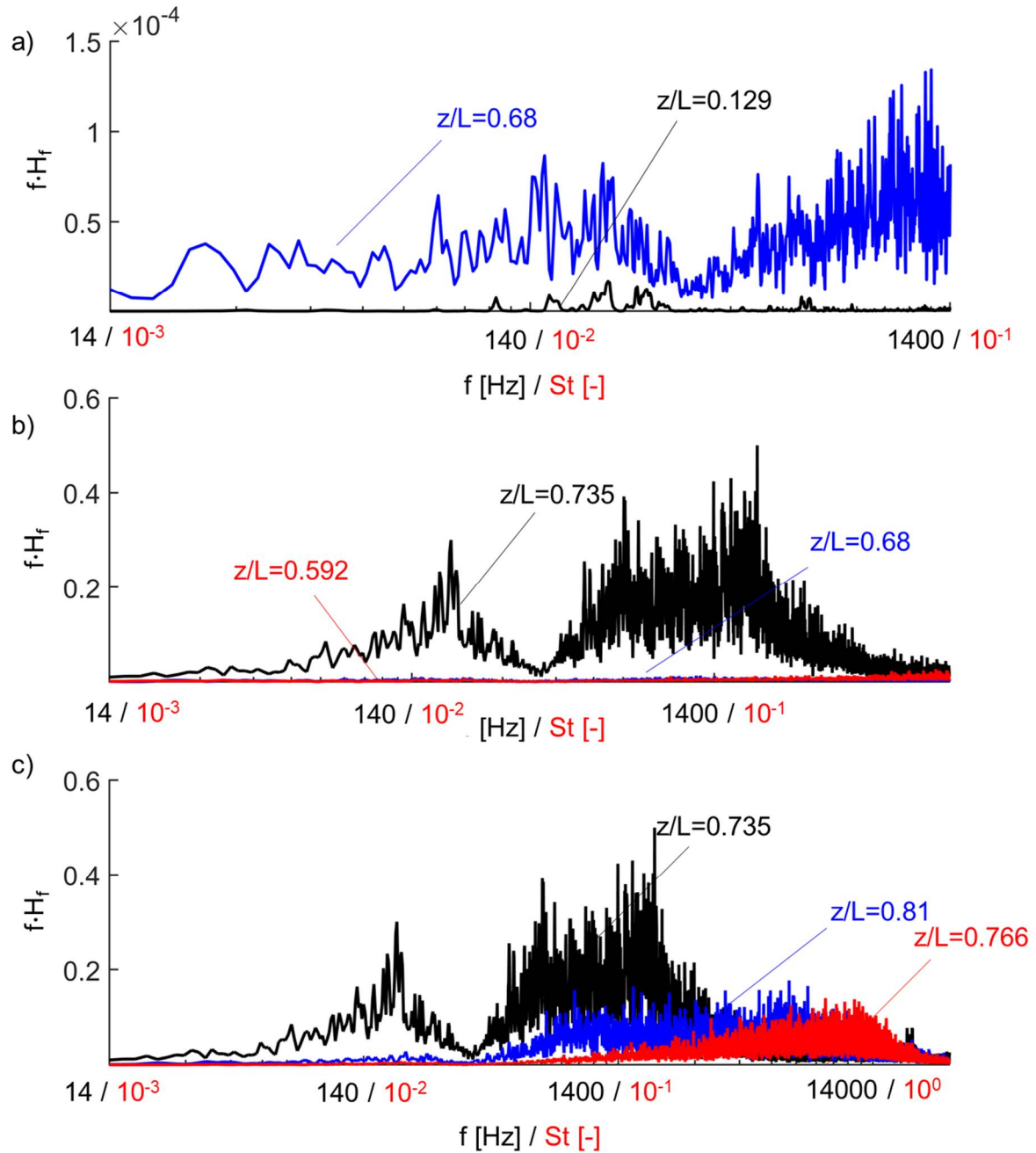
Figure 4.34 Pre-multiplied hub pressure spectra at the hub as a function of the Strouhal number (based on the separation length of separation region 1)

The pre-multiplied shroud spectrum is analyzed at a location upstream of the first compression shock in Figure 4.35 with the frequency as well as the Strouhal number in terms of the first separation shock length in the abscissa. Several peak regions are observed; the first one is around a frequency of 232 Hertz (St 0.017) and 292 (St 0.021). These peaks might be attributed to

the interaction of SBLI1 and SBLI2 because they were not identified as intensively on the hub spectrum. Furthermore, SBLI2 should have a dominant frequency of around 700 Hz, based on the characteristic length of the skin friction of the steady RANS simulations. From the 10 kHz shadowgraph data, however, SBLI2 appeared to be moving and hence the characteristic length is increased which reduces the dominant frequency. Several smaller peaks are found in the high-frequency region (between 300 and 3300 Hertz), which could correspond to the dominant frequency of SBLI1, which lies between 1.4 and 2.3 kHz according to

Table 4.3.
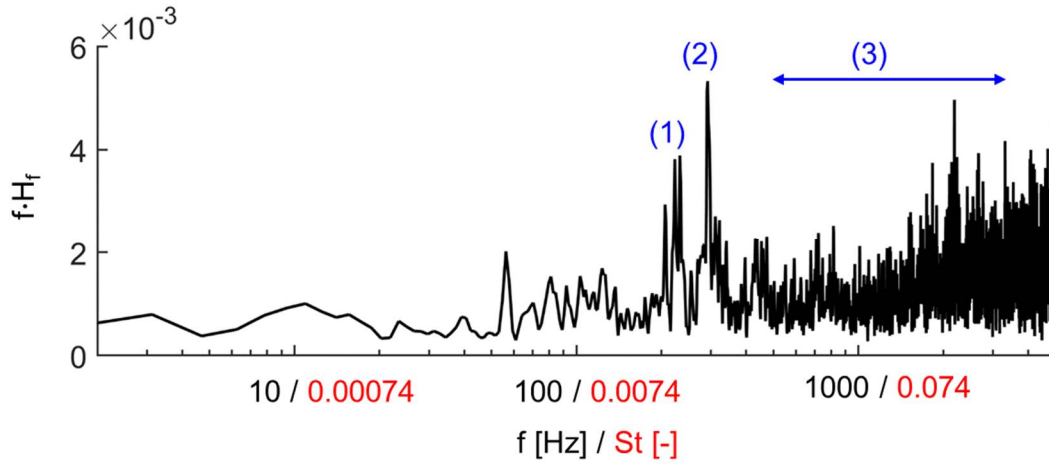
Figure 4.35 Pre-multiplied wall heat flux spectra at the shroud (z/L=0.57) upstream of SBLI1 as a function of frequency and Strouhal number based on the separation length of separation region 1

4.3.5   Spatio-temporal features

The spatial modes (Section 4.3.2) feature a wide array of modes and the hub/shroud spectra highlight a certain amount of dominant frequencies, depending on the axial location. The modes within the flow field that are coherent both in time and space can now be investigated with spectral proper orthogonal decomposition (SPOD). The SPOD modes should complement the information obtained from the hub and shroud spectra as these structures should interact with -or emanate from- the hub or shroud. For the SPOD analysis, 1200 snapshots were used with a window of 600 snapshots and an overlap of 200 images which results in 7 modes. In contrast to Proper Orthogonal Decomposition (POD), each mode has a specific structure at a certain frequency, as discussed in Section 2.1.4. Figure 4.36a shows the SPOD eigenvalue pre-multiplied by the frequency for each of the seven modes as a function of frequency. The eigenvalue corresponds to the energy of the mode and peaks in energy at similar frequencies as the wall spectra are detected. Additionally, the second until the seventh SPOD modes are significantly lower in energy content than the first mode. Figure 4.36b depicts the SPOD eigenvalue normalized by the energy of all the modes at a specific frequency ($\frac{\lambda_i}{\sum_{i=1}^{i=7}\lambda_i}$). Three different frequencies were considered: 117 Hz (red triangles), 1.65 kHz (black diamonds) and the ensemble of frequencies (blue circles). The first mode has on average

60% of all the energy content (but can locally vary up to 85%). This low-rank behavior is typical of SPOD spectra as described by Towne et al. [105]. This contrasts with POD analysis in which at least 80 modes had to be considered to retrieve 80% of the energy content because of the merging of the temporal component in multiple modes.
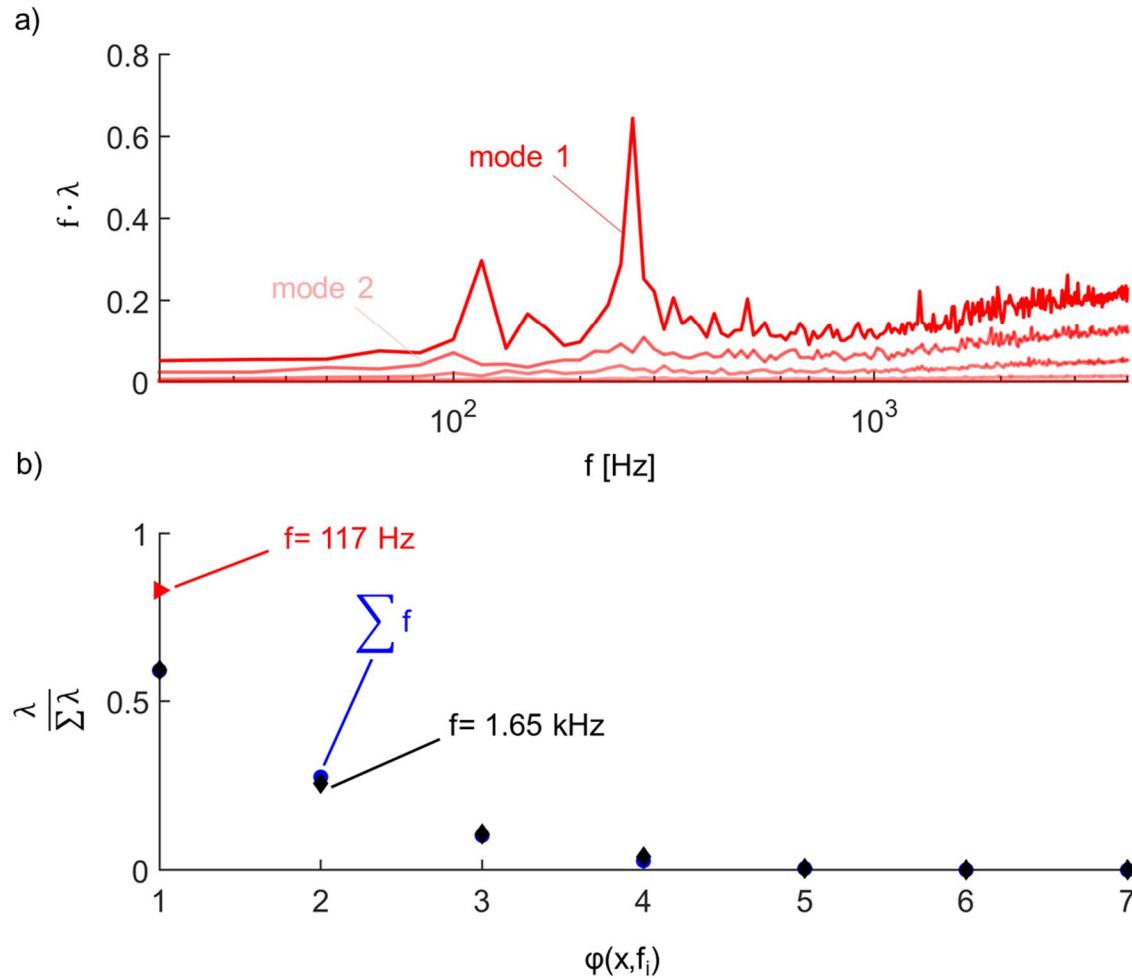
Figure 4.36 a) Pre-multiplied energy of the SPOD mode as a function of frequency and b) spectral SPOD eigenvalues normalized by the total energy at that frequency

In the following section, two frequency bandwidths are considered: a lower-frequency range, in which the frequency content up to 500 Hz is investigated, followed by the phenomena occurring at a higher frequency.

Low-frequency range (10Hz-500 Hz): flapping of the shear layer & SBLI 2 interaction

Figure 4.37 features the pre-multiplied SPOD eigenvalue spectrum in the low-frequency region. Three peaks are observed: in the region between 100 and 180 Hz, one in the region around 250 Hz and one at 500 Hz. Peak (A) corresponds to the observed increase in energy in the hub spectrum. Peak (B) corresponds to peak energy that was sensed by the heat flux spectrum of the ALTP on the shroud. Peak (C) corresponds to a peak that was present in both the hub and the shroud spectra.
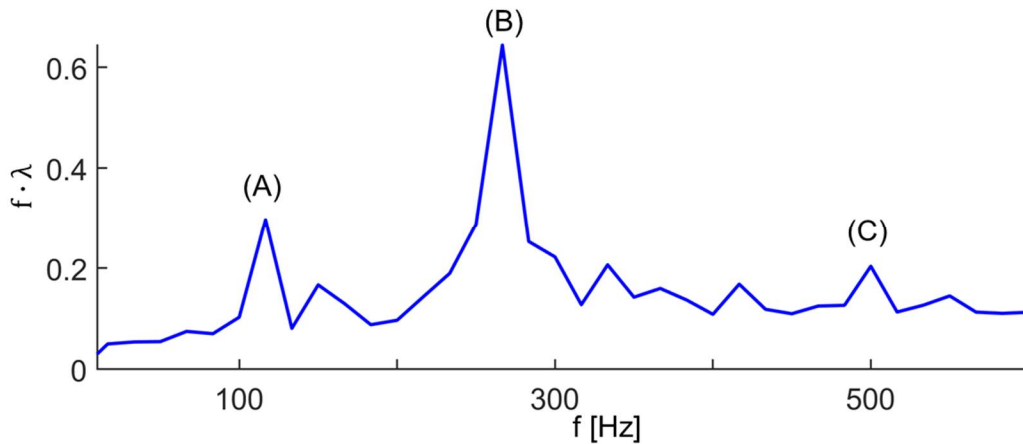
Figure 4.37 Spectrum of the pre-multiplied first SPOD mode from 10 until 500 Hz

The first structure (A) is analyzed in Figure 4.38. Figure 4.38a highlights the region of the first and second separation region which covers SBLI1 and SBLI2, and Figure 4.38b features a close-up on the first separation region. At this frequency, the flapping of the inception of the shear layer is observed, with energy near the first and second separation region, and confirms the increased amplitudes in the hub spectrum in this frequency range (Figure 4.34b).
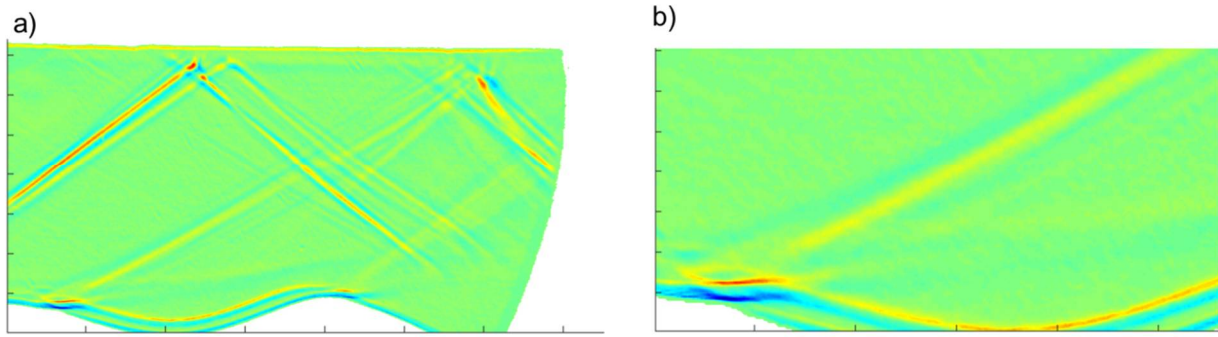
Figure 4.38 The first SPOD mode with fluctuation of the shear layers at 116 Hz: a) the entire flow field and b) close-up on the first separation region

The structure of the mode at the frequency (B) is depicted in Figure 4.39a, with a frequency corresponding to 266 Hz. SBLI 1 and SBLI2 are highly energetic; however, near the hub, no significant energy content was found which is confirmed by the absence of energy in the hub spectrum. Figure 4.39b depicts the second SPOD mode at that same frequency: SBLI 1 and SBLI 2 appear again; however, slight differences in the mode shape are observed. The SPOD eigenvalue of the second mode is about 1/3 of the first mode.
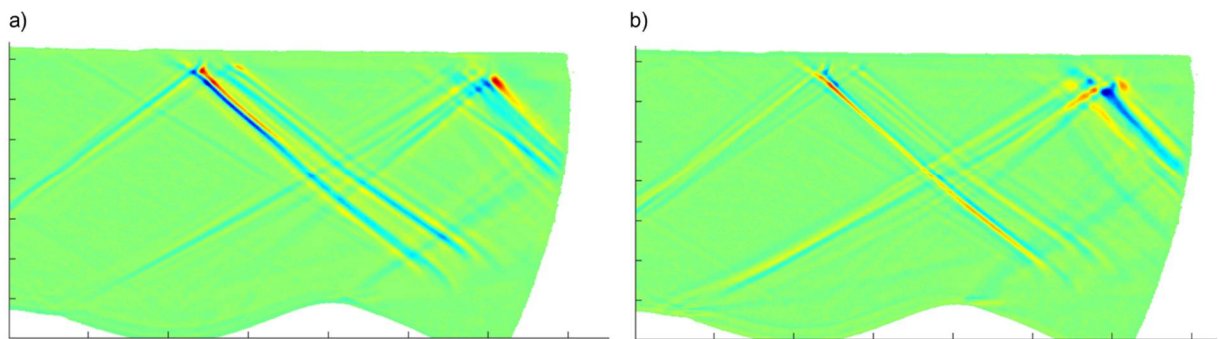
Figure 4.39 Fluctuations of SBLI 1 and SBLI 2: 266 Hertz a) the first mode and b) the second mode

Figure 4.40 plots the structure of the first mode at peak (C), with a frequency of around 500 Hertz. Figure 4.40a shows the first SPOD mode with a zoom on the compression and first separation region. The shear layer flapping, as well as the interaction of the separation shock with the shock-shock interaction, is featured. When taking a closer look at the SPOD result on both the first and second separation region (Figure 4.40b), the second SBLI is highly energetic, suggesting

that the second SBLI might enhance or dominate at this frequency and influence the other shock structures as well.
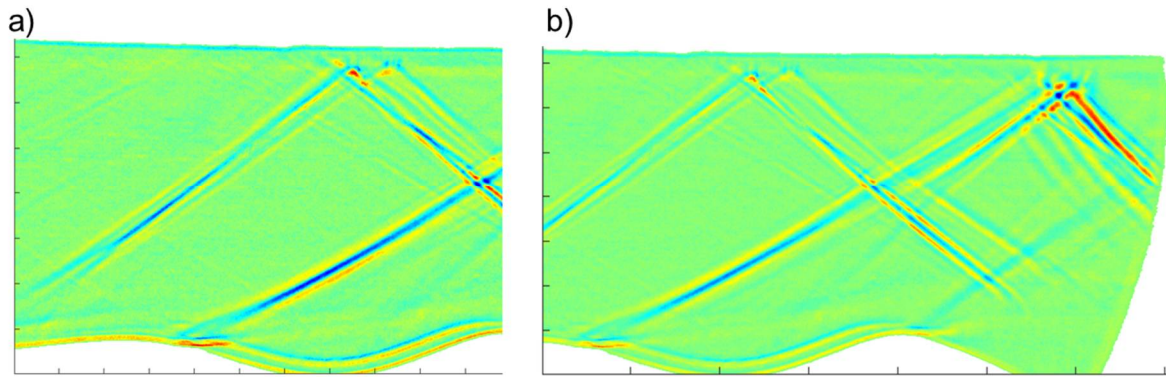
Figure 4.40 The first mode at 500 hertz: a) zoom on the compression and the first separation region and b) zoom on the first and the second separation region as well as SBLI2

Medium frequency range (500Hz-4.5 kHz): separation shock, SBLI1 and SBLI2

In the higher frequency range, several other peaks in the SPOD spectrum are highlighted with letters (D) until (H) on Figure 4.41.
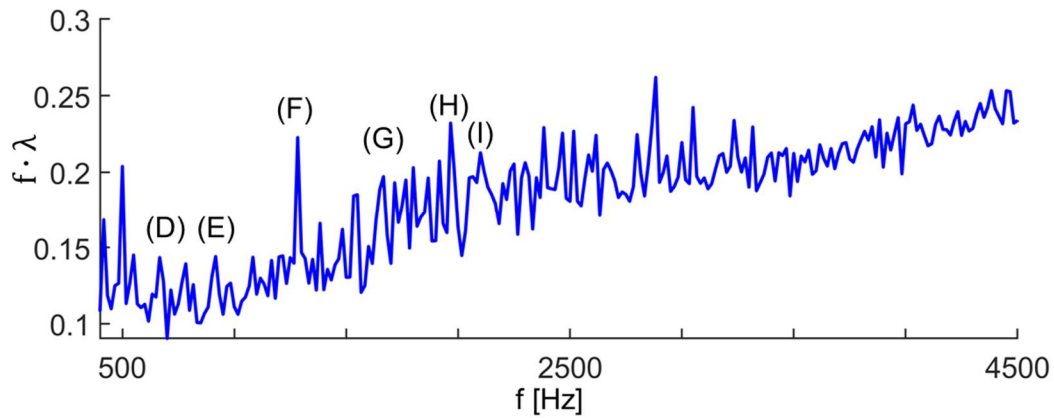
Figure 4.41 Spectrum of the pre-multiplied first SPOD mode for the high-frequency range

The structure of the first mode at frequency peaks (D) and (E) are depicted in Figure 4.42. At 650 Hz, the second shock boundary layer (SBLI2) has the highest intensity, which is confirmed by the range in which the dominant frequency of SBLI2 should lie (

Table 4.3). Figure 4.42b highlights frequency E, at 916 Hz, which also shows a mix of interactions, however in contrast to 650 Hertz, the first separation shock responds to 916 Hz, as also indicated by the high energy in the hub spectrum around a Strouhal of around 0.07.
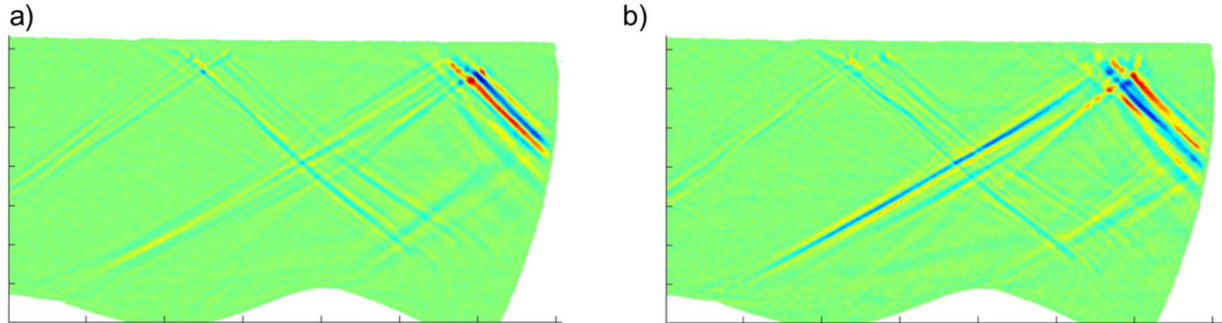
Figure 4.42 a) The first mode at 650 Hz and b) the first mode at 916 Hz

Figure 4.43a describes the structure of the first mode at peak (F), at 1280 Hz, in which the first separation shock is most active and at which the hub spectrum had elevated energy. At higher frequency (peak (G) at 1666 Hz), the reflective shock from SBLI1 as well as the entire structure of SBLI2 is energized with decreased energy in the first separation shock. This peak is also retrieved in the shroud spectrum.
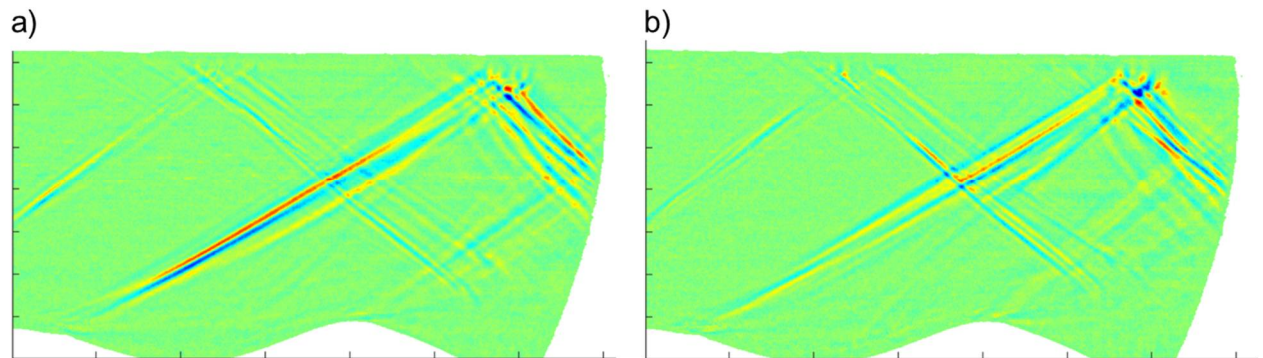
Figure 4.43 a) The first mode at 1280 Hz and b) the first mode at 1666 Hz

The structures at frequency peaks (H) and (I) are plotted on Figure 4.44a and Figure 4.44b. At those frequencies, SBLI1 plays a major role as this is where the dominant frequency of SBLI1 should be (based on a Strouhal~ 0.02). A shift of energy of the incoming shock to the reflected shock is detected, similar to Datta's findings [102]. Furthermore, the first separation shock is energized.
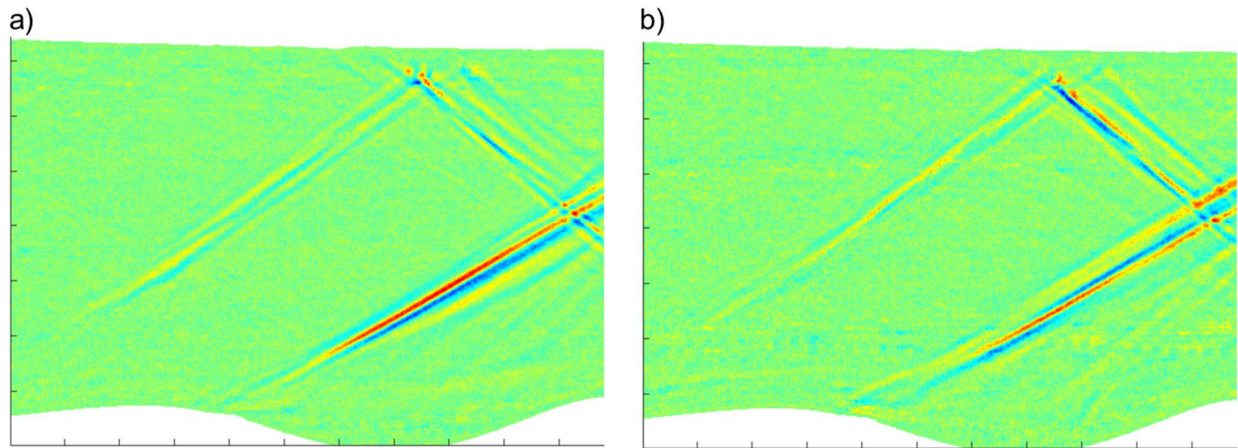
Figure 4.44 a) The first mode at 1966 Hz and b) the first mode at 2100 Hz

4.3.6   Quantification of the flow fluctuations

To determine the changes in local density gradients, background Oriented Schlieren (BOS) with a conventional 105 mm lens was applied. Figure 4.45a shows the mean averaged density gradient change in the axial direction of 400 snapshots at 3 kHz. Upstream compression waves are visible and are followed by the first compression shock. After the compression shock, an expansion fan is visible and is followed by the recompression. A shock reflection from the shroud is also captured by the BOS and agrees well with the RANS prediction. Figure 4.45b depicts the mean averaged density gradient change in the wall-normal direction, and the shear layer is lightning up as well as the recompression zone. The onset of the compression shock is not visible due to the trade-off between the selection of the dot pattern to resolve small gradients and high local density gradients which is typical for shocks.
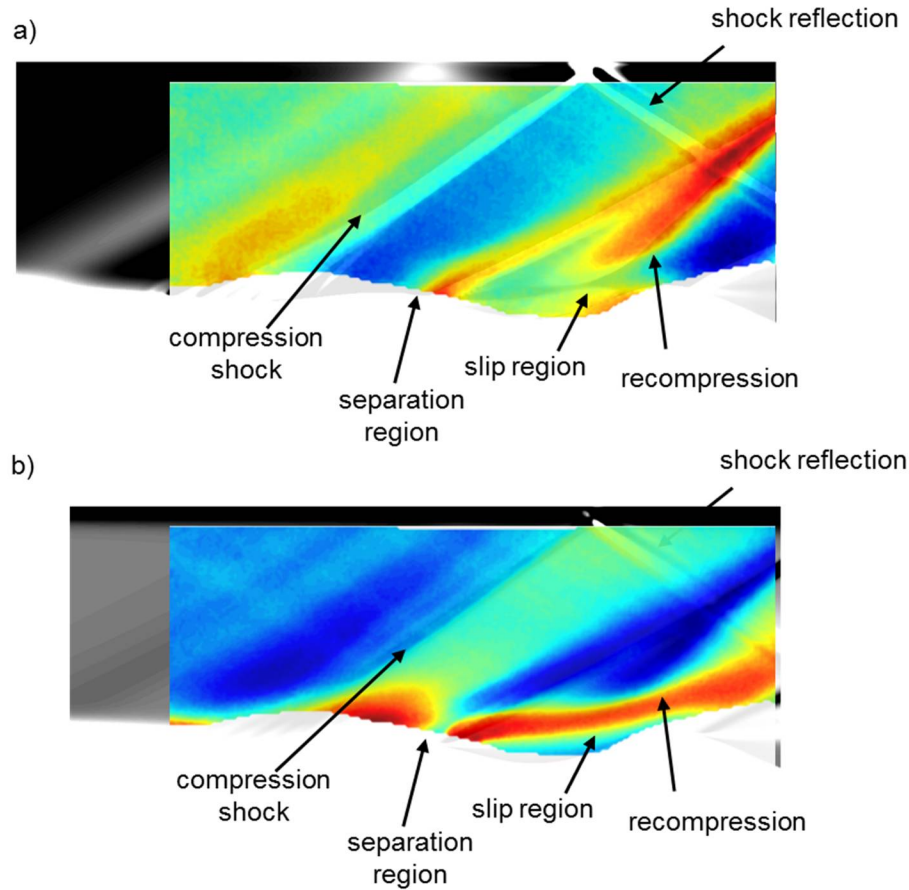
Figure 4.45 a) Mean density gradient in the axial direction and b) mean density gradient in the wall-normal direction, with BOS (color scale) and CFD (greyscale)

After analyzing the mean density gradient profile, the fluctuations in time are investigated. The contour plot of Figure 4.46a visualizes the standard deviation of the unsteady gradients normalized by the local mean. The onset of separation is a zone of high fluctuations with density gradient fluctuations above 34%. Interestingly in the zone of shear, the density gradient change is rather low (3%). In contrast, the reattachment shock just above the shear layer is highly unsteady (20% of fluctuations) as well as the reattachment shock itself with standard deviations exceeding 30%. Figure 4.46b plots the variations in the wall-normal direction, and high zones of unsteadiness are observed in the separation region, with fluctuations of 50%, owing to a higher change in spanwise density gradients axial density gradients. The recompression region around the shear layer has fluctuations of 23% and increases to over 40% at higher wall-normal and downstream axial location, which might be caused by the \ shock-shock interaction.
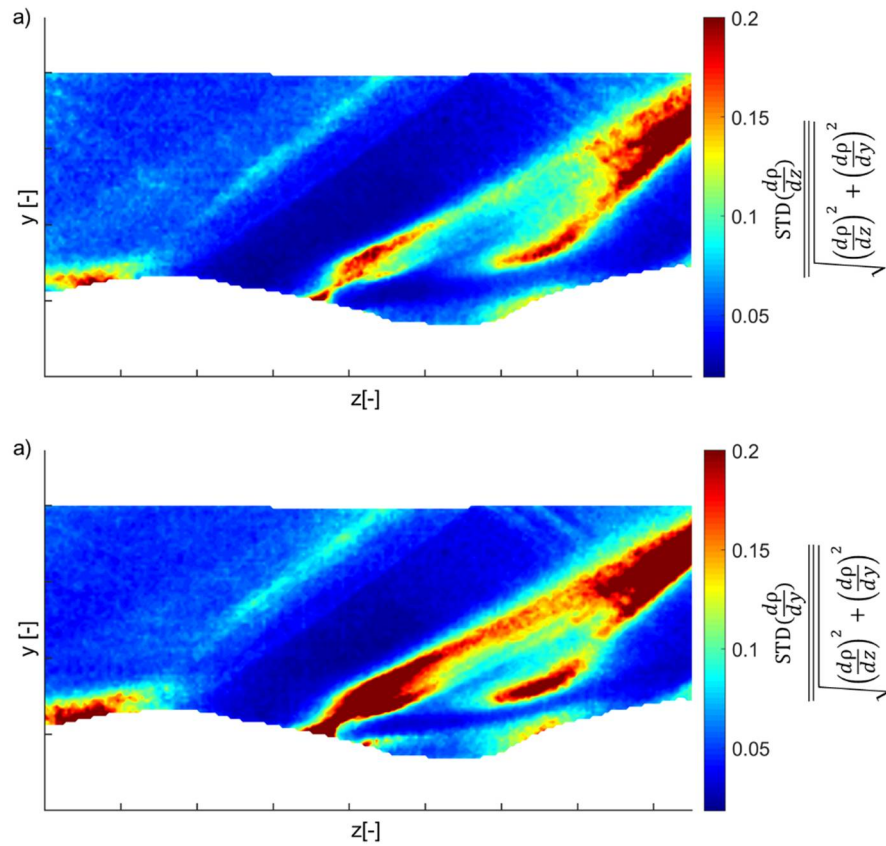
Figure 4.46 Standard deviation of the a) axial density gradient changes and b) wall-normal density gradient changes

The standard deviation normalized by the mean local density gradient is calculated in Figure 4.47 for several wall-normal positions (y/h), in which h is defined as the hub-to-shroud height. Upstream fluctuations are below 10%. At mid-location (y/h= 0.5, red curve), the flow travels through the first separation shock (1) with an increase of fluctuations to 14% and when the flow moves through the reattachment shock (2), the oscillations increase to 20%. At y/h=0.75, closer to the shroud, the highest peak is observed at the separation shock that will merge with the reattachment shock and the reflected shock from SBLI1 to form a shock-shock interaction with fluctuations of around 25% (3). Averaged unsteadiness increases from 7% at the inlet to 12% at the onset of the second wavy contour.

$$\text{STD}\left(\frac{\sqrt{\left(\frac{d\rho}{dx}\right)^2 + \left(\frac{d\rho}{dy}\right)^2}}{\sqrt{\left(\frac{d\rho}{dx}\right)^2 + \left(\frac{d\rho}{dy}\right)^2}} \right)$$
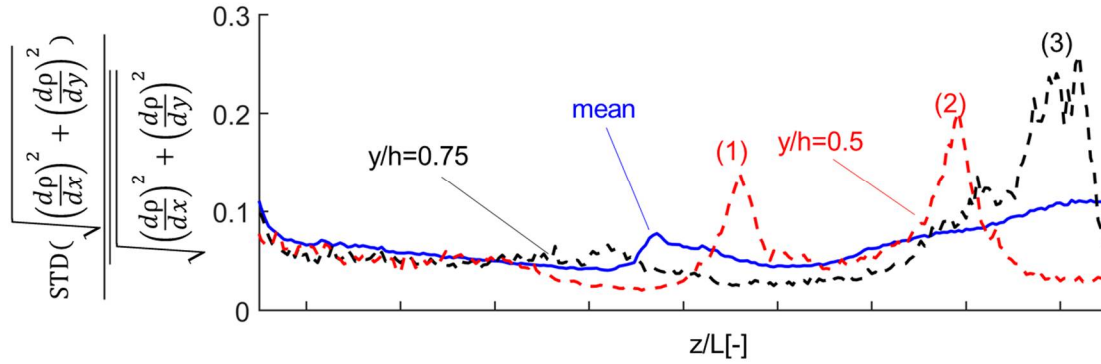
Figure 4.47 Standard deviation of the density gradients along the axial direction at multiple wall-normal locations

To investigate the unsteadiness near the shear layer, molecular tagging was used with a framerate of 1 kHz. Figure 4.48a shows the calibrated dot target and the measurement location relative to the test article. Two small regions (points) were excited with the laser, named as spot 1 (colored in blue) and spot 2 (colored in red) and the location was selected to be close to the separation shock and shear region in which unsteadiness was found with the BOS and shadowgraph data. Figure 4.48b depicts the movement in time of the two dots (framerate = 200 kHz). From time t=1 to t=2, the dots move in the axial and wall-normal direction. For this set of experiments in air, only three consecutive frames could be used to measure the velocity, beyond which the signal to noise ratio was too low.
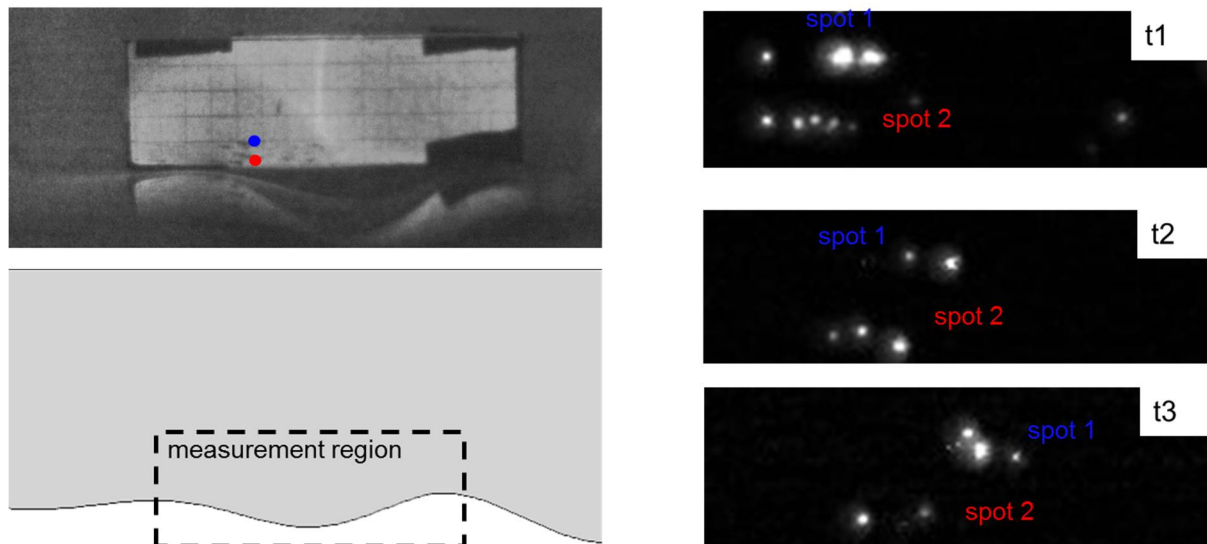
Figure 4.48 a) Calibration target and b) raw images of the tracked dots with FLEET

A set of 14 data tests was collected and each set contained four velocity measurements. Figure 4.49a plots the flow angle of the experiments and underlaid with the RANS simulations. In the expansion fan, relatively high negative flow angles are found (-5 to -10 deg.), downstream of which the separation shock occurs which turns the flow back to the axial direction. Within the separation zone, zones of positive and negative flow angles are present. In the region upstream of the separation shock, the CFD shows good agreement with FLEET with similar flow angles. For the local wall-normal velocity (Figure 4.49b), similar trends are observed and flow velocities locally decrease to values of -40 m/s in the expansion fan. Downstream of the expansion fan, the wall-normal velocity is slightly negative and increases downstream due to the influence of the compression zone of the second wavy contour.
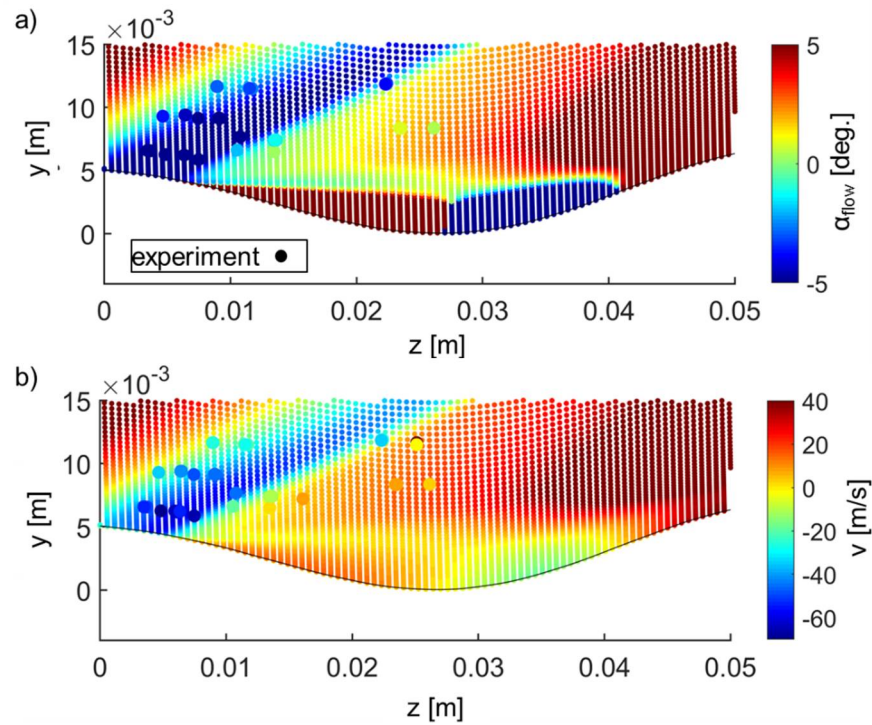
Figure 4.49 a) Flow angle as a function of the axial distance and b) wall-normal velocity

In Figure 4.50 the $\frac{STD}{\text{local mean}}$ of the flow angle is plotted. Upstream of the shock, flow angle fluctuations of around 20% occur (similar to fluctuations in the hub spectrum), and through the separation shock region, values exceed 100%.
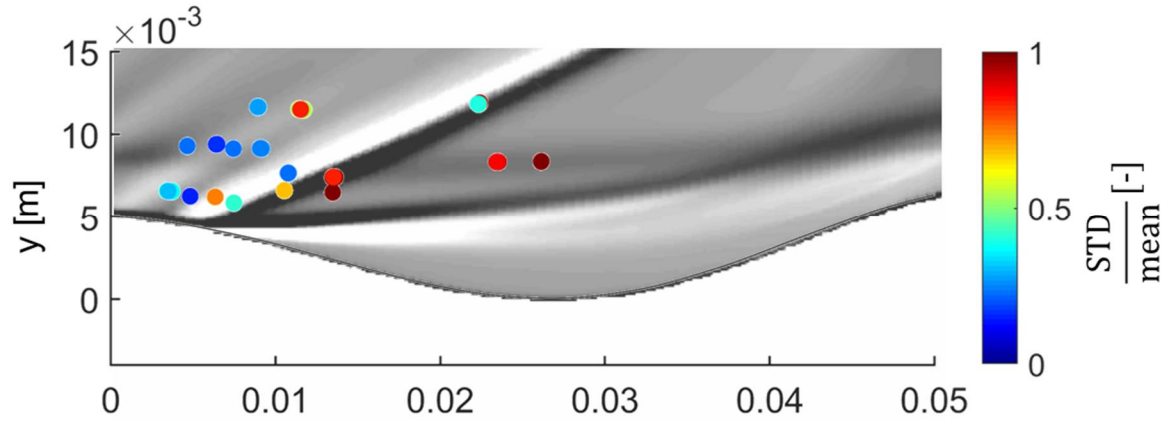
Figure 4.50 Flow angle fluctuations in the rear part of the first wavy contour measured with FLEET

4.3.7 Start-up sequence and establishment time of the bladeless turbine

Figure 4.51 shows the starting of the passage via a shadowgraph visualization at an acquisition rate of 10 kHz. First, subsonic pressure waves pass through the wind tunnel followed by a shock wave at around 60 ms. From the onset of the opening of the valve, approx. 150 ms are required to achieve steady conditions in which the second separation shock is established. This characteristic time is dependent on the pressure ratio upstream and downstream of the shock. Once the shock arrives upstream of the wavy contour, the region is locally started within 20 ms. Shock-boundary layer interactions which trigger separation, characterize the regions near the shroud and hub during startup (observed at t=60 and t=70 ms).
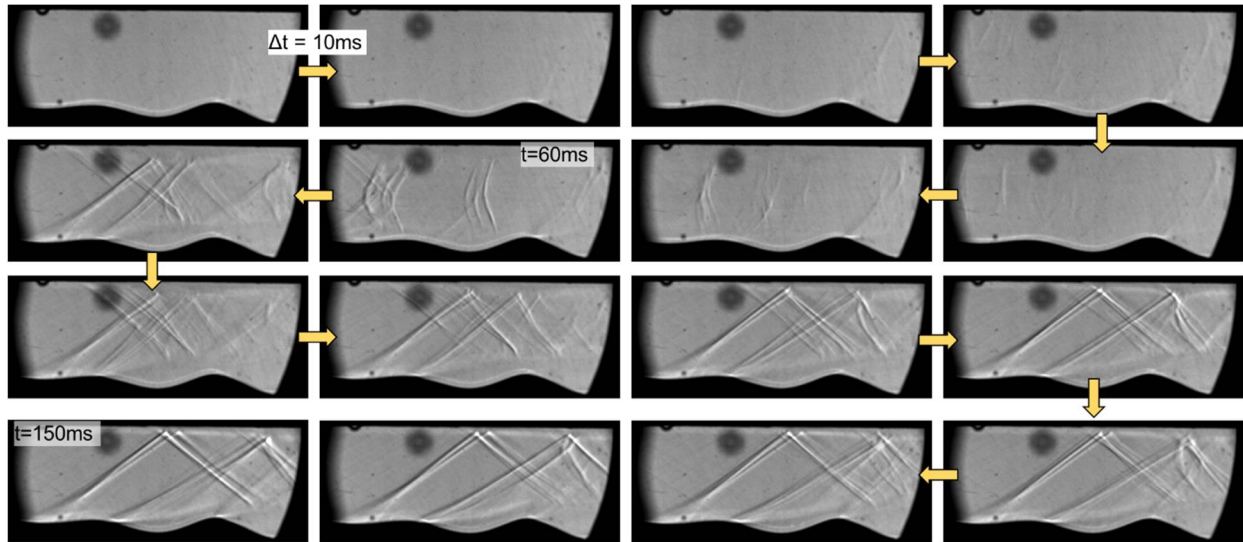
Figure 4.51 Shadowgraph visualization during startup (Δt_{total}=150 ms)

Figure 4.52 highlights a series of snapshots with a timestep (Δt) of 1 ms to emphasize on the events during the transient starting process of the shock passing. After 4 ms, a large shock structure with several smaller shock reflections appears and is moving downstream. About nine milliseconds are required for the shock wave to reach the first compression ramp. The moment before the supersonic shock arrives, the flow is subsonic and large regions of separation are present in the divergent part near the hub surface. The starting shock is accompanied by a separation shock on hub and shroud. This separation zone is pushed downstream by the shock wave until a steady state is reached. To avoid choking of the turbine and allow a smooth transition from subsonic to steady supersonic operation, the designer should ensure that the pressure ratio as well as the area ratio of the passage ensure self-starting, similar to design constraints of supersonic axial turbines [5].
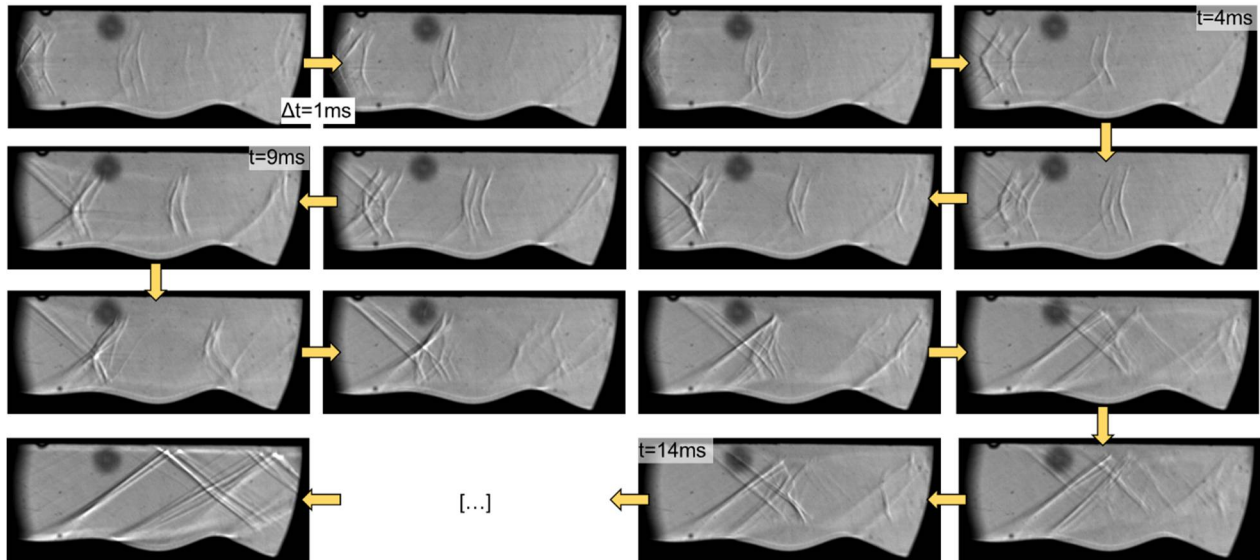
Figure 4.52 Zoom on the shock formation for a duration of 14 ms

Figure 4.53 depicts a startup sequence of a two-dimensional URANS in which the inlet total pressure increase was identical to a selected test. The Mach number during startup (Figure 4.53a) features a similar starting shock as the experiment, and the color scaling was set in such a way that subsonic regions can be recognized. Gradually, the Mach number increases throughout the passage. Numerical shadowgraph results (Figure 4.53b) suggest through the formation of separation shocks that the transient passing of the shock wave is accompanied by large amounts of separation on the hub. The time step between two frames is 0.12s. A shock front travels from left to right with a speed set by the ratio of the upstream total pressure and downstream vacuum level. A large separation zone that is caused by a moving shock boundary layer interaction on the hub moves downstream behind which the bladeless turbine passage is 'started'. On the shroud, a smaller separation bubble is moving downstream as well and is caused by an unsteady shock-boundary layer interaction from the starting shock wave. Similar to the experimental shadowgraph, the separation bubble behind the first wavy surface is already generated during the subsonic portion of the start-up, and once the supersonic flow is established, the separation shock is readily formed.
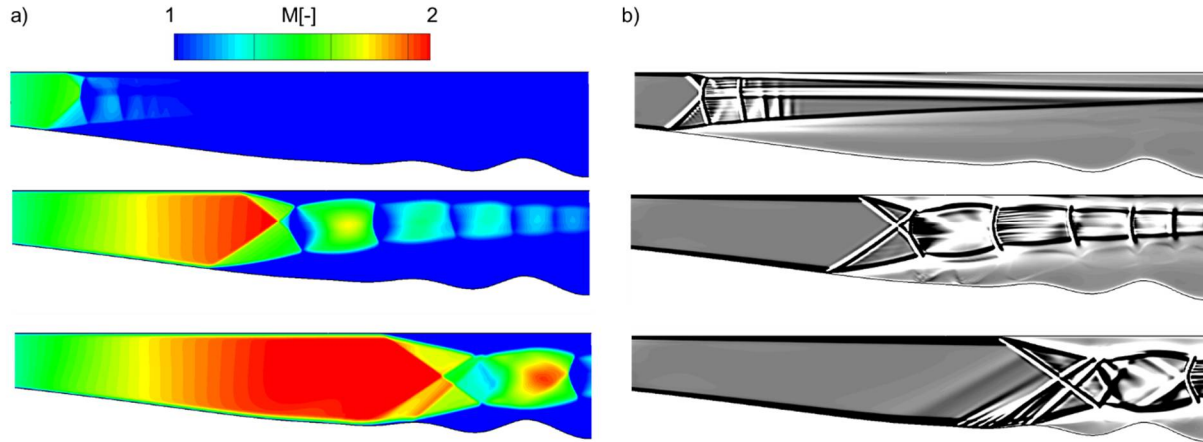
Figure 4.53 Startup simulation with two-dimensional URANS: a) Mach number and b) shadowgraph visualization

Figure 4.54 sketches the hub pressure data as a function of time via which the starting can be analyzed in detail. Figure 4.54a shows the static pressure in the bladeless turbine at an axial location in the subsonic region (z/L=0.129) as well as in the supersonic region. The isentropic Mach number ($p_0 = p_s(1 + \frac{\gamma-1}{2}M_{is})^{\frac{\gamma}{\gamma-1}}$) is plotted in Figure 4.54b and relates the local static pressure to the upstream total pressure. This Mach number is indicative of the speed at that point in the absence of the viscous losses at the wall. Figure 4.54c depicts the ratio of the instantaneous static pressure over the steady-state pressure (p_{ss}). From Figure 4.54a, the entire startup takes around 400 milliseconds to achieve steady mass flow (which is comparable to the settings of the butterfly valve that opens within 100 milliseconds for this test). Although the total pressure is still increasing, the flow can be considered 'steady' or 'started' after 100 ms because the isentropic Mach number is constant and supersonic. Additionally the curves of $\frac{p}{p_{ss}}$ (Figure 4.54c) have a similar growth increase after 100 ms and demonstrate that a certain $\frac{p}{p_{ss}}$ is required to reach a 'started' turbine.

In conclusion, the establishment of the flow occurs faster than the time to reach steady-state mass flow. The establishment time was around 100 milliseconds for this test and is solely defined by when the upstream total pressure ratio is high enough to start the flow. Once this point is reached, the Mach number is constant after the starting shock, and a further increase of pressure would only result in higher pressure forces, skin friction, and heat flux values. The starting phenomenon was also numerically investigated for several opening times (characterized by a

Strouhal number) by Thiry and Paniagua [107] in which shock boundary layer interactions generated high separation regions and choked the intake for large Strouhal numbers.
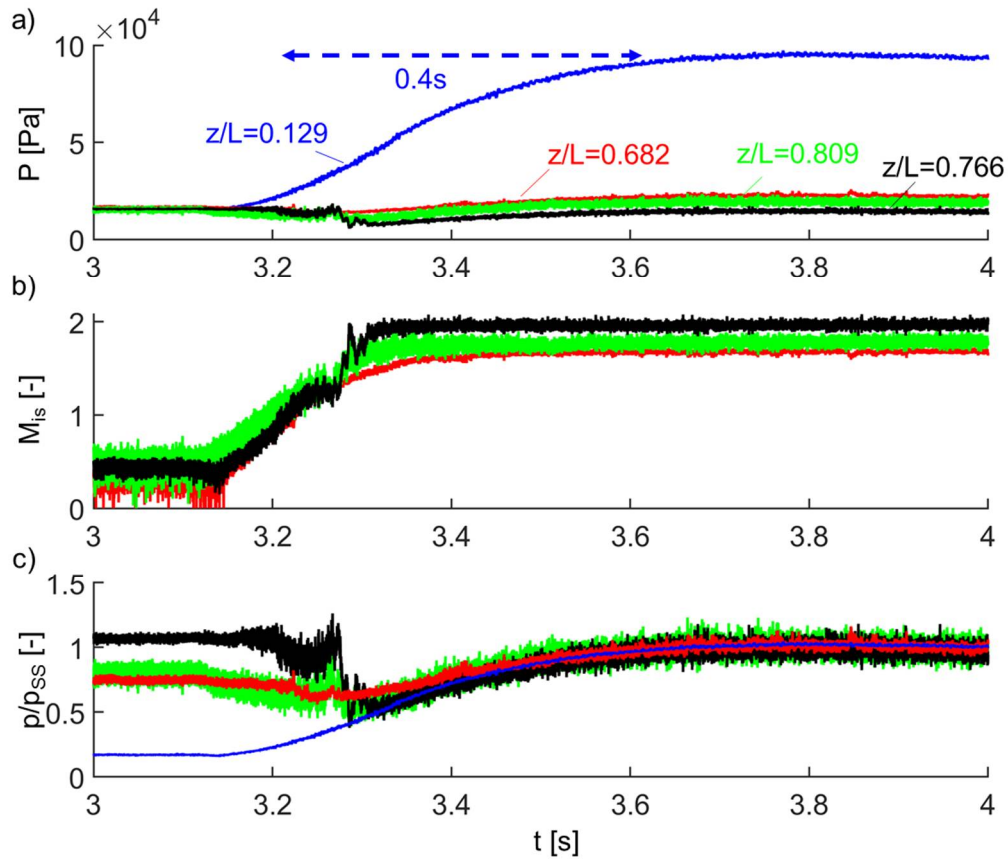
Figure 4.54 a) Raw high-frequency hub pressure data, b) isentropic Mach number at the hub and c) ratio of the instantaneous pressure over the steady-state local pressure

The heat flux at the shroud (z/L=0.57) is plotted on Figure 4.55a together with the isentropic Mach number at a similar axial position. The isentropic Mach number shows a passage starting (from no-flow to M~1.8) with a consequent transient heat flux signature. A large peak of heat flux that overshoots the steady signal is observed and is not captured by the thermocouple (TC). In Figure 4.55b, the non-dimensional heat flux from the URANS startup simulation is extracted at the shroud. The URANS captures the trend of unsteady heat flux well with similar time response (at this back pressure, the transient shock passing sequence was around 150ms). The steady heat flux is only 10% of the maximum unsteady heat flux which is a result of the startup process. The reason for the mismatch between the TC and the ALTP is attributed to the slow transient in the thermocouple. Braun et al. [107], as well as Villafane et al. [108], reported on the

relatively slow response of thermocouples to flow unsteadiness due to the effects of conduction which can be in the order of seconds.
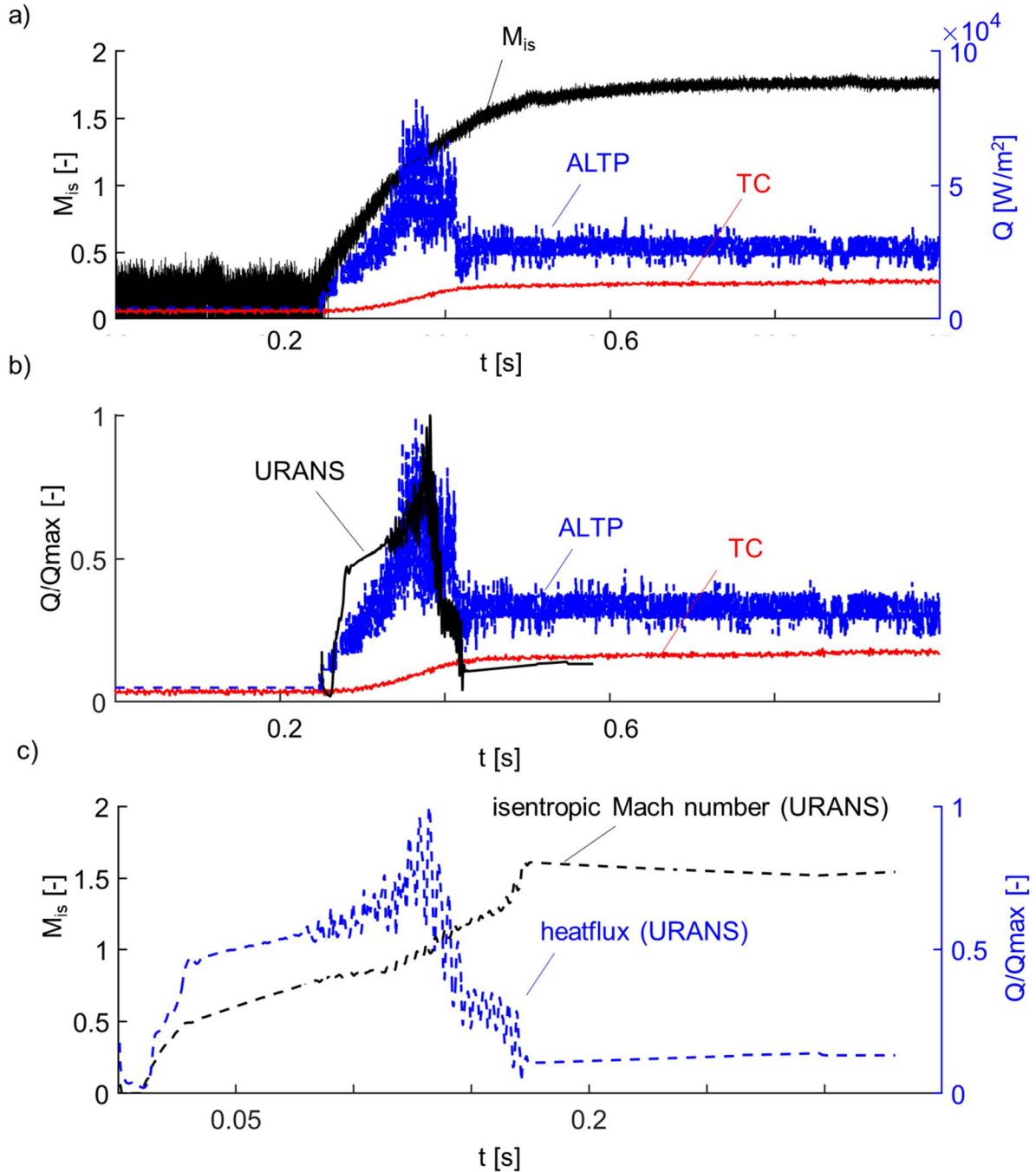
Figure 4.55 a) Isentropic Mach number and heat flux from the ALTP, b) heat flux from the ALTP versus URANS and c) isentropic Mach number and heat flux from the URANS simulations

Figure 4.55c plots the isentropic Mach number, and the heat flux of the URANS results at the shroud at an axial location of z/L=0.57. The test section remains subsonic until around 0.18s upon which the shock passes and the heat flux level decreases to its steady value. The peak heat flux lies in the high subsonic region. The plateau of heat flux downstream of the peak heat flux is a region with local separation due to the transient shock boundary layer interaction at the shroud that is moving downstream. The plateau coincides with the time at which the sonic point is reached, and some milliseconds later, the shock has passed, and the heat flux tends to a steady-state value.

4.3.8 The unstarting of the turbine

The unsteady pressure content (from which the mean was removed) non-dimensionalized by the mean local value on the hub as a function of time is depicted in Figure 4.56 during starting, steady-state operation and shut down. The high-frequency sensor in the subsonic region does not exhibit major changes in fluctuations during startup or shut down since no shock wave is traveling through that portion of the nozzle. For the high-frequency sensor that lies within the Mach 2 divergent section (z/L=0.597), local pressures fluctuations rise to 5% when the shock passes and increases to values of 10% at shutdown (end of the run). This rises to 8% in the region of the first compression shock (z/L=0.68) and for shut down this value rose to 20%. In the separation region (z/L=0.735), the shock passing fluctuations do not exceed those during steady operation. Downstream in the separation and reattachment location (z/L= 0.766 and z/L=0.809), unsteadiness also reached values of above 10% with increased values during the shutdown. The separation region (z/L=0.766) might act as a buffer and protect that region from penetration of potentially harmful shocks.
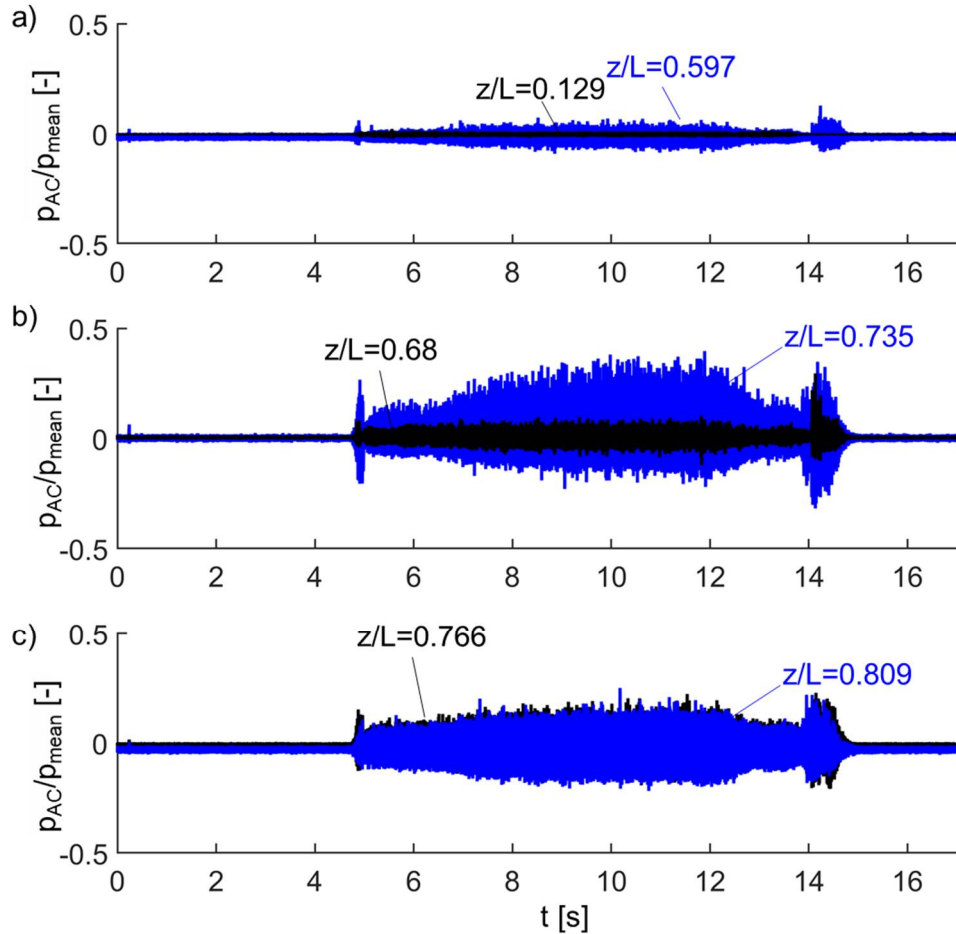
Figure 4.56 Starting, unstarting and steady-state operation: surface pressure fluctuations at multiple locations: a) z/L=0.129 & 0.597, b) z/L=0.68 & 0.735 and c) z/L=0.766 & 0.809

Two possible scenarios occur to unstart the bladeless turbine:

1) Sudden closure due to upstream flow stop
2) Gradual closure due to the increase of the back pressure

Sudden closure

A shadowgraph sequence of the shutdown of the turbine passage is displayed in Figure 4.57. Due to the elevated back pressure at the end of the test, the rear part of the test section was already 'unstarted' (no separation shock is detected near the second wavy surface). When the valve is closed, a shock wave travels upstream followed by a zone of supersonic/subsonic flow until the flow becomes subsonic and ultimately decreases to zero velocity. Total time to 'unstart' for this

experiment is around 160 ms, and the limitation is set by 1) the closing of the upstream valve which was ~ 100 ms and 2) the pressure ratio. Additionally, during shut down, shock waves seem to be locally moving back and forth on top of the shear layer.
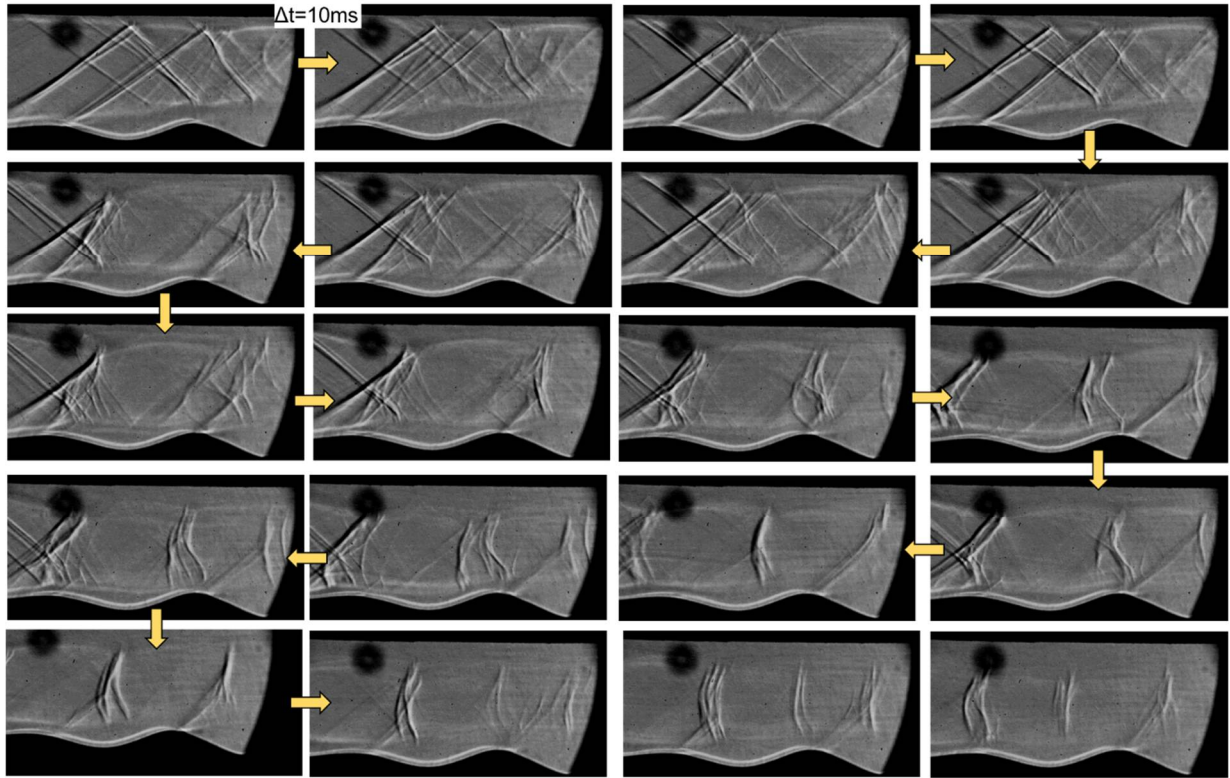
Figure 4.57 Shutdown of the bladeless turbine (time step = 10 ms)

Figure 4.58 portrays the velocity of two points in time near the first separation location through FLEET measurements. The absolute velocity for the lower dot is 423 m/s while the dot at higher y-location moves at 491 m/s (the location of the dot is drawn in Figure 4.48). Figure 4.58b plots the wall-normal speed and depending on the location, mean wall-normal velocity ranges from 20 m/s until -20 m/s for these two points. During the unstarting, the wall-normal flow components tend to a mean flow speed around zero.
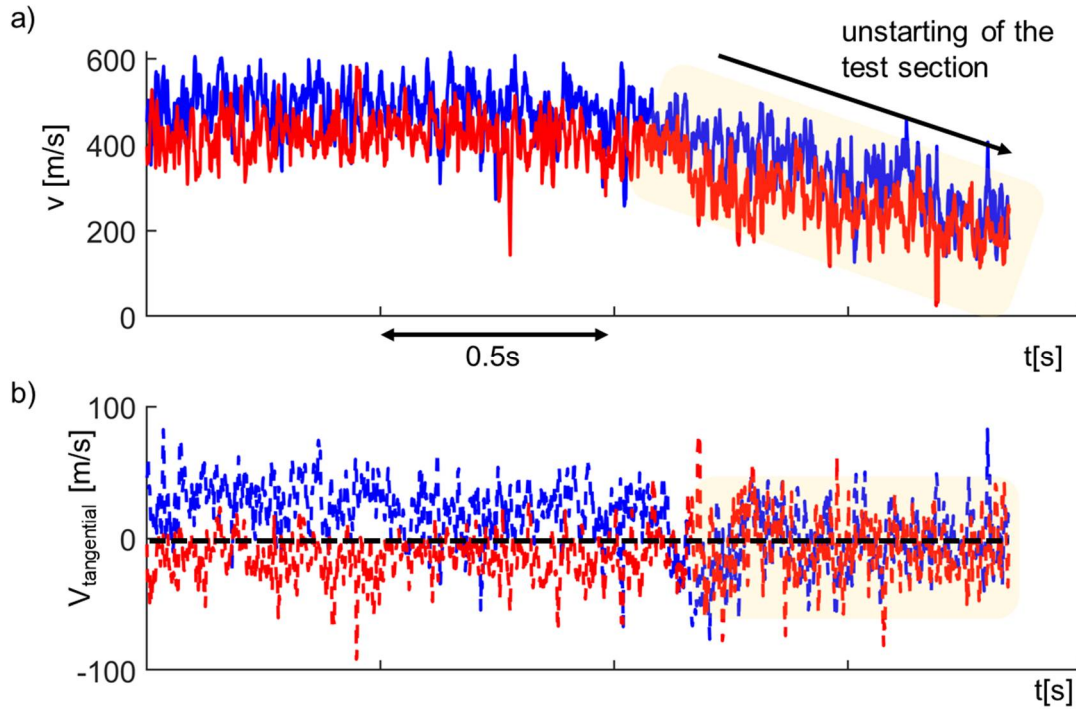
Figure 4.58 Velocity as a function of time during the unstarting of the test article: a) absolute velocity and b) wall-normal velocity

Gradual closure

The gradual increase of back pressure can be modeled according to the model of Dutton [47], and Figure 4.59a depicts the pressure contour of a URANS simulation in which the back pressure is gradually increased according to [47] while Figure 4.59b plots the Mach number. A transient unstarting shock wave is formed, similar to the sudden shutdown procedure. This transient shock wave, however, moves upstream at a lower velocity (which is a function of the mass flow). Interestingly, in the compression region of the wavy contour in which the pressure is locally higher, the shut-down shock wave slows down because that part remains choked for a longer time.
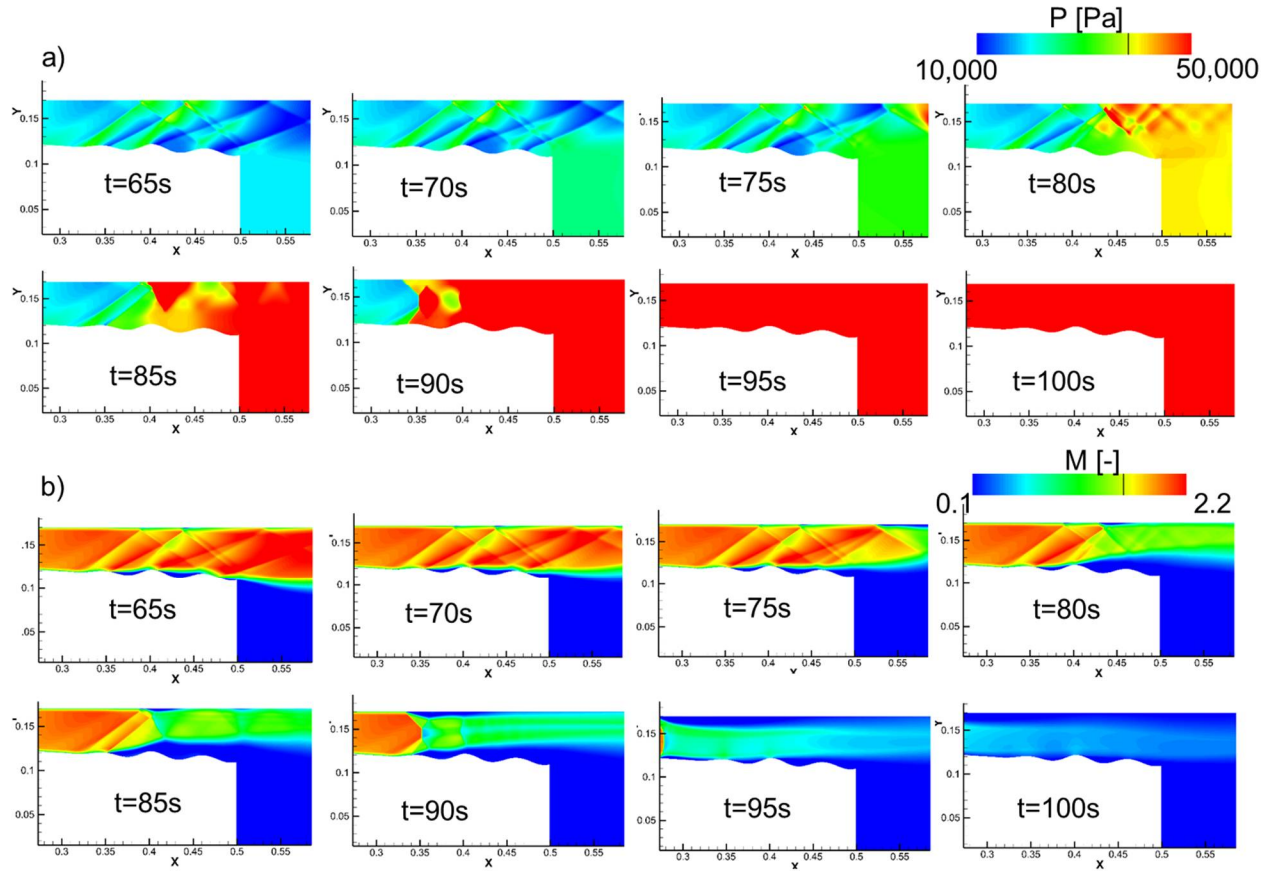
Figure 4.59 The gradual unstarting of the test article via URANS simulations: a) pressure and b) Mach number

Figure 4.60 depicts a Schlieren visualization at a low-frequency rate in which the gradual unstarting behind the first wavy contour is recorded. Several shock waves are interacting with a large separation bubble behind the second separation shock, and the shock structure gradually moves upstream. In contrast to the shroud where SBLI2 causes a strong interaction, the separation region seems to be isolated from major shock unsteadiness and might protect against potentially harmful transient shocks.
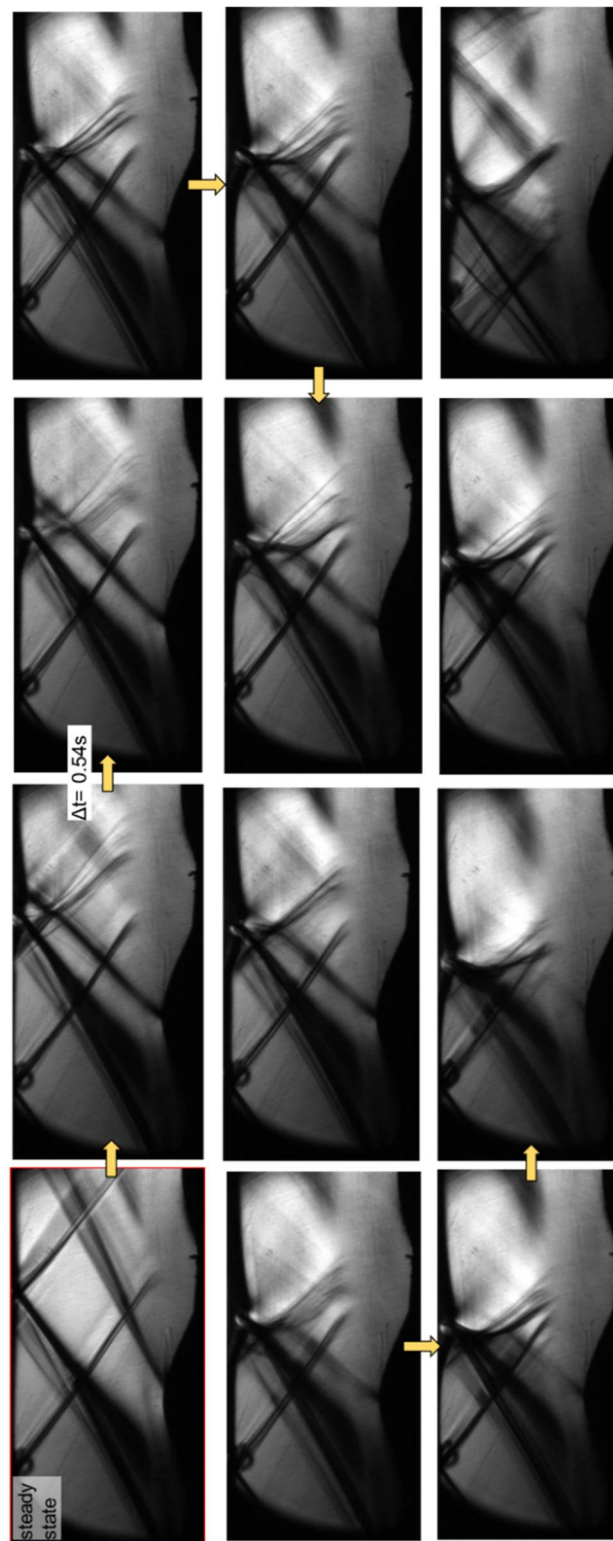
Figure 4.60 Experimental Schlieren visualization of the gradual unstarting

4.4   Fusion of the experiments with the computational analysis

4.4.1   Three-dimensional effects

The final design was also analyzed via a three-dimensional RANS simulation with 22M cells. Figure 4.61a represents the hub pressure contour as a function of the axial direction, and the three-dimensional simulation exhibits good agreement with the two-dimensional RANS, indicating that the flow is predominantly of a two-dimensional nature, however downstream of the second separation (at $z = 0.45$m), three-dimensional effects appear. Figure 4.61b plots the shear stress of the two-dimensional results, and a slight discrepancy is found near the second separation shock as well. Figure 4.61c depicts the heat flux as a function of the axial distance, and the two-dimensional simulation predicts slightly higher heat fluxes.
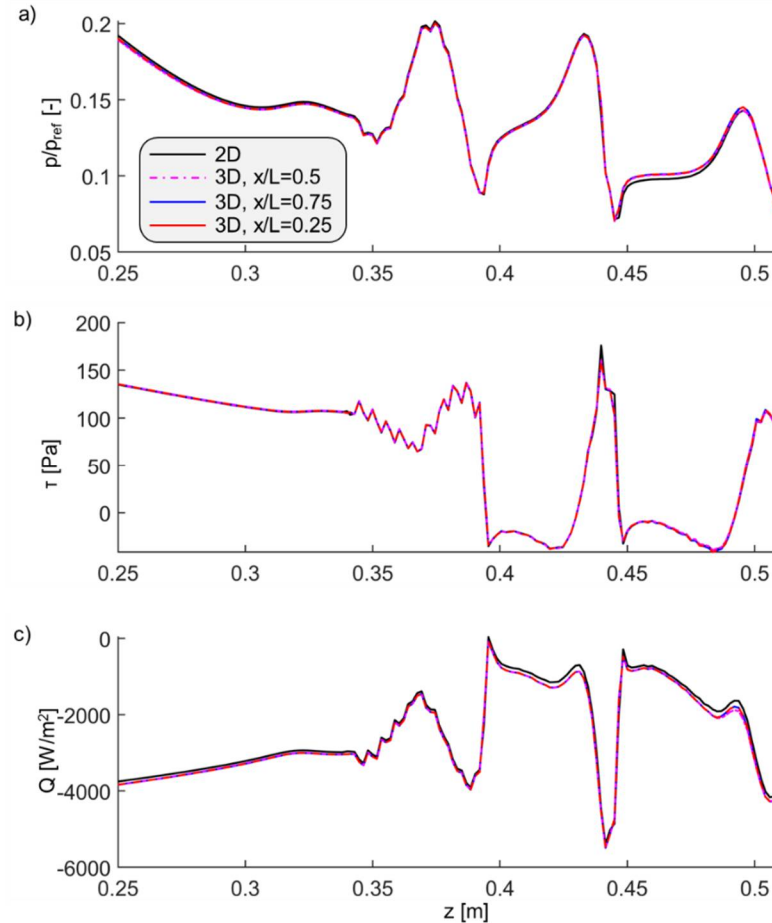
Figure 4.61 Three-dimensionality of the hub properties as a function of the axial length: a) pressure, b) skin friction and c) heat flux

Figure 4.62 depicts the discrepancy of pressure with the experiments as a function of the axial distance. Additionally, uncertainty due to the pressure tap diameter was considered for the 3D simulations according to Figure 2.4. The three-dimensional simulations agree with the two-dimensional model up to z=0.45m behind which the agreement with the experiments is better for the 3D and mostly remains below 10%. This concludes that the RANS model contains two zones of uncertainty: one due to the mismatch of the onset of separation (green) and one in the separation region in which the CFD underpredicts the pressure (brown).
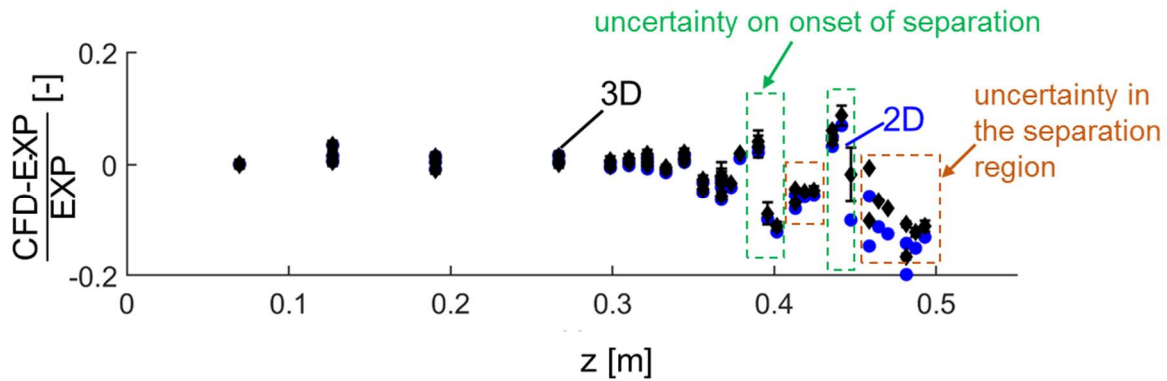
Figure 4.62 Discrepancy between experiment, two-dimensional and three-dimensional RANS simulations

4.4.2 Aerodynamic performance

The different contributions (pressure and skin friction) can be added into an overall uncertainty model that considers the uncertainty of the quantities along the axial direction of the bladeless turbine. In regions of detached flow or flow that does not follow the main flow path (set by the inlet of the turbine and relative motion of the hub), an uncertainty is added. Figure 4.63a shows the tangential shear stress (τ_ϑ) on the hub of the bladeless turbine and the blue regions mark where local flow separation occurs. The separation regions near the inlet are in the acceleration zones, as predicted by the two-dimensional model. Further downstream, however, regions of local separation from the main motion of the flow also appear in compression regions. This information is used to assess the uncertainty based on a Monte Carlo sampling [108] with 5000 simulations. The results in the local power extraction per unit axial length are depicted in Figure 4.63b. From the results of Section 4.2.4, a 20% uncertainty in skin friction (colored in red and was always

underpredicted by the CFD) and a randomly distributed uncertainty in pressure (according to Figure 4.62) were applied in regions of local separation from the core flow. The 95% and 5% confidence interval on the viscous; inviscid and total power extraction per unit axial length is displayed. Figure 4.63c features the power fluctuations due to the unsteadiness and is retrieved via the high-frequency pressure sensor data (which had a quasi-linear increase along the axial direction, as observed in Figure 4.25b). Due to the three dimensional effects in the aft part of the turbine, the uncertainty is only assessed in the part where the flow predominantly follows the two-dimensional model, and this axial length is indicated by '(A)' in Figure 4.63a.
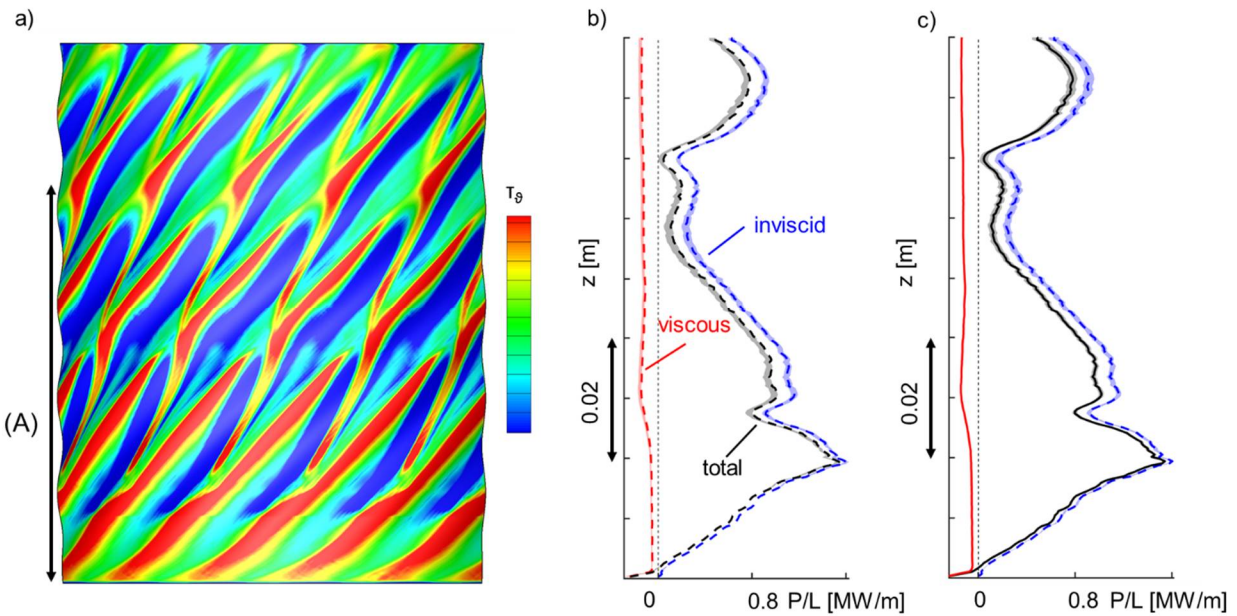
Figure 4.63 Mapping of the uncertainty onto the three-dimensional model: a) tangential shear stress with local deviation from the axial direction highlighted in blue, b) uncertainty on the inviscid, viscid and total power per length and c) fluctuations in P/L due to the unsteadiness

Figure 4.64a reveals the total integrated power and the uncertainty on the nominal power along the axial length (dotted black line = RANS results). 9 cm downstream of the inlet, around 80% of the power is extracted. The uncertainty on this power extraction lies between -11.6% and +4.4%. This non-symmetry in the uncertainty is because the skin friction was always underpredicted. Additionally, because of the growing amount of separation regions downstream the inlet, the uncertainty grows as we move downstream. The power after the first five centimeters of the bladeless turbine (which account for 60% of the power extraction) has an uncertainty of around -7% and +2%. Figure 4.64b sketches the fluctuations of the integrated power along the

axial length. The fluctuations of power are around 4% at the outlet of the turbine and increase linearly with the distance of the bladeless turbine. This increase is attributed to the growing downstream unsteadiness which was recorded by the high-frequency pressure data.
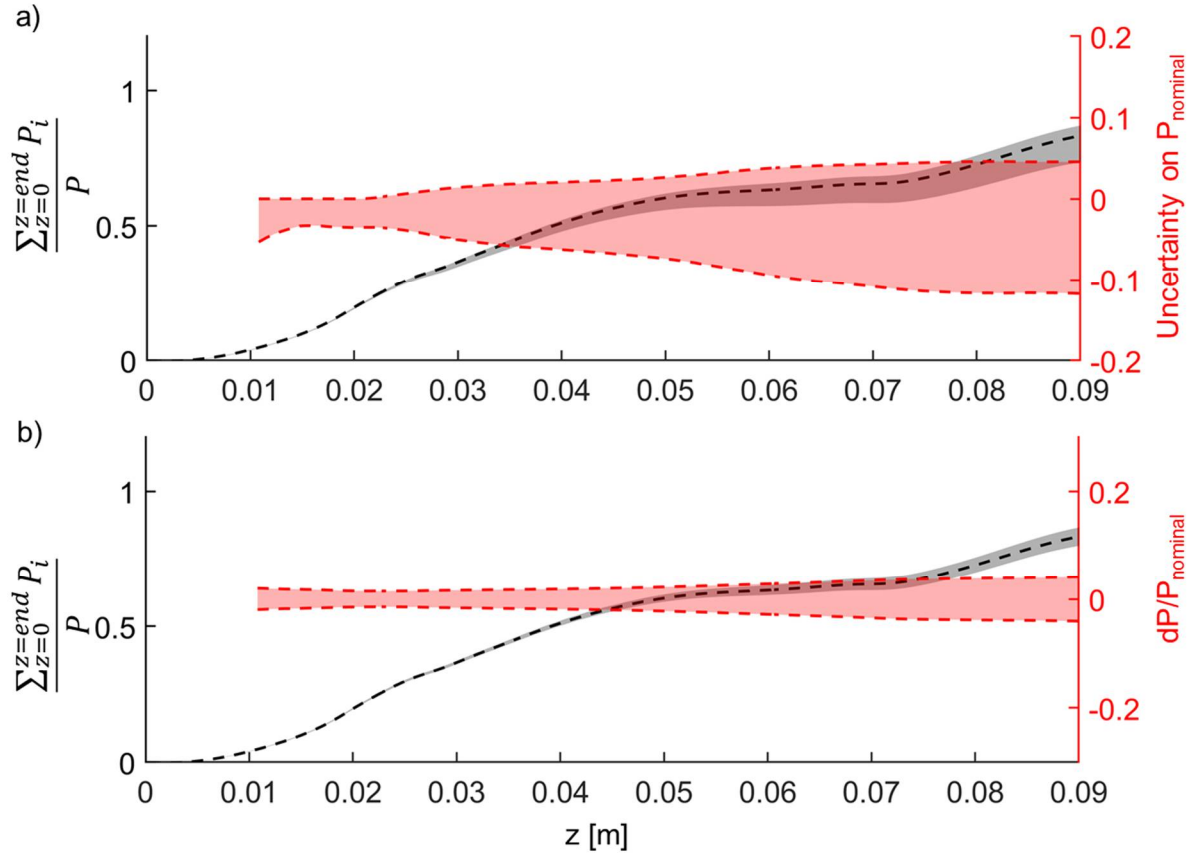
Figure 4.64 a) Uncertainty on the steady power generation along the axial direction and b) power fluctuations due to unsteadiness in the pressure along the axial direction

The total pressure loss is estimated via the shock information from the Schlieren data. Table 4.5 summarizes the assumptions, and via the oblique shock equations, the uncertainty on the total pressure loss is calculated. The shock angle discrepancy at the second separation point is around 2 degrees, which accounts for a 0.4% uncertainty in p_{01}/p_{02}.

Table 4.5 Estimation of the uncertainty on the downstream total pressure

	Shock angle	Mach (M_1)	P_{02}/p_{01}
Experiment	31	2.29	0.9946
CFD	29	2.29	0.9986

In Table 4.6, the resulting uncertainty on the efficiency is calculated. For the uncertainty on the total temperature, the discrepancy of total temperature is calculated for a three dimensional simulation without power extraction (at a rotational speed of $\omega = 0$ rad/s) and a mass-flow averaged total temperature deficit of 0.3K was found which can be attributed to the uncertainty of the numerical solver. However, to get a grasp of the true deficit, a bladeless turbine demonstrator should be built to measure power extraction, and the mass-flow averaged total temperature drop. The influence of total temperature, total pressure, and the viscous and inviscid moment on the uncertainty of the mechanical and thermodynamic efficiency is then analyzed. The total uncertainty is around 10% for the thermodynamic efficiency and 15.6% for the mechanical efficiency. The discrepancy between both lies in the fact that the mechanical efficiency uses the torque that is calculated based on the hub pressure and shear stress data. For the thermodynamic efficiency, the total temperature is the most sensitive parameter. The sensitivity of the viscous moment, inviscid moment and outlet total pressure on the mechanical efficiency had the same magnitude.

Table 4.6 Uncertainty on the efficiency

	%	Sensitivity on $\eta_{thermodynamic}$	Sensitivity on $\eta_{mechanical}$
Outlet total temperature	0.01	700	0
Outlet total pressure	0.4	14.5	79
Viscous moment	20	0	178
Inviscid moment	9	0	108
Total uncertainty	**~10%**	**Total uncertainty**	**~15.6%**

4.4.3 Heat flux

The uncertainty on the normalized average heat flux along the axial direction is visualized in Figure 4.65. A random heat flux uncertainty with a maximum uncertainty of 10% in the attached region and 80% in the detached zones was applied and was based on the heat flux results indicated in Figure 4.19. Zones of relatively low uncertainty are observed right downstream of the inlet and

are also subjected to the highest heat load. Zones of higher uncertainty lie in regions of detached flow.
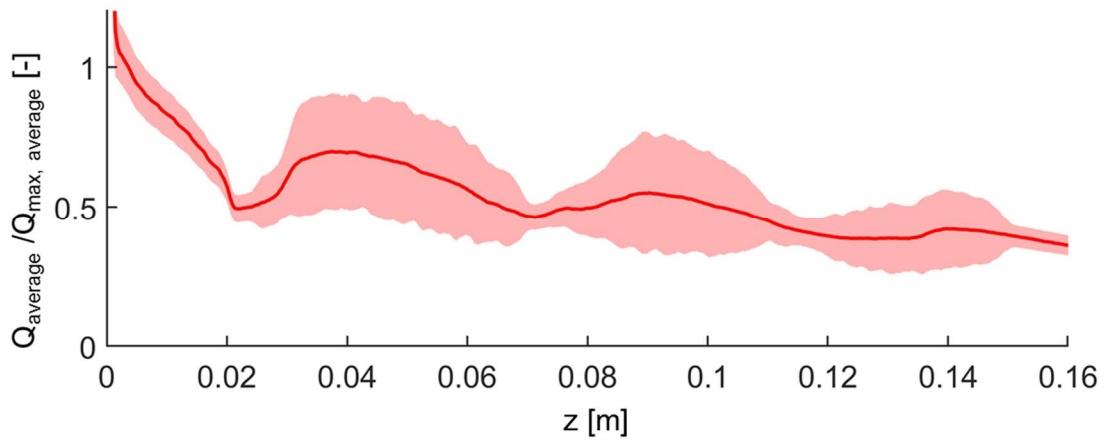
Figure 4.65 Uncertainty on the steady heat flux in the bladeless turbine along the axial direction

4.4.4   Flow field variations

Table 4.7 indicates the fluctuations in Mach number based on the Schlieren visualization and the oblique shock relations. Mach number varies between 10-20% based on the shock fluctuations. Additionally, from the Background Oriented Schlieren, the averaged fluctuations are around 7% before the shocks and can locally increase up to 20% after the separation shock. From FLEET measurements, local flow angle fluctuations right downstream of the separation shock could be beyond 100%.

Table 4.7 Variation in Mach number due to shock angle fluctuations

	$\delta_{shock, mean}$[deg.]	Mach before shock	Mach after shock	Variation in Mach number
compression shock	~34.25	2.18	1.84	~0.013
separation shock	~28.4	2.25	2.15	~0.08
second separation shock	~34	2.29	1.91	~0.17

CHAPTER 5.   OPERATIONAL ENVELOPE AND OPTIMIZATION

5.1   Parametrization of the bladeless turbine

The numerical tools consist of procedure on how to mesh the geometries was explained in the previous section. Parametrization is performed in Matlab and the entire procedure from parametrization till solving is visualized in Figure 5.1.
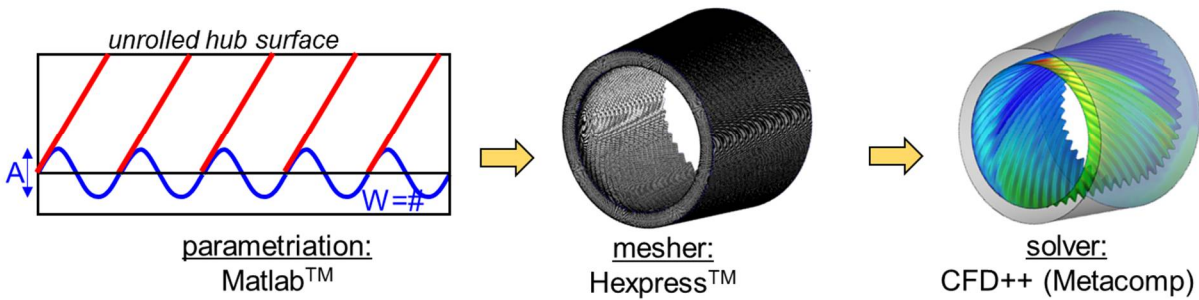
Figure 5.1 Procedure to characterize the bladeless turbine

Figure 5.2 depicts the parametrization of the unrolled hub end wall contoured with a wavy surface. Figure 5.2a sketches an unrolled view of the bladeless turbine. The inlet of the hub is flat which after a distance 'd' evolves into a wavy surface pattern with an amplitude 'A' and 'W' denotes the number of waves. The waves have an inclination of α_{helix} relative to the axis of the turbine, and the flow has a certain flow angle (denoted as $\alpha_{flow\ angle}$). The sense of the angles is defined by the rotation of the hub. Figure 5.2b shows the parametrization to smoothly transition from a flat entrance to a wavy surface. The parametrization consists of a Bezier curve where the first two and last two control points are fixed in height and space and the middle point has two degrees of freedom (horizontal and vertical direction).
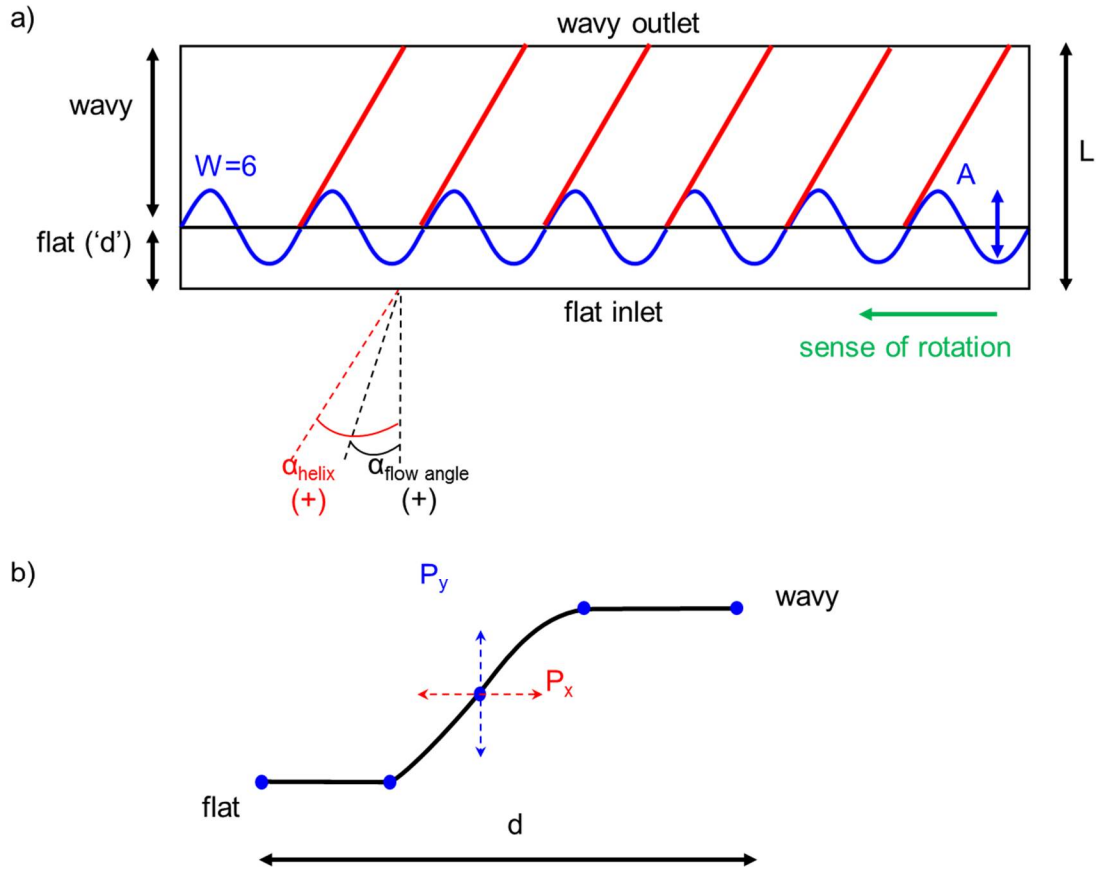
Figure 5.2 a) Parametrization of the hub and b) definition of the Bezier curve at the onset of the hub

5.2 Variation of the geometrical features with a sinusoidal wavy surface

Rather than using the pressure ratio, only upstream quantities can be fixed for a supersonic turbine. Hence a third upstream component needs to be selected. The main contributor to the work output of the bladeless turbine is the local static pressure exerted on the hub. Hence the static pressure was selected to define the reduced torque. This non-dimensional number relates the torque to the static pressure, hub area, and hub radius:

$$\tilde{\tau} = \frac{\tau}{p_{hub} \times A_{hub} \times R_{hub}}$$

Eq. 5.1

Figure 5.3a plots the influence of the number of waves on the reduced torque. A maximum reduced torque and efficiency is achieved for 28 waves. The difference of reduced torque between all of the geometries is less than 20% when the number of waves is more than doubled, owing to a small sensitivity of torque to the number of waves for a given inlet condition.
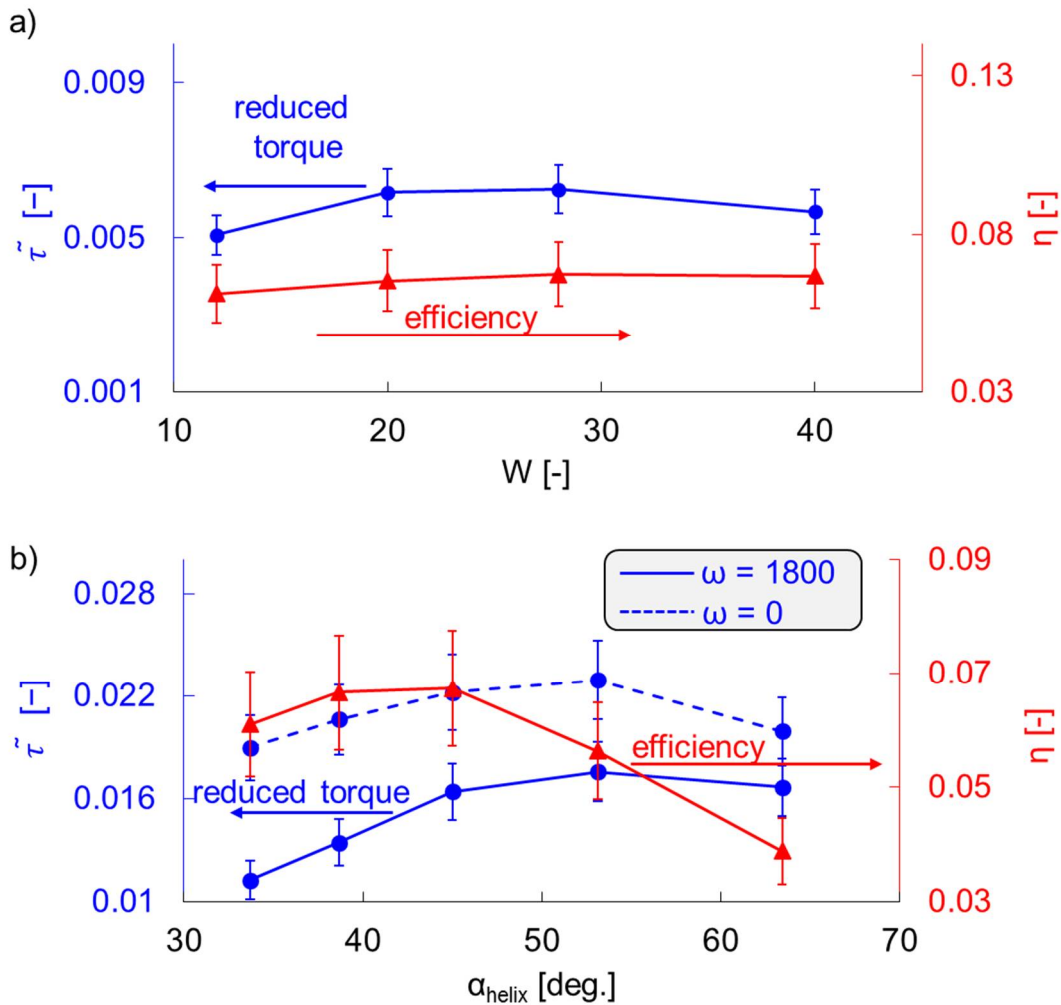
Figure 5.3 a) Reduced torque and efficiency as a function of the number of waves (W) and b) reduced torque and efficiency as a function of the helix angle

In Figure 5.3b the influence of the helix angle on the performance of the bladeless turbines is analyzed. A peak reduced torque was observed near 53 degrees and a similar trend is observed when the hub speed was zero. The efficiency, however, peaks at lower helix angles for this specified rotational speed of 1800 rad/s. Peak efficiencies for higher helix angles are achieved for

higher rotational speed. The uncertainty was calculated from the uncertainty on power and efficiency from Section 4.4. When the hub is fixed (no rotation), the relative difference in torque is less than 20% for the different helix angle, and hence the sensitivity of the helix angle is small for a wide range of helix angles. The ratio of the viscous torque (which has a negative effect) over the total torque exerted on the hub varied between 30% for lower helix angles to 15% for high helix angles.

Figure 5.4 depicts the flow field for several bladeless turbines. In Figure 5.4a, a bladeless turbine with 12 waves is analyzed and has a reduced amount of flow separation due to the increased wavy contour length and with a smeared out compression zone downstream of the inlet. Far downstream of the inlet, the flow is still being compressed and expanded in contrast to the baseline (Figure 5.4b). In Figure 5.4c the flow field of a turbine with 40 waves is plotted. After a short distance downstream of the inlet, flow is separated from the main core flow but the shock strength is higher near the inlet due to the increased curvature of the wave in the compression region, which locally produces a high amount of power.
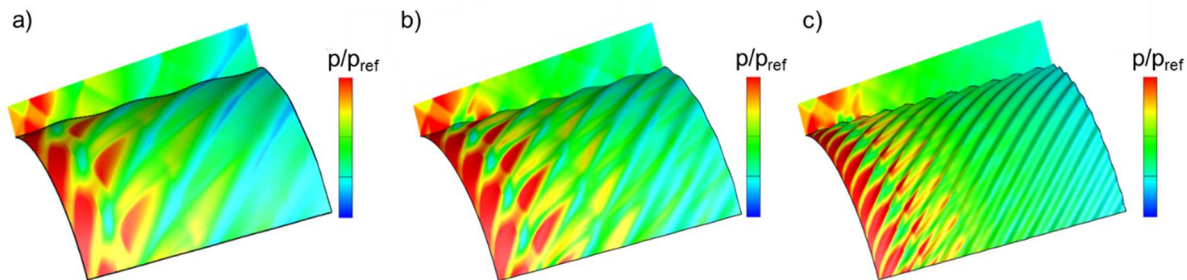
Figure 5.4 Pressure contour of the bladeless turbine with a helix angle of 45 degrees and an inlet Mach number of 1.25: a) 12 waves, b) 20 waves (baseline) and c) 40 waves

In Figure 5.5b the pressure field of a bladeless turbine with a helix angle of 63 degrees and an inlet Mach number of 2.1 is visualized. In contrast to the baseline case (Figure 5.5a), the pressure is decreased in the expansion fans, and the pressure is higher in the compression region for higher helix angle bladeless turbines.
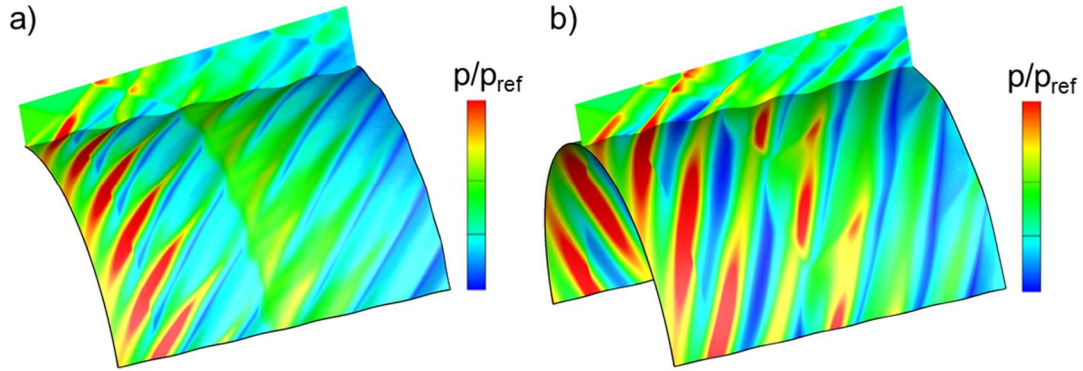
Figure 5.5 Pressure contour of the bladeless turbine for an inlet Mach number of 2.1, a) helix angle of 45 degrees and b) helix angle of 63 degrees

The influence of the amplitude of the wavy surface on the performance of the bladeless turbine is investigated for an inlet Mach number of 2.1. Three different amplitudes of the wavy contour of the bladeless turbine were tested (10% of amplitude-to-channel-height (the baseline), 15%, and 20%). Figure 5.6a shows the amplitude-over-height as a function of power and efficiency. Due to the stronger deceleration, higher local pressures and higher work extraction can be achieved for higher amplitudes. The increase in power was 210% when the amplitude was doubled. The viscous-to-total contribution decreased from 21% (baseline case) to 14% for the highest amplitude case. Additionally, total pressure loss increased from 13% (baseline case) to 21% for the largest amplitude case. The reduced torque has a parabolic trend with an R^2 value of 0.99998, and the trend of the efficiency has an R^2 value of 0.995, hence these slope coefficients can be used for engine models and to extrapolate results for higher amplitudes-over-heights. Figure 5.6b plots the amplitude of the wave for two different hub radii against the reduced torque, and demonstrates that the non-dimensional number 'reduced torque' can be used to predict the power for several radii and that the discrepancy between the points is less than 7%.
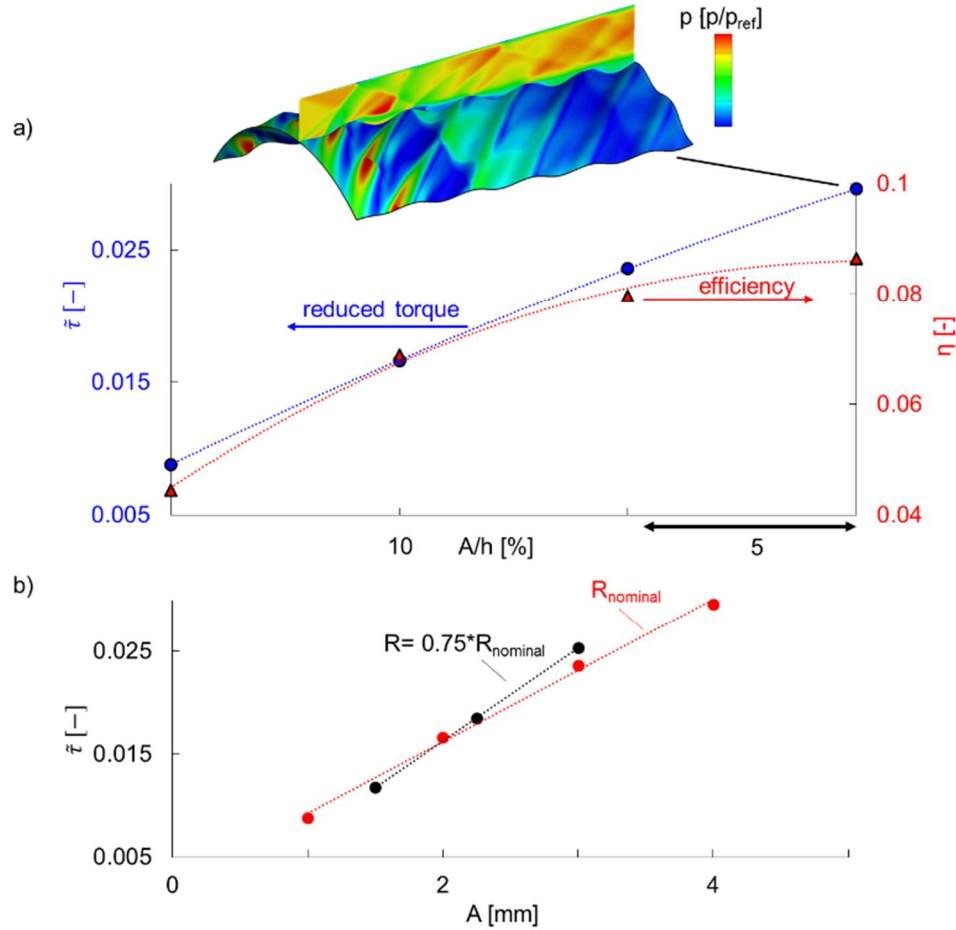
Figure 5.6 a) Influence of the amplitude-to-channel-height of the wavy contour on efficiency and reduced torque and b) reduced torque as a function of the amplitude for two different radii of the bladeless turbines

Figure 5.7 displays the influence of the channel inlet height (h) by keeping the amplitude of the wavy surface constant. By varying the height, the local acceleration and compression rates can locally change; however, the power extraction is only slightly affected when A/h is increased at the inlet from 0.04 to the six-fold and efficiency increased by two %points compared to the baseline value. The efficiency reaches a plateau for higher inlet heights. Power density decreases by a factor 6. This proves that the most sensitive parameter that sets the power is the amplitude of the wavy contour (A). The limitation for turbines operating at low supersonic inlet Mach numbers is A/h: once the inlet speed; mass-flow and radius of the turbine are known, A/h is fixed and sets the maximum power extraction per unit length. In Figure 5.7b, the influence of the length of the turbine is investigated, and the normalized cumulative power is

plotted against the axial length of the turbine. Similar to Section 3.3.1, the baseline (W=20) displays the highest power extraction just downstream of the inlet, and around 80% of the power is extracted in 56% of the length. For an increasing ratio of amplitude-over-height, power extraction is enhanced, and 80% of power is achieved in the first 25% of the turbine. A slight overshoot of power is recorded, followed by a decrease. At constant amplitude, but with an increased number of waves (W), similar features are found. Most of the power is extracted within 12.5% of the turbine length (front-loaded). This can be attributed to the fact that the curvature of the wave in the compression region is higher by increasing the number of waves or by increasing the amplitude-to-height ratio. Hence for this bladeless turbine design, the first portion of the bladeless turbine is the most efficient for power extraction while the latter part mainly accelerates the flow to the desired outlet Mach number. By decreasing the number of waves (W=12), power is also produced in the aft section, hence a more balanced power extraction along the axial direction is obtained.
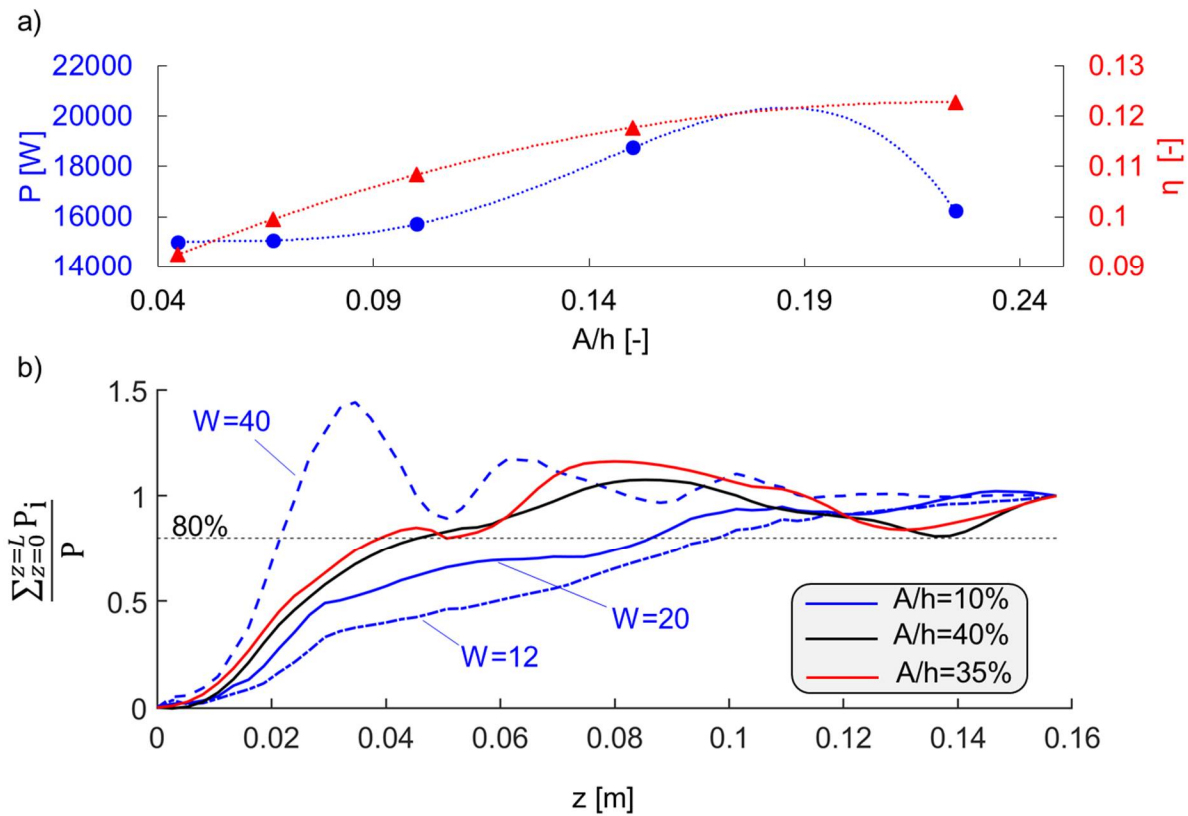
Figure 5.7 a) Power and efficiency by varying the inlet height at a constant amplitude of the wavy surface and b) influence of the length on the distribution of the power

5.3   Operational envelope

5.3.1   Variation of reduced mass flow and reduced speed

In Figure 5.8, the power is plotted as a function of the rotational speed, for a bladeless turbine with a radius of approx. 0.09m. Optimum rotational speed for maximum power extraction lies around 30,000 RPM. This optimum rotational speed depends on the geometrical features as well as the inlet conditions to the turbine. Maximum power of around 75 kW was achieved for a Mach number of 1.25 and an amplitude-to-channel-height of 10%. Figure 5.8 also features the mechanical efficiency as calculated via Eq. 3.4 with the isentropic state defined by the total quantities upstream and downstream of the turbine in the absolute frame of reference. An optimal efficiency was equally reached at around 30,000 rpm. This optimum point of efficiency is related to the rotation of the hub: the shock strength decreases as RPM increases and consequently, entropy losses decrease throughout the channel. The maximum efficiency is ~8% for this design. At optimal RPM, the absolute flow angle at the outlet was 0.7 deg. and because of the high speeds, this change in flow angle produced a power extraction of ~75 kW. The specific Euler work was around 3.9 kJ/kg and is around 50-100 times smaller than typical values for traditional subsonic turbines. At the optimal rotational speed of around 3000 rad/s, the relative inlet flow angle was 14 degrees, and the power extraction corresponds to a temperature drop of approximately 4 K ($T_{01}/T_{02}=1.0015$). The viscous contribution to the torque over the total torque was 43%.
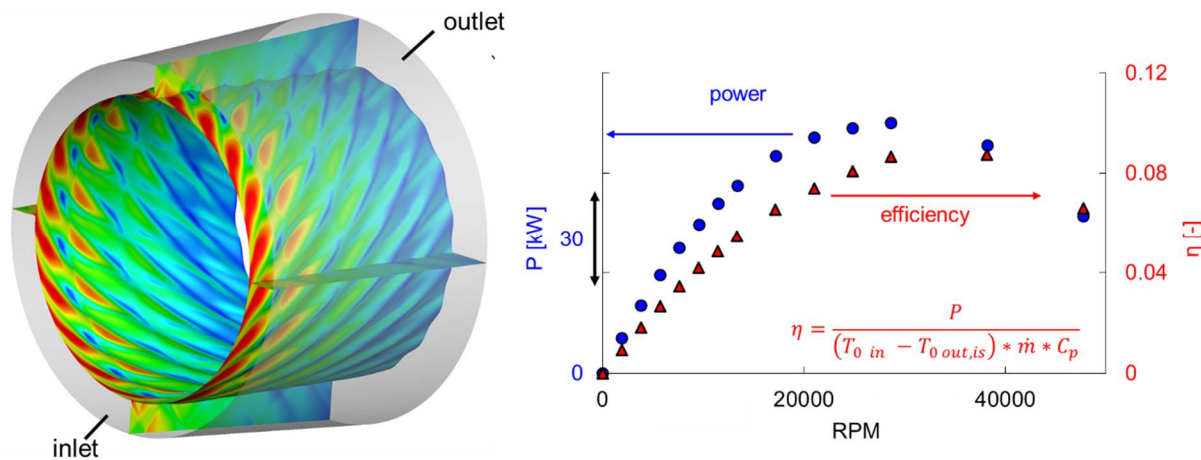
Figure 5.8 Power and mechanical efficiency as a function of the rotational speed

To be able to use the bladeless turbine in engine models and compare with traditional subsonic turbines, the reduced mass flow and reduced speed were defined as:

$$\tilde{m} = \dot{m} \frac{\sqrt{T_{0\ inlet}}}{p_{0\ inlet}} \qquad \text{Eq. 5.2}$$

$$\tilde{n} = \frac{\omega}{\sqrt{T_{0\ inlet}}} \qquad \text{Eq. 5.3}$$

Around 40 conditions were simulated with different inlet Mach numbers; total pressure; total temperatures and RPMs for one single geometry. Figure 5.9a depicts the reduced torque as a function of the product of the reduced speed and reduced mass flow. All points with the same inlet Mach number form iso-reduced-mass lines, typical for supersonic flows in which the mass flow is only dependent on the Mach number and upstream total pressure and total temperature. Simulations were performed over a range of Mach 1.25 to Mach 2.4, and higher Mach number flows result into lower reduced mass flows. The reduced torque is dependent on both reduced mass as well as reduced speed. The reduced torque is highest for low reduced speeds, as seen in Figure 5.9a. Zone A (for which the inlet Mach number is 1.25) and Zone B (for which the inlet Mach number is 2.1) are conditions in which static pressure increases and the total temperature is maintained constant. Although all the data at Mach 1.25 appear to result in a single reduced torque, we observe a larger variation at Mach 2.1, which is associated to the variation in the Reynolds number, and drives the extent of the separation bubble. Figure 5.9b shows the mechanical efficiency as a function of the product of reduced mass flow and the reduced speed with values above 10%. Iso-reduced mass flow lines are also represented, and lower reduced mass flow yielded higher efficiencies, but corresponded to higher reduced speeds.
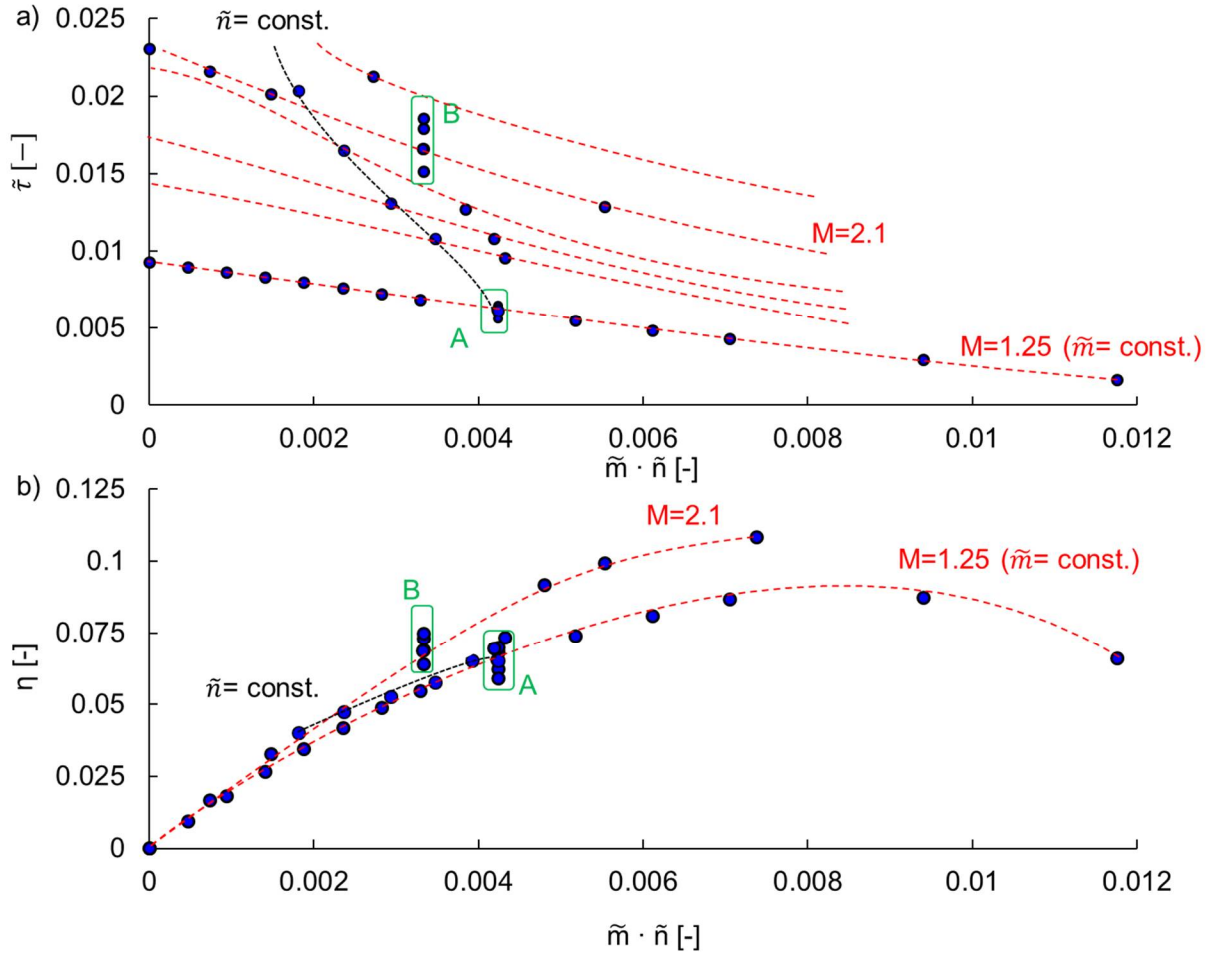
Figure 5.9 a) Reduced torque as a function of the product of the reduced speed and reduced mass flow and b) efficiency as a function of the product of the reduced speed and reduced mass flow

Figure 5.10 elaborates on the Reynolds effect. The reduced torque is plotted as a function of $\rho_{inlet} \cdot u_{axial, inlet}$ (which can be related to the Reynolds number based on the diameter of the channel and viscosity of the fluid). For Mach 1.25, the points at several Reynolds numbers form a quasi- horizontal line whereas for Mach 2.1 the slope is increased and tends to an asymptotic behavior at higher Reynolds numbers. Additionally, the pressure on the hub and the pressure at a constant tangential slice reveal a strong pressure wave near the mid-axial location. As Mach number rises, the local separation increases downstream of the hills which negatively affects local power extraction.
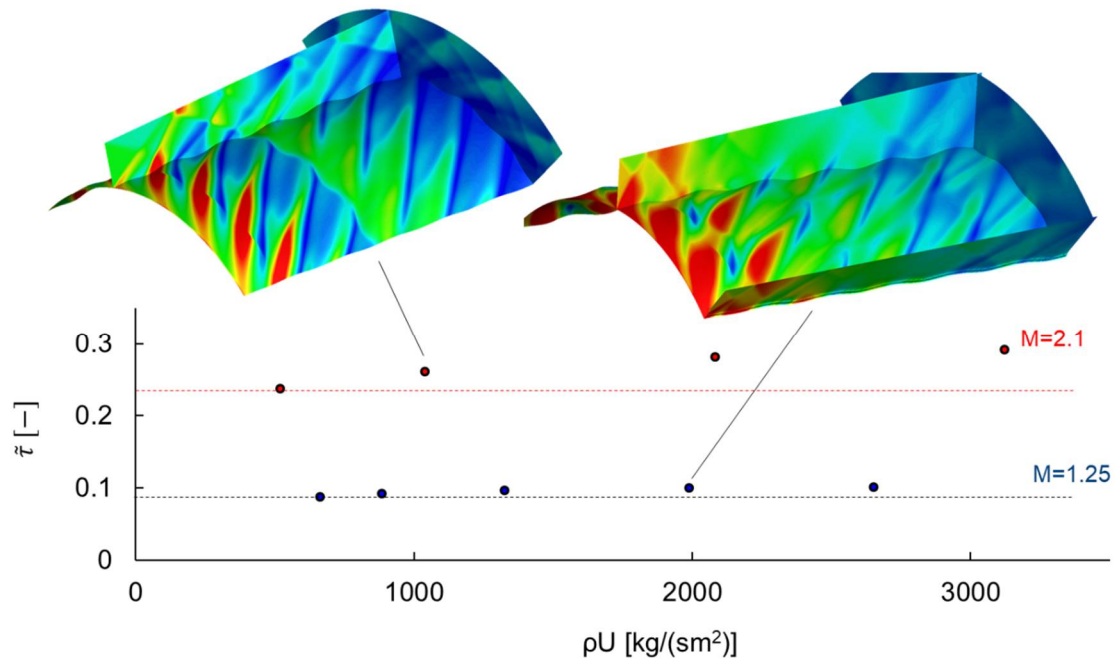
Figure 5.10 Reduced torque as a function of ρU

The increased separation for high Mach number cases is evidenced in Figure 5.11a in which the tangential shear stress is shown at the hub. An increase of negative shear stress indicates that a higher amount of flow does not follow the axial direction. This also penalizes the local power density (Figure 5.11b) with negative contributions at 0.06 m downstream of the inlet due to the local flow detachment.
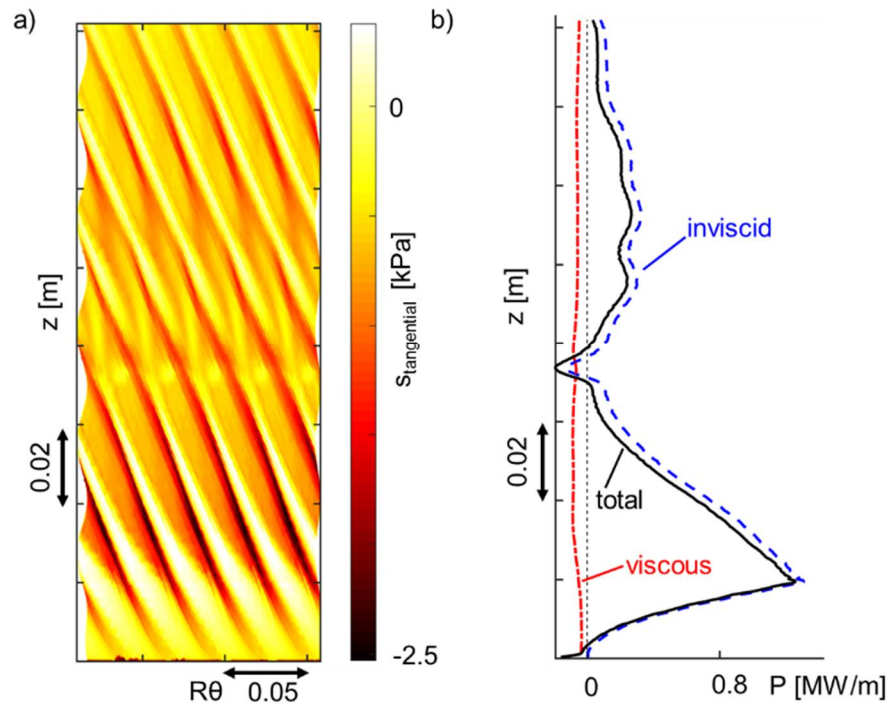
Figure 5.11 a) Tangential shear stress and b) power density for an inlet Mach number of 2.1

The maximum power density at 0.02 m downstream of the inlet is slightly lower than the Mach 1.25 case (Figure 3.6). The effect of the Mach number is investigated in Figure 21, where the reduced torque is depicted as a function of the inlet Mach number (for a constant speed line). A reduction of reduced torque is observed, which can be related to a decrease of static pressure at the inlet. The power extraction is maximal for a Mach number of around 1.4. This optimum Mach number could be dependent on the geometry because the inclination and the strength of the compression shocks at the hub and its reflections on the shroud affect the local flow separation which penalizes power extraction. For this reduced speed line, maximum efficiency was found in the low Mach number region.
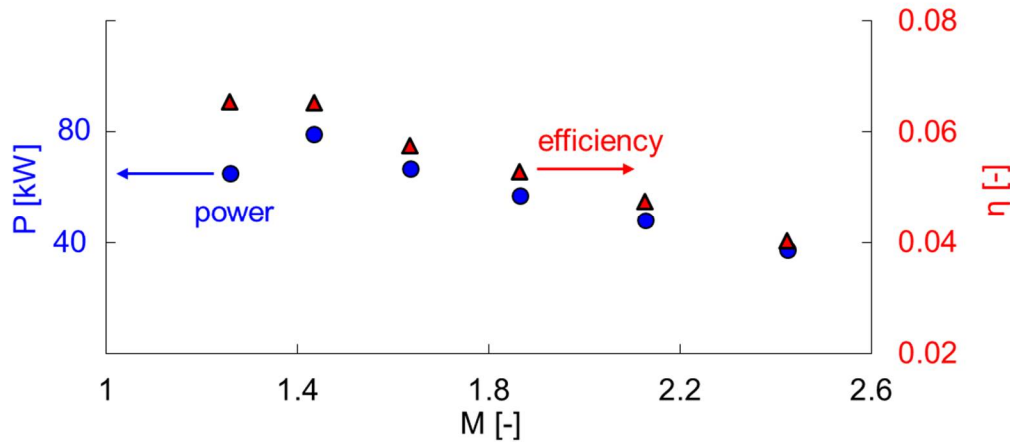
Figure 5.12 Power and efficiency as a function of the Mach number at constant reduced speed

Figure 5.13a illustrates the relationship between the relative flow angle (β) and the helix angle (α_{helix}):

$$\gamma = \alpha_{helix} - \beta$$

Eq. 5.4

Figure 5.13b plots the efficiency of the turbine as a function of γ which indicates the angle of the flow compared to the helix in the relative frame of reference, because this will be the angle at which the flow undergoes the subsequent compression and expansion waves. The graph plots several ratios of amplitudes-over-heights (ranging from 10% to 35%). Additionally, several helix angles are plotted, ranging from 34 to 64 degrees. All these simulations are for one reduced mass flow. The maximum efficiency was around 28% for the highest amplitude-over-height (A/h) and a helix angle of 53 degrees. The maximum efficiency is mostly dictated by the amplitude-over-height. For an A/h of 10%, the maximum efficiency of 10% can be tripled by tripling the amplitude over height. Optimal γ values are around 20-30 degrees. For increased RPMs, which results in reduced γ values, high helix angles are preferred, and a plateau of steady efficiency is found for helix angles of 63 degrees at low A/h. If the RPM is fixed, an optimal helix angle exists with a corresponding maximum efficiency and power (see Figure 5.3b).

In terms of power (Figure 5.13c), similar trends are detected. Up to 0.4 MW can be extracted for high amplitude bladeless turbines, corresponding to a T_{01}/T_{02} of around 1.02 (~30K). For lower

amplitude-to-height turbine designs, the power extraction is lower. For high RPM requirements and fixed radius, higher helix angles are needed. However, for low RPM, medium helix angle turbines share a similar overall performance than high helix angle bladeless turbines. For a fixed A/h, a helix angle of 63 provided the highest power. The torque scales linearly with γ and highest torque was retrieved at highest γ because the flow tends to be more perpendicular to the helicoidal wavy hub surface.
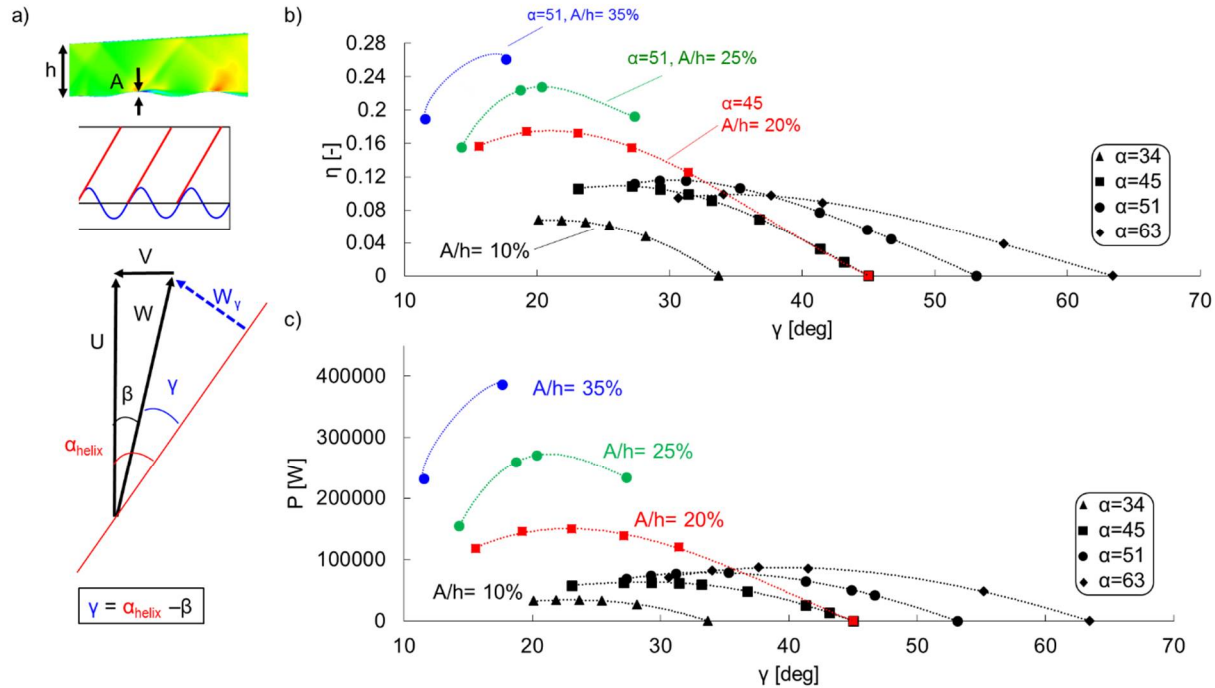
Figure 5.13 a) Definition of the angles, γ as a function of efficiency (b) and power (c) for several amplitude-over-heights

5.3.2   Range: subsonic to hypersonic

The range of operation in terms of Mach number is investigated in Figure 5.14. The pressure ratio (total-to-static) was selected to represent the different operating points. For low pressure ratios, the turbine is choked and operates at subsonic inlet speeds, similar to a transonic turbine stage at high subsonic Mach number as studied by Liu et al. [109]. For this design and area opening, the Mach number at the inlet was 0.94. Up to a pressure ratio of around 5.9, the inlet was subsonic. The maximum thermodynamic efficiency in the subsonic region and low supersonic regime was around 7%. At pressure ratios above 1540, Mach 6 was reached, depicting the

capability of the bladeless turbine to deliver power in subsonic to hypersonic velocities. By increasing the pressure ratio, higher supersonic speeds are achieved, however at the expense of power, due to a reduction of local static pressure. Higher power extraction is achieved by increasing the amplitude-over-height, which is justified due to the increase in area ratio for which the turbine will not choke. For subsonic use, the area ratio is of critical importance to choke the flow locally and generate shock waves which are needed for power extraction.
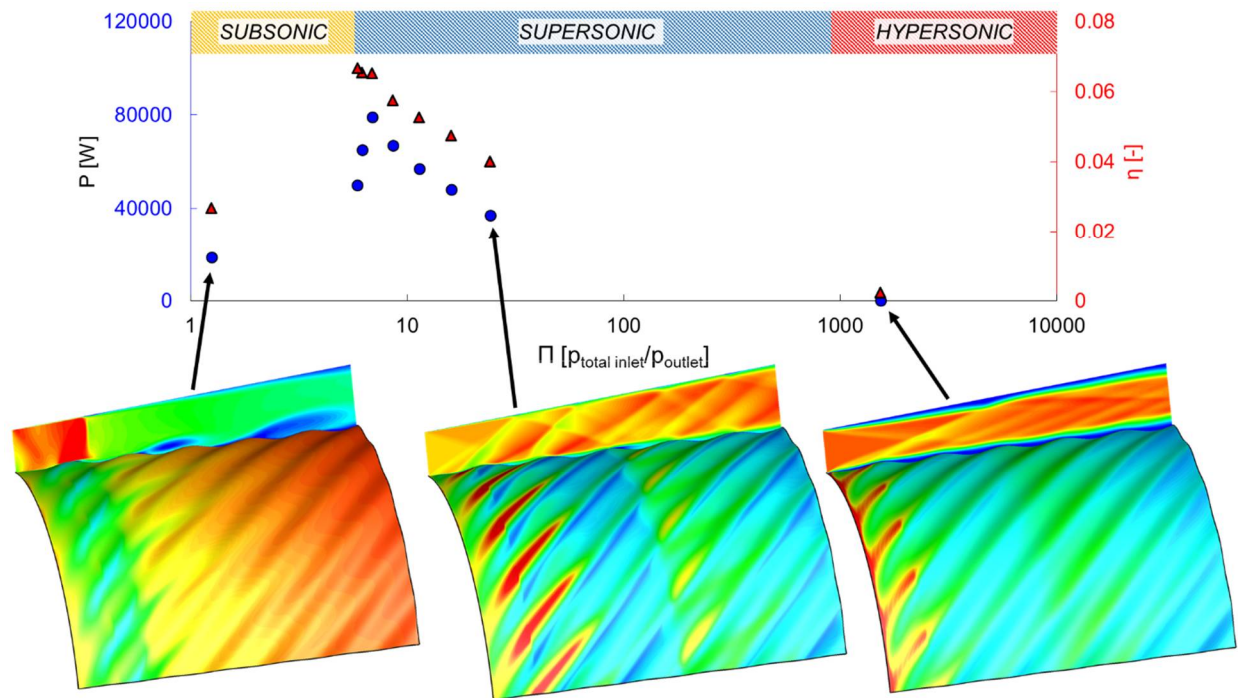
Figure 5.14 Range of operation of the bladeless turbine for one geometry (A/h = 10%)

5.3.3   Swirled supersonic inflow

The influence of swirl upstream of the bladeless turbine (e.g., via transonic or supersonic stators) is investigated by imposing an absolute flow angle at the inlet. Figure 5.15 shows the power extraction as a function of γ. The red curve is an iso-reduced mass flow as well as an iso-reduced speed line as a function of the flow angle. By increasing the flow angle (α_{flow}), γ is reduced, and hence, the flow feels less compression and expansion with a consequent drop in power extraction and efficiency. Negative flow angles, however, increase power extraction and efficiency as the wavy hub surface tends more perpendicular compared to the relative flow motion. The power can be tripled with an inflow angle of -30 degrees. For two flow angles, several reduced speeds

are plotted in black and blue. Each curve has a maximum power extraction, and a drift towards higher powers is obtained by decreasing the flow angle. A similar pattern is identified for the efficiency (Figure 5.15b). Peak efficiency for the baseline with inlet swirl is around 25% and is a function of γ and the reduced speed.

Conclusively, compared to no inlet-swirl, the operational map is shifted towards increased power extraction and efficiency for negative swirl angles.
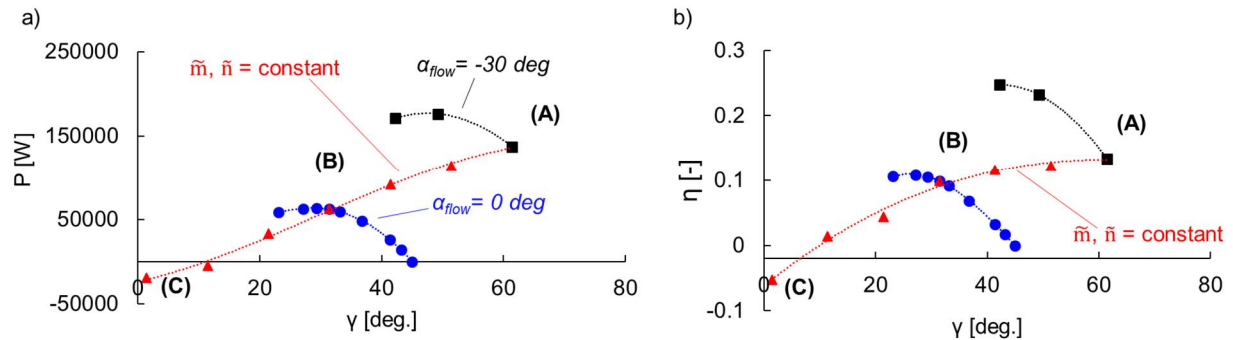
Figure 5.15 Pre-swirled bladeless turbine: a) power as a function of γ and b) efficiency as a function of γ

Figure 5.16 depicts the static pressure contour for three different inlet flow angles ranging from -30 degrees to 30 degrees (the same profiles are also indicated in Figure 5.15). For the lowest inflow angle (A), stronger compression waves and expansion waves are formed, resulting in higher momentum on the hub. For a flow angle of 30 degrees (C), the γ angle is 1.4 and results in negative power extraction.
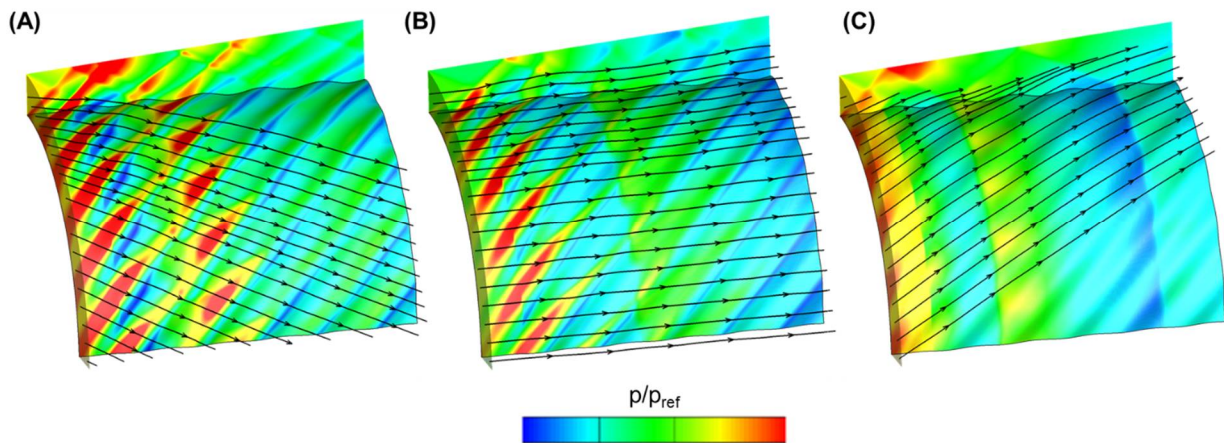
Figure 5.16 Flow field for three inlet swirl angles: $\alpha_{flow\ angle}$ = -30 deg. (A), b) $\alpha_{flow\ angle}$ = 0 deg. (B) and c) $\alpha_{flow\ angle}$ = 30 deg. (C)

Additionally, the ratio of the viscous moment over the total moment decreases with decreasing flow angle: the contribution is around 30% at a flow angle of 0 degrees and decreases to 4.4% for a flow angle of -30 degrees.

5.4 Irreversibility

Figure 5.17 dissects the irreversibility that is present within the bladeless turbine. The losses, for steady-state adiabatic simulations, can be derived from the entropy transport equation [110]:

$$\frac{\partial \rho s}{\partial t} + \frac{\partial}{\partial x_j}\left(\rho u_j s - \frac{k}{T}\frac{\partial T}{\partial x_j}\right) = \frac{k\frac{1}{T}\frac{\partial T}{\partial x_j}\frac{\partial T}{\partial x_j} + \tau_{ij}\frac{\partial u_i}{\partial x_j}}{T} \qquad \text{Eq. 5.5}$$

If adiabatic walls and steady-state operation are assumed, this can be approximated by:

$$\text{irreversibility} = \tau_{ij}\frac{\partial u_i}{\partial x_j} \sim T\rho U_j \frac{\partial}{\partial x_j}(s)$$

The derivatives of entropy are calculated by the temperature and pressure gradients which were provided by CFD++:

$$\frac{\partial s}{\partial x} = \frac{c_p \frac{\partial T}{\partial x}}{T} - \frac{R\frac{\partial p}{\partial x}}{p}, \qquad \frac{\partial s}{\partial y} = \frac{c_p \frac{\partial T}{\partial y}}{T} - \frac{R\frac{\partial p}{\partial y}}{p}, \qquad \frac{\partial s}{\partial z} = \frac{c_p \frac{\partial T}{\partial z}}{T} - \frac{R\frac{\partial p}{\partial z}}{p} \qquad \text{Eq. 5.6}$$

Hence, the final irreversibility is as follows:

$$\text{irreversibility} \sim \left(T\rho u \frac{\partial s}{\partial x}\right) + \left(T\rho v \frac{\partial s}{\partial y}\right) + \left(T\rho w \frac{\partial s}{\partial z}\right) \qquad \text{Eq. 5.7}$$

This accounts for all the aerodynamic losses or irreversibility generated either because of the boundary layer or across the shock. Two geometries were investigated with two different

amplitudes-over-heights (A/h=25% and A/h=10%. The entropy loss is visualized in Figure 5.17b and Figure 5.17c. High regions of irreversibility occur across the shock as well as the boundary layer. The losses are further investigated in Figure 5.17a. From the hub onwards, the normalized cumulative loss is calculated. At 20% of the passage volume, which represents 20% of the integral passage volume starting from the hub radius and hence includes the hub boundary layer, accounts for 40% of all the generated loss for small amplitude-over-heights and decreases for higher amplitudes-over-heights to 30%. Additionally, 30% of loss is generated in the shroud for small amplitude bladeless turbine while this was 15% for higher A/h.

For higher amplitude bladeless turbine, around 55% of the irreversible entropy is generated in the core of the passage and is reduced to 30% for the low amplitude case. This increase is explained by the increased strength of the shocks for higher wavy surface amplitudes.
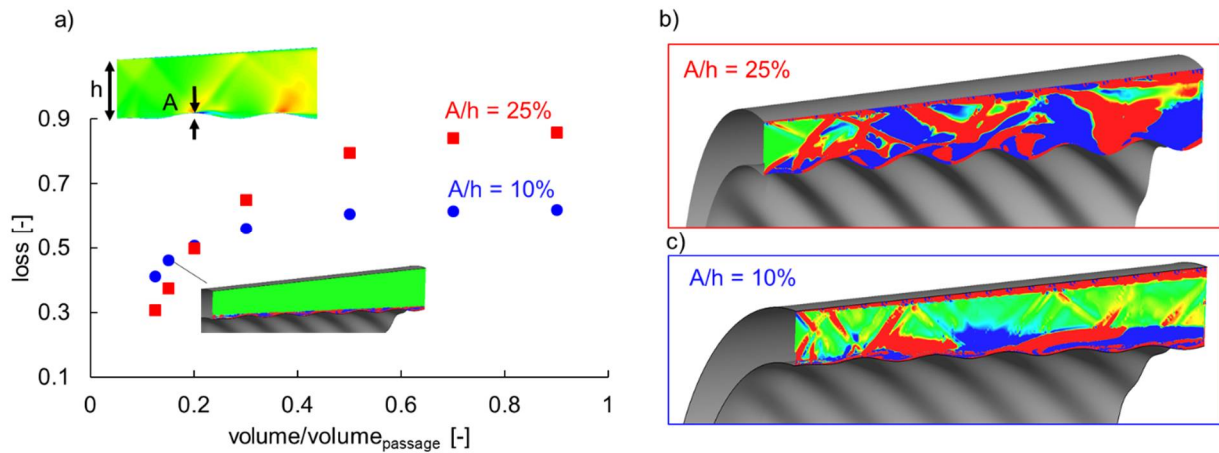
Figure 5.17 Irreversibility in the turbine a) dissection of the cumulative irreversibility according to the passage area b) local irreversibility for a turbine with A/h=25% and c) local irreversibility for a turbine with A/h=10%

The efficiency based on the irreversibility ('loss'), can be calculated as follows:

$$\eta_{irr} = \frac{P}{loss+P}$$

Eq. 5.8

Figure 5.18 plots the efficiency as a function of power for the baseline turbine, together with the associated uncertainties. All efficiencies predict similar trends and fall within the uncertainty of the measurements (defined in Section 4.4.2). Efficiency is lower in bladeless

turbines compared to conventional subsonic turbines because power is generated through shock waves which inherently have a higher entropy generation.
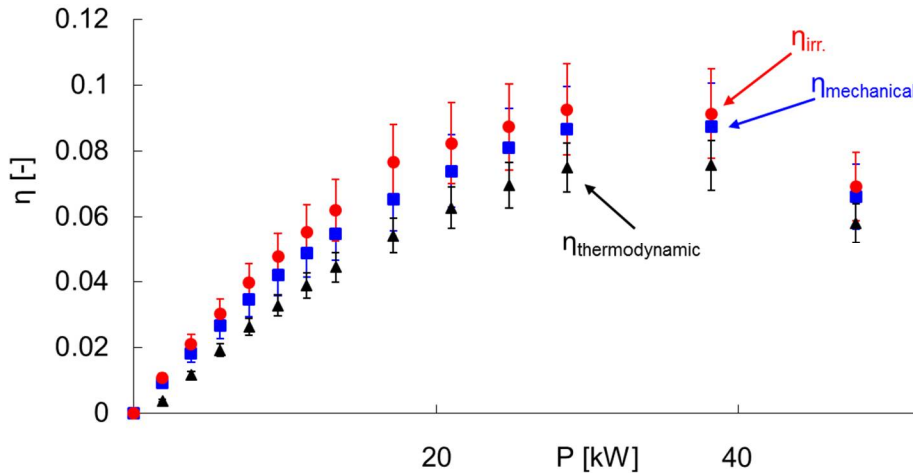
Figure 5.18 Power as a function of thermodynamic efficiency, mechanical efficiency and the efficiency based on the irreversibility

5.5   The bladeless turbine as bottoming/topping cycle for a nozzle/diffuser

It was proven that higher amplitudes give rise to higher power output and higher efficiency. This, however, only considers one function of the bladeless turbine, which is power generation. The bladeless turbine is unique in a sense that it can be a combined as a power device as well as an expansion device (supersonic nozzle or supersonic diffuser). This can be reasoned because the outlet flow angle is mostly axial (the actual degree of turning is less than 2.5 degrees, even for the highest amplitude bladeless turbine) and the bladeless turbine does not have blades within the flow field. This can represented as a bottoming cycle in the T-s diagram (Figure 5.19), in which the nozzle first expands the flow to the correct Mach number with associated total pressure drop to p_{02}, followed by the expansion through the bladeless turbine. Only the expansion from p_{02} to p_{03} should be accounted for in the efficiency evaluation if the turbine is used as a bottoming cycle.
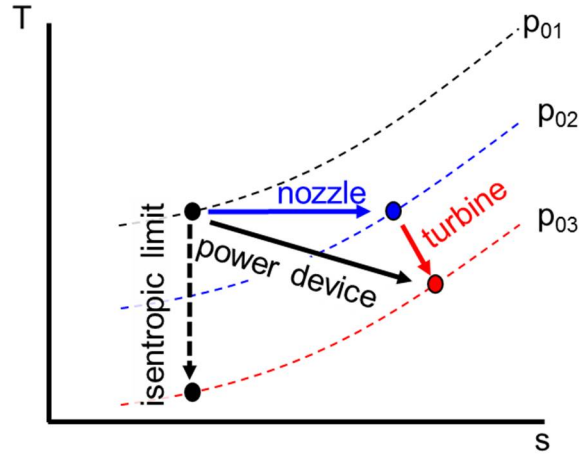
Figure 5.19 Black trajectory: conventional definition of the isentropic power extraction, blue and red path: bladeless turbine used as bottoming cycle

Hence, the different definitions are given in the following equations:

$$\eta_{\text{thermodynamic, power}} = \frac{T_{01} - T_{03}}{\left(T_{01} \left(1 - \left(\frac{p_{03}}{p_{01}}\right)^{\frac{\gamma-1}{\gamma}} \right) \right)} = \frac{1 - \frac{T_{03}}{T_{01}}}{\left(\left(1 - \left(\frac{p_{03}}{p_{01}}\right)^{\frac{\gamma-1}{\gamma}} \right) \right)} \qquad \text{Eq. 5.9}$$

$$\eta_{\text{thermodynamic, bottoming}} = \frac{1 - \frac{T_{03}}{T_{01}}}{\left(\left(1 - \left(\frac{p_{03}}{p_{02}}\right)^{\frac{\gamma-1}{\gamma}} \right) \right)}$$

Figure 5.20a depicts a conventional baseline nozzle, and Figure 5.20b integrates the nozzle bottomed by a bladeless turbine with the typical shock structure inherent to the bladeless turbine. Both nozzles accelerate the flow from a Mach number of 1.26 to 2.1 at the outlet. In Figure 5.20c, the cumulative power that was generated at each axial location is displayed, and a high increase within the first part of the turbine is observed similar to   Figure 5.7. Efficiency peaks at values of around 15% and then decreases towards 10% at the outlet. This decreasing trend arises because of the irreversibility generated during the acceleration in which no significant power is extracted. If the bladeless turbine is used as bottoming cycle to a nozzle, the pressure ratio due to the

acceleration should not be taken into account, and this is represented in the red dotted curve and a peak efficiency of almost 60% is found in the front part of the bladeless turbine which decreases to 20% in the aft-part.
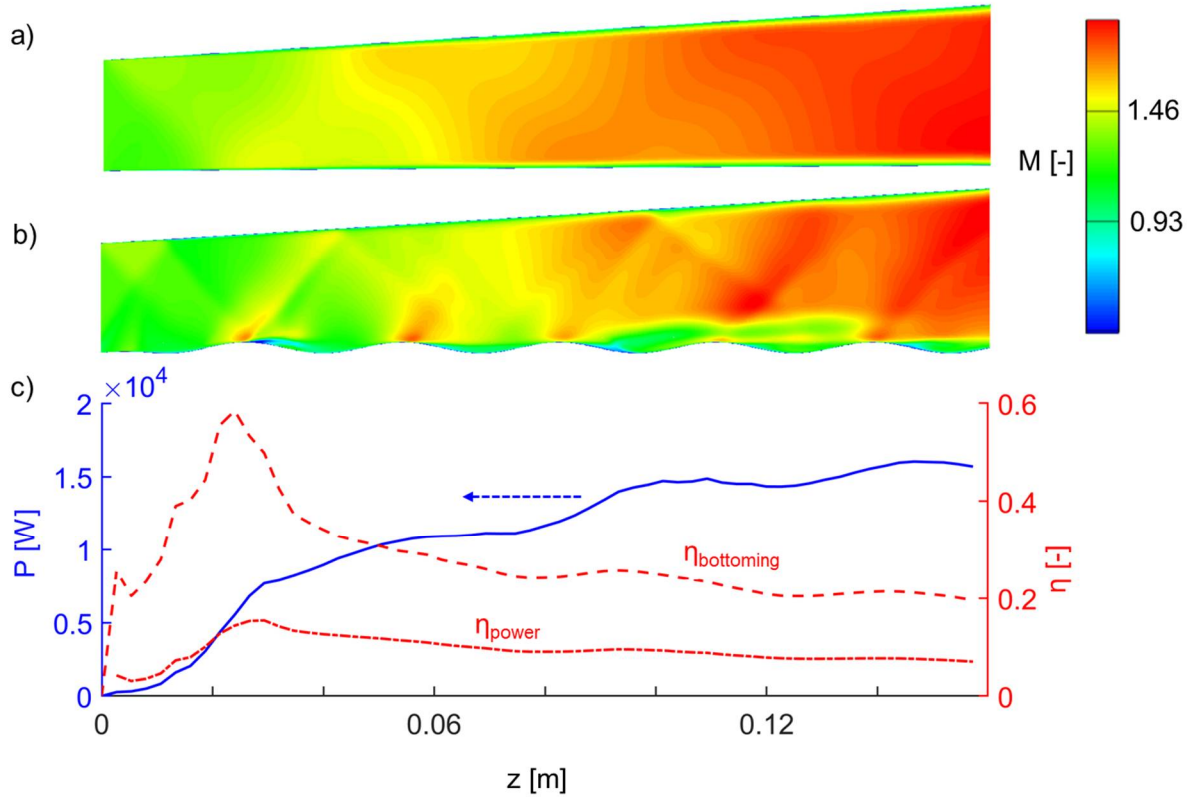
Figure 5.20 a) Baseline nozzle, b) bladeless turbine and c) power and efficiency along the axial length for a power extraction cycle and bottoming cycle

Figure 5.21a visualizes the thermodynamic efficiency of the bladeless turbine for several ratios of amplitudes-over-heights (A/h). For small A/h, the efficiency drops quickly over the axial distance, which could signify that the turbine has a large potential to be optimized to increase power extraction. For higher A/h the power efficiency peaks less (around 40%), however, the power extraction keeps being significant downstream in the bladeless turbine. Hence the efficiency at the outlet is still around 40% for higher amplitude turbines. Figure 5.21b shows the minima and maxima efficiency values found along the axial direction when the bladeless turbine is either used as a bottoming cycle or for power extraction. For low A/h, the efficiency has a wide band, however, decreases when A/h rises. For high A/h, $\eta_{bottoming}$ and η_{power} overlap. Conclusively, bladeless turbines lend themselves as suitable expansion devices in combination with a nozzle or diffuser.
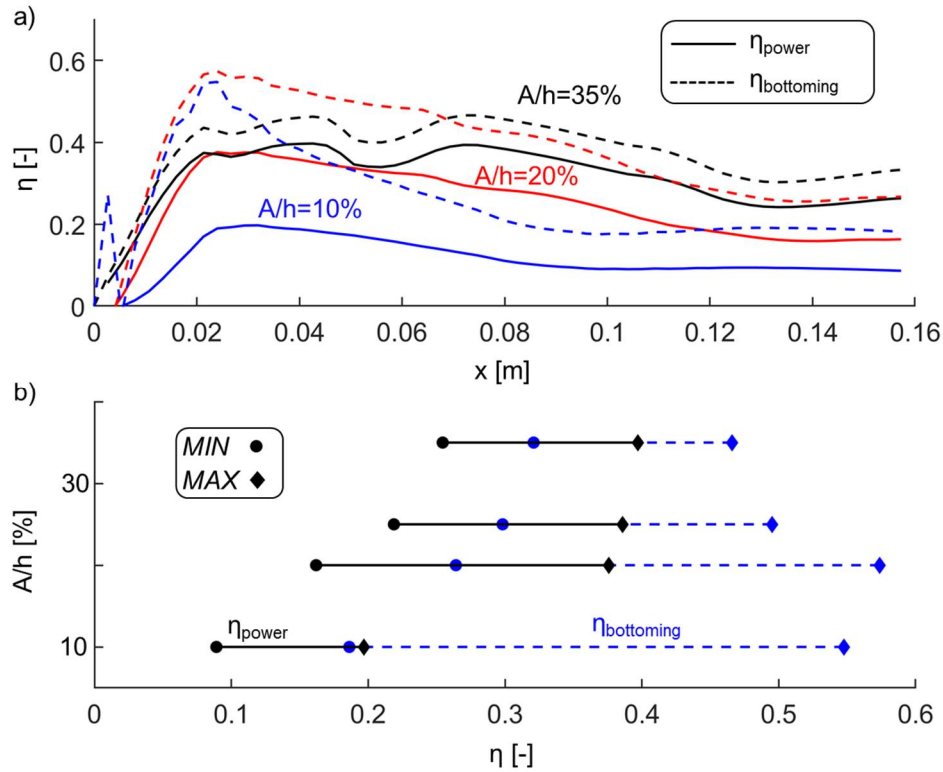
Figure 5.21 a) Efficiency for a bladeless turbine as bottoming cycle for several ratios of amplitude-over-height as a function of the axial length and b) efficiency range of $\eta_{bottoming}$ and η_{power} for several A/h

5.6 Shape optimization for bladeless turbines

The reason behind the optimization of the shape of the wavy surface is threefold:

1) Increase the pressure buildup at the onset of the wavy surface

2) Decrease heat flux levels on the hub

3) Decrease total pressure drop across the channel

The first step is a robust parametrization strategy. Figure 5.22a shows the parametrization of one isolated wavy contour. The wavy contour consists of a Piecewise Cubic Hermite Interpolating Polynomial ('pchip' in Matlab) with eight control points of which five are free to move in the normal direction. The last two points are fixed to guarantee continuity, which is necessary when the wavy contour is repeated, and results in a periodic wavy pattern. Additionally, the shroud can be parametrized by Bezier control points to ensure starting of the turbine and use the curvature of the shroud to control the shock reflection that could negatively interact with the

separation zone. Figure 5.22b illustrates a two-dimensional profile of a randomly generated wavy surface. This geometry has six identical wavy contours; however, the number of wavy contours could be a design parameter.
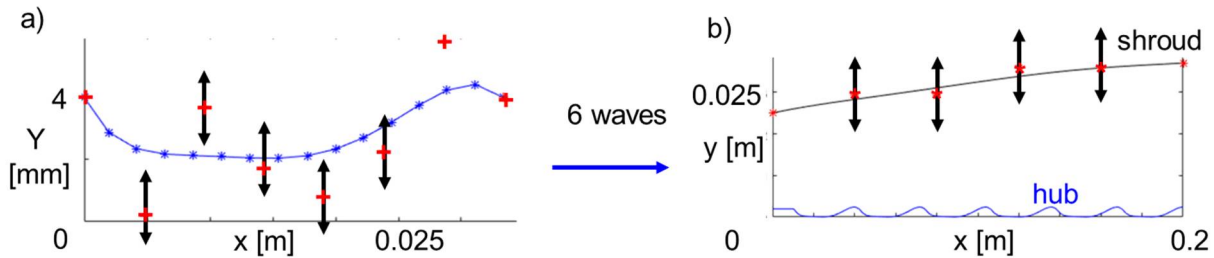
Figure 5.22 Parametrization for the multi-objective optimization: a) single wavy contour and b) the hub and the shroud of a randomly generated individual

Figure 5.23a outlines the optimization routine. The routine consists of the parametrization, followed by the meshing which is performed in Hexpress through a journal script and the solving step is performed in CFD++. The mesh contains around 130.000 numerical cells and y+ was ensured to be below 1. The hub and shroud are set as isothermal viscous walls and the outlet to supersonic conditions. At the inlet, a steady static pressure, temperature, and velocity were imposed. Post processing is completed in Tecplot & Matlab. Quantities that are extracted are pressure load, heat flux, pressure loss, the geometry, and a contour of the several flow quantities. To detect choking (the unstarting) of the channel, a script was implemented so that the individual would be discarded from the optimization. This script is based on the detection of subsonic flow near the inlet. The entire routine for a single individual requires approx. 45 minutes on Purdue's RICE supercomputer. The optimization is initialized by a Design of Experiments in which 65 geometries are generated through a fractional factorial approach [111] to maximize the variability in the design space. From those 65 geometries, 60 are selected to start the optimization. The objective is to maximize pressure force, minimize mass-flow averaged total pressure loss, and minimize integral heat flux on the hub.
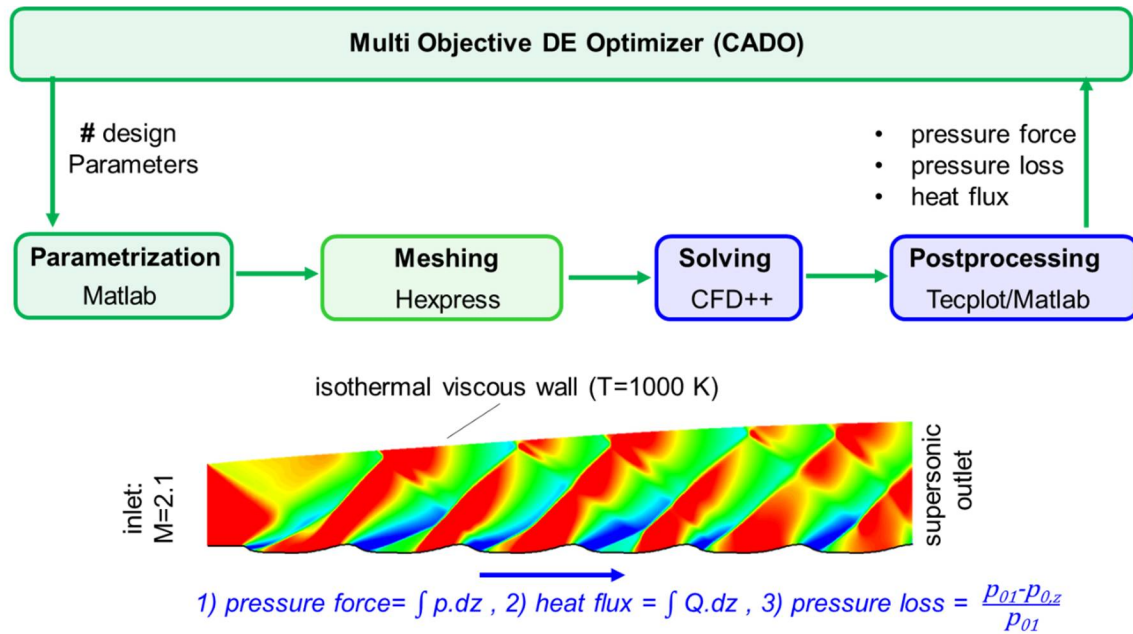
Figure 5.23 Optimization routine, boundary conditions, and objective functions

For the first optimization, a ratio of amplitude-over-height of 10% is considered. The optimizer can select lower values but is constrained by a maximum ratio. Additionally, the shroud is kept conical, to study the influence of the hub profile. To account for the three-dimensional effects within the bladeless turbine, only the first 50% of the two-dimensional model is considered for the pressure force and the total pressure loss. The length of the bladeless turbine was fixed as well as the number of waves. Figure 5.24 depicts the Pareto front as a function of pressure loss and pressure force for the small amplitude bladeless turbine for approx. 1100 individuals. The baseline has a pressure force of 485 N/m, and the mass-flow averaged total pressure loss at mid passage is 12%. Several optimized profiles are highlighted. Profile A is a low loss profile with a reduction of pressure loss of 8% points and a reduction of pressure force of 60%. Profile B has a similar pressure loss as the baseline case however has an increase of pressure force of 30% and profile C has an increase of pressure force of 60% at the expense of 4% points of total pressure loss. At the Pareto front, a quasi-linear relation between total pressure loss and pressure force exists.
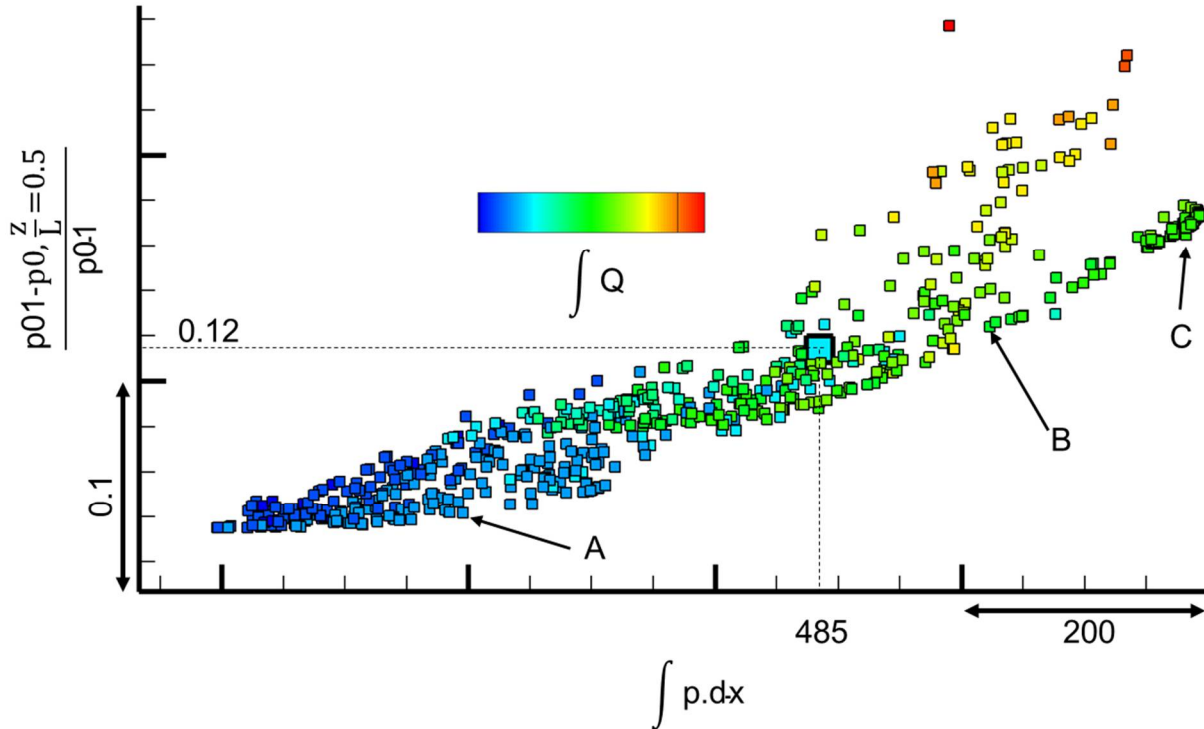
Figure 5.24 Pareto front as a function of pressure loss and pressure force for small amplitude bladeless turbines

The profiles are visualized in Figure 5.25. Profile A has a low amplitude with decreased pressure force and consequent pressure loss. Profile B is characterized by a steep compression wave and slow expansion fan. The steep compression results in high pressure forces. Additionally, a small recirculation bubble is found near the compression ramp of the third wavy contour. Profile C has a higher total pressure loss; however, the second wavy contour is characterized by a higher pressure force, due to a more aggressive curvature in the compression region. Interestingly, shock reflections impinge on the compression ramp.
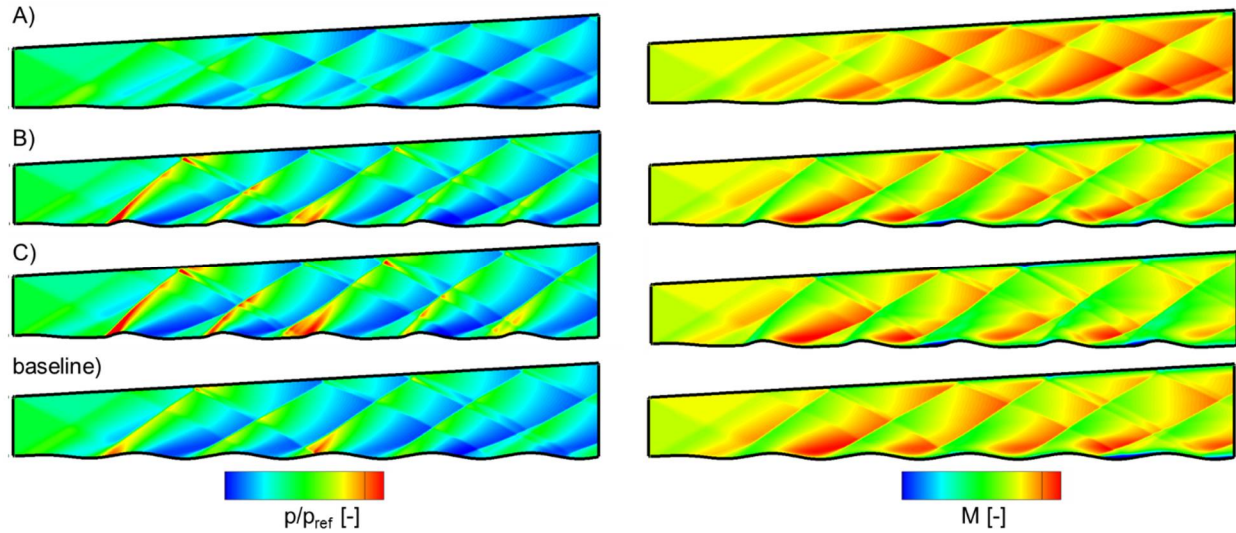
Figure 5.25 Optimal geometries from the Pareto front: left) pressure field and right) Mach number for several investigated profiles

Figure 5.26 depicts the Pareto front for two other parameters. In Figure 5.26a, the ratio of the amplitude-over-height (measured at the inlet) is analyzed. Amplitudes below 5% are found for low-pressure loss bladeless turbines, however, depending on the geometry, a large variety of optimal turbine geometries exist with an amplitude-over-height of around 10% (like the baseline case and geometries B and C). In Figure 5.26b, the viscous loss generated through the boundary layer is compared to the total loss (analogously to Section 5.4). For low power extraction with consequent less intense shocks, the viscous contribution rises to 60% of the total contribution. Interestingly, the baseline turbine is characterized by a high amount of inviscid (shock) losses compared to other individuals at the Pareto front, which might be indicative for a sub-optimal individual.
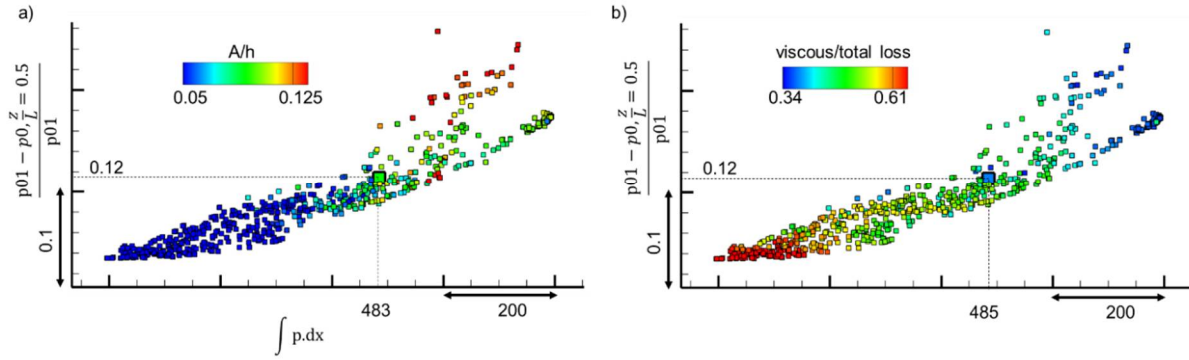
Figure 5.26 a) Pareto front colored by the maximum amplitude-over-height and b) Pareto front colored by the ratio of the viscous-over-total losses

The heat flux on the hub is plotted on Figure 5.27ab. Interestingly, the baseline (which has a sinusoidal shape) lies on the Pareto front for the heat flux and another individual "D" which has a similar heat flux but with an increase of power of 40%, is investigated. The wavy surface is similar; however, axially slightly shifted and hence the shock boundary layer impacts on the compression side of the third wavy surface. The total pressure loss of this individual is 1%point higher compared to the baseline. The mass-flow averaged Mach number is calculated (Figure 5.27b), and for higher pressure forces, Mach number at the exit decreased by around 0.5 for individuals with a high pressure force.
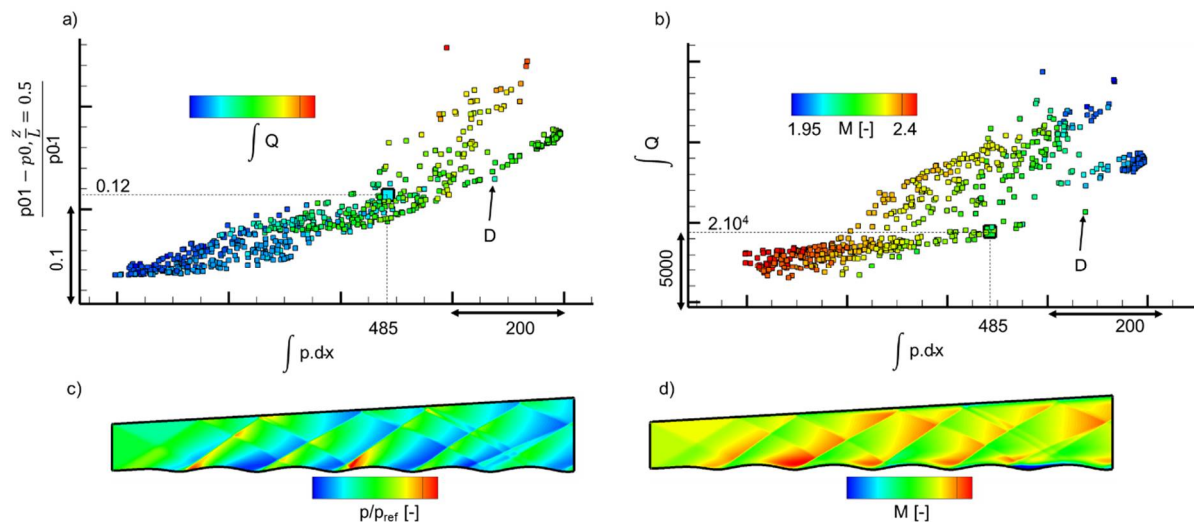
Figure 5.27 a) Pareto front as a function of the heat flux, b) heat flux as a function of pressure force colored by the outlet Mach number, c) pressure contour of an optimal geometry to minimize heat flux and d) Mach contour of an optimal geometry to minimize heat flux

Figure 5.28 represents the multi-objective optimization for higher amplitude bladeless turbines. A reference amplitude-over-height (A/h) of 20% was adopted for the baseline case. From the power versus the total pressure loss (Figure 5.28a), two individuals are investigated. Profile A has a pressure loss reduction of 14% and a pressure force increase of 109%. Profile B has a similar pressure loss than the baseline case; however, has a pressure force increase of 190%. From the heat flux, a profile with similar pressure force, but a decrease of heat flux by almost 35% was identified (profile C).
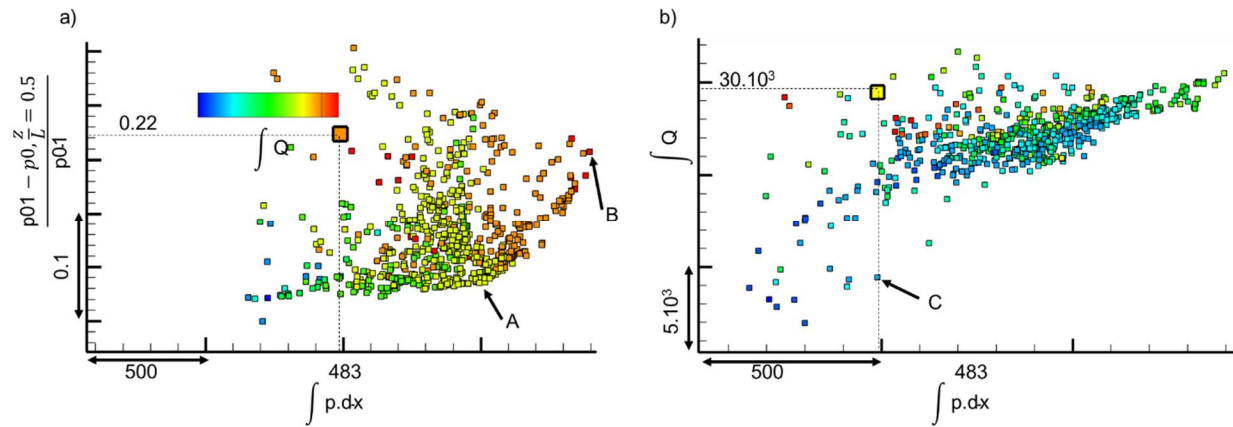
Figure 5.28 Optimization for a larger amplitude bladeless turbine: a) Pareto front as a function of pressure force and pressure loss and b) heat flux versus pressure force

Figure 5.29 depicts the investigated profiles for a higher amplitude-over-height (A/h) optimization. The baseline case exhibits separated flow in most of the expansion zones of the waves. The high-pressure force individuals are characterized by a steep curvature in the compression region as well as a recirculation in the front part of the wavy contour at the onset of the 'hill' (profiles A and B). Lower heat fluxes are obtained by elongating the expansion zone with less severe compression zones.

A)

B)

C)

baseline)

p/p$_{ref}$ [-]

M [-]
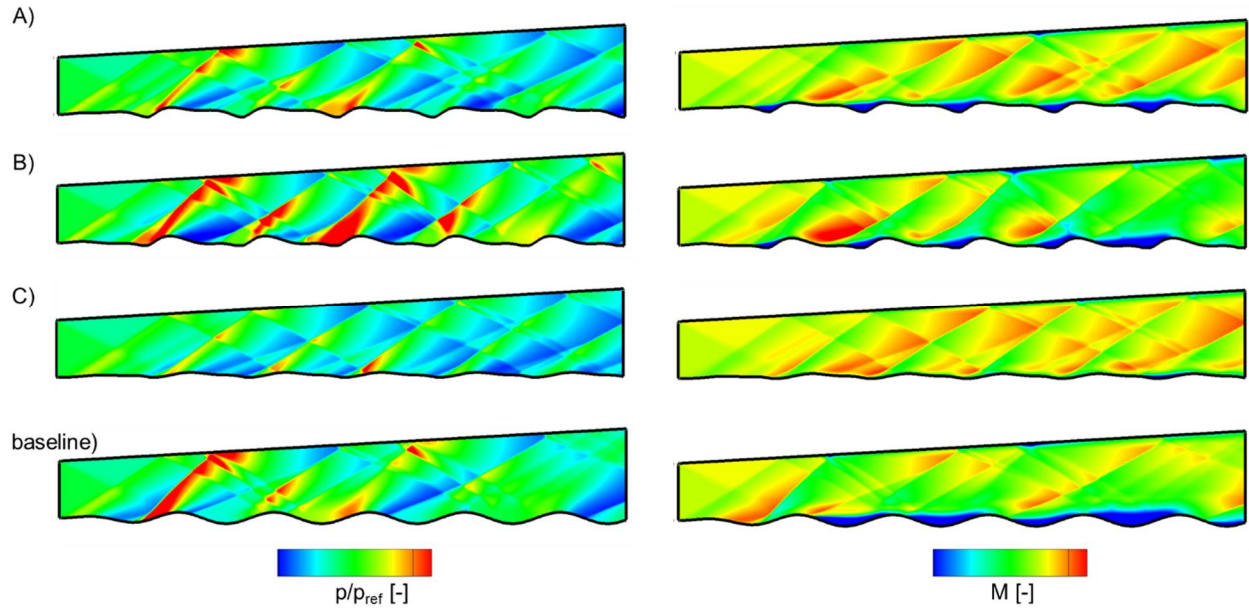
Figure 5.29 Investigated bladeless turbine geometries for the larger amplitude bladeless turbine for: A) maximum pressure force and minimum pressure loss, B) maximum pressure force, C) minimum heat flux, and the baseline. The pressure flow field is plotted on the left and Mach number on the right

5.7   Design guidelines for the bladeless turbine

To design the turbine, following inlet and outlet conditions can be given or are required and will impose limitations:

- **<u>Inlet conditions:</u>**
  - o Inlet flow angle

The inlet flow angle will set a requirement on the minimum helix angle required for power extraction

  - o Inlet total conditions / mass flow

The reduced mass flow will set the maximum amount of reduced torque that can be generated based on the geometrical design space

  - o Inlet Mach number

The inlet Mach number will set the maximum amplitude-over-height that needs to be respected within the turbine passage and will also set the maximum amount of reduced torque per unit axial length

  - o The rotational speed of the hub/shroud

The reduced speed is set by the total inlet temperature and RPM. This will set the limits in terms of power and efficiency as well as an optimal helix angle.

  - o Downstream static pressure

The downstream static pressure will set a limit to which the flow can be expanded, considering over-and-under expansion of the nozzle.

- **<u>Constraints</u>**
  - o Length and size of the component

Length and radius will determine the maximum amount of power and torque that can be generated

  - o Heat flux limitations

Heat flux limitations will constrain the maximum amplitude-over-height of the bladeless turbine

- **<u>Operating condition of the bladeless turbine</u>**
  - o Power extraction device

If the bladeless turbine is used as a power extraction device, the size of the bladeless turbine could be kept as short as possible and the maximum amplitude of the wavy surface is set by the area ratio and the Kantrowitz limit. The shroud can additionally be optimized to reach higher Mach numbers within the passage to increase the wavy surface amplitude-over-height ratio and possibly expel the flow at sonic speeds. Shorter lengths and higher amplitudes might yield higher efficiencies, however, local heat flux values increase with larger amplitude of the wavy surface. The minimum required helix angle is set by Figure 5.13.

o Bottoming/topping cycle

If the bladeless turbine is used as a bottoming cycle, the size is fixed by the nozzle requirements and the maximum amplitude is set by the Kantrowitz limit and power requirements. The shroud could be optimized to minimize pressure loss shapes, minimize either flow disturbance or heat flux signature. If low flow fluctuations are desired, separation regions (as well as shock-boundary layer interactions) should be avoided, and hence, a design with fewer wavy contours (W) along the axial directions can be selected.

CHAPTER 6. OPERATION OF THE BLADELESS TURBINE WITH ROTATING SHOCKS

6.1 Characteristics to generate a generic oblique shock wave

In this chapter, the canonical test case of a rotating shock propagating through the bladeless turbine channel is investigated. Figure 6.1 shows a typical set of transient boundary conditions to generate the rotating shock at one timestep. Figure 6.1a plots the static pressure with a pressure wave moving from left to right. The ratio of the maximum pressure over the mass-flow averaged value is around 4, while the ratio of the minimum pressure to the mass-flow averaged value is 0.45, and the maximum pressure over the minimum pressure is 8.7. For scaling purposes, the latter characteristic non-dimensional pressure ratio was chosen to represent rotating shocks:

$$\varPi_{\text{SHOCK,nom}} = \frac{p_{\text{max}}}{p_{\text{min}}} \sim 8.7 \qquad\qquad \text{Eq. 6.1}$$

The second graph displays the Mach number. Tangentially upstream of the shock, the Mach number reaches 1.6 and decreases to values around the transonic range. The mass-flow averaged Mach number is around 1.25. The flow angle (depicted in Figure 6.1c) ranges from -60 tangentially downstream of the shock to 40 degrees tangentially upstream of the shock.

To achieve an unsteady rotating oblique shock, the oblique shock relation in the relative frame of reference needs to be respected, and this relates the shock angle (s) to the upstream Mach number $M_{\text{relative flow,upstream}}$ in the relative frame of reference of the shock as well as the pressure ratio across the shock:

$$\Pi_{\text{SHOCK}}{}^{-1} = \frac{2\gamma M_{\text{relative flow, upstream}}^{2} \sin^{2}(s) - (\gamma - 1)}{(\gamma + 1)} \qquad\qquad \text{Eq. 6.2}$$

The steady shock angle can be defined by a shock ratio and initial flow components in the relative frame of reference. If one applies a rotation of the absolute flow components, a rotating oblique shock can be achieved. E.g. to achieve a rotating oblique shock with a shock angle of 54 degrees [112], a relative Mach number of approx. 3.4 needs to set upstream of the shock. If one

respects the boundary conditions of Figure 6.1abc, this corresponds to a rotation of the components with a speed equal to 1900 m/s.

All critical characteristics that define the generic description of a rotating oblique shock throughout a passage are:

$$s = f(M_{flow,\,upstream}, \Pi_{SHOCK}, \alpha_{flow,\,upstream}, M_{shock}, L_{period})$$

<div align="right">Eq. 6.3</div>

M_{shock} defines the speed at which the boundary conditions need to be rotated and is referred to as the mechanical Mach number of the shock, and L_{period} is the tangential length over which one period of the oblique shock extends.
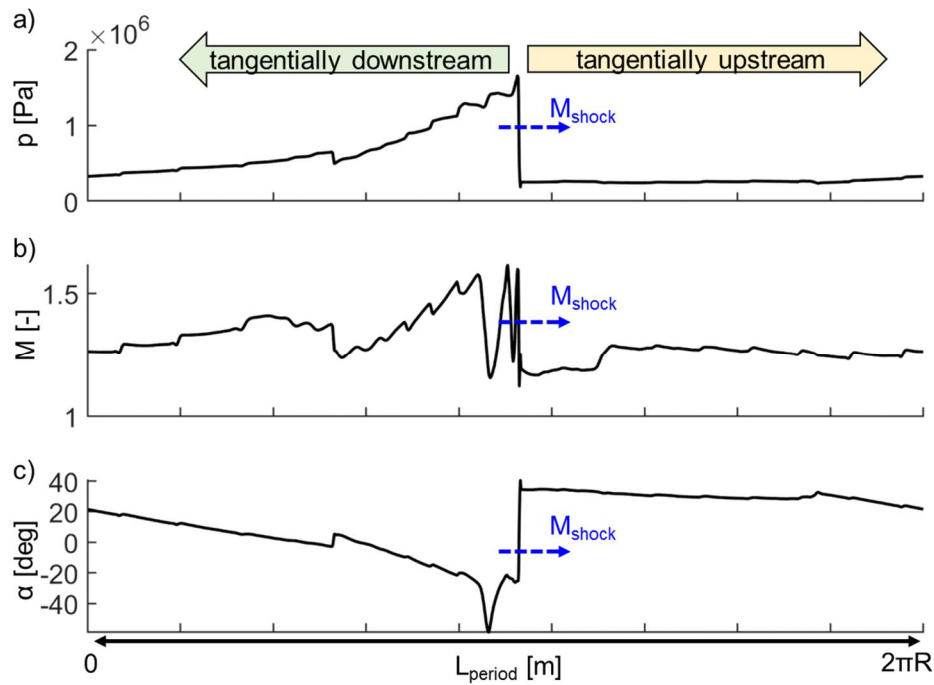
Figure 6.1 Boundary conditions for the canonical test case of a rotating shock: a) static pressure, b) Mach number and c) flow angle variation

6.2 Computational setup

The computational mesh for this unsteady simulation is depicted in Figure 6.2a. The entire bladeless turbine passage is modeled to quantify the transient behavior with a total mesh count of

around 32 million grid cells. The timestep is 1.18 microseconds with at least an inner convergence of 0.1 orders of magnitude per timestep. Figure 6.2b shows the pressure contour of a clockwise running oblique shock wave. The simulated oblique shock angle was around 58 deg. on the shroud and 70 degrees on the hub. Figure 6.2c illustrates the instantaneous streamlines tangentially upstream and tangentially downstream of the shock. The streamlines tangentially upstream of the shock (in the low-pressure region) have a similar orientation than the oblique shock angle. However, the flow angle tangentially downstream of the shock is opposed to the shock angle. The knowledge of the flow angle is important because it strongly affects power extraction, as proven in Section 5.3.3. Additionally, the relationship between the Mach number of the shock wave, Mach number of the flow and pressure ratio across the shock are related to the oblique shock angle by Eq. 6.3.
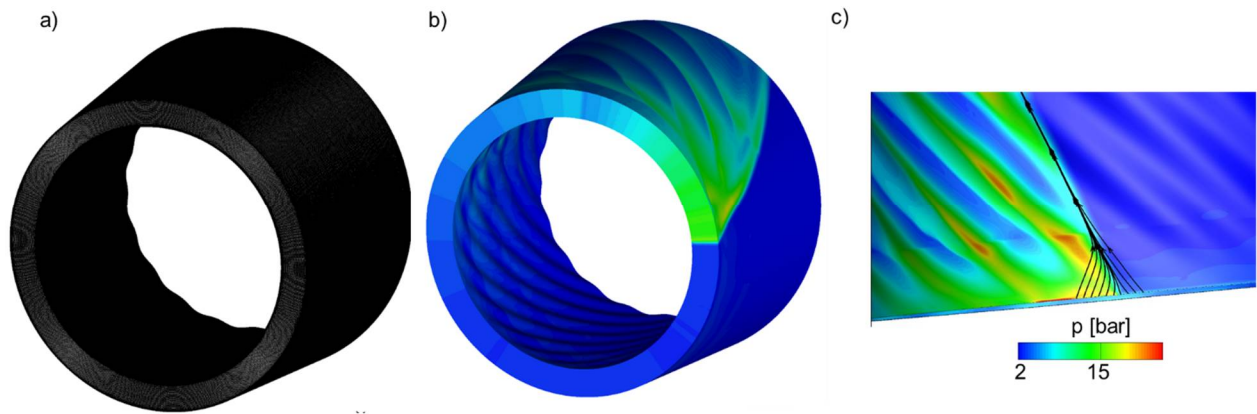
Figure 6.2 a) Mesh for the unsteady simulation, b) pressure signature at one timestep and c) zoom on the shock zone with instantaneous streamlines in the absolute frame of reference

6.3 Aerodynamic assessment at a single operational point

6.3.1 Operational envelope

In addition to the operational envelope for steady supersonic inflow, new scenarios occur for unsteady flows. For power extraction in the bladeless turbine, the helix angle was required to be positive compared to the relative motion the hub (Figure 5.2). For a rotating oblique shock, the helix angle can either be negative or positive compared to the shock wave. Figure 6.3 plots three different scenarios in which the hub rotation has the same orientation as the oblique shock angle. Figure 6.3a details the flow field in which the shock angle is opposite to the helix angle, and no

power extraction was achieved. In Figure 6.3b, the helix angle is around 0 and is without power extraction. At positive helix angles, however (Figure 6.3c), power extraction was achieved.
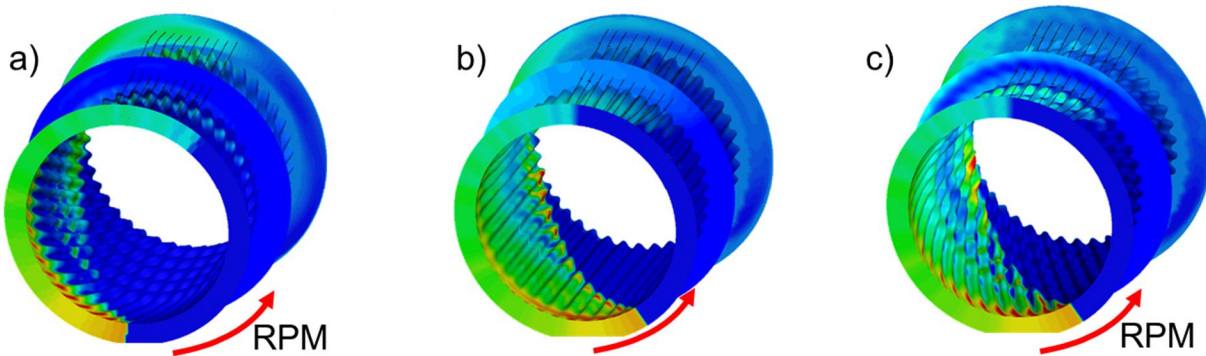
Figure 6.3 Influence of the helix angle for three different scenarios

Four possible scenarios describe the complete envelope of the bladeless turbine for unsteady rotating shocks. The oblique shock rotates either clockwise or counterclockwise compared to the hub, and the direction of the helix angle can be either positive or negative for each situation. Figure 6.4 depicts the regions in which positive power extraction was obtained. The first mode is the 'oblique shock' mode, in which the oblique shock angle has the same orientation as the helix angle and the RPM. To achieve positive power extraction, the helix angle needs to be positive compared to the hub rotation (hence turning in the same direction of the shock wave). The other power extraction mode is the 'reversed mode'. In this mode, the oblique shock is reversed to the helix angle, and the only possibility to generate power is to rotate the hub against the direction of the shock (maintain positive helix angles). Hence power extraction can only occur when the helix angle and the rotation of the hub have the same orientation. For the two other scenarios (at negative helix angles compared to the RPM) energy is added into the system and is called 'stirring or mixing' as overall a total pressure loss was still observed.
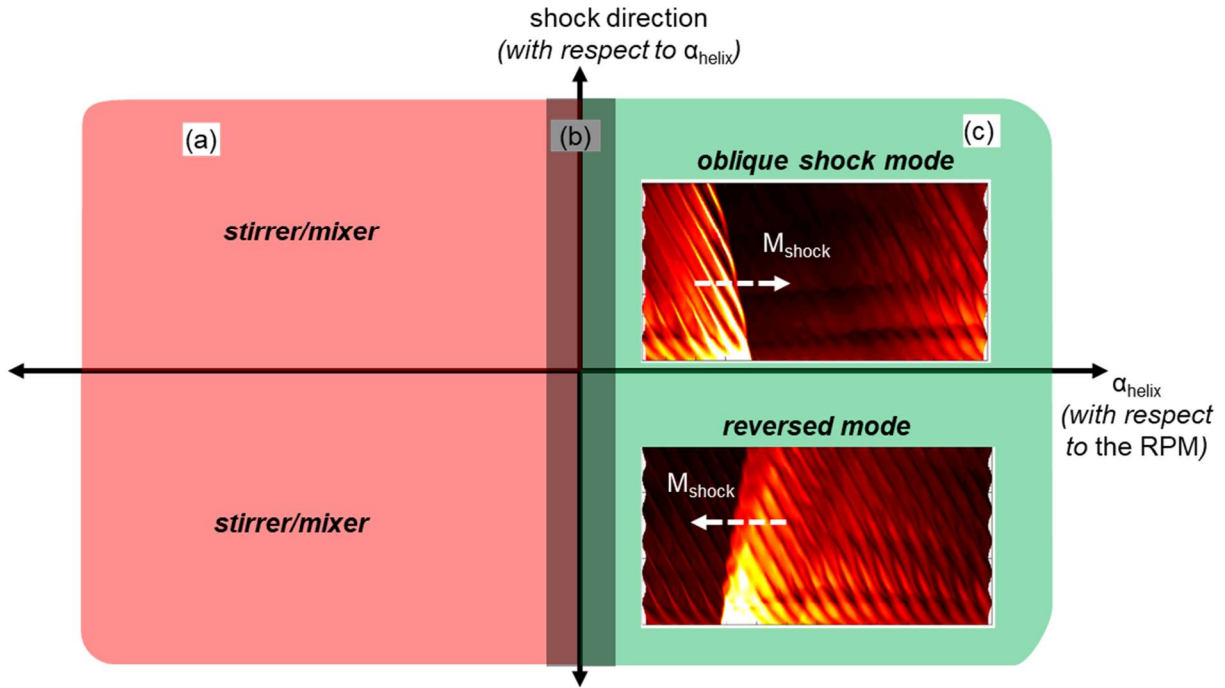
Figure 6.4 Operational envelope of the bladeless turbine exposed to rotating shocks

6.3.2 Oblique shock mode

First, the oblique shock mode is analyzed. In Figure 6.5a and Figure 6.5d, the pressure flow field for the unwrapped bladeless turbine is displayed for two timesteps. During the passing of the transient oblique shock wave, the pressure ratio across the shock on the hub was ~8. The maximum hub pressure is 140% higher compared to the maximum inlet static pressure due to the compression at the onset of the wavy contour. Additionally, smaller increase and decrease of pressure are observed tangentially downstream of the oblique shock at a constant axial length with consequent power extraction. The pressure contour of the unwrapped bladeless turbine also reveals regions in which the pressure is almost constant along the tangential direction, hence without the possibility to locally extract power.
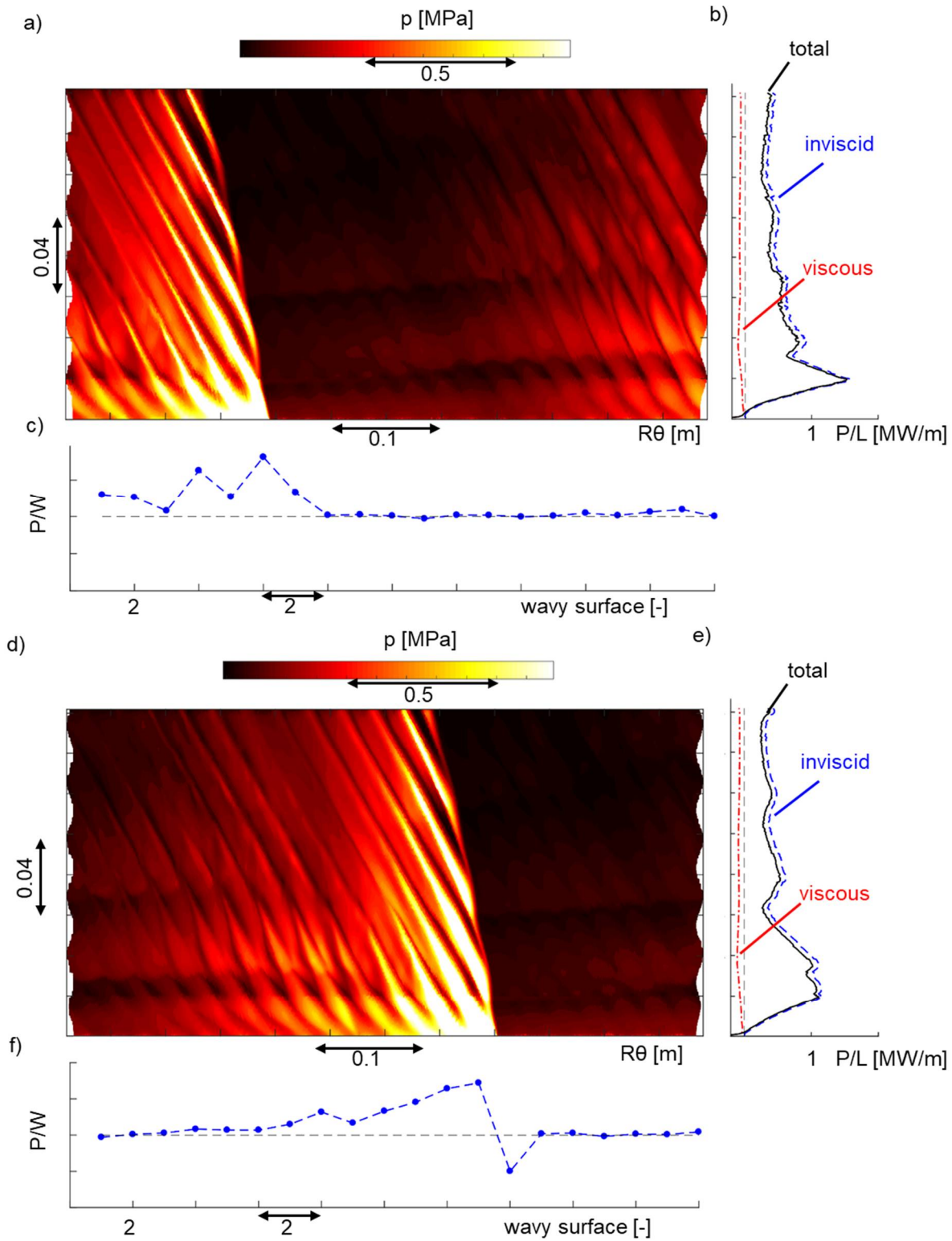
Figure 6.5 Oblique shock mode operation: a) hub pressure contour for t=1/3 t_{period}, b) average power extraction along the axial direction, c) power extraction per wave at z/L=6%, d) hub pressure contour (t=2/3t_{period}), e) P/L (t=2/3t_{period}) and f) power extraction per wave (t=2/3t_{period})

Figure 6.5b and Figure 6.5e show the average power extraction along the axial direction. The viscous contribution is steady across the axial direction, and the viscous-to-total contribution accounts for 16%, whereas the steady simulation predicted 30%. This decrease is due to the flow angle distribution: for a large region, the viscous shear stress is not opposed to the hub motion and hence will not counteract the power. The unsteady pressure fluctuations are limited, and the P/L has a similar magnitude as a bladeless turbine in steady operation in the front part. In the aft part of the turbine, however, the power per unit length remains high in contrast to the bladeless turbine with steady inflow in which the power decreases to zero at some axial locations. This could be because the oblique shock keeps generating large pressure gradients in the aft part across multiple wavy contours, and consequently, the power extraction is kept high. Figure 6.5c and Figure 6.5f depict the local power generation per wave at a location of z/L=6% downstream of the inlet. This is a quantitative measure to analyze on which wavy contour power extraction occurs. In Figure 6.5c, the position of the oblique shock is between wavy contour 6 and 8, and hence the power extraction in those regions is highest. Upstream of the wave, the power extraction is negative, and all these zones do not participate in the power extraction. In Figure 6.5f, the oblique shock reached wavy contour 13 and power extraction is now locally highest in those regions, with zero power extraction after wavy contour 13.

These features arise because of the instantaneous streamlines and the flow angle. The steady analysis prove that power extraction was only possible in regions where γ was positive and higher than a certain threshold (Section 5.3.3) which also depends on the RPM. Hence, α_{flow} cannot decrease below ~30 degrees to avoid acting as a mixer. This is confirmed by calculating the inlet γ angle (Figure 6.6): the maximum angle occurs right downstream of the shock with maximum values from 60 to 90 degrees. The minimum angle is 2 degrees and is below the requirements to achieve torque and a large section of the bladeless turbine will thus not actively participate in the power extraction and can locally even act as a mixer.
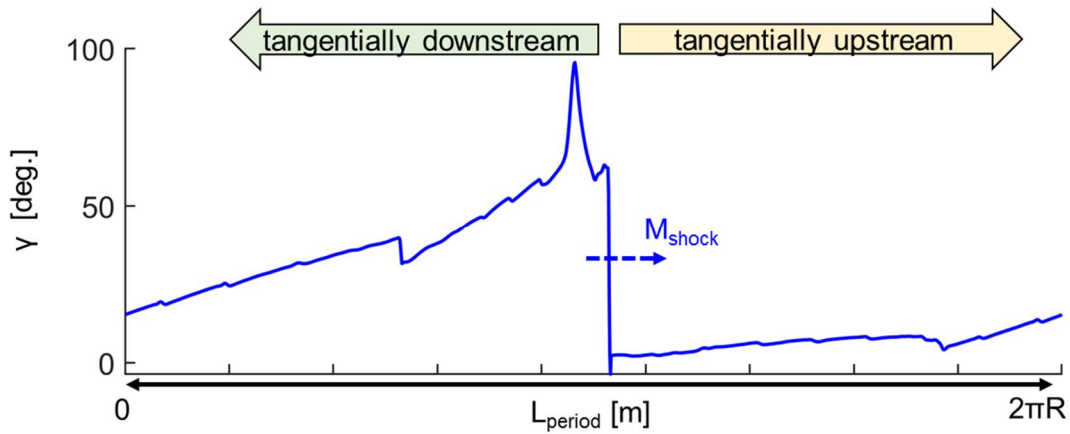
Figure 6.6: γ angle at the inlet of the bladeless turbine at one time instant for the oblique shock mode

Figure 6.7 depicts the instantaneous flow field colored by the Mach contour and the hub colored by pressure during the transient passage of the shock. The time step between shots is 2.4 microseconds. Before the passage of the shock, the flow streamlines have a similar inclination as the helix angle, hence no power is possible. The Mach contours visualize some shock structures as well as reflections that appear and a flow acceleration from around transonic at the inlet towards Mach 2 near the exit due growth in area ratio. Upon the passing of the shock that travels from inlet to outlet, strong local acceleration and deceleration patterns are formed because of the strong negative flow angles over the wavy surface geometry. This leads to a locally high power generation. On the 5th frame, no separation shock is seen after the second wavy contour (region highlighted by the arrow), however after some microseconds (frame 7 and 8), a local small separation bubble is formed with a consequent downstream pressure rise that reaches the upstream acceleration zone and results in the formation of a separation shock that slightly moves upstream.
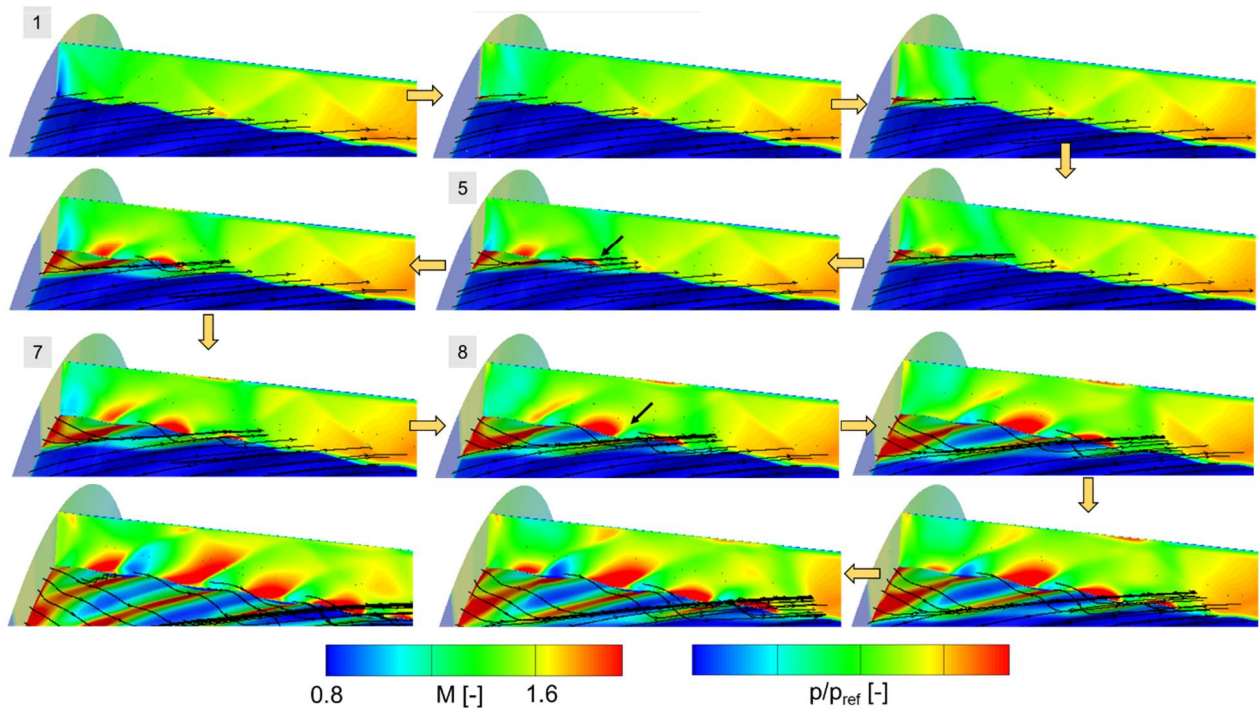
Figure 6.7 Pressure contour of the hub and Mach contour of the flow field at the passage of the oblique shock

This effect is also highlighted in Figure 6.8 by investigating the local tangential shear stress on the hub and with the main passage flow now colored by the static pressure. Only after a few microseconds, the separation zone becomes visible (a dark blue region on the hub) on the second wavy contour. At the first time instants, however, the flow remains attached, which might instantaneously enhance power extraction. As the shock travels further away, the pressure reduces, and flow angle keeps increasing with a reduction in separation regions because of the alignment of the flow with the orientation of the helix angle.
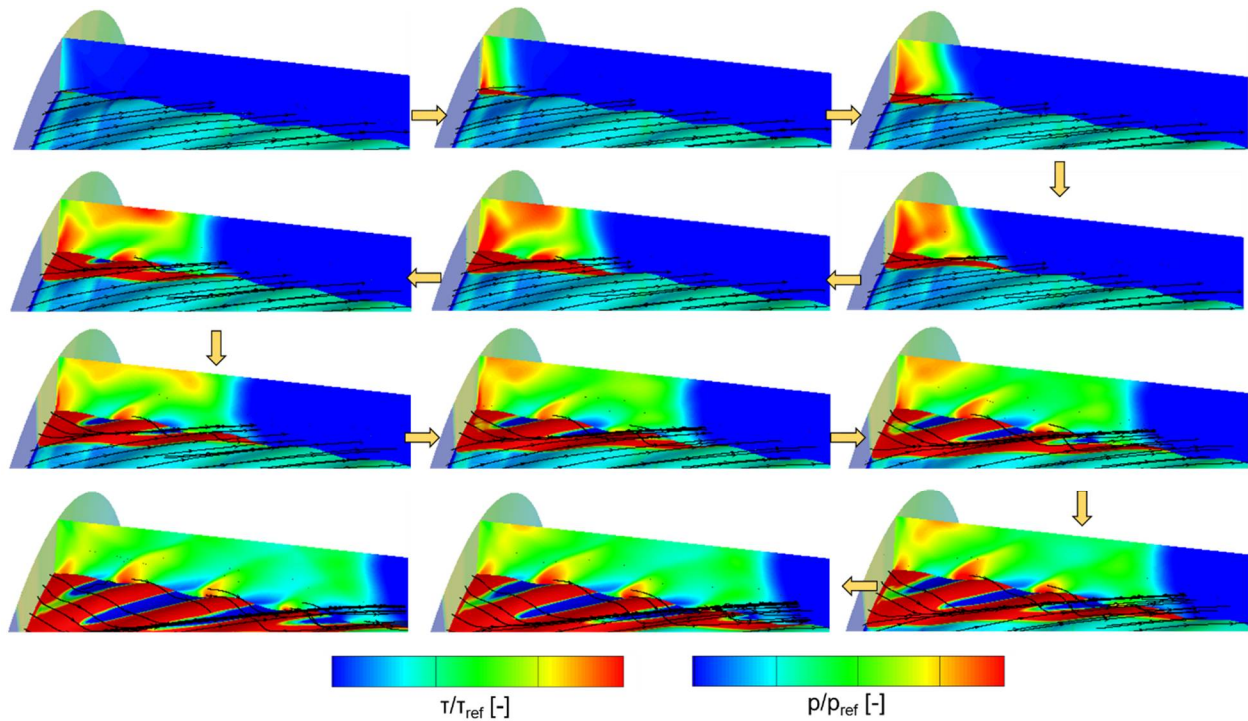
Figure 6.8 Flow field colored by static pressure and hub colored by skin friction contour at the passage of the oblique shock

6.3.3 Reversed mode

The pressure signature on the hub for a bladeless turbine in reversed mode is plotted in Figure 6.9a. The unsteady shock rotates opposite to the direction of the helix angle and the hub rotation. In contrast to the oblique shock mode, the hub pressure tangentially downstream of the shock does not exhibit peaks and valleys. Instead, tangentially upstream of the shock, zones of acceleration and deceleration are observed. In Figure 6.9b, the different contributions to the power along the axial position are calculated, and similar features as in the oblique shock mode appear (highest P/L in the front part and no negative P/L in the aft part of the turbine). Interestingly, Figure 6.9c features the power extraction per wave at one axial location and in contrast to the oblique shock mode, power extraction occurs in all waves except for the location where the oblique shock impacts on the hub. The mean power extraction is constant over a wide range of waves, indicating that torque is generated over a large tangential interval.
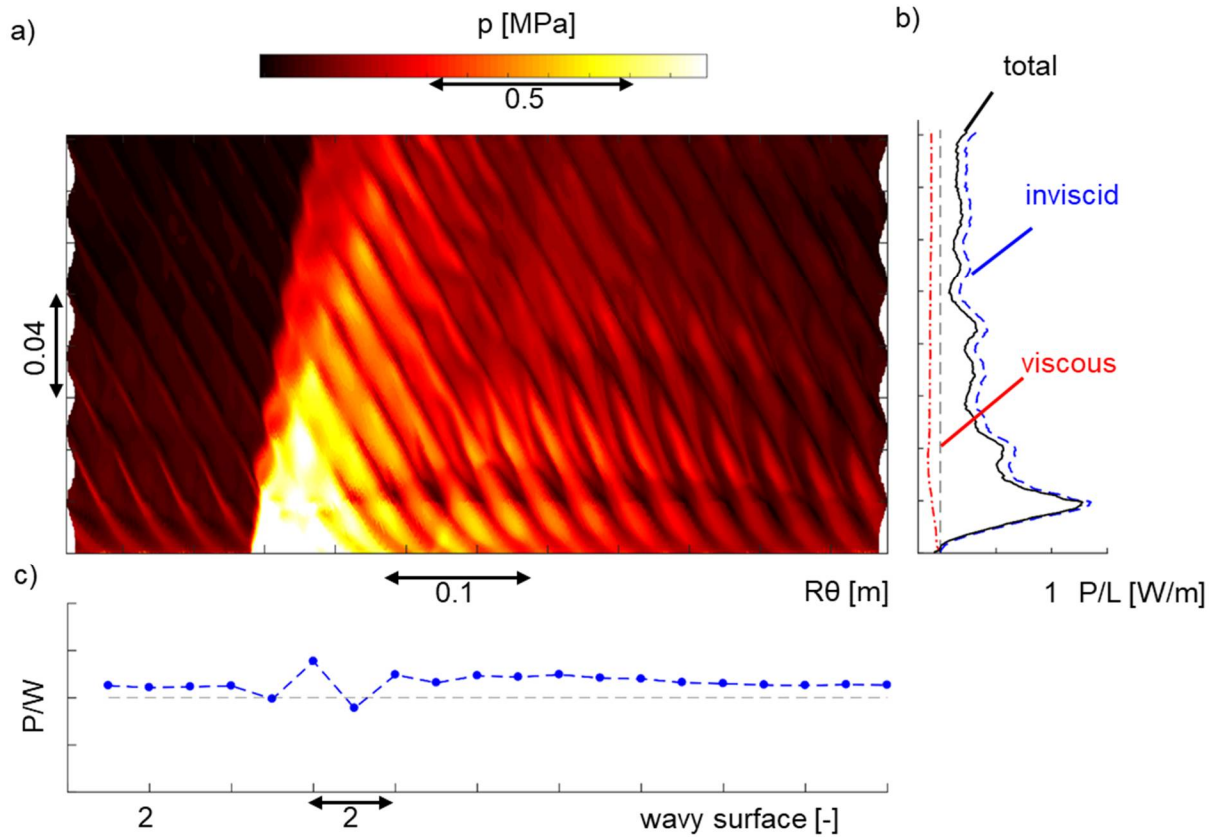
Figure 6.9 Reversed mode: a) hub pressure contour, b) P/L and c) power per wave at z/L=6%

This phenomenon can be related to the inlet γ angle (Figure 6.10). Directly downstream of the shock, values below -20 degrees are found, indicating that locally this bladeless turbine will act as a mixer. Tangentially upstream of the oblique shock; however, a wide area of higher γ angle is retrieved.
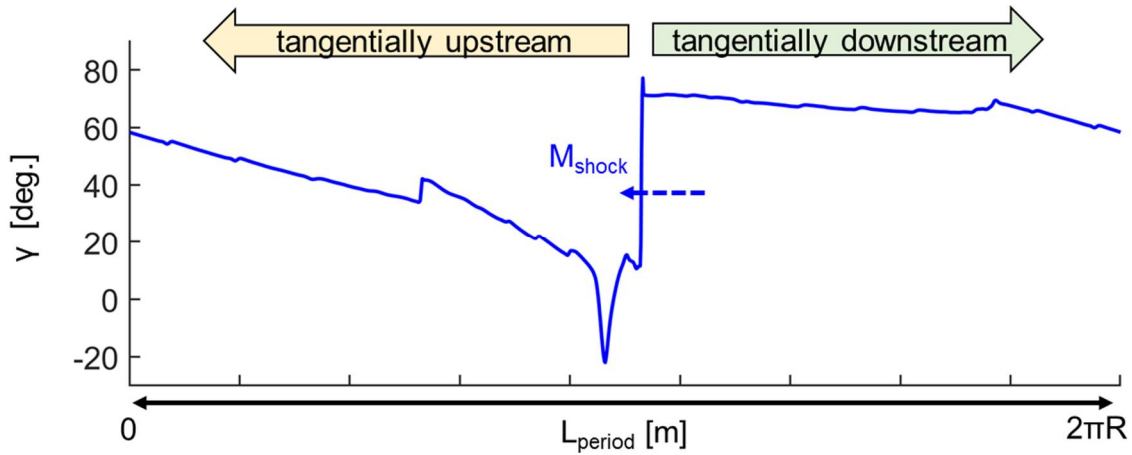
Figure 6.10: γ angle at the inlet of the bladeless turbine for one period of the reversed mode

Figure 6.11 summarizes the differences between the oblique mode, the reversed mode, and the steady-state simulation with the same mass-flow averaged total pressure and total temperature as the rotating shock. Figure 6.11a compares the local averaged power extraction as a function of the axial location and both the reversed as the oblique mode do not advertise a large oscillatory behavior in the aft part because the shock perpetually sweeps and excites the downstream wavy contours. Additionally, the contribution of the skin friction in the oblique shock case is reduced compared to both the steady and reversed mode. In Figure 6.11b the contributions are summed along the axial direction and both for the steady case and the reversed mode, the shear stress contribution is around 30% while this is only 16% for the oblique shock mode. This effect is similar to when decreasing the flow angle for negative swirls: the negative viscous contribution decreases, and the viscous forces could even contribute to the power extraction in the regions of negative flow angle. Figure 6.11c depicts the pressure profile along the tangential direction for the three simulations at a location z/L=6%. For the oblique shock simulation, a region of a periodic high- and low-pressure is seen tangentially downstream of the shock, while this is opposite for the reversed mode, for which this phenomenon mostly appears in the low-pressure region tangentially upstream of the oblique shock. For the steady simulation, the entire tangential span has a similar acceleration and deceleration pattern. Figure 6.11d plots the pressure profile axially downstream, at a location z/L=68%. At this axial location, local power extraction is almost zero for the steady simulation because most of the flow is locally separated from the core flow motion (which is axial). In the oblique shock mode and the reversed mode, however, the cyclic pressure oscillations which

generate torque are still visible, confirming the earlier observation, that the power extraction for this geometry is increased in the aft part of the turbine when a shock periodically sweeps the hub surface.
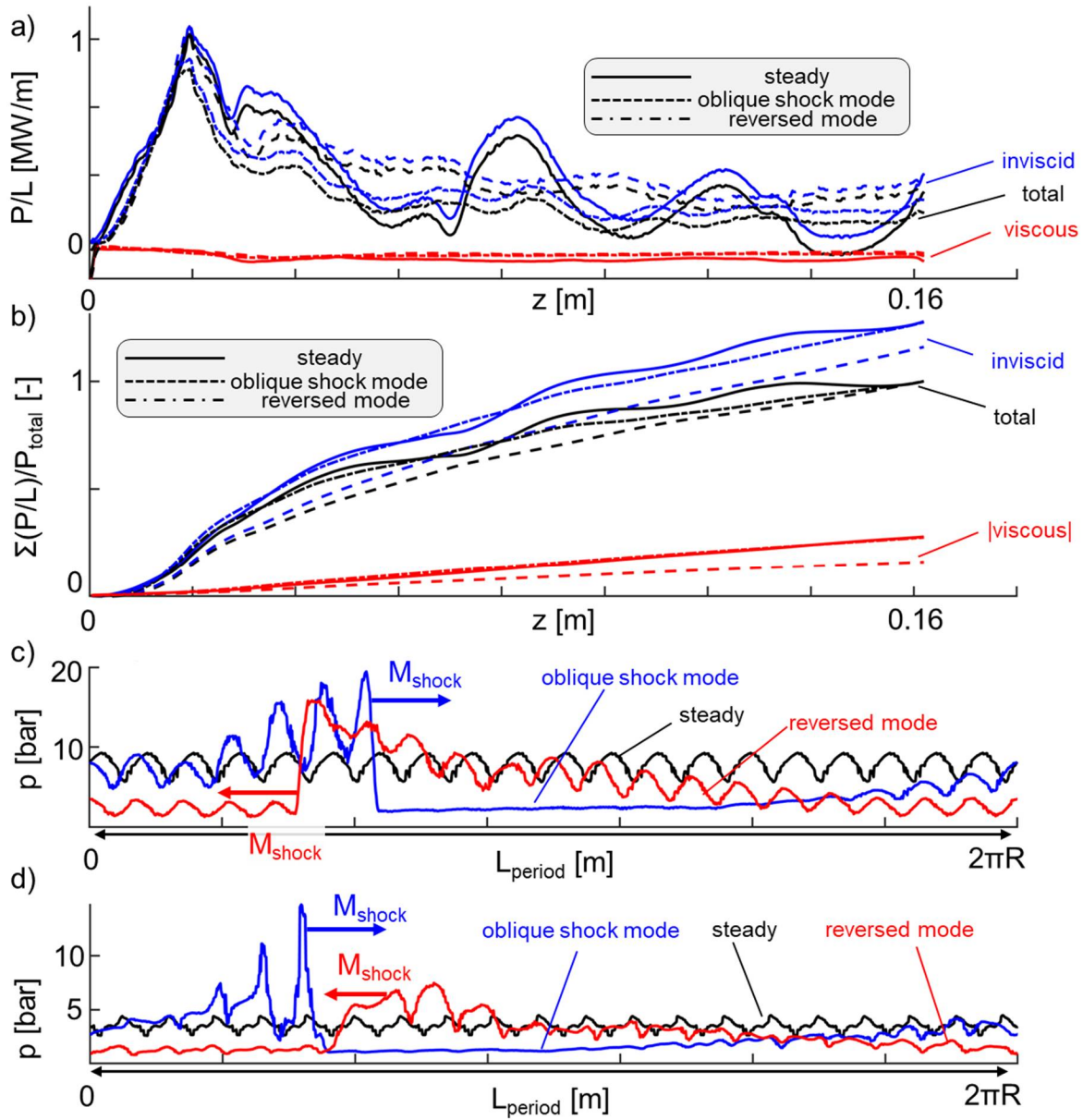
Figure 6.11 Comparison of the oblique shock mode, reversed mode and steady-state simulation on: a) local power extraction, b) cumulative power extraction, c) hub pressure at z/L=6% and d) hub pressure at z/L=68%

6.4   Parametrization and characterization of the shock parameters

Three critical parameters that define the rotating shock are now investigated. Figure 6.12a shows power as a function of several shock speeds (M_{shock}). The nominal shock speed was obtained with the boundary conditions from Figure 6.1 and was around 2.5 based on the temperature tangentially upstream of the shock. By doubling the shock speed, a slight increase in power was observed (3%), and by decreasing the shock speed, the power decreased by 6%. The mass-flow averaged steady value is plotted as a black diamond, and the oblique shock mode delivers approx. 20% more power compared to the steady simulation, whereas the reversed mode delivers 22% less power than the steady simulation. In reversed mode, the power extraction is about 35% smaller compared to the oblique shock mode. The power increases once the wave speed slows down in reversed mode, while this is opposite for the oblique shock mode and both tend to an asymptotic value for higher wave speeds. In theory the oblique shock mode and reversed mode should converge to the same power at 0 wave speed, however this solution is not stable without altering the flow components in the absolute frame of reference. In terms of mass-flow averaged total pressure loss (Figure 6.12b) both the reversed mode and oblique shock mode have an increase of total pressure loss by a factor 3.5 compared to the steady-state simulation because of the nature of the oblique shock. The time-averaged of mass-flow averaged total pressure loss for the oblique shock mode was 32% and 28% for the reversed mode. Conclusively, the oblique shock mode delivers higher power at a higher efficiency than the reversed mode and by reducing the speed of the shock, total pressure losses were lowered.
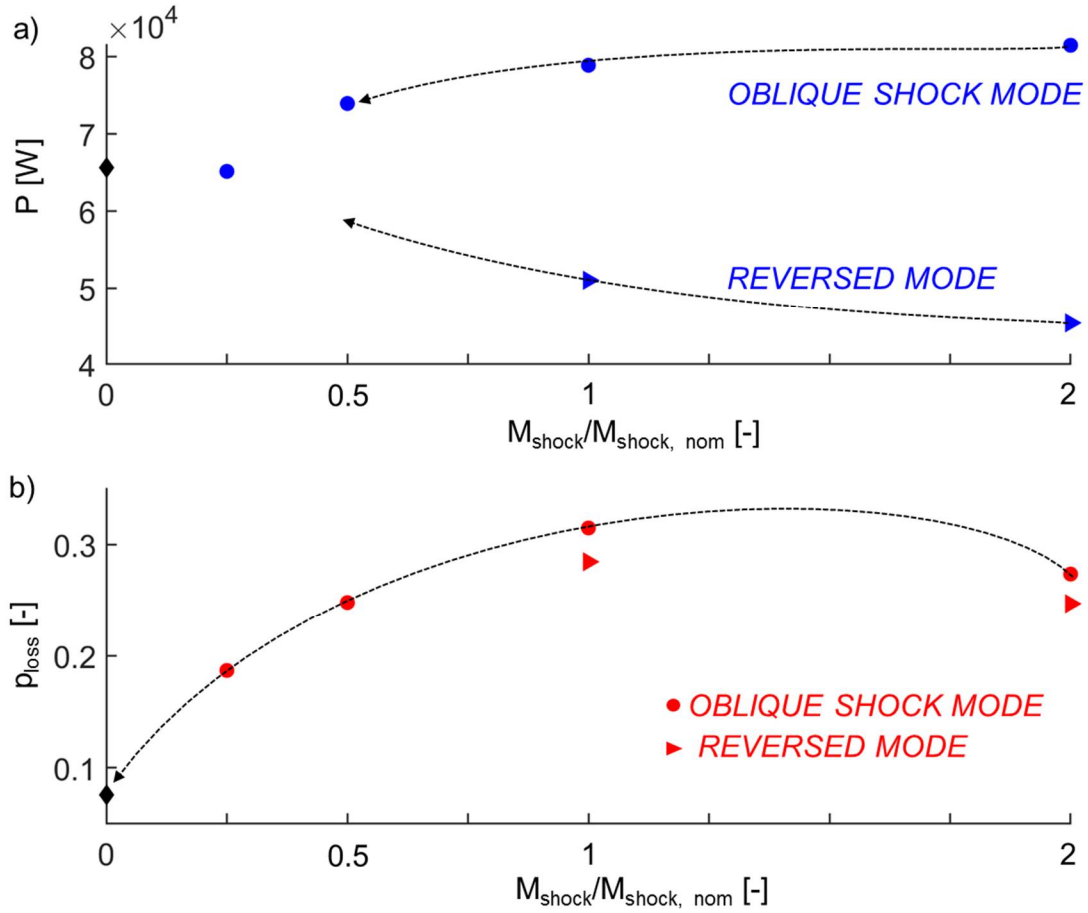
Figure 6.12 Influence of the shock speed (M_{shock}) on: a) power and b) total pressure loss

Figure 6.13 visualizes the flow field of three different wave-speeds for the oblique shock mode. In Figure 6.13b, the nominal shock speed is represented which results in an oblique shock angle at the shroud of 58 degrees and on the hub of 70 degrees. By increasing the shock speed (Figure 6.13c), the oblique shock tends to a lower oblique angle. By decreasing the shock speed, the angle increases, as observed in Figure 6.13a.
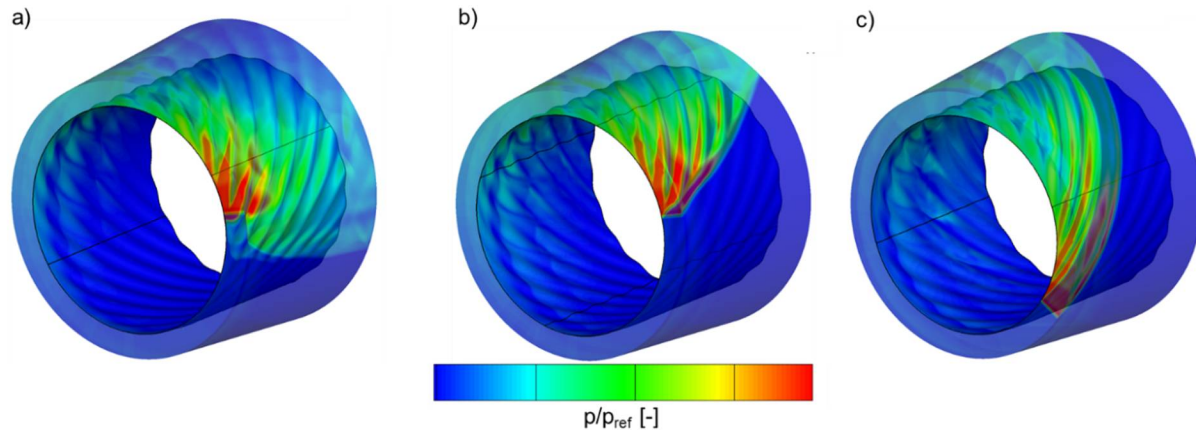
Figure 6.13 Pressure field at multiple shock speeds in the oblique shock mode: a) M_{shock} =0.5$M_{shock, nom}$, b) M_{shock} =$M_{shock, nom}$ and c) M_{shock} =2$M_{shock, nom}$

The shock wave strength (Π_{shock}) is investigated in Figure 6.14. The shock wave strength was reduced from the nominal case towards 30% strength (compared to the nominal pressure ratio) and the power decreases and reaches the steady simulation (black diamond in Figure 6.14a). Interestingly the shock strength drastically affects the total pressure loss. Time-averaged of mass-flow averaged pressure loss (Figure 6.14b) decreases from 30 % to below 10% (close to the steady value) for an oblique shock with a pressure ratio of 30% of the nominal case.
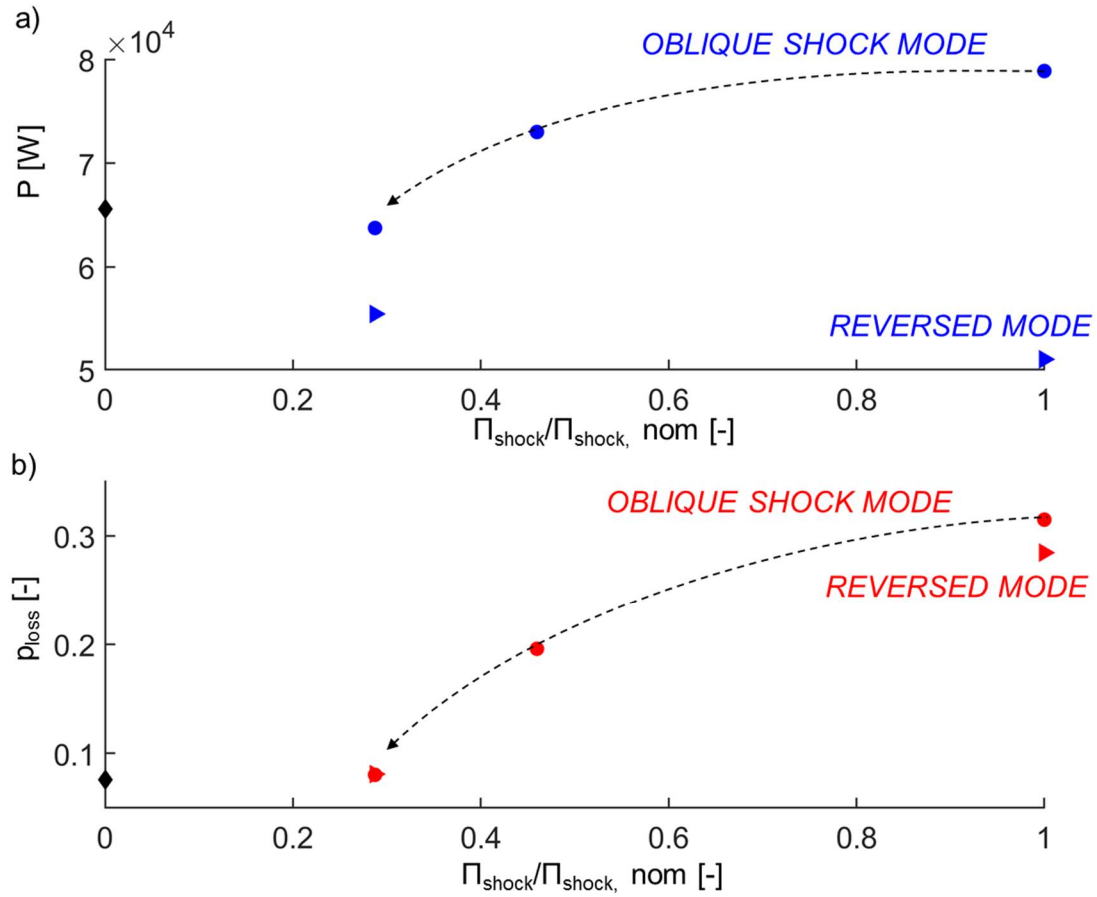
Figure 6.14 Influence of the amplitude of the shock wave on a) power and b) total pressure loss

The period of the wave (L_{period}) was studied in Figure 6.15, which resulted in the generation of a bladeless turbine with two and three rotating oblique shock waves. Figure 6.15 displays the power as a function of the waves, and this has a similar effect as increasing the wave speed. By decreasing the characteristic length by half, an increase of power of 30% was observed, while this increased to 54% if the length was reduced to a third.
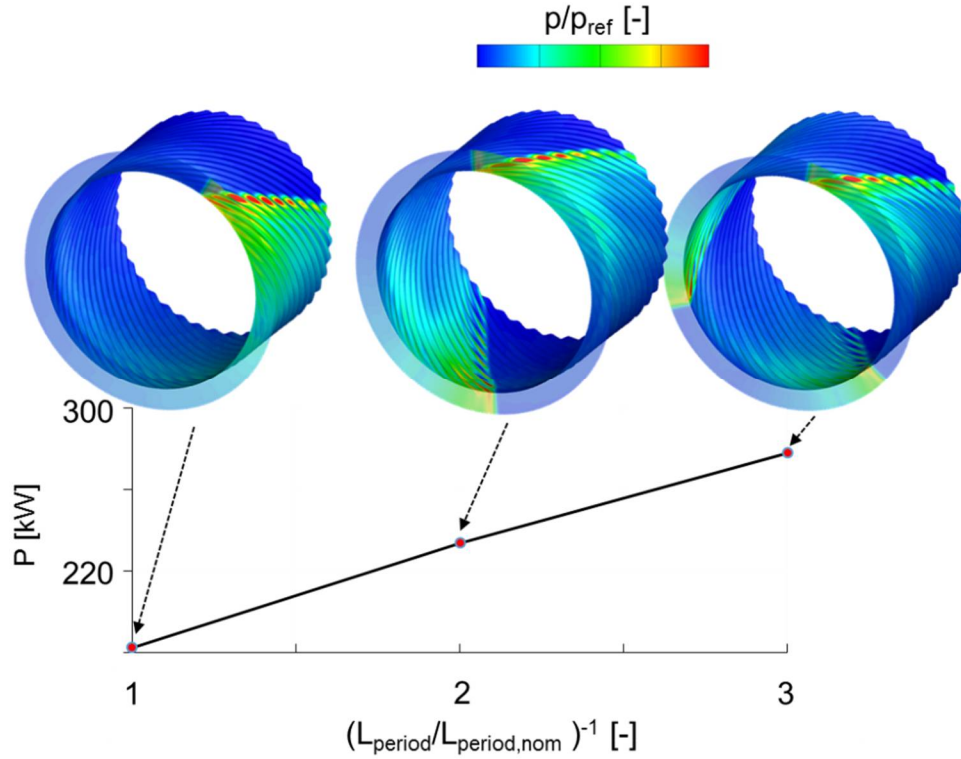
Figure 6.15 Influence of L_{period} on the power

Figure 6.16a displays the torque as a function of time with contributions from pressure (inviscid part) and the shear stress (viscous part). The fluctuations in torque are around 4% and can be attributed to the fact that the angle of the oblique shock and the helix angle are not equal and hence several compression and acceleration regions are simultaneously excited with consequently low torque fluctuations. Figure 6.16b illustrates the power fluctuations, which decreased to 2% for the reversed mode and the fluctuations of the oblique shock mode and the reversed mode decrease when the shock strength was lowered.
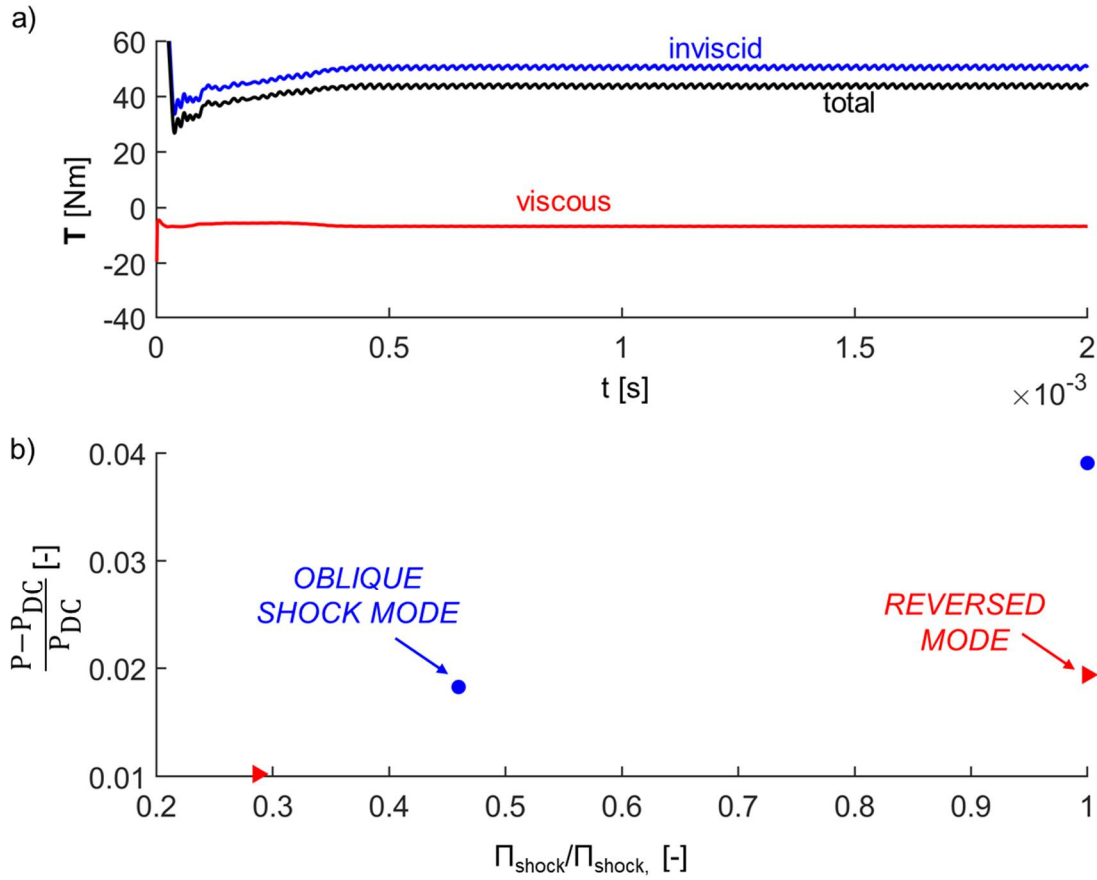
Figure 6.16 a) Fluctuations of torque as a function of time and b) power fluctuations for several modes as a function of the shock strength

Finally, if one obtains all the parameters that define the rotating oblique shock, the time-averaged of the mass-flow averaged pressure loss and power can be estimated by a steady simulation with the same mass-flow averaged total pressure, total temperature and Mach number as the rotating oblique shock with corrections based on Figure 6.12, Figure 6.14 and Figure 6.15.

6.5   Heat flux at one operating condition

Figure 6.17a describes the method to assess the unsteady heat flux in the bladeless turbine. Three wall temperatures are calculated, and for each phase of the shock (φ) which represents the position of the oblique shock (φ has a value between 0 and 1), a corresponding heat flux exists for each location on the turbine hub. A two-dimensional representation of the heat flux in the z-θ plane of the turbine hub is displayed for a wall temperature of 1000K and 1400 K, and it is observed that the highest heat flux appears directly downstream of the shock due to the increased pressure and temperature. At a constant φ value on the three-dimensional T_{wall}- φ –Q graph, the temperature at which the heat flux is zero, is called the adiabatic wall temperature (blue line). The slope of this curve is the adiabatic heat flux coefficient. Figure 6.17b portrays the heat flux in T_{wall}- θ –Q plane just upstream of the shock (θ =0 deg.) and 15 % downstream of the shock (θ =60 deg.). The heat flux is 16 times higher when the shock passes compared to the level upstream of the shock, and several smaller increases and decreases are observed in the heat flux due to the presence of the wavy surface. The grey surface depicts the plateau at which the heat flux is zero, and their intersection with the temperature axis results in the adiabatic wall temperature. To analyze the unsteady heat flux, Pinilla et al. [113] further decomposed the unsteady heat flux into several steady and unsteady components.
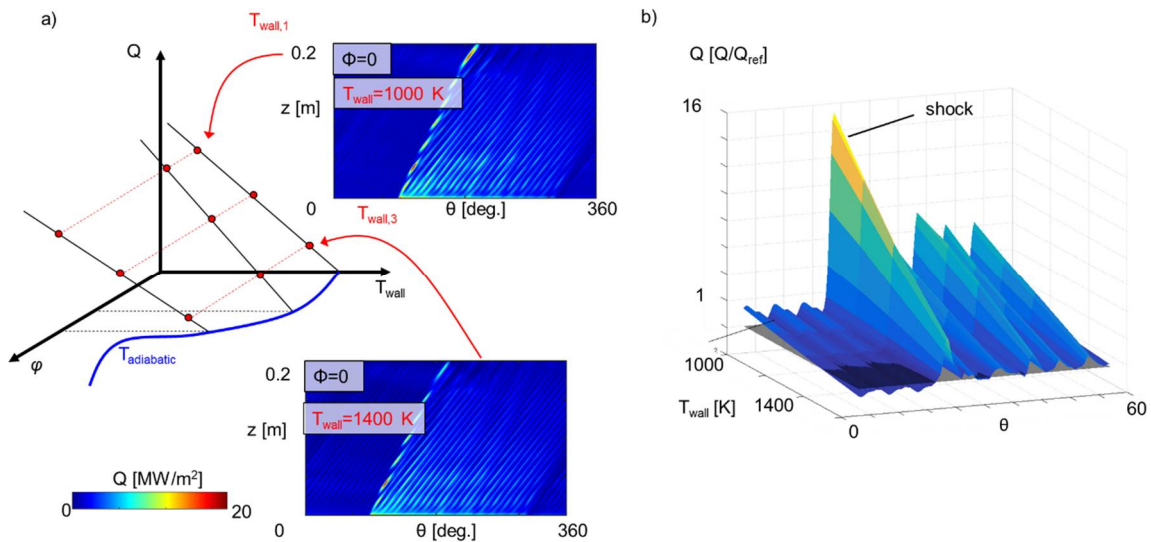
Figure 6.17 a) Heat flux methodology and b) zoom on the heat flux for several isothermals upstream and downstream of the oblique shock

Figure 6.18a depicts the instantaneous heat flux at a certain time step. The sudden pressure rises behind the oblique shock (p_{max}/p_{min}~8) causes a jump in heat flux beyond a factor 100. The isothermal simulation was started from an adiabatic converged solution, and Figure 6.18b plots the convergence of the average heat flux as a function of time. After two periods of the oblique shock, the average heat flux was converged.
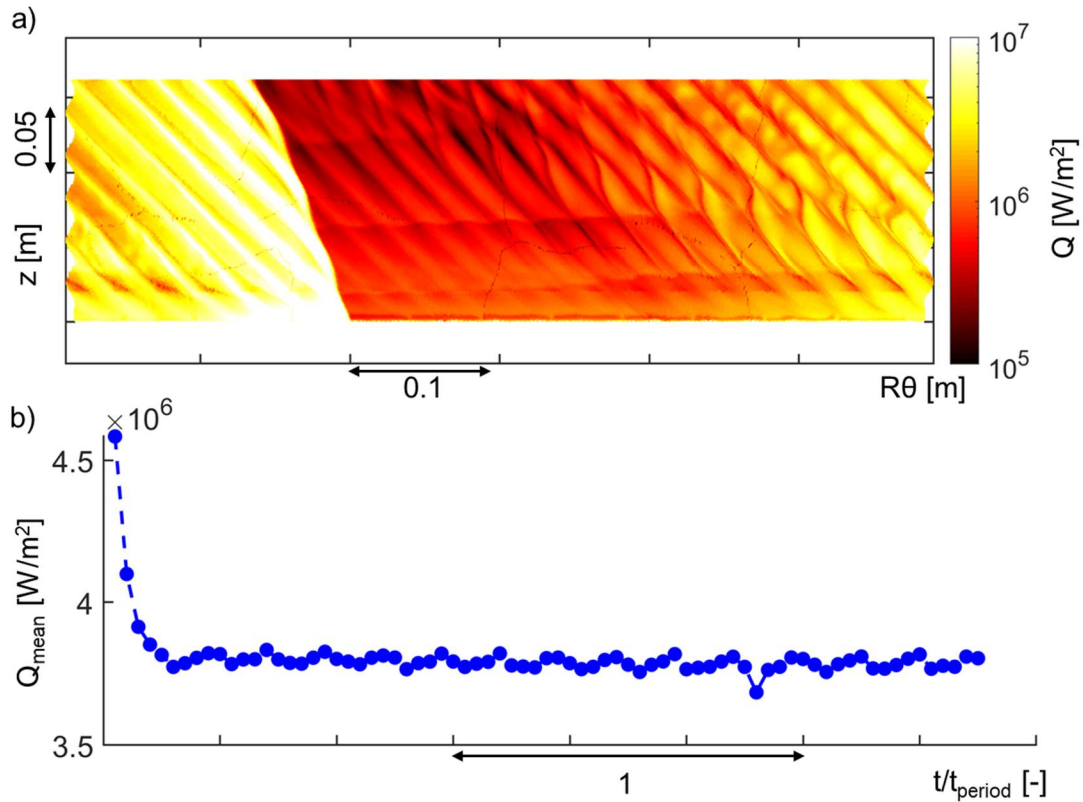
Figure 6.18 a) Instantaneous heat flux for the operation of the oblique shock mode and b) convergence of the average heat flux in time

Figure 6.19a plots the tangentially averaged heat flux for two isothermal simulations (T=1000K and T=1400K), and the heat flux is compared to the steady-state simulation. At each axial location, the oblique shock mode generates more heat flux than its mass flow-averaged steady-state simulation and is attributed to the sweeping oblique shock and difference in flow angle. In Figure 6.19b, the discrepancy between the oblique shock mode and the steady simulation is evaluated, and a discrepancy between 10% and 30% was found depending on the axial position. This can be used in engine models to correct for the unsteady shock sweeping and will be a function of all parameters found in Eq. 6.3.
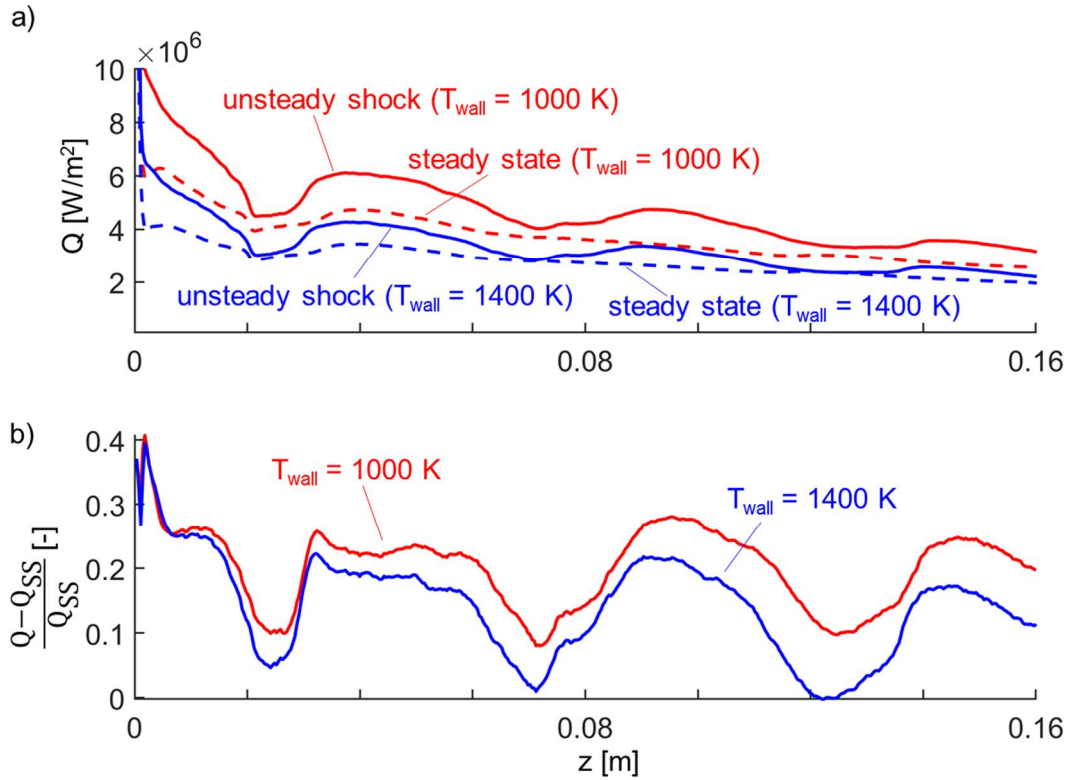
Figure 6.19 Oblique shock mode versus the steady-state simulation: a) averaged heat flux along the axial direction and b) discrepancy between steady-state simulation and the oblique shock mode

The heat flux of the oblique shock mode versus the steady-state simulation at two axial locations ($z/L=0.05$ and $z/L=0.5$) is depicted in Figure 6.20a. At $z/L=0.05$, the ratio of the difference between the maximum heat flux at one axial location and minimum compared to the local mean ($\frac{\text{max-min}}{\text{mean}}$) is 40% for the steady simulation and is around 600% for the oblique shock mode. Furthermore, the maximum heat flux value is around 70 times larger than the minimum value. At $z/L=0.5$, the steady simulation has a $\frac{\text{max-min}}{\text{mean}}$ of around 120% and for the unsteady signature this rises to 870%. Hence, further downstream the spatial oscillations rise, but the mean heat flux reduces. Figure 6.20b plots the relative discrepancy between the steady-state simulation and the oblique shock mode at those two axial locations. Directly downstream of the oblique shock impingement, heat flux discrepancy rises to a factor 6 difference, while tangentially upstream of the shock, heat flux discrepancies are negative with values below -0.8.
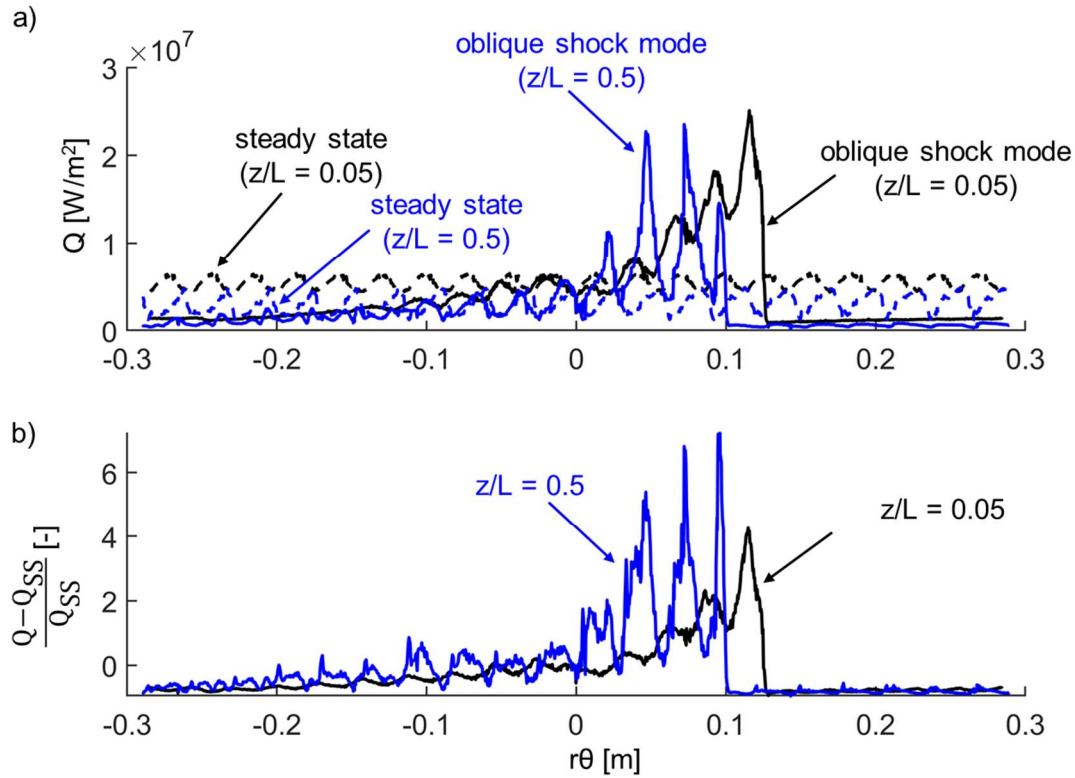
Figure 6.20 a) Tangential heat flux: steady versus unsteady operation at two axial locations and b) discrepancy between the steady-state simulation and the oblique shock mode

Finally, the adiabatic wall temperature and adiabatic heat flux coefficient are calculated in Figure 6.21, according to Eq. 3.6. In contrast to the steady-state simulation, the adiabatic wall temperature features a large variation due to the passing of the oblique shock (Figure 6.21a), with values tangentially upstream of the shock of around 1800K and rising to above 3000K during the oblique shock passing. Similar observations can be made for the adiabatic heat flux coefficient, in which the value of the adiabatic heat flux coefficient increases by a factor 20 when the oblique shock passes and decays tangentially downstream until the next propagation of the oblique shock.

a)

b)
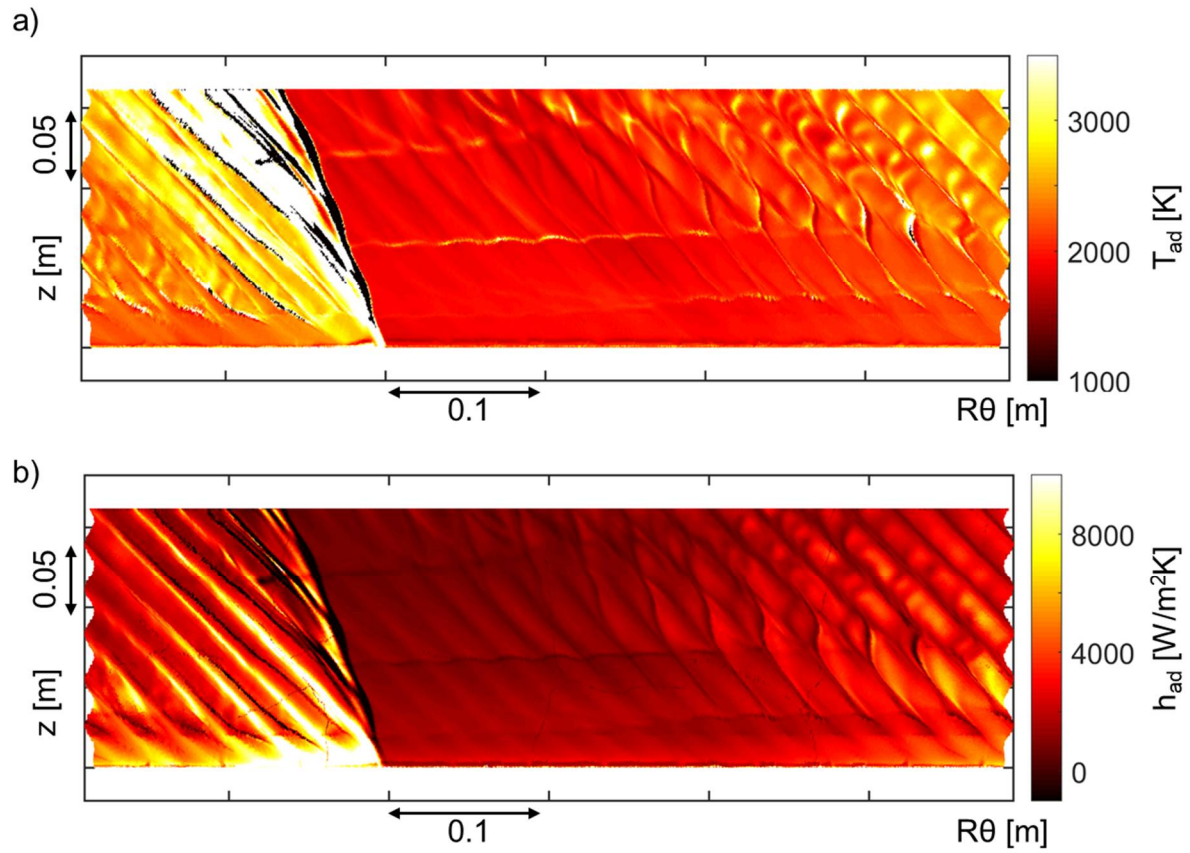
Figure 6.21 a) Unsteady adiabatic heat transfer coefficient and b) unsteady adiabatic wall temperature for the oblique shock mode

.

CHAPTER 7.   CONCLUSIONS

In this section, we summarize how the different objectives of the manuscript (outlined in Section 1.2) were successfully completed. ***The main objective was to engineer and characterize a power extraction device without airfoils suitable for high inlet Mach numbers and understand the fundamental flow principles that control the work exchange.*** A baseline turbine for a small engine with a radius of 9 cm and a length of 16 cm was designed with a sinusoidal wavy hub surface that had an amplitude-to-channel-height of 10% and a helix angle of 45 degrees. The inlet Mach number was 1.25 and was purely axial. Due to the rise and descent of the wavy contour and its inclination (helix angle), subsequent shock waves and expansion fans were generated which triggered favorable power extraction.

In terms of <u>aerodynamic performance</u>, the machine at optimum RPM provided around 75 kW of power. This corresponded to a total temperature drop of around 4 K or a T_{01}/T_{02} of around 0.15%. The viscous forces acted against the hub resulting in a viscous-to-total torque ratio of 43% and a mass-flow averaged total pressure loss of around 7%.

Average <u>heat flux</u> from inlet to outlet decreased to 44% of its peak. The maximum heat flux discrepancy at one axial position non-dimensionalized by the mean heat flux was limited to around 120% and was found in the aft part of the turbine.

A two-dimensional model was proposed by connecting the power extraction principle to a sequence of a compression wave, followed by an expansion fan, detachment shock and separation zone. For 50% of the axial length, which accounts for 80% of the power generation, this reduced two-dimensional model had a discrepancy in pressure force below 15% with the baseline three-dimensional simulation.

To further strengthen this new concept, three complimentary steps were required.

First, the uncertainty on the numerical results was addressed. An experimental validation was performed based on the proposed two-dimensional model. A modular test article with a convergent-divergent nozzle to accelerate the flow to Mach 2 was designed for the Linear Experimental Aerothermal Facility (LEAF) at the Purdue Experimental Turbine Aerothermal Lab (PETAL) based on several RANS simulations.

First, low-frequency measurements were performed. Uncertainty level was below 2% for the hub pressure in zones of attachment; however, this increased to 10% in the separation regions. The compression shock angle was matched accurately using RANS; however, the first separation shock was underpredicted by 2 degrees. Low-frequency unsteadiness of the shock angles was also reported. For the skin friction, an average discrepancy of 20% between the test and RANS was found. In the attached regions, heat flux discrepancy was below 20% however increased to up to 100% in zones of separation. It is worth noting that manufacturing roughness can also pose an uncertainty on the shock strength and separation point.

Second, high-frequency effects were assessed: fluctuations steadily increased behind each successive shock. Values of maximum fluctuations compared to the local static pressure up to 20-30% on the hub were found, and the standard deviation was around 3%. Flow field measurements, performed through BOS and FLEET, showed an increased unsteadiness behind the separation and reattachment shocks. Proper Orthogonal Decomposition (POD) and Spectral POD revealed several dominant low-frequency and medium frequency phenomena (up to 5 kHz) of the separation regions and the two shock boundary layer interactions in the shroud and were compared to the dominant frequency found in the literature. The system mainly responded to lower frequency excitations (below 3 kHz), which needs to be considered for future structural analysis. During startup and shut down, pressure fluctuations up to 20% were found, and zones within the separation seemed to be less affected by the transient. Heat flux signature during start-up was investigated and peaks were associated to the transient shock passing.

Finally, a fusion of the experiments with the numerical analysis resulted in a precise estimation of the uncertainty in power ranging from -11% to 7% based on the bias error on the shear stress and the uncertainty on the hub pressure. Flow field unsteadiness yielded power fluctuations of 4%. Uncertainty on efficiency was estimated to be 10 to 15%. Hence, the technology concept was well documented.

Second, we focused on the geometrical optimization of this new class of axial bladeless turbines and defined its operational envelope which is critical to assess new engine models equipped with a bladeless turbine module. The RPM for which the bladeless turbine delivers maximum efficiency and power was around 30,000 for the baseline geometry. Reduced torque was defined as a non-dimensional parameter for the bladeless turbine and was plotted against the

reduced mass flow and reduced speed as well as the efficiency. A wide range of helix angles was modeled and a sensitivity below 20% was observed in terms of torque. Similarly, the effect of the number of waves on the reduced torque and the efficiency was studied. The impact of the wavy contour's amplitude was considerable, with a 210% increase in power production when the amplitude was doubled. Several hub radii were investigated, and the reduced torque proved to be a good non-dimensional parameter to scale the performance of the bladeless turbine for a wide range of geometries.

The range of the bladeless turbine covered the high subsonic (Mach 0.94) to the hypersonic regime.

By analyzing irreversibility, 40% of the aerodynamic loss originated from the hub region and was found to be a function of the amplitude-over-height of the wavy contour.

The shape was optimized through a multi-objective optimization in which the pressure force was maximized, while minimizing the heat flux or pressure loss. Pressure force was increased by more than 100%, and geometries with lower loss and heat flux were discussed in detail.

The efficiency of a bladeless turbine for a bottoming cycle was also analyzed, and component efficiency of up to 60% was achieved with the baseline geometry.

To assess the viability of the bladeless turbine for novel supersonic engine cycles, ***the operation of the bladeless turbine was explored when the turbine passage is exposed to rotating shocks.*** A strategy to non-dimensionalize rotating shocks was derived based on the oblique shock equation. The operational envelope was extended with two modes of operation. The first mode is the *oblique shock mode* where the rotating oblique shock has the same orientation as the helix angle. The second mode is the *reversed mode* where the helix angle and the oblique shock angle were opposite.

A parametric study was performed on the variables defining the rotating oblique shock to identify the critical factors that affect the unsteady operation of the turbine. The *oblique shock mode* delivered higher power compared to the *reversed mode*, by approx. 35%. The time-averaged of mass-flow averaged total pressure loss was around a factor 3.5 higher than the steady simulation in which the Mach number and mass-flow averaged quantities were kept constant. Additionally, power extraction was increased in the aft part of the turbine because of the sweeping oblique shock.

The unsteady heat flux in the oblique shock mode was dissected. The tangentially averaged heat flux was between 10% and 30% higher than the steady simulation, and instantaneous heat flux values could be up to six times larger due to the presence of the rotating oblique shock.

By calculating the relevant non-dimensional parameters that define the rotating oblique shock, corrections for total pressure loss, heat flux, and power were proposed for both the *oblique shock mode* and *the reversed mode*.

In conclusion, this thesis covered the fundamental analysis of power harvesting through shock waves, in which a new class of bladeless turbine was developed, CFD was validated, and optimization strategies were proposed. Finally, the proof of concept was tested up to a technological readiness level (TRL) of two.

The broader impact of this work is threefold. First, for the development of compact turbines that are suitable to extract power in harsh high Mach number flows (e.g., novel combustors, scramjets, ramjets and rockets). Currently, no other turbine concept has been proven to be a viable alternative. Bladeless turbines can deliver power to drive the pumps, provide on-board electricity and trust as bottoming cycle.

Second, the understanding of shock-boundary layer interactions in internal flows which has a dearth of experimental data in terms of heat flux and pressure. This is not only important for the operation and structural integrity of bladeless turbines but also for supersonic axial and supersonic radial bladed turbomachines. Furthermore, supersonic inlets, nozzles and diffusers in which multiple shocks merge also suffer from these potentially harmful interactions.

Finally, a canonical test case is proposed to non-dimensionalize rotating shock waves and to quantify their impact which is crucial for the detailed assessment of the unsteady turbine performance for higher TRL tests. This will ensure that the prime parameters that define the unsteadiness at the outlet of the combustor are conserved on top of the non-dimensional numbers such as Reynolds, Mach, reduced speed and reduced mass flow that are already extensively used for conventional turbomachinery testing.

REFERENCES

[1] J. Braun, B. H. Saracoglu, and G. Paniagua, "Unsteady Performance of Rotating Detonation Engines with Different Exhaust Nozzles," *J. Propuls. Power*, vol. 33, no. 1, pp. 121–130, Jan. 2017.

[2] G. Paniagua, M. C. Iorio, N. Vinha, and J. Sousa, "Design and analysis of pioneering high supersonic axial turbines," *Int. J. Mech. Sci.*, vol. 89, pp. 65–77, 2014.

[3] A. Kantrowitz and C. duP. Donaldson, "Preliminary Investigation Of Supersonic Diffusers," 1945.

[4] Z. Liu, J. Braun, and G. Paniagua, "Three Dimensional Optimization for Subsonic Axial Turbines Operating at High Unsteady Inlet Mach Number," in *Joint Propulsion Conference*, 2018, pp. 1–10.

[5] J. Sousa and G. Paniagua, "Entropy minimization design approach of supersonic internal passages," *Entropy*, vol. 17, no. 8, pp. 5593–5610, 2015.

[6] U. Vyas, V. Andreoli, and G. Paniagua, "Effect of transonic inlet design on the performance of a mico-turbojet engine," in *2018 AIAA Aerospace Sciences Meeting*, 2018, no. January.

[7] J. Sousa, G. Paniagua, and E. Collado Morata, "Thermodynamic analysis of a gas turbine engine with a rotating detonation combustor," *Appl. Energy*, vol. 195, pp. 247–256, 2017.

[8] L. B. Inhestern, J. Braun, and G. Paniagua, "Design, Optimization and Analysis of Supersonic Radial Turbines," in *ASME TurboExpo*, 2019, pp. 1–15.

[9] L. Inhestern, Benjamin, J. Braun, and G. Paniagua, "Non-Axial Turbomachine," 36185663, 2019.

[10] N. Vinha, G. Paniagua, J. Sousa, and B. H. Saracoglu, "Axial Bladeless Turbine Suitable for High Supersonic Flows," *J. Propuls. Power*, vol. 32, no. 4, pp. 975–983, 2016.

[11] N. Vinha, G. Paniagua, J. Sousa, and B. H. Saracoglu, "Axial fluid machine and method for power extraction," EP 2 868 864 A1, 2015.

[12] N. Tesla, "Improved Method of Imparting Energy to or Deriving Energy From a Fluid and Apparatus for Use Therein," BP24001, 1910.

[13] R. Li, H. Wang, E. Yao, M. Li, and W. Nan, "Experimental study on bladeless turbine using incompressible working medium," *Adv. Mech. Eng.*, vol. 9, no. 1, pp. 1–12, 2017.

[14] A. L. Neckel and M. Godinho, "Influence of geometry on the efficiency of convergent-divergent nozzles applied to Tesla turbines," *Exp. Therm. Fluid Sci.*, vol. 62, pp. 131–140, 2015.

[15] N. Patel and D. D. Schmidt, "Biomass Boundary Layer Turbine Power System," in *2002 International Joint Power Generation Conference*, 2002, pp. 931–934.

[16] A. Ferri, "Hypersonic flight testing," *Int. Sci. Technol.*, 1964.

[17] C. D. Donaldson, "Effects of Interaction between Normal Shock and Boundary Layer," 1944.

[18] F. R. . Fage and R. F. Sargent, "Shock-wave and boundary-layer phenomena near a flat surface," *Proc. R. Soc. London. Ser. A. Math. Phys. Sci.*, vol. 190, no. 1020, pp. 1–20, Jun. 1947.

[19] R. J. Lubbock and M. L. G. Oldfield, "Turbulent velocity and pressure fluctuations in gas turbine combustor exit flows," *Proc. Inst. Mech. Eng. Part A J. Power Energy*, vol. 232, no. 4, pp. 337–349, 2018.

[20] F. H. Falempin, G. Paniagua Perez, J. Braun, and B. Le Naour, "Bladeless turbines for unsteady high speed flows," in *21st AIAA International Space Planes and Hypersonics Technologies Conference*, 2017, no. March, pp. 1–12.

[21] Z. Liu, J. Braun, and G. Paniagua, "Characterization of a Supersonic Turbine Downstream of a Rotating Detonation Combustor," *J. Eng. Gas Turbines Power*, vol. 141, no. 3, p. 031501, 2018.

[22] M. Fernelius, S. E. Gorrell, J. Hoke, and F. Schauer, "Effect of Periodic Pressure Pulses on Axial Turbine Performance," in *49th AIAA/ASME/SAE/ASEE Joint Propulsion Conference*, 2013, pp. 1–15.

[23] T. Verstraete, Z. Alsalihi, and R. A. Van den Braembussche, "Multidisciplinary Optimization of a Radial Compressor for Micro Gas Turbine Applications," in *Volume 6: Turbo Expo 2007, Parts A and B*, 2007, vol. 132, no. July 2010, pp. 1291–1299.

[24] S. Amaral, T. Verstraete, R. Van den Braembussche, and T. Arts, "Design and Optimization of the Internal Cooling Channels of a HP Turbine Blade: Part I—Methodology," in *Volume 4: Heat Transfer, Parts A and B*, 2008, vol. 2008, no. 51080, pp. 967–976.

[25] R. Knobloch, J. Mlýnek, and R. Srb, "The classic differential evolution algorithm and its convergence properties," *Appl. Math.*, vol. 62, no. 2, pp. 197–208, 2017.

[26] S. Chakravarthy, O. Peroomian, U. Goldberg, and S. Palaniswamy, "The CFD++ Computational Fluid Dynamics Software Suite," *SAE Tech. Pap. Ser.*, vol. 1, 2010.

[27] E. F. Toro, *Riemann Solvers and Numerical Methods for Fluid Dynamics*, Third Edit. Springer, 2009.

[28] A. Bonfiglioli and R. Paciorri, "Convergence Analysis of Shock-Capturing and Shock-Fitting Solutions on Unstructured Grids," *AIAA J.*, vol. 52, no. 7, pp. 1404–1416, Jul. 2014.

[29] J. Braun, J. Sousa, and G. Paniagua, "Numerical Assessment of the Convective Heat Transfer in Rotating Detonation Combustors Using a Reduced-Order Model," *Appl. Sci.*, vol. 8, no. 6, p. 893, May 2018.

[30] I. B. Celik, U. Ghia, P. J. Roache, C. J. Freitas, H. Coleman, and P. E. Raad, "Procedure for Estimation and Reporting of Uncertainty Due to Discretization in CFD Applications," *J. Fluids Eng.*, vol. 130, no. 7, p. 078001, 2008.

[31] J. P. Clark and E. A. Grover, "Assessing Convergence in Predictions of Periodic-Unsteady Flowfields," *J. Turbomach.*, vol. 129, no. 4, p. 740, 2007.

[32] C. Farhat and D. Amsallem, "Model reduction, Proper Orthogonal Decomposition (POD)," no. Spring, pp. 3–5, 2017.

[33] A. Towne, O. T. Schmidt, and T. Colonius, "Spectral proper orthogonal decomposition and its relationship to dynamic mode decomposition and resolvent analysis," *J. Fluid Mech.*, vol. 847, pp. 821–867, Jul. 2018.

[34] P. J. Schmid, "Dynamic mode decomposition of numerical and experimental data," *J. Fluid Mech.*, vol. 656, pp. 5–28, Aug. 2010.

[35] C. W. Rowley, I. Mezic, S. Bagheri, P. Schlatter, and D. S. Henningson, "Spectral analysis of nonlinear flows," *J. Fluid Mech.*, vol. 641, pp. 115–127, Dec. 2009.

[36] M. Sieber, C. O. Paschereit, and K. Oberleithner, "Spectral proper orthogonal decomposition," *J. Fluid Mech.*, vol. 792, pp. 798–828, Apr. 2016.

[37] O. T. Schmidt, A. Towne, G. Rigas, T. Colonius, and G. A. Brès, "Spectral analysis of jet turbulence," *J. Fluid Mech.*, vol. 855, pp. 953–982, Nov. 2018.

[38] O. T. Schmidt, A. Towne, and T. Colonius, "SpectralPOD," 2018. [Online]. Available: https://github.com/SpectralPOD.

[39] I. Rahbari and C. Scalo, "Quasi-Spectral Sparse Bi-Global Stability Analysis of Compressible Channel Flow over Complex Impedance," no. 2, pp. 1–16, 2017.

[40] I. Rahbari and C. Scalo, "Linear Stability Analysis of Compressible Channel Flow over Porous Walls," in *Whither Turbulence and Big Data in the 21st Century?*, A. Pollard, L. Castillo, L. Danaila, and M. Glauser, Eds. Cham: Springer International Publishing, 2017, pp. 451–467.

[41] K. Deb, A. Pratap, S. Agarwal, and T. Meyarivan, "A fast and elitist multiobjective genetic algorithm: NSGA-II," *IEEE Trans. Evol. Comput.*, vol. 6, no. 2, pp. 182–197, Apr. 2002.

[42] V. Andreoli … L. Langford, "Aerothermal Optimization of Fully Cooled Turbine Blade Tips," *Vol. 5C Heat Transf.*, vol. 141, no. June, p. V05CT22A001, 2018.

[43] C. De Maesschalck, S. Lavagnoli, and G. Paniagua, "Blade Tip Shape Optimization for Enhanced Turbine Aerothermal Performance," in *Volume 3C: Heat Transfer*, 2013, vol. 136, no. April 2014, p. V03CT14A011.

[44] J. Braun, J. Sousa, and C. Pekardan, "Aerodynamic Design and Analysis of the Hyperloop," *AIAA J.*, vol. 55, no. 12, pp. 4053–4060, Dec. 2017.

[45] G. Paniagua … D. Lawrence, "Design of the Purdue Experimental Turbine Aerothermal Laboratory for Optical and Surface Aero-Thermal Measurements," in *Volume 6: Ceramics; Controls, Diagnostics and Instrumentation; Education; Manufacturing Materials and Metallurgy*, 2016, p. V006T05A025.

[46] G. Paniagua … D. Lawrence, "Design of the Purdue Experimental Turbine Aerothermal Laboratory for Optical and Surface Aerothermal Measurements," *J. Eng. Gas Turbines Power*, vol. 141, no. 1, Jan. 2019.

[47] J. C. Dutton and R. E. Coverdill, "Experiments to study the gaseous discharge and filling of vessels," *Int. J. Eng. Educ.*, vol. 13, no. 2, pp. 123–134, 1997.

[48] J. Saavedra, "Determining the Dynamic Scales of the Boundary Layer and Flow Separation Inception: Analysis towards Efficient Flow Control," Purdue University, 2018.

[49] J. Naughton and J. Brown, "Surface interferometric skin-friction measurement technique," in *Advanced Measurement and Ground Testing Conference*, 1996.

[50] J. L. Brown and J. W. Naughton, "The Thin Oil Film Equation," *Nasa Tm-1999-208767*, no. March, 1999.

[51] N. M. Husen, T. Liu, and J. P. Sullivan, "Luminescent Oil Film Flow Tagging Skin Friction Meter Applied to FAITH Hill," *AIAA J.*, vol. 56, no. 10, pp. 3875–3886, Oct. 2018.

[52] N. M. Husen, "Skin Friction Measurements Using Luminescent Oil Films," Purdue University, 2017.

[53] J. C. Ross and D. M. S. Nesc, "Orion Multi-Purpose Crew Vehicle (MPCV) Capsule Parachute Assembly System (CPAS) Wake Deficit Wind Tunnel Testing," 2014.

[54] T. Liu, A. W. Burner, T. W. Jones, and D. A. Barrows, "Photogrammetric techniques for aerospace applications," *Prog. Aerosp. Sci.*, vol. 54, pp. 1–58, Oct. 2012.

[55] T. Liu and A. W. Burner, "Photogrammetry Toolbox Reference Manual," Nov. 2014.

[56]   G. Zilliac, "Further developments of the fringe-imaging skin friction technique," *Nasa Tm 110425*, no. 110425, 1996.

[57]   P. Barricau, G. Pailhas, Y. Touvet, and L. Perret, "Friction Measurement in Zero and Adverse Pressure Gradient Boundary Layer Using Oil Droplet Interferometric Method," in *ERCOFTAC Series*, vol. 14, 2011, pp. 393–402.

[58]   J. W. Naughton and M. D. Hind, "Multi-image oil-film interferometry skin friction measurements," *Meas. Sci. Technol.*, vol. 24, no. 12, p. 124003, Dec. 2013.

[59]   L. Villafañe, G. Paniagua, G. Bonfanti, and T. Yasa, "Local surface shear stress measurements from oil streaks thinning rate," *Sensors Actuators, A Phys.*, vol. 223, pp. 31–39, 2015.

[60]   R. J. Moffat, "Describing the uncertainties in experimental results," *Exp. Therm. Fluid Sci.*, vol. 1, no. 1, pp. 3–17, Jan. 1988.

[61]   J. Saavedra, G. Paniagua, and B. H. Saracoglu, "Experimental Characterization of the Vane Heat Flux Under Pulsating Trailing-Edge Blowing," *J. Turbomach.*, vol. 139, no. 6, p. 061004, Feb. 2017.

[62]   L. Bhatnagar and G. Paniagua, "Deelopment of High Speed and High Temperature Atomic Layer Thermopiles," in *ASME TurboExpo*, 2019, pp. 1–12.

[63]   J. Fisher … S. Roy, "Burst-Mode 100 kHz - 1 MHz Velocimetry in Supersonic and Hypersonic Flows," in *AIAA Scitech 2019 Forum*, 2019, no. January, pp. 1–9.

[64]   D. B. Helmer, "Measurements of a three-dimensional shock-boundary layer interaction," *Thesis*, no. July, 2011.

[65]   D. B. Helmer, L. M. Campo, and J. K. Eaton, "Three-dimensional features of a Mach 2.1 shock/boundary layer interaction," *Exp. Fluids*, vol. 53, no. 5, pp. 1347–1368, Nov. 2012.

[66]   R. A. Burns and P. M. Danehy, "FLEET Velocimetry Measurements on a Transonic Airfoil," in *55th AIAA Aerospace Sciences Meeting*, 2017, pp. 1–24.

[67]   R. A. Burns, C. J. Peters, and P. M. Danehy, "Unseeded velocimetry in nitrogen for high-pressure, cryogenic wind tunnels: part I. Femtosecond-laser tagging," *Meas. Sci. Technol.*, vol. 29, no. 11, p. 115302, Nov. 2018.

[68]   M. Raffel, "Background-oriented schlieren (BOS) techniques," *Exp. Fluids*, vol. 56, no. 3, p. 60, Mar. 2015.

[69]   S. B. Dalziel, G. O. Hughes, and B. R. Sutherland, "Whole-field density measurements by 'synthetic schlieren,'" *Exp. Fluids*, vol. 28, no. 4, pp. 322–335, Apr. 2000.

[70]   M. Raffel, H. Richard, and G. E. A. Meier, "On the applicability of background oriented optical tomography for large scale aerodynamic investigations," *Exp. Fluids*, vol. 28, no. 5, pp. 477–481, May 2000.

[71]   L. K. Rajendran, S. P. M. Bane, and P. P. Vlachos, "Dot Tracking and Cramer-Rao Lower Bound for Background Oriented Schlieren (BOS) measurements," *19th Int. Symp. Appl. Laser Imaging Tech. to Fluid Mech.*, p. paper 209, 2018.

[72]   A. Eckstein and P. P. Vlachos, "Digital particle image velocimetry (DPIV) robust phase correlation," *Meas. Sci. Technol.*, vol. 20, no. 5, 2009.

[73]   B. Singh, L. K. Rajendran, M. Giarra, P. P. Vlachos, and S. P. M. Bane, "Measurement of the flow field induced by a spark plasma using particle image velocimetry," *Exp. Fluids*, vol. 59, no. 12, p. 179, Dec. 2018.

[74]   Z. Liu and G. Paniagua, "Design of Directional Probes for High-Frequency Turbine Measurements," *J. Eng. Gas Turbines Power*, vol. 140, no. 1, p. 011601, 2017.

[75]   G. Paniagua and R. Dénos, "Digital compensation of pressure sensors in the time domain," *Exp. Fluids*, vol. 32, no. 4, pp. 417–424, Apr. 2002.

[76]   H. Lengfellner, G. Kremb, A. Schnellbögl, J. Betz, K. F. Renk, and W. Prettl, "Giant voltages upon surface heating in normal YBa 2 Cu 3 O 7−δ films suggesting an atomic layer thermopile," *Appl. Phys. Lett.*, vol. 60, no. 4, pp. 501–503, Jan. 1992.

[77]   T. Roediger, H. Knauss, U. Gaisbauer, E. Kraemer, S. Jenkins, and J. von Wolfersdorf, "Time-Resolved Heat Transfer Measurements on the Tip Wall of a Ribbed Channel Using a Novel Heat Flux Sensor—Part I: Sensor and Benchmarks," *J. Turbomach.*, vol. 130, no. 1, p. 011018, 2008.

[78]   S. Jenkins, J. von Wolfersdorf, B. Weigand, T. Roediger, H. Knauss, and E. Kraemer, "Time-Resolved Heat Transfer Measurements on the Tip Wall of a Ribbed Channel Using a Novel Heat Flux Sensor—Part II: Heat Transfer Results," *J. Turbomach.*, vol. 130, no. 1, p. 011019, 2008.

[79]   R. J. Moffat, "What's new in convective heat transfer?," *Int. J. Heat Fluid Flow*, vol. 19, no. 2, pp. 90–101, 1998.

[80]   O. Popp … W.-F. Ng, "Steady and Unsteady Heat Transfer in a Transonic Film Cooled Turbine Cascade," in *Volume 3: Heat Transfer; Electric Power; Industrial and Cogeneration*, 1999, no. C, p. V003T01A077.

[81]   Z. Sun, Y. Zhu, Y. Hu, and S. Zhang, "Direct numerical simulation of a fully developed compressible wall turbulence over a wavy wall," *J. Turbul.*, vol. 19, no. 1, pp. 72–105, 2018.

[82]   C. J. Tyson and N. D. Sandham, "Numerical simulation of fully-developed compressible flows over wavy surfaces," *Int. J. Heat Fluid Flow*, vol. 41, pp. 2–15, 2013.

[83]   C. Gorlé, M. Emory, J. Larsson, and D. G. Iaccarino, "Epistemic uncertainty quantification for RANS modeling of the flow over a wavy wall," *Cent. Turbul. Res. Annu. Res. Briefs*, pp. 81–91, 2012.

[84]   T. Leger, N. Bisek, and J. Poggie, "Detached-Eddy Simulation of a Supersonic Reattaching Shear Layer," *AIAA J.*, vol. 55, no. 11, pp. 3722–3733, 2017.

[85]   A. S. Deshpande and J. Poggie, "Unsteadiness in a Compressible Reattaching Shear Layer," in *AIAA Scitech 2019 Forum*, 2019, no. January, pp. 1–17.

[86]   F. Tomasoni, B. H. Saracoglu, and G. Paniagua, "A decision-making algorithm for automatic flow pattern identification in high-speed imaging," *Expert Syst. Appl.*, vol. 41, no. 8, pp. 3935–3943, Jun. 2014.

[87]   N. M. Husen, T. Liu, and J. P. Sullivan, "The ratioed image film thickness meter," *Meas. Sci. Technol.*, vol. 29, no. 6, 2018.

[88]   D. S. Dolling, "Fifty years of shock-wave/boundary-layer interaction research - What next?," *AIAA J.*, vol. 39, no. 8, pp. 1517–1531, 2012.

[89]   N. T. Clemens and V. Narayanaswamy, "Low-Frequency Unsteadiness of Shock Wave/Turbulent Boundary Layer Interactions," *Annu. Rev. Fluid Mech.*, vol. 46, no. 1, pp. 469–492, 2014.

[90]   J. Poggie and A. J. Smits, "Shock unsteadiness in a reattaching shear layer," *J. Fluid Mech.*, vol. 429, no. 2001, pp. 155–185, Feb. 2001.

[91]   E. Touber and N. D. Sandham, "Low-order stochastic modelling of low-frequency motions in reflected shock-wave/boundary-layer interactions," *J. Fluid Mech.*, vol. 671, pp. 417–465, Mar. 2011.

[92]   M. Wu and M. P. Martin, "Analysis of shock motion in shockwave and turbulent boundary layer interaction using direct numerical simulation data," *J. Fluid Mech.*, vol. 594, pp. 71–83, Jan. 2008.

[93]   V. Narayanaswamy, L. L. Raja, and N. T. Clemens, "Control of a Shock/Boundary-Layer Interaction by Using a Pulsed-Plasma Jet Actuator," *AIAA J.*, vol. 50, no. 1, pp. 246–249, Jan. 2012.

[94]   Z. Zhao, J.-M. Li, J. Zheng, Y. D. Cui, and B. C. Khoo, "Study of Shock and Induced Flow Dynamics by Nanosecond Dielectric-Barrier-Discharge Plasma Actuators," *AIAA J.*, vol. 53, no. 5, pp. 1336–1348, May 2015.

[95]   M. Kiya and K. Sasaki, "Structure of a turbulent separation bubble," *J. Fluid Mech.*, vol. 137, pp. 83–113, Dec. 1983.

[96]   A. S. Deshpande and J. Poggie, "Statistical Analysis of Unsteadiness in a Compressible Reattaching Flow," in *AIAA Aviation 2019 Forum*, 2019, no. June, pp. 1–16.

[97]	J. P. Dussauge, P. Dupont, and J. F. Debiève, "Unsteadiness in shock wave boundary layer interactions with separation," *Aerosp. Sci. Technol.*, vol. 10, no. 2, pp. 85–91, 2006.

[98]	J. Saavedra and G. Paniagua, "Transient Performance of Separated Flows: Experimental Characterization of Flow Detachment Dynamics," pp. 1–12, 2019.

[99]	F. Lozano, J. Saavedra, J. Fisher, G. Paniagua, A. Martinez-Cava, and E. Valero, "Experimental approach to characterize base region Coanda flow topology induced by pulsating blowing," in *8th European Conference for Aeronautics and Space Sciences (EUCASS)*, 2019.

[100]	R. Örlü and P. H. Alfredsson, "On spatial resolution issues related to time-averaged quantities using hot-wire anemometry," *Exp. Fluids*, vol. 49, no. 1, pp. 101–110, 2010.

[101]	F. O. Thomas, C. M. Putnam, and H. C. Chu, "On the mechanism of unsteady shock oscillation in shock wave/turbulent boundary layer interactions," *Exp. Fluids*, vol. 18–18, no. 1–2, pp. 69–81, Dec. 1994.

[102]	N. C. S. Datta, "An Experimental Study of Coherent Structures in Shock Boundary Layer Interaction at Mach 3," The University of Alabama, 2017.

[103]	P. J. Schmid, L. Li, M. P. Juniper, and O. Pust, "Applications of the dynamic mode decomposition," *Theor. Comput. Fluid Dyn.*, vol. 25, no. 1–4, pp. 249–259, Jun. 2011.

[104]	M. G. Berry, M. Y. Ali, A. S. Magstadt, and M. N. Glauser, "DMD and POD of time-resolved schlieren on a multi-stream single expansion ramp nozzle," *Int. J. Heat Fluid Flow*, vol. 66, pp. 60–69, 2017.

[105]	A. Towne, O. T. Schmidt, and T. Colonius, "Spectral proper orthogonal decomposition and its relationship to dynamic mode decomposition and resolvent analysis," *J. Fluid Mech.*, vol. 847, pp. 821–867, Jul. 2018.

[106]	N. Thiry and G. Paniagua, "Characterization of the time-resolved starting process of supersonic diffusers," in *52nd AIAA/SAE/ASEE Joint Propulsion Conference*, 2016, pp. 1–14.

[107]	J. Braun, S. Lu, and G. Paniagua, "Development of High Frequency Virtual Thermocouples," in *Volume 6: Ceramics; Controls, Diagnostics and Instrumentation; Education; Manufacturing Materials and Metallurgy*, 2017, p. V006T05A026.

[108]	F. Montomoli, M. Carnevale, A. D'Ammaro, M. Massini, and S. Salvadori, *Uncertainty Quantification in Computational Fluid Dynamics and Aircraft Engines*. Cham: Springer International Publishing, 2015.

[109]	Z. Liu, J. Braun, and G. Paniagua, "Performance of axial turbines exposed to large fluctuations," in *53rd AIAA/SAE/ASEE Joint Propulsion Conference*, 2017, no. July, pp. 1–14.

[110] B. Cantwell, "Entropy generation and transport," Stanford University.

[111] D. C. Montgomery, *Design and Analysis of Experiments*, 9th ed. Wiley, 2017.

[112] J. Sousa, J. Braun, and G. Paniagua, "Development of a fast evaluation tool for rotating detonation combustors," *Appl. Math. Model.*, vol. 52, pp. 42–52, Dec. 2017.

[113] V. Pinilla, J. P. Solano, G. Paniagua, and R. J. Anthony, "Adiabatic Wall Temperature Evaluation in a High Speed Turbine," *J. Heat Transfer*, vol. 134, no. 9, p. 091601, 2012.

VITA

James Braun graduated in 2014 from the KU Leuven in Belgium as mechanical engineer and performed a research master at the von Karman Institute for Fluid Dynamics within the domain of Aerospace and Aeronautics. He embarked the PhD Program in fall 2015 at Purdue University where he is enrolled in the Mechanical Engineering department and carries out research at Zucrow Laboratories.

PUBLICATIONS

Patents

1. Bloxham, M. J., Ebacher, J. V., Paniagua, G., Andreoli, V., De Maesschalck, C. G. M., Braun, J., "Tip Structure for a Turbine Blade with Pressure Side and Suction Side Rails", United States Patent Application 20180245469.
2. Paniagua, G., Cuadrado, D.G., Braun, J., Andreoli, V., Liu, Z., "Directional Probe for High Temperature Flows", Provisional Application; 68020-01; 62/571774.
3. Inhestern L., Braun J., Paniagua G., "Non-Axial Turbomachine", Provisional Application, EFS ID: 36185663

Journal Proceedings

1. Braun, J., Saracoglu, B. H., Magin, T. E., and Paniagua, G., One-Dimensional Analysis of the Magnetohydrodynamic Effect in Rotating Detonation Combustors, AIAA Journal, Vol. 54, No. 12, 2016, pp. 3761-3767, DOI: 10.2514/1.J054989
2. Braun, J., Saracoglu, B. H., and Paniagua, G., Unsteady Performance of Rotating Detonation Engines with Different Exhaust Nozzles, Journal of Propulsion and Power, pp. 1-10. 2016, DOI 10.2514/1.B36164,
3. Ornano F., Braun. J., Saracoglu B.H., Paniagua G., Multi-stage nozzle-shape optimization for pulsed hydrogen–air detonation combustor, Advances in Mechanical Engineering, 2017, Vol. 9(2) 1–9, DOI: https://doi.org/10.1177/1687814017690955
4. Sousa, J., Braun, J., and Paniagua, G., Development of a fast evaluation tool for rotating detonation combustors, Applied Mathematical modeling., Vol 52-pp42-52, 2017, DOI:10.1016/j.apm.2017.07.019,
   http://www.sciencedirect.com/science/article/pii/S0307904X17304572
5. Braun J., Sousa J., Pekardan C., Design Procedure and assessment of the Hyperloop pod, AIAA Journal, Vol 55, No 12, December 2017, https://arc.aiaa.org/doi/pdf/10.2514/1.J055634

6. Braun J., Sousa J., and Paniagua G., Numerical assessment of the convective heat transfer in rotating detonation combustors using a reduced order model, Applied Sciences, 2018, 8(6), 893, DOI: 10.3390/app8060893 http://www.mdpi.com/2076-3417/8/6/893

7. Andreoli V, Braun J, Paniagua G, De Maesschalck C., Bloxham M., Cummings W., Langford L., Aerothermal Optimization of Fully Cooled Turbine Blade Tips. ASME. J. Turbomach. 2019;141(6):061007-061007-10. doi:10.1115/1.4041961.

8. Liu Z., Braun J., and Paniagua G., Characterization of A Supersonic Turbine Downstream of A Rotating Detonation Combustor, Journal of Engineering for Gas Turbines and power 141(3), 2018, doi: 10.1115/1.4040815

9. Inhestern L. B., Braun J., Paniagua G., Serrano J.R., Design, Optimization and Analysis of Supersonic Radial Turbines, Journal of Engineering for Gas Turbines and Power, accepted for publication

10. Braun J, Paniagua G., Falempin F., Le Naour F., Design and Experimental Assessment of Bladeless Turbines for Axial Inlet Supersonic Flows, Journal of Engineering for Gas Turbines and Power, accepted for publication

11. Liu Z, Braun J., Paniagua G. Three Dimensional Optimization for Subsonic Axial Turbines Operating at High Unsteady Inlet Mach Number, Energy, currently under review

Book Contributions

1. Braun J., Saracoglu B.H., Paniagua G., 2014, Analysis of continuous detonation wave combustor outlet conditions. Transient Combustion and Detonation Phenomena: Fundamentals and Applications, Torus Press, Moscow, ISBN 978-5-94588-149-5y. ISBN 978-5-94588-149-5

Fully Reviewed Conference Proceedings

1. Braun J., Lu S., and Paniagua G., Development of high frequency virtual thermocouples, Proceedings of the ASME Turbo Expo, June 2017, Charlotte, (GT2017-64669), Charlotte 2017

2. V. Andreoli, J. Braun, G. Paniagua, C. De Maesschalck, M. Bloxham, W. Cummings, and L. Langford, Aerothermal Optimization of Fully Cooled Turbine Blade Tips, Journal of Turbomachinery, Proceedings of the ASME Turbo Expo, June 2018, GT2018-75099, Oslo

3. Liu Z., Braun J., and Paniagua G., Characterization of a Supersonic Turbine Downstream of a Rotating Detonation Combustor, Proceedings of the ASME Turbo Expo, June 2018, GT2018-76798, Oslo

4. Liu Z., Inhestern L., Braun J., and Paniagua G., Unsteady Heat Transfer Assessment of Supersonic Turbines Downstream of a Rotating Detonation Combustor, Proceedings of the ASME Turbo Expo, June 2019, GT2019-91460, Phoenix

5. Inhestern L. B., Braun J., Paniagua G., Serrano J.R., Design, Optimization and Analysis Of Supersonic Radial Turbines, Proceedings of the ASME Turbo Expo, June 2019, GT2019-91756, Phoenix

6. Braun J, Paniagua G., Falempin F., Le Naour F., Design and Experimental Assessment of Bladeless Turbines for Axial Inlet Supersonic Flows, Proceedings of the ASME Turbo Expo, June 2019, GT2019-91047, Phoenix

Conference Proceedings

1. Braun J., Saracoglu B.H., Paniagua G., Analysis of continuous detonation wave combustor outlet conditions. International Colloquium on Pulsed and Continuous Detonation Combustors, June 2014, St. Petersburg

2. Braun J., Saracoglu B.H., Paniagua G., Magin T.E., Mono-dimensional analysis of the MagnetoHydrodynamic effect in Rotating Detonation Combustors, AIAA Science and Technology Forum and Exposition, January 2016, San Diego (AIAA 2016-0898)

3. Braun J., Sousa J., Paniagua G., Assessment of the Boundary Layer within a Rotating Detonation Combustor, AIAA Propulsion and Energy Forum and Exposition, July 2016, Salt-Lake City, (AIAA 2016-4557)

4. Braun J., Sousa J., Pekardan C., Aerodynamic Design and Analysis of the Hyperloop Pod , AIAA Propulsion and Energy Forum and Exposition, July 2016, Salt-Lake City, (AIAA 2016-4812)

5. Braun J., Paniagua G. Unsteady Temperature Measurements through Digital Compensation of Dual Wire Thermocouple, XXIII Bi-annual symposium on measuring techniques in turbomachinery, September 2016, Stuttgart

6. Braun J., Saavedra J., and Paniagua G., Evaluation of the unsteadiness across nozzles downstream of rotating detonation combustors, 55th AIAA Aerospace Sciences Meeting, AIAA SciTech Forum, January 2017, Grapevine, (AIAA 2017-1063)

7. Braun J., Paniagua G., Falempin F.H., and Le Naour B. Bladeless turbines for unsteady high speed flows, 21st AIAA International Space Planes and Hypersonics Technologies Conference, International Space Planes and Hypersonic Systems and Technologies Conferences, Xiamen, February 2017 (AIAA 2017-2422)

8. Liu Z, Braun J., and Paniagua G. Performance of axial turbines exposed to large fluctuations, 53rd AIAA/SAE/ASEE Joint Propulsion Conference, AIAA Propulsion and Energy Forum, Atlanta, July 2017 (AIAA 2017-4817)

9. Liu Z, Braun J., and Paniagua G. Three Dimensional Optimization for Subsonic Axial Turbines Operating at High Unsteady Inlet Mach Number, 54rd AIAA/SAE/ASEE Joint Propulsion Conference, AIAA Propulsion and Energy Forum, Cincinnati, July 2018 (AIAA 2018-4480)

10. Bhatnagar L., Braun J., Andreoli V., Gonzalez D., Liu Z., Paniagua G., Developments In High Frequency Directional Probes For High Temperature Applications, XXIV Biennial Symposium on Measuring Techniques in Turbomachinery, Prague, 2018

11. Braun J., Paniagua G., Analysis of continuous detonation wave combustor outlet conditions, International Colloquium on Pulsed and Continuous Detonation Combustors, September 2018, St. Petersburg